Radiative properties of dry and crystal-bearing lavas

Jonas Biren

To cite this version:

Jonas Biren. Radiative properties of dry and crystal-bearing lavas. Earth Sciences. Université d'Orléans, 2022. English. NNT : 2022ORLE1015 . tel-04087234

HAL Id: tel-04087234
https://theses.hal.science/tel-04087234v1

Submitted on 3 May 2023

UNIVERSITÉ D'ORLÉANS

ÉCOLE DOCTORALE Energie, Matériaux, Sciences de la Terre et de l'Univers
UMR 7327 INSTITUT DES SCIENCES DE LA TERRE d'ORLÉANS

THÈSE présentée par :

Jonas BIREN

Soutenue le : 22 juin 2022

Pour obtenir le grade de : **Docteur de l'Université d'Orléans**
Discipline/ Spécialité : Sciences de la Terre

Radiative properties of dry and crystal-bearing lavas

THÈSE dirigée par :

SLODCZYK Aneta	Ingénieure de recherche CNRS HDR, ISTO–CEMHTI
ANDÚJAR Juan	Chargé de recherche CNRS, ISTO

RAPPORTEURS :

DELMAS Agnès	Maîtresse de conférences HDR, INSA Lyon–CETHIL
VILLENEUVE Nicolas	Maître de conférences HDR, IPGP–OVPF

JURY :

BELLOT-GURLET Ludovic	Professeur des universités, Sorbonne université
DELMAS Agnès	Maîtresse de conférences HDR, INSA Lyon–CETHIL
MARTEL Caroline - Présidente	Directrice de recherche CNRS, ISTO
VILLENEUVE Nicolas	Maître de conférences HDR, IPGP–OVPF

Intelligence is the ability to adapt to change

– Stephen Hawking

À ma mère,

À mon père,

Acknowledgements

J'aimerais chaleureusement remercier mes encadrants, Aneta et Juan, qui m'ont épaulé tout au long de ma thèse. Durant ces années, ils m'ont préparé au métier de chercheur et montré la voie d'une science faite avec précision, passion, et détermination. Les leçons tirées de leurs enseignements sont innombrables pour être énoncées mais elles sont ancrées dans ma mémoire et ma pratique.

Viennent en second mes proches collègues de recherche, Leire, Lionel, Domingos, Aurélien et Olivier. Vous avez été mes personnes ressources et vous n'avez jamais tari de réponses face à mes questionnements. C'est grâce à vous que j'ai appris le plus, que j'ai exploré la spectroscopie vibrationnelle. Je vous remercie de m'avoir laissé puiser dans votre immense richesse intellectuelle.

Je voudrai remercier aussi les équipes administratives (je pense notamment à Marie-Noëlle, Marie-France, Fabienne, Lionel, Olivier, mention spéciale pour Virginie, les informaticiens, ceux qui travaillent au CNRS et à l'université). Vous avez pu répondre à toutes mes questions et mes doutes administratifs ; cela fait du bien de pouvoir compter sur votre expertise mais aussi sur votre gentillesse. J'ai apprécié que tous les services rendus ont été dans la bonne humeur.

Cette bonne entente et bonne humeur, je l'ai retrouvé aussi parmi tous les autres collègues. Les gars de l'atelier, Fred, Esteban, les Rémi, Didier, mais aussi Fabrice, Giada, Ida, Sandra, Emmanuel, Cécile. J'ai pris beaucoup de plaisir à travailler avec vous tous. Vous êtes généreux, compréhensifs, et toujours prêt à aider. Quelle ambiance à l'ISTO !
Je remercie aussi les enseignants, Adrien, Eric, Anne-Aziliz, Julien F., qui m'ont donné l'opportunité d'enseigner (le plus beau métier du monde) dans les meilleures conditions possibles.

Les thésards… Nous ne sommes que « de passage » ; nous nous rencontrons pour un court laps de temps (1 an à 4 ans selon les promotions). Mais durant ma thèse, j'ai partagé cette aventure avec vous et créé des liens forts. Grâce à vous, je n'ai passé que des moments heureux inoubliables. Vous êtes nombreux mais vous êtes tous rentrés dans mon cœur : Nicolas, Zineb, Morgane, Clément, David, Lucille, Federica, Fabien, Valentin, Benjamin, Camille, Monica, Diletta, Elena, Khadija, et tous ceux que j'oublie. J'inclue dans ces remerciements tous ceux que j'ai rencontrés à travers vous. J'espère que nos chemins se croiseront une nouvelle fois.

Mes prochains remerciements sont dédiés aux personnes qui ont compté le plus lors de cette aventure et ceux qui l'ont suivie au plus proche de moi. Maria, je n'aurais pas pu rêver une plus mémorable rencontre. J'ai pu profiter de la personne merveilleuse que tu es, au travail comme en-dehors. Au travail, tu m'as constamment motivé ; tu m'as poussé à donner le meilleur de moi-même. Nous avions créé notre propre énergie au bureau. Et en-dehors du travail, j'avais une amie toujours pétillante qui offrait ces moments de déconnexion. Julien, tu es devenu mon meilleur ami. Merci de m'avoir écouté, conseillé, prodigué ces moments hors du temps qui sont plus que nécessaires lors d'une thèse. Agathe, tu m'as permis de garder le cap sans céder au moment crucial des derniers mois de fin de thèse. L'émotion est forte…

Le support et l'amour de ma famille s'est fait ressentir jusqu'à Orléans. Ces fondations infaillibles sont des motivations inégalables. Cette thèse est aussi la vôtre en quelque sorte. Merci d'avoir préparé le plus beau pot de thèse au monde ! Merci à la famille étendue qui s'est déplacée (ou pas), je pense à ma marraine, Sophie, mes tantes, Bernard et Isabelle, mamy, Zazou, … Merci à tous ceux que j'ai oublié, le cœur y est tout autant.

Il ne me reste plus qu'à remercier mes amis proches de longue date : Boris, Maxime, Pauline, Stefano, Clara, Reaksa, Eléonore, Lauralee, JM, les copains de l'école ou d'ailleurs en Belgique, les copains de l'université ou d'ailleurs en France, … Vous avez été mes symboles d'assurance, de confiance, de persévérance et de détente. Vous m'apportez tant.

La musique m'a accompagnée tout au long de ma thèse et a amplifié toutes mes émotions, dans les meilleurs comme dans les pires moments. Mais la musique a cette énergie qui vous rend invincible et capable de réaliser une thèse. L'album que j'ai le plus écouté durant ces années fut : Ólafur Arnalds – Island Songs. Enregistré en Islande, il se prête parfaitement bien à la lecture de ce manuscrit.

Je remercie celle ou celui qui lira cette thèse car nous partageons un point commun : la passion des volcans.

Contents

Chapter Introduction

This chapter introduces the problematic that gave rise to the present study. The problematic is related to the measurement of temperature in an active lava flow. The techniques to measure the lava temperature are presented, with emphasis on remote sensing techniques and their limitation. The definition of spectral emissivity, parameter at the heart of this study, is given. Finally, the outline of the thesis is described.

Bárðarbunga eruption 4th of September 2014. Credit: perterhartree – https://www.flickr.com/photos/41812768@N07/15146259395/

1.1. Motivation: lava flow dependence on temperature

Lava flows are one of the main hazards related to effusive basaltic volcanism as demonstrated in recent eruptions of Piton de la Fournaise on Réunion Island (2007-2021; Chevrel et al. 2021), Bárðarbunga in Iceland (2014; Kolzenburg et al. 2017), Etna or Stromboli in Italy (2021; Calvari et al. 2021), Kilauea on Hawaii Island (2014, 2018; Neal et al. 2019; Biren et al. 2020) and La Palma on Canary Islands (Carracedo et al. 2022). Although lava may threaten a community relatively slowly and with due warning, its progression into a vulnerable population will be at best difficult to control. Since active lava flows burn and bury all in its path, the community evacuation is always necessary. For instance, the lavas from the recent eruption of La Palma (Canary Islands) affected one of the most populated and most prosperous agricultural and tourist areas of this island, destroying 2800 buildings and almost 350 hectares of farmland. Around 8000 inhabitants (10% of La Palma population) were relocated during this eruption considered as the most disastrous in the recorded history of the island (Carracedo et al. 2022). Fortunately, no human casualties were deplored thanks to the effective volcanic crisis management. To achieve this "feat", and for minimizing lava flow impact on surrounding locations, it is strictly necessary to continuously monitor the lava surface evolution and accurately model their propagation as to predict their potential run-out distance. The understanding and modelling of these processes require accurate data on the radiative properties of magmas and surrounding media. To this end, temperature (T) becomes one of the key parameters to be precisely determined since it strongly controls the rheological properties (crystal content, viscosity, density) of the progressing lava flow (Pinkerton and Wilson 1994; Harris et al. 2005; Kolzenburg et al. 2018; Chevrel et al. 2019). That is these temperature-dependent properties control the lava flow capacity to flow or to inflate.

Magmas are a complex mixture of silicate melt, crystals of various sizes, types, compositions, and different amounts of volatiles at depth. The ascent of magmas and emplacement at surface promotes their degassing, cooling, and crystallization. Consequently, the material emplaced at the surface is a dry and more or less crystal rich lava that evolves with temperature (up to ~1473 K for basalts) and composition (Takeuchi 2011). The lava heat loss, the effusion rate and the underlying topography exert an important control in the final physico-chemical properties of the lava flow, but also on the surface morphology evolution and the lava distance-to-run (i.e., distance at which the lava would stops; Peterson and Tilling 1980; Pinkerton and Norton 1995; Calvari and Pinkerton 1999; Rogic et al. 2019a; Giordano et al. 2020). The most challenging part during eruptions is to predict the future evolution and the dynamics of lava flows owing to the continuous temporal and spatial transformation of the rheological properties during lava emplacement. Hence, a detailed understanding of the rheological evolution measured *in situ* (e.g., temperature, viscosity) or estimated from remote sensing data, combined with detailed petrological information (gained from 1 bar crystallization experiments simulating the cooling and crystallization of the magma at surface) is necessary. To achieve this goal, the temperature of the magma at the emission point and its evolution along the flow must be determined as precisely as possible. As shown in Figure I-1, the exact knowledge of temperature is crucial since small temperature variation (i.e., 25–30 K) can increase the crystal cargo of the magma by 50% (red arrow in Figure I-1a), which, in turn, can shift the magma properties from low to high viscosity regime (i.e., ~2 log units, red arrow in Figure I-1b) (Andújar and Scaillet, 2012; Costa et al., 2009, Scaillet et al., 1998).

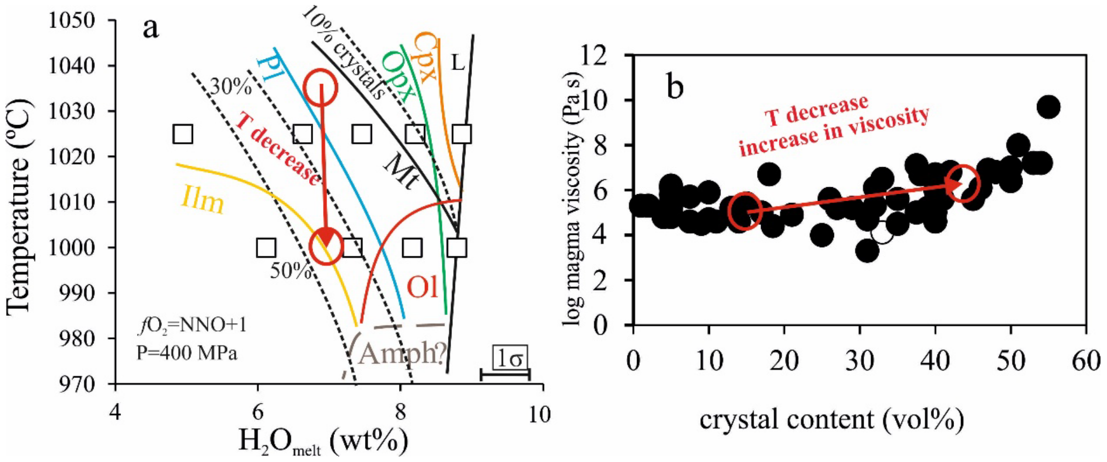

Figure I-1: a) Phase diagram of a basaltic andesite at 4 kbr. Note the increase in crystal content at 7 wt.% H_2O melt when T is decreased by 35 ºC (modified from Andújar et al. 2017). b) Evolution of viscosity vs. crystal content in magmas (modified from Andújar and Scaillet 2012).

1.1.1. Lava temperature determination

Lava temperature at the emission point can be accurately retrieved by laboratory post-mortem analytical and petrological analyses of volcanic products (i.e., rocks and minerals; Putirka 2008; Scaillet et al. 2008; Andújar et al. 2013). Although this experimental approach is very precise allowing tight constraints on temperature up to ±15 K, it is highly time consuming (Re et al. 2021) and can then hardly be applied to gain temperature information during time-sensible eruption. Consequently, *in situ* field measurements of newly emitted lava are widely applied.

In this case, a thermocouple (T_c) is manually inserted into the accessible hot parts of progressing lava to retrieve local temperature (Figure I-2a). Despite the accuracy of these direct measurements, they are difficult and impractical to carry out because of the hazardous and unpredictable behavior of eruptions. Moreover, because of the slow T_c response time, its punctual character (Roberts et al. 2011) and the rheological complexity of distal products (i.e., high crystal content, high viscosity, variable melt composition) compared to those at emission point (i.e., higher temperatures and lower crystallinity), these measurements suffer from poor representativeness and are unable to provide data over extended periods and spatial coverage.

In this light Remote Sensing (RS)-based techniques (e.g., pyrometers, thermal cameras, and satellites; Figure I-2b-c) allowing the temperature monitoring of lava without contact appear especially advantageous.

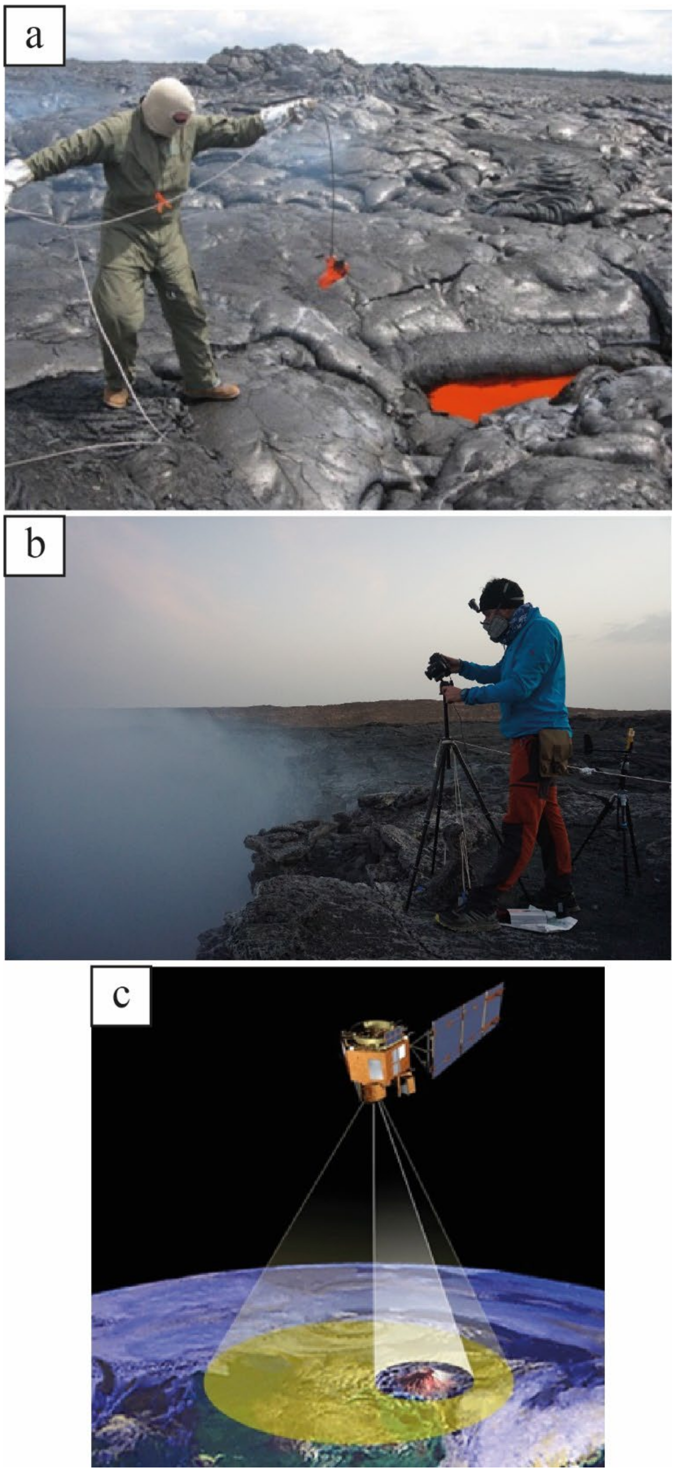

Figure I-2: Lava flow temperature measurements: a) field contact method using thermocouples, b) field remote sensing using thermal camera, c) satellite-based remote sensing.

1.1.2. InfraRed Remote Sensing of volcanic surface activity

The Remote sensing-based devices measure the thermal emission flux (radiance) of a magmatic body which is later converted into temperature using Planck's law (Figure I-3a, Aufaristama et al., 2019; Blackett, 2017; Chevrel et al., 2019; Harris, 2013; Ramírez-González et al., 2019; Rogic et al., 2019). All objects with temperatures greater than absolute zero (T>0 K) emit electromagnetic radiation. The energy emitted from an object (i.e., radiant flux or total emissive power) is quantified in terms of spectral radiance (in units of W m^2 sr^{-1} m^{-1}) that in the case of blackbody (ideal radiator that totally absorbs and re-emits all received energy, in thermal equilibrium conditions) is given by the Planck function:

$$L_\lambda(T) = \frac{2hc^2}{\lambda^5\left(exp^{\frac{hc}{\lambda kT}} - 1\right)} \qquad \text{I-1}$$

In which h is Planck's constant (6.6256×10^{-34} J s), c is the speed of light (2.9979×10^8 m s^{-1}), k is the Boltzmann gas constant (1.38×10^{-23} J K^{-1}) and λ is the wavelength. Because temperature and wavelength are the only variables, Equation I-1 can be simplified (King et al. 2004) by combining the constants:

$$c_1 = 2hc^2 = 1.19 \times 10^{-16}\, W\, sr^{-1}\, m^2$$

and

$$c_2 = \frac{hc}{k} = 1.4393 \times 10^{-2}\, m\, K$$

Equation I-1 can be then rewritten as follows:

$$L_\lambda(T) = \frac{c_1}{\lambda^5\left(exp^{\frac{c_2}{\lambda T}} - 1\right)} \qquad \text{I-2}$$

Figure I-3a shows the spectral distribution of the emitted energy (radiation curve) of a blackbody at different temperatures, thus graphically representing Equation I-2. Planck's law, which relates directly emitted radiance and body temperature, can be finally transformed into Equation I-3:

$$T = \frac{c_2}{\lambda \ln\left(\frac{c_1\lambda^{-5}}{L(\lambda, T)} + 1\right)} \qquad \text{I-3}$$

In order to detect Earth surface (and volcanic activity) thermal emission, the RS instruments have detectors working from Infrared (IR) to visible (VIS) regions of the electromagnetic spectrum (Figure I-3b): 1) TIR: Thermal InfraRed range, 8–14 µm; 2) MIR: Mid InfraRed range, 3–5 µm; 3) SWIR: Short-Wave InfraRed range, 1–2.5 µm, and 4) VIS: VISible, range , 0.4–0.7 µm. As shown in Figure I-3b, the choice of these spectral regions and the associated measured spectral RS bands is governed by the Earth atmospheric window where the detection of a body radiation is maximum due to the minimum atmospheric absorption (CO_2, H_2O and O_3).

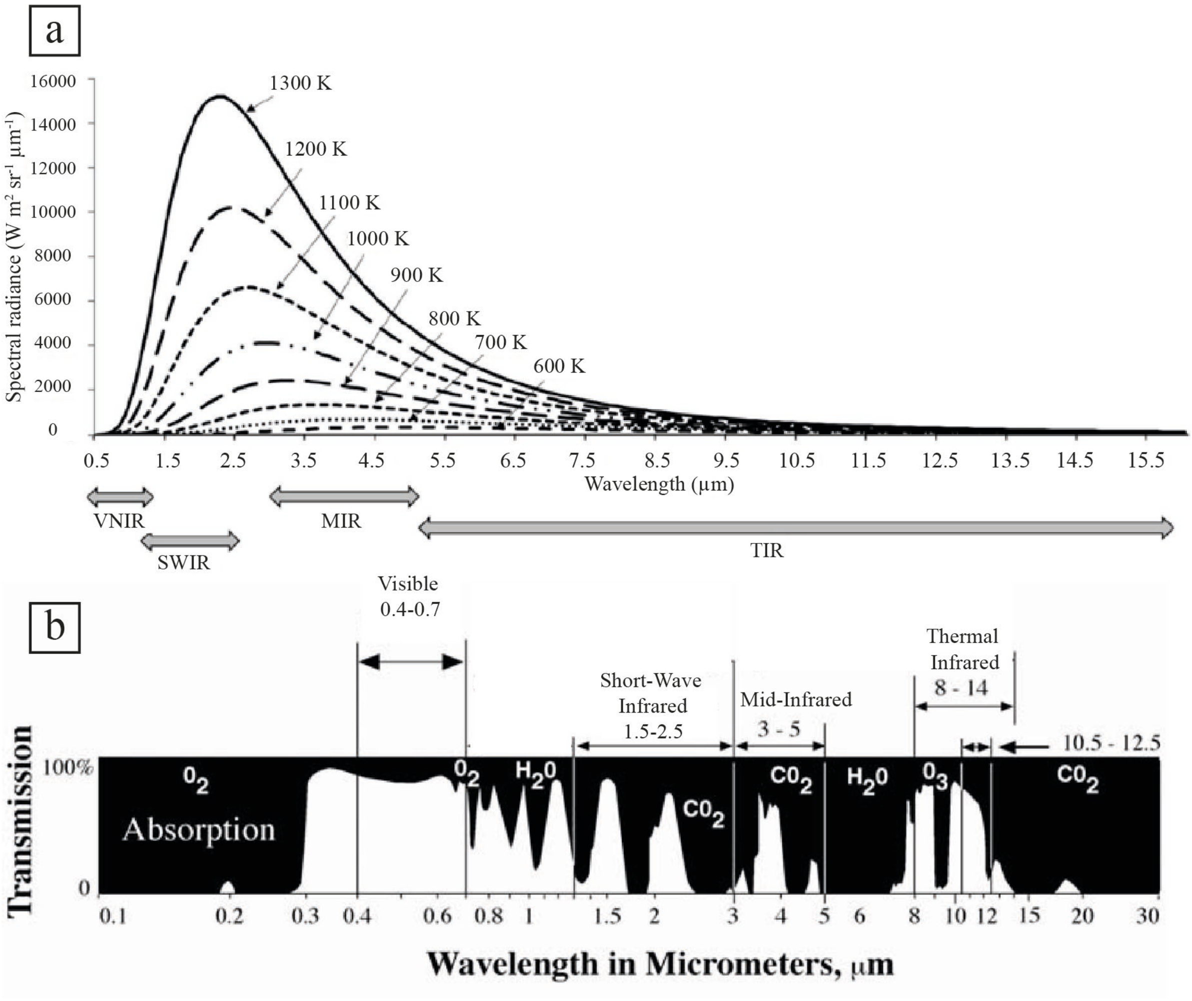

Figure I-3: a) Relationship between the spectral radiance and temperature of the emitting surface representing Planck function; different IR spectral ranges are depicted (from Blackett 2017). b) Earth atmospheric window used in Remote Sensing Application: characteristic bands through measured spectral regions: Thermal InfraRed–TIR, Mid InfraRed–MIR, Short-Wave InfraRed–SWIR and Visible–VIS (from Alavipanah et al. 2010).

Different instruments are used to IR monitor eruptions (thermal cameras, ground based pyrometers or on board airplanes or satellites: Terra/Aqua, Sentinel, Landsat, GOES, etc., (Ramsey and Harris 2013; Thompson and Ramsey 2020a), all of them working at different wavelengths, and hence having different sensibilities. Their efficiency relies on fundamental relationships between spatial (the area that is imaged by one pixel), spectral (the capacity of a sensor to distinguish different parts of the electromagnetic spectrum, number of spectral bands) and temporal (the frequency at which the sensor images the same surface area) resolutions.

These devices cover a broad range of temperatures and wavebands of the spectrum (Figure I-3b), the TIR being the range most commonly used (Harris 2013 and references therein; Ramsey et al. 2016). The choice of TIR among other spectral regions is related to the fact that 1) terrestrial lavas have anticipated emissivity maximums located broadly within this region and 2) interferences with atmospheric H_2O, CO_2 and O_3 is weak in the usable spectral bands 8–9 and 10–12 μm. However, information from the MIR and SWIR regions can be also used for volcanic monitoring purposes (Ramsey and Harris 2013). Yet, the daytime data obtained in these regions often contain non-negligible solar radiation contributions, which complicate the subsequent analysis of the bulk radiative signal (Ramsey et al. 2016). On the contrary, sun interferences decrease in the TIR allowing a better determination of the surface brightness temperature. However, the experience shows that TIR datasets acquired over large areas of extremely hot targets result in a saturation of the signal, thereby rendering quantitative analyses often impossible (Rose et al. 2014). In this case, a new and currently massively used multisensor approach is preferred to interpret radiative signals: SWIR-night, high- spatial resolution information (down to 10 m in Sentinel-2 satellite) is used first to retrieve potential magmatic temperatures and then to predict the TIR day radiance of the surface (Lucey et al. 2017; Aufaristama et al. 2018, 2019a; Massimetti et al. 2020). The combination of two distinct infrared bands to formulate a system of two equations as to find the simultaneous solution of the Planck equation for the pixel-integrated radiance is at the base of the so called dual-band method developed by Dozier (1981). In consequence today, the combination of TIR–SWIR datasets represents a major improvement for retrieving realistic thermal radiances and temperature of targets (Alvez Rolim et al., 2016; Harris et al., 2005; Rogic et al., 2019b; Wright et al., 2000, etc.).

These well-established RS techniques are however subjected to assumptions and limitations that can propagate important errors from measurements to derived eruptive parameters, especially for temperature. Measurements can be impacted by the variation of surrounding environment (e.g., atmospheric absorption, Gillespie et al. 1998; Harris 2013; Yang et al. 2020), and the constant changes in temperature, composition and texture of the cooling lava (Ramsey et al. 2019). Even if the uncertainties of environmental and thermal gradients can be reduced, measuring emission flux, and determining temperature is ultimately challenging since today the variation of radiative properties of lava flow with temperature is poorly understood (Gillespie et al. 1998). Decorrelation of emissivity and temperature from infrared measurements is not a trivial task. Since the surface is characterized by its temperature and by one emissivity for each spectral band, there always remain more unknowns than measurements. Inversion methods (e.g., Sobrino et al. 1994; Gillespie et al. 1998; Dash et al. 2002) have to make assumptions to bypass this difficulty. In particular, the Temperature Emissivity Separation (TES) algorithm, developed for ASTER data by Gillespie et al. (1998), combines the iterative removal of atmospheric radiance and an empirical relationship allowing absolute emissivity recovery. Thus, the radiative properties, and especially hitherto poorly known and oversimplified parameter, namely the spectral emissivity (ε) of lava appears as the greatest source of inaccuracy (Harris 2013; Zakšek et al. 2013; Rogic et al. 2019a). This parameter is crucial to invert remotely sensed data from lava flow's emission flux and to retrieve its temperature. For instance, 10% change in emissivity results in a measured temperature difference of 83 K (Mouginis-Mark et al. 1991; Ball and Pinkerton 2006) and up to 300 m difference in lava distance-to-run (Rogic et al., 2019a, 2019b). The temperature difference given in this simple example has non negligible rheological consequences on the state of lava, which can change from liquid-dominated to solid-dominated flow (Andújar et al. 2015).

1.1.3. Spectral Emissivity

Spectral emissivity (ε) is the physical capacity of a material (e.g., lava flow) to emit heat radiation. The inner microscopic and macroscopic structure of the body (i.e., degree of polymerization; composition; presence of heterogeneities such as crystals, bubbles) exert an important control on phonon propagation and emissive behavior. Since magma composition and crystal content is strongly dependent on temperature (Takeuchi 2011; Andújar and Scaillet 2012), the progressive cooling and crystallization of an evolving lava necessarily result in a continuous evolution of its radiative properties. Hence, to retrieve more precise temperature values using remote sensing techniques, it is necessary to have precise knowledge on the magma spectral emissivity. In order to determine the thermal radiative properties of a semitransparent body, two complementary methods of emissivity measurements can be applied: a direct and indirect.

In the direct method, the spectral emissivity (ε_λ) is defined as the ratio between the normal spectral radiance of the sample (L_λ) and that of the blackbody (L_λ^0) in the same thermal and optical conditions (Stefan 1879; Boltzmann 1884):

$$\varepsilon_\lambda(\sigma, T, \theta) = \frac{L_\lambda(\sigma, T, \theta)}{L_\lambda^0(\sigma, T, \theta)} \qquad \text{I-4}$$

The indirect method is based on the second Kirchhoff's law where the spectral emissivity (ε_λ) is indirectly derived from measurements of spectral reflectance (ρ_λ) and spectral transmittance (τ_λ), such as:

$$\varepsilon_\lambda(\sigma, T, \theta) = 1 - \rho_\lambda(\sigma, T, \theta) - \tau_\lambda(\sigma, T, \theta) \qquad \text{I-5}$$

Note that for opaque materials with $\tau_\lambda = 0$ (the case of many magmatic/geological rocks and minerals, cf. Chapter 1) ε_λ relies exclusively on ρ_λ measurement:

$$\varepsilon_\lambda(\sigma, T, \theta) = 1 - \rho_\lambda(\sigma, T, \theta) \qquad \text{I-6}$$

Both methods have important advantages and drawbacks. The direct method allows to measure spectral emissivity up to very high temperatures, (i.e., >2000 K; Rozenbaum et al. 1999), but at low temperatures (i.e., ≤500 K) only a limited spectral range can be measured, not exceeding 3000 cm^{-1} (MIR). On the contrary, the indirect method is impractical at temperatures >1000 K (Rozenbaum et al. 1999) because of the sample self-emission that hinders the reflection measurements and saturates the detector, but gives access to wide spectral range (up to ~10000 cm^{-1}) at lower temperatures.

Figure I-4 shows an example of emissivity spectrum characteristic of a semitransparent magmatic mineral, plagioclase (Labradorite) measured using the direct method at 647 K (Figure I-4a) and determined using the indirect method based on previous ambient temperature transmittance and reflectance measurements (Figure I-4b). The typical broadband emissivity spectrum of such dielectric material (e.g., silicate mineral, here plagioclase) can be divided into three spectral windows:

1- The so-called opaque region at <1500 cm^{-1} (covering the TIR) that reveals the lattice vibrations of the main silicate structure network. This region is characterized by the presence of fundamental absorption bands with the so-called Reststrahlen bands (corresponding to the highest values of reflectivity or lowest value of emissivity). Moreover, the opaque region includes the so-called Christiansen wavenumber or Christiansen Feature (CF), defined as the wavenumber (or wavelength) at which a dielectric material behaves as a perfect blackbody ($\varepsilon = 1$). The CF is an intrinsic feature of a given material and together with the Reststrahlen bands, is commonly used as a diagnostic tool for mineral/rock identification, cf. Chapter 1: (Logan et al. 1973; McMillan 1984; Ruff et al. 1997; Christensen et al. 2000; Cooper et al. 2002; King et al. 2004; Colomban and Prinsloo 2009). CF can be also used to precisely determine the object temperature, cf. Chapter 2 (Rozenbaum et al. 1999; De Sousa Meneses et al. 2015);

2- The spectral region between 1500 and 3500 cm^{-1} (covering the MIR) is assigned to multiphonon processes. In this region, semitransparent objects are characterized by the presence of a transmission front (TF), i.e., a spectral feature around 2000–2300 cm^{-1} where ε significantly decreases;

3- The spectral region >3500 cm^{-1} (covering the SWIR) is related to electronic processes/absorptions (Rozenbaum et al. 1999; De Sousa Meneses et al. 2006). Note that many materials appear transparent in this spectral region.

The radiative properties of a semitransparent object measured in the low wavenumber spectral region, i.e. TIR, are exclusively representative of its surface. On the contrary, the radiative properties recorded in the multiphonon and electronic regions (i.e. MIR and SWIR) are characteristic of the probed volume, which depends on optical thickness and object absorption coefficient (De Sousa Meneses et al. 2004).

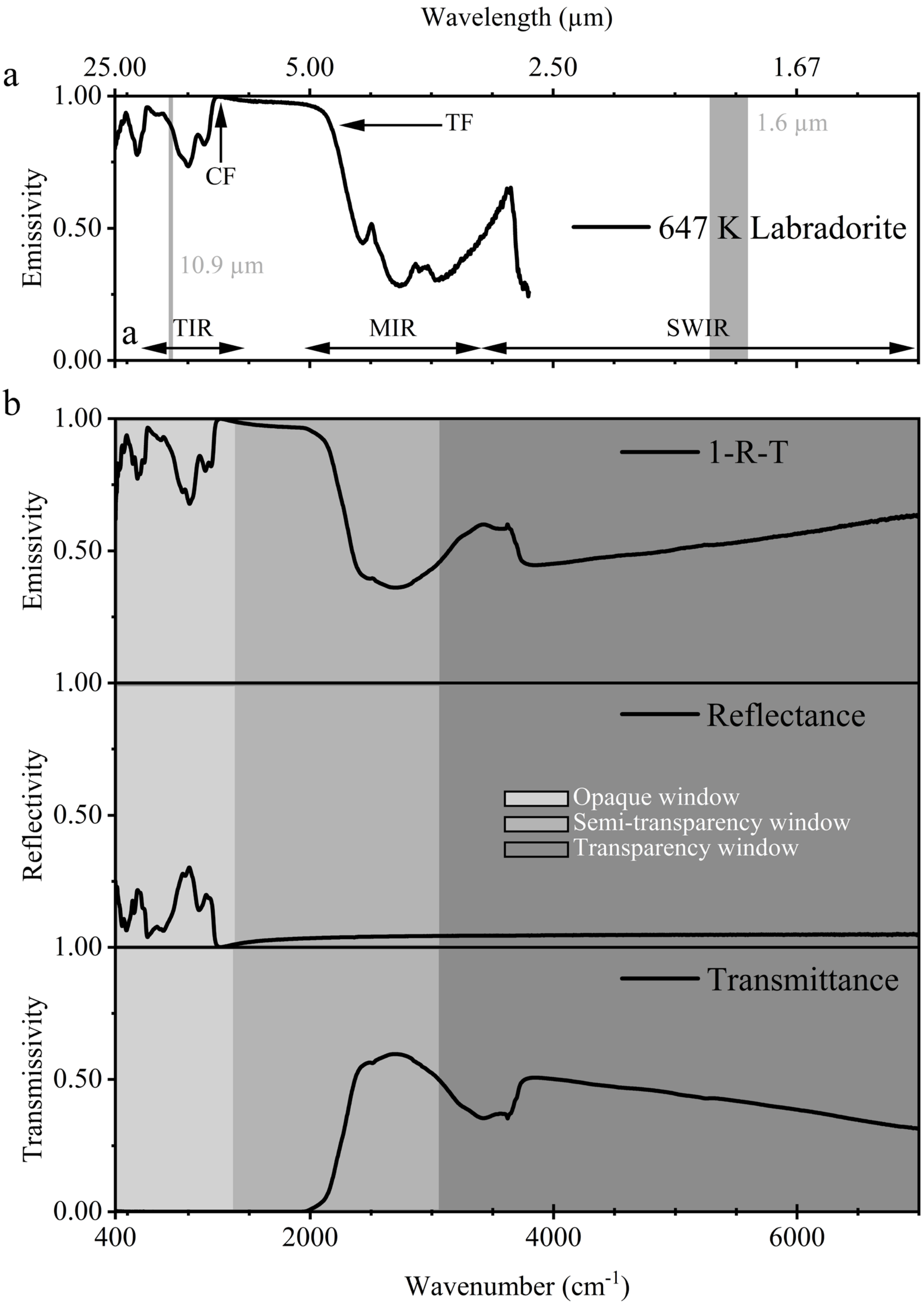

Figure I-4: Emissivity spectrum of Labradorite (Na, Ca rich plagioclase): a) measured using direct method at 647K. Characteristic spectral bands used in the remote sensing application: 10.9 µm and 1.6 µm are also shown. b) determined using indirect method at room temperature from the reflectance and transmittance measurements. Characteristic spectral regions (TIR, MIR, SWIR), opaque, semitransparent, and transparent as well spectral features CF: Christiansen Feature. TF: Transmission Front are marked.

As we will show in detail in Chapter 1, ε of many silicates samples is well known at room and low temperatures (<353 K). There is, however, an apparent lack of spectral emissivity data for natural compositions recorded at magmatic temperature conditions. In remote sensing application, this lack of experimental data prompt to the default approach of using a constant, room temperature ε value for a given rock family, for example 0.9 for basalts (Crisp et al. 1990; Thomson and Salisbury 1993; Oppenheimer 1993; Harris and Thornber 1999; Calvari et al. 2005; Harris 2013; Chen et al. 2015; Ramsey et al. 2016; Kaneko et al. 2021; Thompson and Ramsey 2021). Recent works (Rogic et al. 2019; Thompson and Ramsey 2020b; 2021) claim that such emissivity oversimplification can in turn under- or over-estimate the derived effective field radiation temperature and impact the modeled distance-to-run of the lava flow.

To date, only few laboratory works measured the ε–T dependences with relative success (Lee et al. 2013; Bouvry et al. 2017; Rogic et al. 2019; Thompson and Ramsey 2020a; Lombardo et al. 2020; Thompson et al. 2021). Most of these works have been performed on crystals or synthetic glasses over limited temperature range (typically at temperature not exceeding the glass transition T_g) and spectral range (typically the TIR region; Ramsey and Christensen 1998; Byrnes et al. 2007; Harris 2013 and references therein; Lee et al. 2013; Rogic et al. 2019; Pisello et al. 2019). Moreover, the use of different apparatus having different set ups, sensibilities, loaded with synthetic compositions and different textures (e.g., rock powders, glassy materials), results in the production of a variable dataset of spectral emissivity values and contrasting ε–T relationships.

All these works highlight the complex relationship existing between emissivity and temperature and recommend a tightly constrain on the ε–T dependence for each magma composition (information which is today missing) over a wider spectral range (including MIR and SWIR) and at relevant magmatic temperatures (up to ~1500 K) as to select ε values adapted to the targeted magma.

1.2. Thesis Outline

The importance of radiative properties in lava flow risk mitigation and the necessity of providing more accurate constrains on spectral emissivity are evident. Spectral emissivity is the crucial parameter to invert remotely sensed data from lava flow's emission flux in order to retrieve its temperature. In this framework, the aim of this study is to fulfill the knowledge gap related to spectral emissivity–temperature relationship on different magmatic compositions as well as on the factors controlling this parameter (e.g., crystal type and relative proportions).

To achieve this goal, the evolution of the radiative properties of dry and crystals rich basaltic magmas were measured *in situ* over a large range of temperatures (from room temperature up to 1800 K) and in a wide spectral range (400–8000 cm^{-1}) covering TIR, MIR and SWIR using IR thermal emission apparatus (De Sousa Meneses et al. 2015; Li et al. 2021). Basaltic compositions were especially addressed since this magma type is the most common on Earth (Walker 1993).

This experimental approach allowed studying the following scientific objectives:

1) The ε–T relationships, at relevant magmatic temperatures (up to 1600 K), of four different basaltic compositions *lato sensu*, both homogenous glasses and heterogeneous natural crystal-rich rocks. The effect of basalt composition and texture on spectral emissivity was carefully investigated.

2) The impact of the crystal content and composition on radiative properties of basaltic dry magmas. For this, the ε–T relationships of three major mineral phases found in basaltic magmas (plagioclase, pyroxene, and Fe-rich oxide) were measured *in situ* over the same spectral and temperature conditions.

3) The refinement of the temperature of Bárðarbunga lava flow (Holuhraun eruption) derived previously by RS technique using our variable f(T, λ) laboratory measured emissivity values. These data provide a basis for minimizing the uncertainty in RS temperature retrieval of lava flows.

This manuscript is organized into seven chapters as follows:

Chapter 1 presents the state-of-the-art on spectral emissivity measurements performed on magmatic rocks and minerals both at ambient and up to high temperatures (1600 K). It also describes recent remote sensing applications to lava flows using spectral emissivity as input parameters. The description of Holuhraun eruption as geological settings closes this chapter.

Chapter 2 frames the experimental methods used in this study with the focus on *in situ* high temperature spectral emissivity measurements. The experimental protocol of sample preparation and the description of other analytical techniques allowing chemical, textural, structural, and thermal analyses are also detailed.

Chapter 3, at the heart of this work, deals with the emissivity–temperature relationship of different basalts *lato sensu*, especially Bárðarbunga basalt composition. The effect of composition on high temperature radiative properties of basalts and the origin of the opacification phenomenon are discussed before being compared with previous works. The emissive behavior of basaltic glass is compared to that of a fully crystallized basalt at the end of this chapter.

Chapter 4, the most exploratory and innovative part of this work, describes the spectral emissivity evolution with temperature of major basaltic minerals present in the Bárðarbunga samples. The mineral radiative properties are used to model that of natural Bárðarbunga basalt as well as of two synthetic samples containing different crystal contents. The comparison of modeled and measured results allowed us discussing the impact of mineral presence on spectral emissivity of basaltic magmatic rocks. Finally, the determined conclusions are applied to the description of an Oceanite (a case study from Piton de la Fournaise).

Chapter 5, dedicated to the application of our laboratory measurements, is devoted to the refinement of the Holuhraun lava flow temperature determined previously by RS methods. Namely, our laboratory measured spectral emissivity values were used to refine thermal maps obtained from field-based models. The temperature gain allows discussing the importance of spectral emissivity in remote sensing applications.

The last chapter, Conclusions and Perspectives, first gives the main highlights and relates the novelty of this study, then proposes the future roadmap of laboratory and remote sensing approach in volcano crisis, rheology applications, and material sciences.

The bibliography and appendices are enclosed in the last chapter at the end of this manuscript.

Chapter 1:

State-of-the-art

This chapter details first the literature studies related to the spectral emissivity considered in volcanology: the case of magmatic rocks and lavas, as well as magmatic minerals. Afterwards, the Bárðarbunga Holuhraun eruption is described.

Pahoehoe lava lobe at Kilauea (Hawaii). Credit: USGS

1.1. Spectral Emissivity in volcanology: State-of-the-art

As stated in previous chapter, spectral emissivity is the critical parameter to be precisely determined for RS applications. Accordingly, in the recent decades, spectral emissivity of rocks and minerals was thoroughly studied at ambient temperature or low temperature (<350 K) mostly for identification purpose. The resulting rock and mineral libraries of emissivity spectra were then extensively used in volcano remote sensing for the same purpose. The progression through time from the first emissivity spectra acquisition to remote sensing applications is succinctly presented here.

1.1.1. Spectral Emissivity measurements at low temperatures (<350 K)

Two of the first pioneering studies that explored the spectral emissivity of different types of rocks and mineral were carried out by Buettner and Kern, (1965); and Lyon, (1965, 1964). The latter determined the emittance, reflectance, and transmittance spectra of more than 300 unpolished rock and mineral surfaces in the 8–25 µm spectral range. Buettner and Kern, (1965), derived the emittance spectra of polished rock samples, from 8 to 12 µm, using reflectance measurements. In the case of minerals, Lyon's studies were based on the principle that vibrational motions occur within a crystal lattice at specific frequencies that are directly related to the crystal structure and elemental composition. Since for a given composition with local structure, characteristic spectral features such as Christiansen Feature (CF) and Reststrahlen band are detected at very specific wavenumbers (or wavelengths) they can be used as an excellent identification tool. They allow not only to differentiate between mineral types, but also, to identify and discriminate between the mineral species of a single mineral solid solution (e.g., differentiate between Mg-rich and Fe-rich olivine; Donaldson Hanna et al., 2012; Hamilton, 2010, 2000). Concurrently to minerals, each individual rock type is characterized by a typical emission spectrum which varies accordingly with composition (Lyon 1964, 1965; Buettner and Kern 1965); this information can be hence used to identify the type of rock that is under studies.

In the following years, few emissivity data were published except the work of Logan et al., (1973) that unravels the effects of particle size, packing, temperature (350 or 568 K) in which a reference background spectrum is recorded, atmospheric pressure and the use of an uniform heating on the radiative properties of 72 rocks. Note that similar studies were later conducted on olivine by Eckes et al., (2013); on feldspar by Hecker et al., (2010) and Li et al., (2021), and on silica by Rozenbaum et al., (1999). Further on, Vincent et al., (1975) reported the emittance spectra (measured indirectly from reflectance data in the 7.5–14 µm) of 26 igneous rocks covering basalt to rhyolitic compositions, as well as granite, diorite, peridotite *inter alia* (Figure 1-1). They found uniform high emissivity values (0.958±0.008) for 25 samples whereas the peridotite, had a significantly lower mean emissivity (0.895). The authors suggested that this result, combined with the dependence of emissivity on chemical composition, should permit the separation between temperature and chemical composition effects in RS application. However, based on the actual knowledge concerning the emission of different materials, such type of separation seems unlikely.

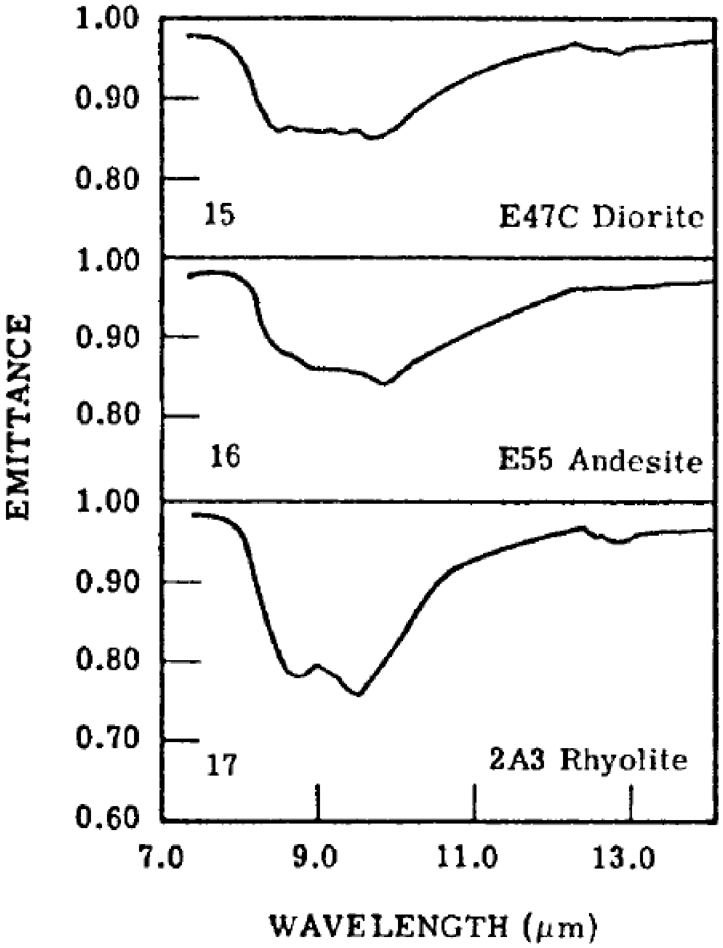

Figure 1-1: Example of TIR emissivity spectra of a diorite, andesite and rhyolite (modified from Vincent et al. 1975).

More recently, Salisbury and D'Aria, (1994, 1992) explored the spectral reflectance of coarse grained and fresh rough surfaces of a wide variety of igneous, sedimentary, and metamorphic rocks in the well-known 8–14 µm region, as well as in a newly proposed spectral range from 3 to 5 µm. Note that such MIR range was poorly used in RS applications at that time although it offered an advantage since RS temperature estimates are more than two times less sensitive to emissivity errors in this region. Their TIR results showed that the CF position systematically decreases with composition from felsic to ultramafic rock types, which is in good agreement with previous works (Lyon 1964; Logan et al. 1973; Vincent et al. 1975). They also observed that spectral emissivity is featureless (i.e., no absorption band) but highly variable in 3–5 µm range due to the presence of relatively transparent silicate rock-forming minerals.

The most recent emissivity spectra were documented by Cooper et al., (2002) and Wyatt et al., (2001). Cooper et al. (2002) examined 70 thermal IR spectra of solid rock samples and their powder equivalents (10 acidic, 10 intermediate, 11 basic, and 4 ultrabasic) as to better understand the relationships between spectral features, particle size, and composition. They revealed that the sample texture (powder vs. crystal), the particle size and vacuum environment have important impact on both CF and transmission front (TF) habits.

To summarize, in last ~30 years, these few but extensive works constitute the reference catalog that contains the vast majority of ambient temperature emissivity spectra of silicate rocks and minerals. These works clearly showed that each rock type and mineral can be identified by a unique emissivity spectrum characterized by the position, shape, and intensity of Reststrahlen bands, the CF and the TF (when visible). The analysis of these specific parameters allows therefore a successful material identification, emphasizing the usefulness of emissivity spectra for remote sensing application (some examples of application can be found in Cui et al., 2015; King et al., 2004; McMillan, 1984; Ramsey and Christensen, 1998; Rose et al., 2014; Ruff et al., 1997; Sprague et al., 2009; Wyatt et al., 2001; for extra-terrestrial surfaces: Donaldson Hanna et al., 2014; Glotch et al., 2004; Nuevo et al., 2014; Vaughan et al., 2003). Moreover, these literature data demonstrated that spectral emissivity is highly dependent on the sample composition, its physical properties (grain size, packing, surface roughness), its environment (temperature, atmospheric pressure) and on the instrumental and analytical conditions (spectral range, viewing angle, controlled atmosphere, etc.).

Despite the important amount of works that have addressed the emissivity measurements at low (T<350 K) temperature, there is a critical need for obtaining laboratory-based emissivity data retrieved at conditions approaching real environments (i.e., magmatic temperatures, complex natural samples, etc.). This lack of detailed experimental data prompt to the default approach of using a constant spectral emissivity value retrieved at ambient temperature (or T~350 K) for a given rock family (Calvari et al., 2005; Chen et al., 2015; Crisp et al., 1990; Harris, 2013; Harris and Thornber, 1999; Kaneko et al., 2021; Oppenheimer, 1993; Ramsey et al., 2016; Thompson and Ramsey, 2021; Thomson and Salisbury, 1993; Wooster and Rothery, 1997;). Table 1-1 illustrates well the latter statement and further shows that for a given composition the choice of a constant spectral emissivity value varies significantly from one study to another (e.g., from 0.5 to 1.0 for basalts only).

In consequence, the use of these emissivity libraries in RS monitoring of volcanological objects poses a double problem. First, flowing lava cannot be considered as an object with constant emissivity because of an important temperature gradient (from hot vent to much colder crust) rheological properties permanently evolve. Second, nowadays, thermal radiances are measured over a large spectral range, covering the TIR-MIR-SWIR spectral ranges; however, the constant emissivity values are mostly exclusively characteristic of TIR. Therefore, the use of oversimplified assumptions when considering the radiative properties of a surface material having a variable temperature results in important error propagation, that can distort the final derived parameters, i.e., temperature, thermal flux, emitted magma volume; Harris, 2013; Harris et al., 2016; Oppenheimer, 1993; Price, 1983; Ramsey et al., 2016; Burgi et al., 2002; Thomson and Salisbury, 1993).

Emissivity	Wavelength	Sample	Author
1	3.6-5.0	Basalt (Erta Ale)	Oppenheimer and Yirgu 2002
1	0.55-12.4	ash clouds (Pinatubo)	Oppenheimer et al. 1998
1	7-15	Basalt (Kilauea)	Hon et al. 1994
1	0.4-5	Basalt (Kilauea) and ultramafic	Davies et al. 2016
1	0.8-1.1	Basalt	Pieri et al. 1990
0.95-1	0.8-1.1	Basalt	Pinkerton 2001
0.95-0.97	0.8-1.1	Basalt	Crisp et al. 1990
0.5-0.9	0.8-1.1	Basalt	Rothery et al. 1988
0.995	0.8-1.1	Basalt (Kilauea)	Flynn et al. 1993
0.97	8-14	Basalt (Bardarbunga)	Aufaristama 2018
0.989	8-14	Basalt (Bardarbunga)	Bonny et al. 2018
0.973-0.984	7.5-13	smooth and rough basalts	Ball and Pinkerton 2006
0.95 / 0.93	8-14	Basalt (Etna)	Rogic et al. 2019
0.95	0.4-2.5	Basalt (Etna, Nyamuragira)	Wright et al. 2010
0.95	1.55-1.75	Basalt (Etna)	Wright et al. 2000
0.95	1.61 / 10.95-11.65	Andesite (Agung)	Aufaristama et al. 2018, 2019
0.95	7.5-13.5	Basalt (Krýsuvík)	Ramirez-Gonzalez et al. 2019
0.74	1.1-1.7	Basalt (Erta Ale)	Burgi et al. 2002
0.96 /0.6	0.4-14.4	Basalt (Tolbachik)	Ramsey et al. 2019
0.98	8.1-11.3	Andesite (Sinabung)	Carr et al. 2018
0.898	8-11.5	Basalt (Kilauea)	Thompson and Ramsey 2020
0.6-0.95	1.65-2.2	Basalt (Etna)	Rogic et al. 2019b
0.7	9	Deserts (quartz sand)	Prabhakara and Dalu 1976
0.90-0.95	1.55-14	Basalts (Momotombo and Etna)	Oppenheimer et al. 1993
0.92	1.6	Andesite (Lascar)	Wooster and Rothery 1997
0.95	7.5-14	Basalt (Stromboli)	Calvari et al 2005
0.965	7.5-13	Deserts (quartz sand)	Mushkin et al 2020
0.95	1.6	Basalt (Nishinoshima)	Kaneko et al. 2021
0.95	7.5-13.5	Andesite (Shiveluch)	Shevchenko et al. 2021
0.95	8-12	basalt (Solfatara, Campi Flegrei)	Silvestri et al. 2021
0.97	-	Basalt	Garel et al. 2016
0.9	-	Basalt	Allred 1998
0.85	-	Basalt (Kilauea)	Conroy and Lev 2021
0.95	-	basanite (Gran Canaria)	Rodriguez-Gonzalez et al. 2021
Variable	2.17-21	Basalt (Etna)	Rogic et al. 2022
Variable	8-14	Tholeiitic (Vulcano) and alkaline (Snake River Plain)	Pisello et al. 2019
Variable	8-25	Rocks (gabbro, basalt, dunite)	Lyon 1965
Variable	0.7-1.2	Venus rock and mineral analogs	Helbert etal 2015, 2017
Variable	8-12	Basalts	Ramsey etal 2016
Variable	1.8-2.4	Basalt (Etna)	Lombardo et al. 2020

Table 1-1: Emissivity values, at different wavelength ranges, of volcanic rocks (mostly basalts) used in RS application. Most of study considered emissivity as constant parameter. Note that the four studies (Allred 1998; Garel et al. 2016; Conroy and Lev 2021; Rodriguez-Gonzalez et al. 2021) related to lava flow modelling do not consider the spectral range. Few studies with variable emissivity can also be find in literature (cf. main text); this list is non-exhaustive.

1.1.2. Spectral Emissivity of magmatic rocks at high temperatures

In order to overpass the above mentioned limitations, recent works attempt to measure the emissivity of rocks at temperatures approaching such of magmas with relative success (Abtahi et al. 2002; Lee et al. 2013; Bouvry et al. 2017; Rogic et al. 2019a; Pisello et al. 2019; Lombardo et al. 2020; Thompson and Ramsey 2020a; Li et al. 2021; Thompson et al. 2021; Rogic et al. 2022a). Although these works were mostly limited to temperatures <1300 K and to TIR spectral range (Table 1.2); they confirmed that the oversimplification related to the use of a constant ε as well as neglect of the composition or temperature effects on the radiative properties of lava flow is detrimental for RS applications. In consequence, the authors started to highlight the importance of obtaining spectral emissivity data at higher temperatures (up to 1500 K) and recommend better constraining the ε–T dependence for each magma composition over a wider spectral range (TIR–MIR–SWIR).

In the following, we first summarize these few laboratory works focusing on their findings on the complex relationship existing between emissivity and temperature (ε–T), and on limitations of their methodology. Note, for direct comparison Table 1-2 resumes the studied rocks, analytical conditions (i.e., investigated temperature and spectral ranges, experimental setups and measuring devices) as well as main observations-results of these works.

Table 1-2: Literature compilation on the high temperature emissivity studies comparing samples, measuring parameters and main observations regarding ε–T relationship of magmatic rocks used in each study.

Sample	Preparation	T_{max} (K)	Wavelength (µm)	Instrument	T-ε behavior	Reference
Pu‘u ‘Ō‘ō (Hawaii) basalt	-	1323	1.25-15	hemispheric reflector and field	ε decreases with T in TIR	Abtahi et al. 2002
Rhyolite	synthetic glass powder, 20-80 µm	1773	6-15	FTIR Nicolet Nexus 670	ε decreases with T in TIR	Lee et al. 2013
Phonolites (El Teide, Erebus)	polished glasses, 1.5 mm thick	1600	1-25	FTIR Brucker Vertex 80v et 70	ε increases with T in TIR, variable in MIR, SWIR	Li et al. 2021
7 Mediterranean Basalts	polished, 3.0 mm thick	1273	1-25	FTIR Brucker Vertex 80v et 70	ε increases with T in TIR, constant in MIR, SWIR	Bouvry et al. 2017
alkaline + subalkaline series	synthesized glasses, powder <25 µm	873	7-14	FTIR Brucker Vertex 80v	ε decreases with T in TIR	Pisello et al. 2019
Basalt (Etna)	granulate	1573	1.5-2.5	Spectroradiometer ASD FieldSpec Pro	No significant variation of ε (>0.9) in SWIR	Lombardo et al. 2020
Basalt (Etna)	powder, 1000–3000 µm	900	5-15	FTIR MIDAC M2000, Brucker Vertex 80v	ε decreases with T in TIR	Rogic et al. 2019;2019b
Mg-O rich carbonatite and ijolite	powder, 63-250 µm	1000	1-16	FTIR Brucker Vertex 80v	ε increases with T in TIR for Ijolite and ε constant for carbonatite	Mueller et al. 2013
Basalt (Kilauea)	powder, 100–350 µm	1573	2.5-20	FTIR Nicolet Nexus 670	ε decreases with T in TIR, MIR	Thompson and Ramsey 2021
Basalt (Etna)	powder, 100–350 µm	1373	2.17-21	Nicolet Nexus 870 FTIR	ε decreases with T in TIR, MIR, SWIR	Rogic et al. 2022

The work of Abtahi et al., (2002) presented in AGU (American Geology Union) Conference can be considered as pioneering study addressing the issue pointed above through field measurements of the radiative properties of Hawaiian basalts up to 1323 K. In their short abstract, the authors claimed that the emissivity of cold crust is higher than that of hot lava flow. Lee et al., (2013) expanded on the work of Abtahi et al., (2002) and developed a micro furnace coupled to a Fourier-Transform InfraRed (FTIR) spectrometer to measure emissivity spectra of synthetic quartzofeldspathic glasses during melting and cooling (to and from 1673 K) (Figure 1-2). They observed in the glass-melt spectra (above 1573 K) an important broadening of the main absorption feature, a significant decrease of the emissivity minimum (from 0.85 to 0.55 at ~9.5µm) and quasi-loss of CF. Note however that in most of their emittance spectra the measured emissivity exceeds unity, implying that the sample emissivity is higher than that of a blackbody. This anomalous behavior may be potentially related to temperature gradients occurring inside the furnace, which leads to sample dimension changes, or to contributions from the micro furnace heating system used in this work. Therefore, this emissivity behavior questions the representativeness of their spectra and the potential application of these to natural systems.

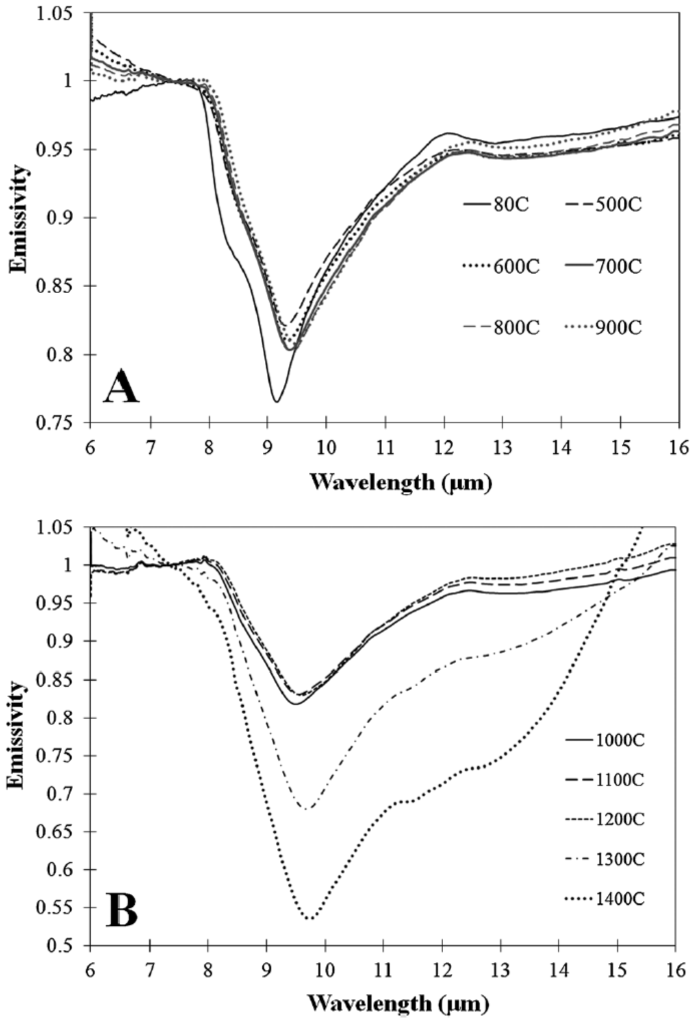

Figure 1-2: Emissivity spectra of quartzofeldspathic glass: a) from 353 to 1173 K, and b) from 1273 to 1673 K (from Lee et al. 2013). Note that spectra above 1573K clearly show emissivity >1 in the spectral regions <8 µm and >14 µm.

These previous works were then followed by that of Pisello et al., (2019), which represents the largest dataset of emissivity/reflectivity spectra retrieved at moderate temperatures (<873 K). They documented emissivity and reflectivity spectra of synthetic glasses with various compositions similar to alkaline (from basanite to phonolite) and subalkaline (from basalt to rhyolite) series. As in previous works performed at low T (see above), they observed that CF is dependent on polymerization degree of the glass, i.e., the more polymerized the glass structure, the shorter the wavelength at which CF is observable. They also showed that for a given composition CF shifts with temperature increase. Although their work is extensive in terms of composition, they only measured spectral emissivity up to 873 K and did not reach magmatic, molten conditions. Moreover, they focused exclusively of identification purpose and did not consider the emissivity–temperature relationships Figure 1-3.

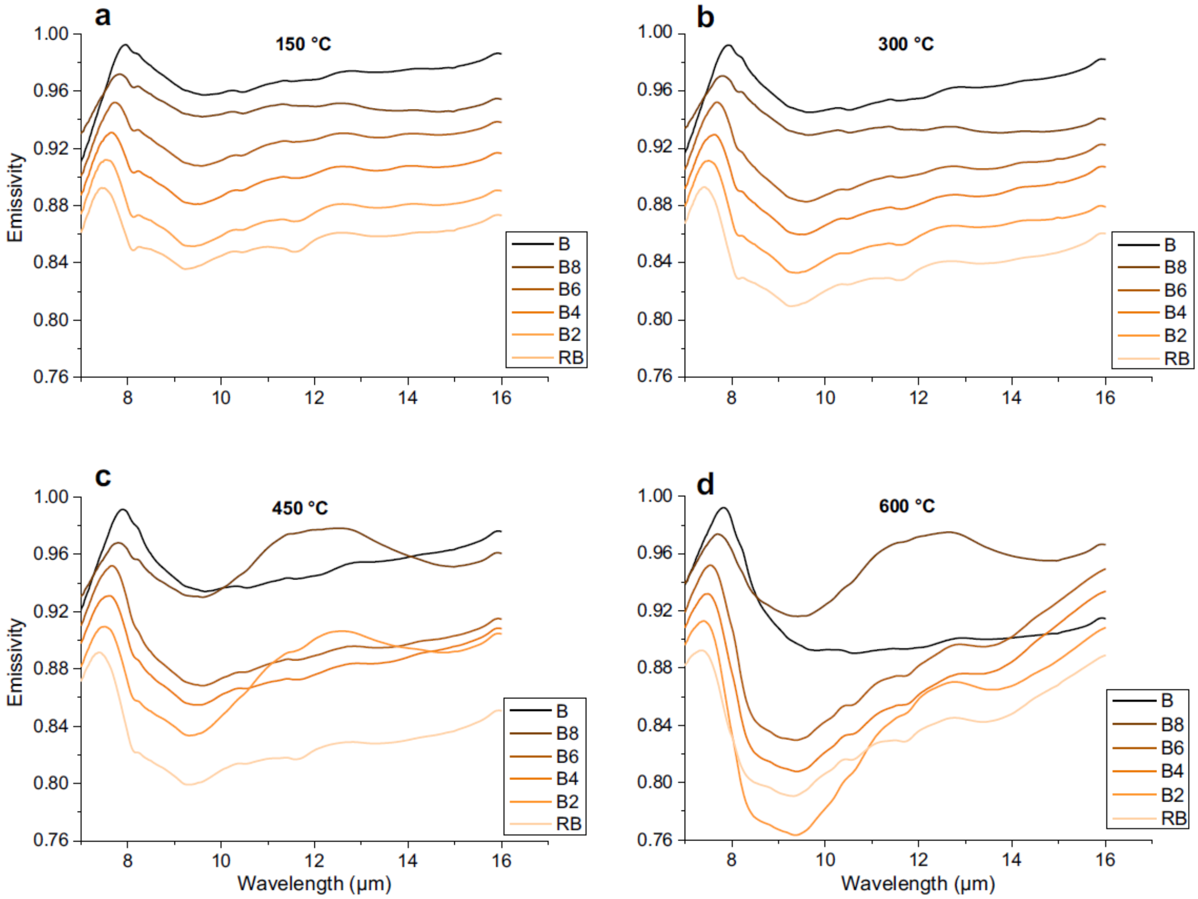

Figure 1-3: Emissivity spectra for the basalt (B)–Rhyolite (RB) serie in the 7–16 µm wavelength range collected at 423, 573, 723, and 873 °C (from Pisello et al., 2019). The manner of how the spectra is displayed does not allow to determine the basalts ε–T.

In parallel to Pisello's work, Rogic et al., (2019a, 2019b) performed the emissivity–temperature study of Etna basalts. They measured the spectral emissivity up to 900 K only, thus not exploring melting conditions. As shown in Figure 1-4, their emittance spectra are presented in a raw state without the Christiansen feature fixed to 1 (as usually in IR emission spectroscopy for dielectric materials showing clearly CF, see further our data or those of Lee et al., 2013 in

Figure 1-2a), precluding investigation of the emissivity–temperature relationship. Nonetheless, the authors concluded a steady decrease in emissivity with every increasing temperature step and clearly pointed to a negative ε–T relationship (Figure 1-4), a trend that converges with observations made in previous works (Abtahi et al. 2002; Lee et al. 2013; Rogic et al. 2019a; Pisello et al. 2019). The authors concurred then the following conclusion: the spectral emissivity of molten lava is lower than its solid counterpart, even though the investigated temperatures are far from lava flow regime.

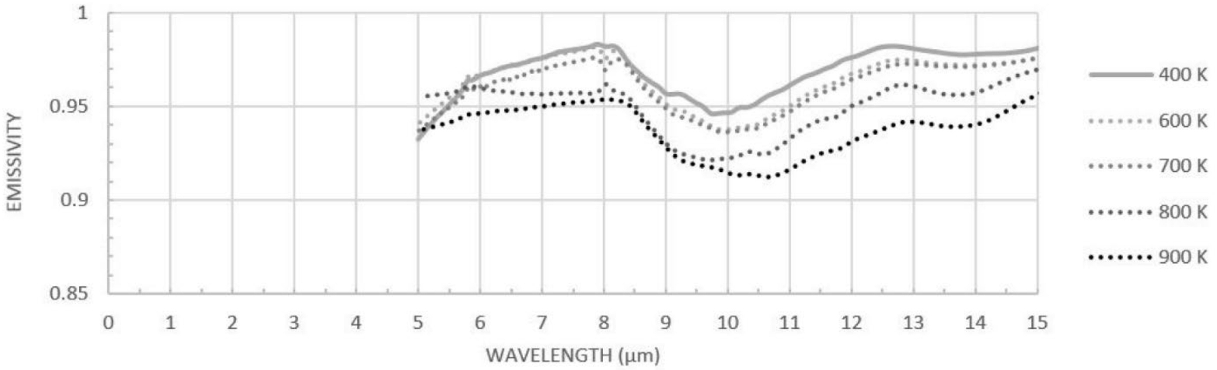

Figure 1-4: Emissivity spectra evolution with temperature from 400 to 900 K of Etna basalt (modified from Rogic et al., 2019a).

The above observations contrast with those of Bouvry et al., (2017), who explored the emissivity of different natural basalts (i.e., containing different MgO contents) at temperatures up to 1273 K (3 thermal cycles) and, for the first time, in a wide spectral range (from TIR to SWIR, 12000–370 cm^{-1}). The authors did not observe the emissivity decrease with temperature increase and showed quite stable, very reproducible thermal behavior during 3 heating cycles for every investigated sample. The spectral emissivity of all the explored compositions is very high, i.e. >0.80 in whole investigated spectral range and shows the highest variations (~0.2 maximum) from one sample to another in the 2000–8000 cm^{-1} spectral region (MIR-SWIR; Figure 1-5). The authors finally concluded that the spectral emissivity of alkaline basalts is less sensible (i.e., spectral emissivity intensity varies less) to thermal history compared to evolved basaltic rocks, which show more important emissivity variation with T (Figure 1-5). Although those are interesting results, the disadvantage of this study is related to the limited number of temperature steps and temperature range excluding melting conditions. Note that similar rather constant emissivity behavior was also observed by Lombardo et al., (2020) on Etna basalts when these were heated from ambient temperature to ~1600 K. Lombardo et al., (2020) have studied the spectral emissivity at that temperature solely using field thermal cameras, thus being slightly out-of-scope for laboratory-based review. Therefore, their work will not be discussed further.

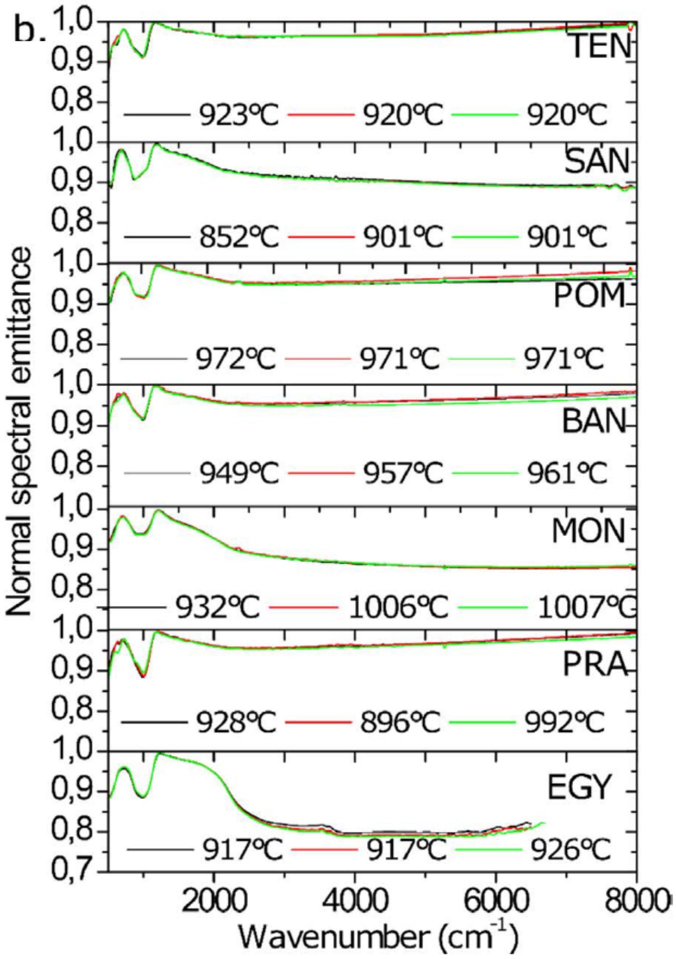

Figure 1-5: Emissivity spectra at moderate temperatures (up to 1273 K, 3 heating cycles) for basalts from different locations in the Mediterranean basin (modified from Bouvry et al., 2017).

More recently, Thompson et al., (2021) developed an experimental setup to acquire high temperature emissivity spectra in TIR and MIR. Their results for a Hawaiian basalt (Figure 1-6) showed that emissivity decrease with the temperature increase in the whole measured spectral range and decreases above 2000 cm^{-1}. Consequently their results are similar to Rogic et al., (2019a) in TIR pointing to the negative **ε**–T relation, and simultaneously agree with Bouvry et al., (2017). To interpret their emittance spectra, they compared them with those of quartz. They did not explain however, how the ε–T relation for Si-rich basalt in TIR is inverse to that of quartz. We can speculate about the causes that produce such contrasted ε–T relation and relate them to the experimental setup and the spectrum acquisition procedure. The sample, host inside a metal crucible, is placed in micro-furnace setup and heated exclusively from below. Such configuration can generate vertical thermal gradients all along the crucible and then thermal gradient in the sample. The sample temperature is measured with the thermocouple placed not far from heating element. During the sample emission acquisition, the furnace is open for 10 s, thus allocating enough time for thermal gradient to develop into the sample chamber or at least, disrupt the environmental conditions on which the emissivity measurement relies. Moreover, the crucible and thermocouple can absorb part of the thermal emission from the material and transfer it out of the system by conduction. Finally, the used blackbody reference is based on alumina ceramic, so although is stable with temperature it shows 9% emissivity variations. In this case, all these interferences mask the real radiance of the material or instead, decrease the bulk emissivity of the sample (e.g., Roberts et al. 2011; De Sousa Meneses et al. 2015; Li et al. 2021). Even if the authors developed instrumental and mathematical corrections for limiting these environmental contributions and downwelling radiance, they admitted that these effects could be considerable and affect the measured ε–T relation.

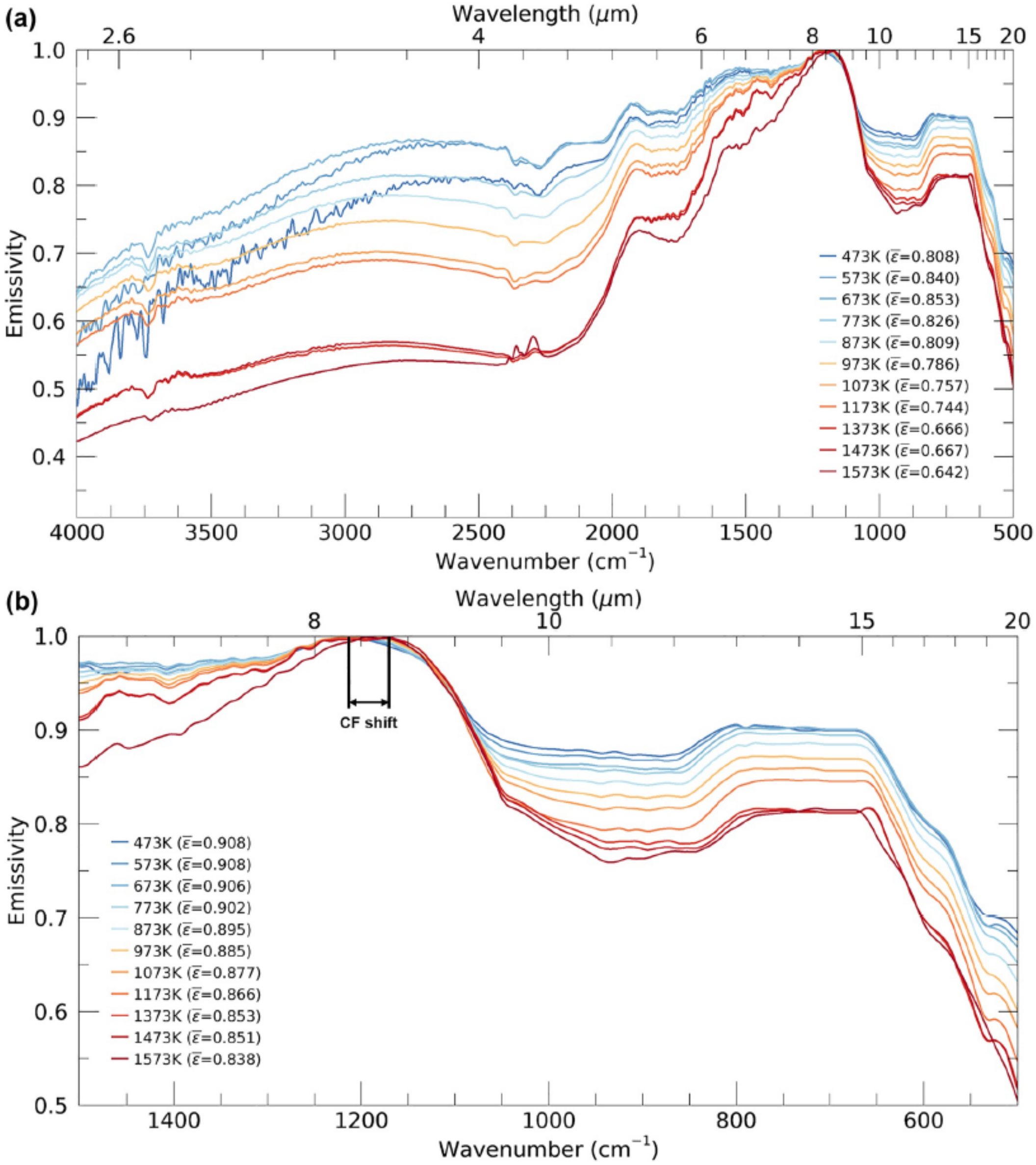

Figure 1-6: Spectral emissivity evolution with temperature (during cooling) for a Etna basalt (from Thompson et al., 2021).

Thompson and Ramsey, (2020b) performed also the first calibrated field emissivity measurements of actively emplaced lava (Kilauea) using a ground-based thermal camera (MMT–Cam) imaging system as to quantify the spatiotemporal variability of active lava radiative properties. Results indicated a strong positive correlation between kinetic temperature, fraction of exposed melt, and heat flux, as well as a negative correlation between emissivity and temperature during cooling. The temporal results reveal low- and high- frequency changes in radiative properties, up to 25% and 5% variability, respectively. Consequently, according to their results, these authors stated that molten lava surfaces have lower efficiency in terms of radiant heat flux than crusted lava surfaces. To date, there is no previous equivalent as to evaluate the relevance of these measurements or compare their field-based emissivity measurements with those retrieved at the laboratory.

The recent work of Li et al., (2021), performed on two glassy phonolites (from Teide Canary Islands and Erebus in Antarctica volcanoes), in a wide spectral range and up to magmatic temperatures, showed that spectral emissivity varies significantly as a function of temperature, composition, structure, and thermal history (Figure 1-7). The results revealed that emissivity increase slightly in TIR region with temperature increase for both magmatic rocks whereas in the MIR and SWIR spectral ranges the important ε differences are detected. The authors related these differences in ε–T behavior mainly to the difference in the relative proportion of Fe contents. They also highlighted that the presence of crystals (type, size, and thickness) in magma could additionally modify the already complex emissivity behavior of these magmas. Despite the difference in the studied magma compositions, the results of Li et al., (2021) concurs with those of Bouvry et al. (2017), Lombardo et al. (2020), and questions the negative ε–T relationships established in works of Lee et al., (2013); Rogic et al., (2019a); and Thompson et al., (2021).

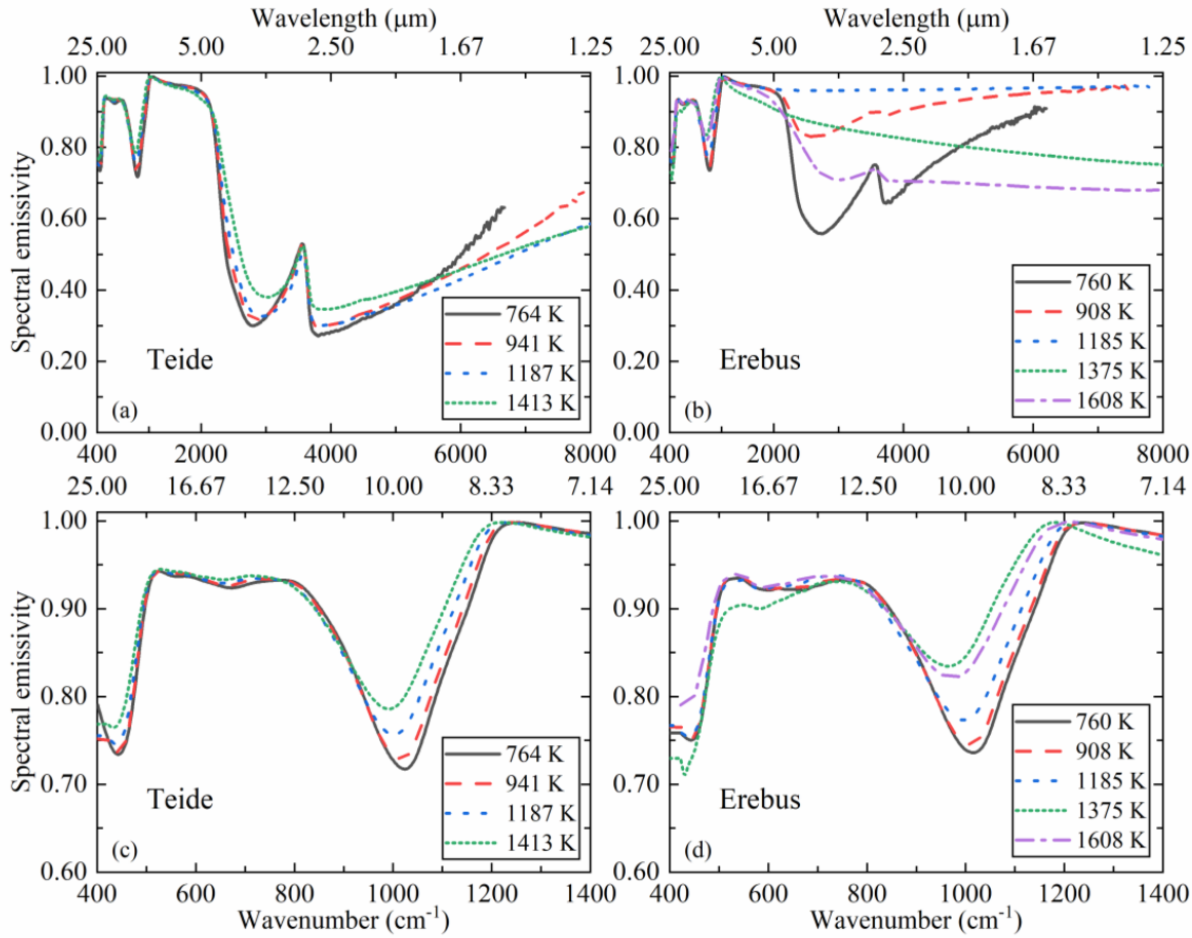

Figure 1-7: Emissivity spectra evolution with temperature for phonolites from Teide (a,c) and from Erebus (b,d) (from Li et al., 2021).

In summary, all the presented studies demonstrate that the radiative properties of magmatic rocks vary considerably along spectral range, composition, and temperature. Despite a few datasets available, the application to natural systems is limited by the fact that experimental conditions strongly differ from current determined magmatic temperatures. In that, most of the works are performed on powders, crystals, or synthetic glasses over a limited temperature range (usually in the vicinity of T_g) and a limited spectral range (typically the TIR region exclusively; Table 1-2). Moreover, the current experimental setups suffer from caveats that affect the precise measurement of spectral emissivity. The use of glass/natural-rock/rock-powders having different particle sizes, compositions and porosities can introduce additional bias to ε measurements. In fact, the use of rock or glass powders can give rise to important volume and textural changes that induce thermal radiation scattering in the sample, which can artificially increase the effective emissivity response of the material when heated (Rozenbaum et al. 2009). This gives anomalous values of ε, which in some cases exceeds that of an ideal blackbody (Figure 1-2). To that can be added the frequent lack of precision in the methodology used (i.e., missing information about the instrument used, the spectral range investigated, or the sample preparation etc.) and the poor description of spectra, both of which contributing to the difficulty of comparing studies which have already heterogeneous datasets and results. All these discrepancies result in the production of a variable dataset of spectral emissivity values and contrasting ε–T relationships (Table 1-2), which ultimately confuses the scientists that include ε in their lava flow models.

1.1.3. Spectral Emissivity of minerals at high temperature

As mentioned in Introduction, the radiative properties of an active lava flow should be considered as a complex response of melt/glass, crystals, and vesicles. Since crystals have a long range order crystalline structure compared to disordered melts, their emissive behavior is different as demonstrated by several authors (for pyroxene, Hamilton, 2000; Arnold et al., 2014; for olivine, Hamilton 2010; for feldspars, Donaldson Hanna et al., 2012; Hecker et al., 2010; Lee et al., 2010; Ye et al., 2019; for Metal–Oxygen oxides, Izawa et al., 2019; Lane et al., 2002; Veneranda et al., 2018; and for amphibole, Thomson and Salisbury, 1993). Hence, depending on the mineral assemblage of the magma and on the relative proportion and composition of each crystalline phase, the impact of crystals on the radiative signature can be important (Figure I-1). To this end, for a better comprehension of lava flow radiative properties, it is crucial to understand the separate spectral emissivity of each individual component (i.e., crystals and melts) at relevant magmatic conditions.

Unfortunately, since lava flows have varying temperature and contains magmatic minerals whose structure and composition can change as well with temperature, the lava flow radiative properties cannot be straightforwardly deconvolved using solely emissivity data retrieved at ambient temperature. Accordingly, while lava flows are emplaced their surfaces cool down and their crystal content increases, a factor that could change the lava radiative properties. In the following, we address the few works that explored the ε–T relationship of magmatic rock minerals (or equivalents). The main analytical parameters and findings of these studies are summarized in Table 1-3.

Table 1-3: Literature compilation describing samples, measuring parameters and main observations regarding ε−T relationship of magmatic minerals.

Sample		T_{max} (K)	Wavelength (µm)	Instrument	ε-T behavior	Reference
Quartz, Oligoclase	powder, 20-80 µm	1773	6-15	FTIR Nicolet Nexus 670	ε increases with T in TIR, but ε >1	Lee et al. 2013
Quartz, MgO	polished, oriented	2500	1.25-25	FTIR Brucker Vertex 80v et 70	ε increases with T in TIR, MIR, SWIR	Rozenbaum et al. 1999, De Sousa Meneses et al. 2014
Quartz, Forsterite	powder, 100–350 µm	1573	2.5-20	FTIR Nicolet Nexus 670	ε increases with T in TIR, MIR	Thompson and Ramsey 2021
Forsteriste	synthesized, oriented, polished	2500	1.25-25	FTIR Brucker Vertex 80v et 70	ε increases with T in TIR, MIR, SWIR	Eckes 2012
Forsteriste	powder, 100-160 µm	773	1-16	FTIR Brucker Vertex 80v	ε decreases with T in TIR	Helbert et al. 2013
Labradorite, Quartz	powder, <25 µm	673	1-16	FTIR Brucker Vertex 80v	ε decreases with T in TIR	Helbert and Maturilli 2009
Diopside, Hedenbergite	powder, <125 µm	773	1-16	FTIR Brucker Vertex 80v	ε decreases with T in TIR	Ferrari et al. 2014
Anorthoclase	polished, oriented	1600	1-25	FTIR Brucker Vertex 80v et 70	ε increases with T in TIR, variable in MIR, SWIR	Li et al. 2020
Ruby, $NdGaO_3$, Platinum	polished	2500	1.25-25	FTIR Brucker Vertex 80v et 70	ε increases with T in TIR, MIR, SWIR	De Sousa Menes et al. 2015

Quartz mineral was largely studied in literature by Thompson et al., (2021) up to 1573 K, Rozenbaum et al., (1999) up to 2252 K, and De Sousa Meneses et al., (2014) up to 1880 K (Figure 1-8). As shown in Figure 1-8, the room temperature spectra show a few well resolved, thin absorption bands, for example strong doublet at ∼1240 cm^{-1} and 1050 cm^{-1} consistent with previous measurements (Christensen et al. 2000; Baldridge et al. 2009; Helbert and Maturilli 2009; Lee et al. 2010). This doublet merge with increasing temperature to form a single feature at 845 K, this evidencing the complete transformation from α-quartz to β-quartz (Figure 1-8). Above 1743 K, β-quartz is further transformed into β-cristobalite (i.e., spectra lose the absorption band at ~800 cm^{-1}). Below 1500 cm^{-1}, the progressive increase of emissivity with the elevation of temperature is due to the increase of phonon damping at ~470 and ~1100 cm^{-1}. At higher wavenumbers, the increase of emissivity is due to the strengthening of multiphonon processes. This should be stressed that this temperature evolution of spectral emissivity of quartz is a good example showing that room temperature and high temperature radiative properties of a mineral can be very different due to the presence of structural phase transitions and important anharmonicity increase. In consequence, similarly to the magmatic rocks, the spectral emissivity of crystals has to be well determined at relevant lava flow temperatures.

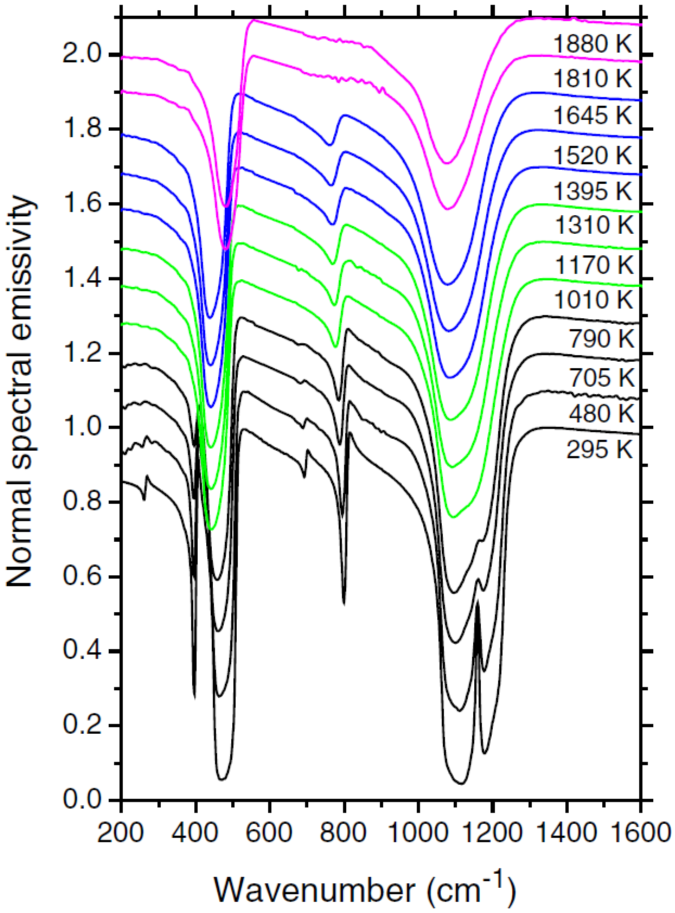

Figure 1-8: Spectral Emissivity evolution with temperature of quartz. Note important spectral modifications occuring at the α- to β-quartz transition (846 K) and at the formation of β-cristobalite (at 1743 K) (from De Sousa Meneses et al., 2014).

Diopside and Hedenbergite, which are different types of Ca-rich clinopyroxenes, were studied by Ferrari et al., (2014) up to 773 K. The emissivity spectra show three main bands (at ~900, ~950, and ~1100 cm^{-1}) that shift towards lower wavenumbers with increasing temperature (Figure 1-9). The spectra of both minerals are similar but exhibit different values of emissivity and show relatively different evolution with temperature increase. The position of the bands is function of the Mg# (with Mg# = Mg / Mg + Fe), which is in good agreement with Adams, (1974); Arnold et al., (2014); Christensen et al., (2000); Hamilton, (2000); Thomson and Salisbury, (1993). Their data also suggested that changes in spectral signature of Ca-rich pyroxenes that occur with temperature can be restricted to specific wavelengths and are closely related to the change in thermal expansion volume coefficients. For example, Mg-rich and Fe-rich pyroxene have similar thermal expansion volume coefficients, thus explaining why their absorption bands behave similarly.

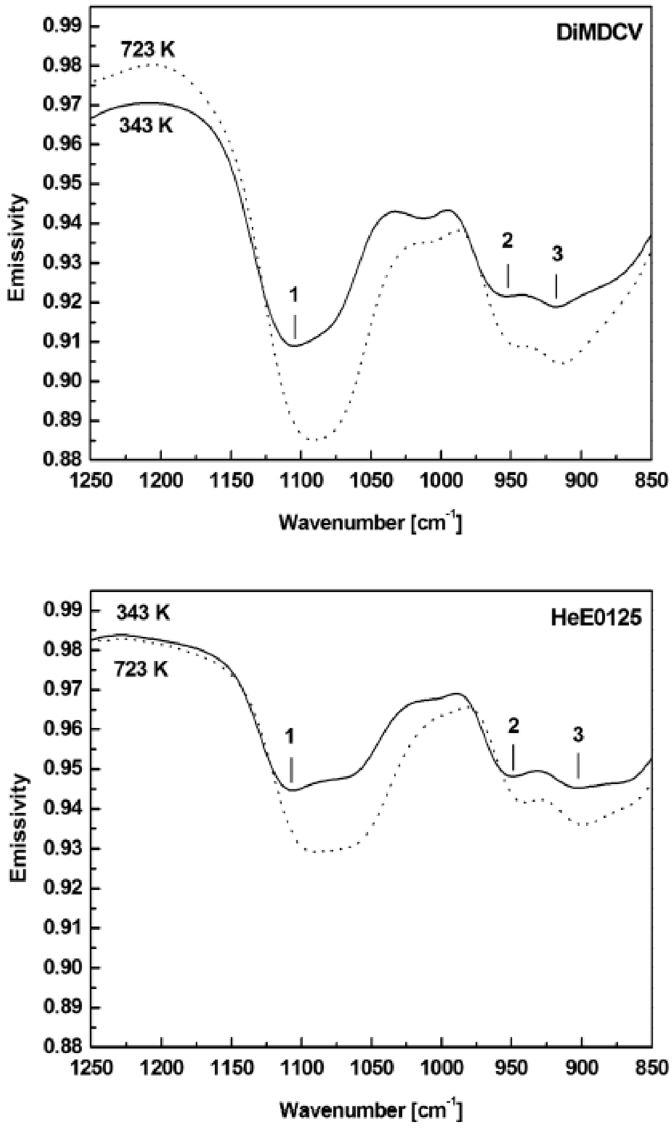

Figure 1-9: Emissivity spectra collected at 343 and 723 K for two Ca-rich clinopyroxene minerals: diopside (upper) and hedenbergite (lower). The significant absorption bands at~1100 , ~950, and ~900 cm^{-1} are labeled 1, 2, 3 (from Ferrari et al., 2014).

Forsterite (Mg-rich olivine) mineral was thoroughly studied by different authors over different temperature ranges: Eckes et al. (2013) up to 2500 K, Thompson et al., (2021) up to 1573 K, and Helbert et al., (2013) up to 773 K. All authors observed the strong absorption bands between 850 and 1050 cm^{-1} and other weak absorption features for which the position depends on crystal orientation (Figure 1-9). The position and shape of these bands are in good agreement with previous studies performed at room temperature (Aronson et al. 1970; Christensen et al. 2000; Hamilton 2010). When temperature increases to 1173 K, the CF and all absorption bands shifts towards lower wavenumbers and emissivity increases. Since no phase transition occurs, there is no major spectral changes in forsterite (Figure 1-10). Nonetheless, Thompson et al., (2021) mentioned that iron oxidation or amorphization can influence the spectral absorption bands. At temperature ~1200 K, the cation mobility is sufficiently high to allow important changes in the lattice dynamics and the structural evolution of the silicate, leading to deep changes in radiative properties. On the other hand, the emissivity of forsterite in MIR–SWIR range increased in Eckes et al., (2013) from 0 to 0.50 (Figure 4-9), whereas it decreased in Thompson et al., (2021) (Figure 1-11) from 0.70 to ~0.30, illustrating an example of material for which it can be delicate to extrapolate its radiative properties to high temperature. In all, their results show that the enhancement of the lattice anharmonicity and the increasing mobility of the magnesium cations with temperature are closely linked and are at the origin of the anomalies observed in the evolution of the radiative properties (Figure 1-10).

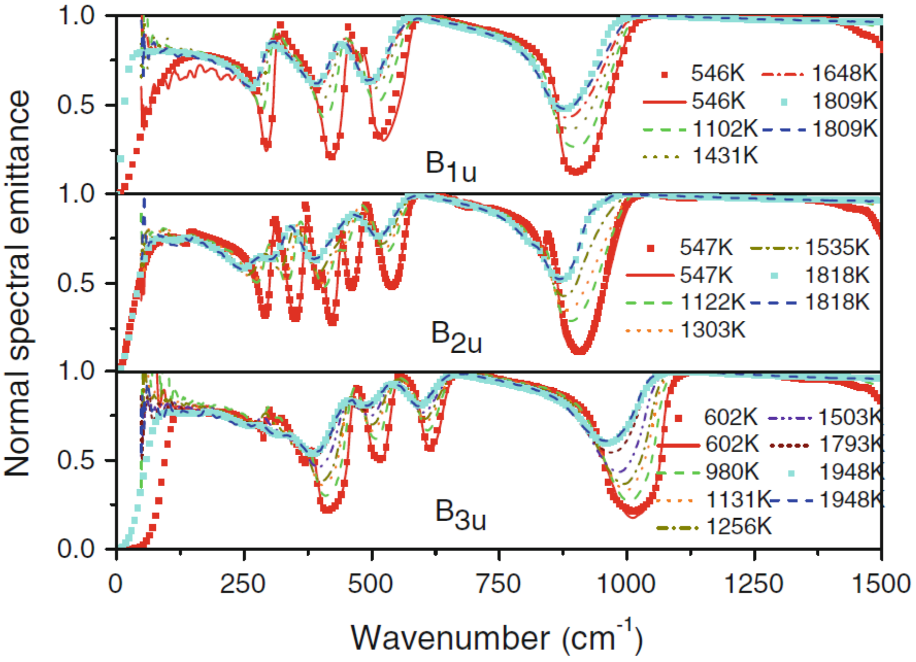

Figure 1-10: Spectral emissivity evolution with temperature of forsterite mineral for three crystallographic directions (B$_{1u}$, B$_{2u}$, B$_{3u}$ from Eckes et al., 2013).

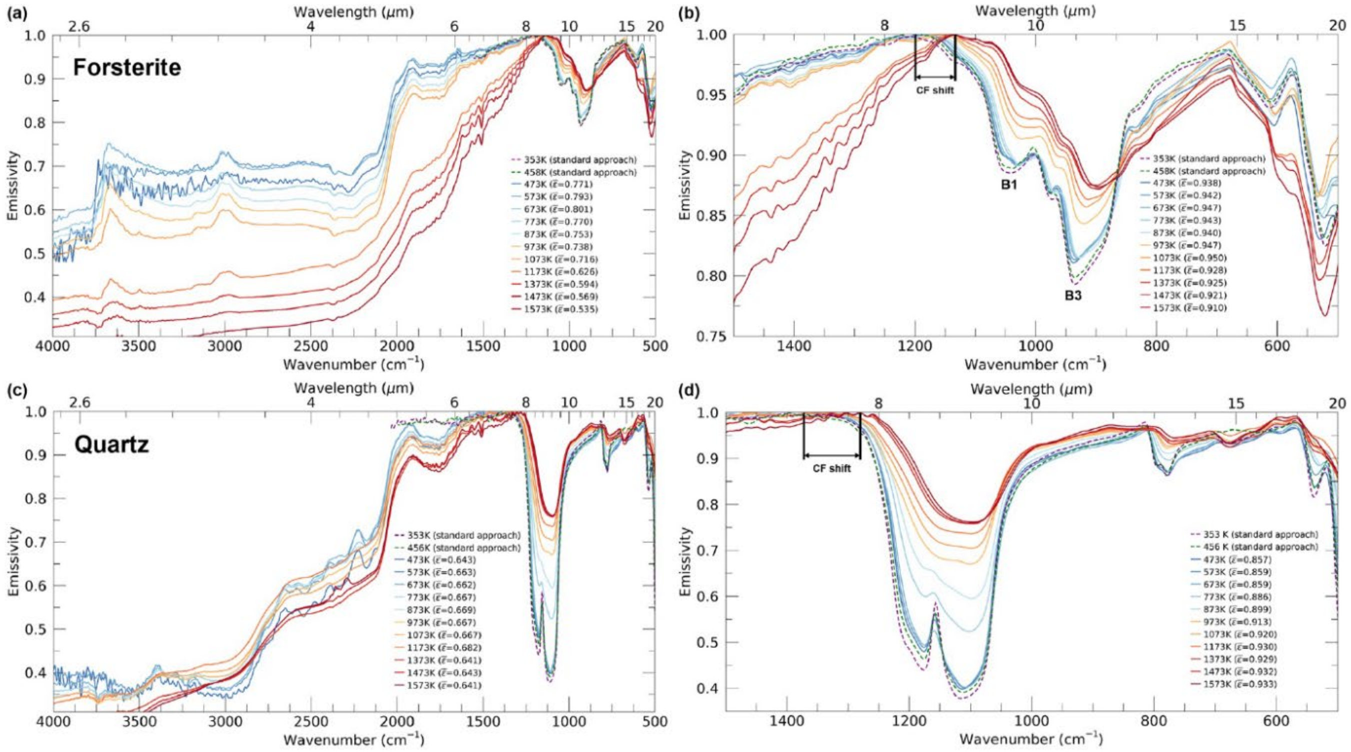

Figure 1-11: Spectral emissivity evolution with temperature of forsterite and quartz (from Thompson et al., 2021).

Spinel and titanate structures were studied by Sako et al., (2020) at 1273 and 1773 K. Emissivity spectra of these oxides show high emissivity values (0.90–1.00) in TIR and low emissivity values (0.10–0.40) in MIR–SWIR range with no particular absorption bands. These ε values are however doubled when Ti^{4+} cation is changed in octahedral and tetrahedral sites, thus distorting the lattice parameter (Figure 1-12). The authors concluded that oxide have complex optical properties and that the presence of ions containing electrons at the “d” valence layer increases spectral emissivity in MIR–SWIR at high temperature changing their properties from (semi)transparent to almost opaque ones. This example emphasizes that small composition differences can have important impact on optical and then radiative properties.

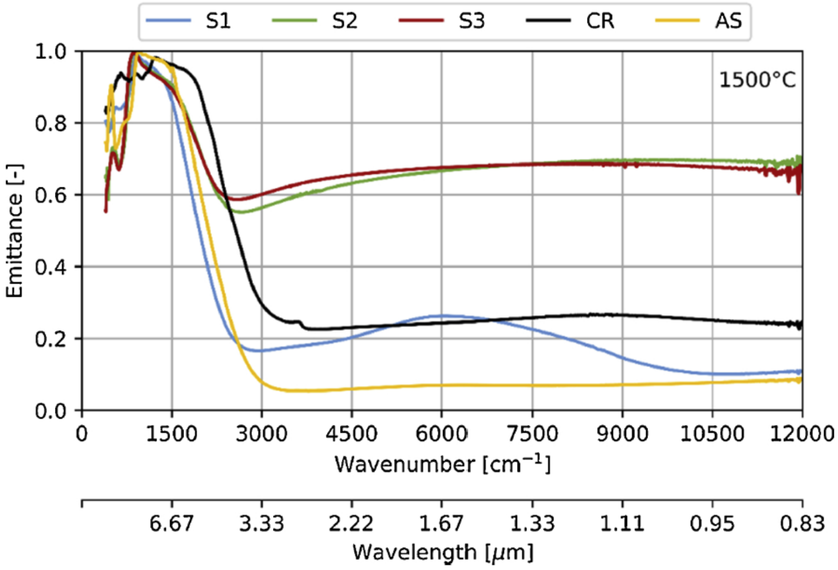

Figure 1-12: Emissivity spectra at 1773 K for different spinels (from Sako et al., 2020).

Spectral emissivity of Labradorite (Ca-rich feldspar) was studied by Helbert and Maturilli, (2009) at 773 K in short temperature range (Figure 1-13). The low T spectrum of polished labradorite mineral resembles that of Hanna et al., (2014); Hecker et al., (2010); Johnson et al., (2006); Ye et al., (2019). With the temperature increase, the authors observed the broadening and damping of Reststrahlen absorption bands and a shift in TF, which they attributed to the enhanced volume scattering due to the increased lattice vibrations.

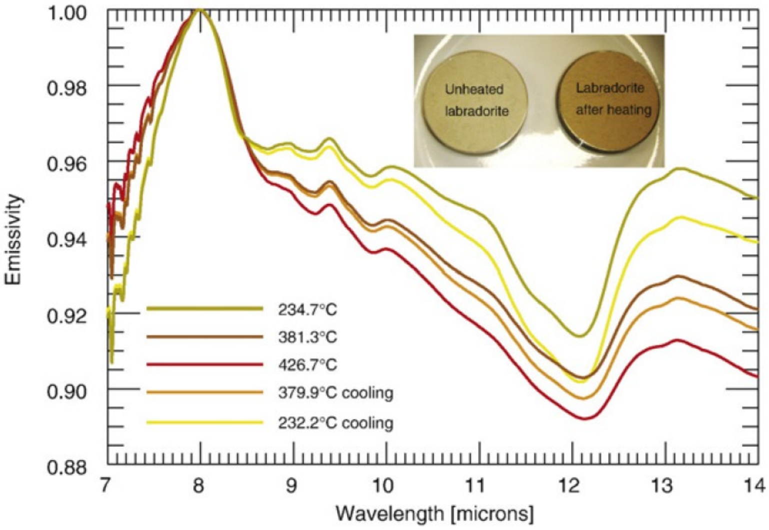

Figure 1-13: Spectral emissivity evolution with temperature (heating and cooling) for a labradorite (from Helbert and Maturilli, 2009).

On the other hand, Li et al., (2021) explored the radiative properties of anorthoclase (Na-K rich feldspar) up to 1542 K and their effect on phonolitic magma emissivity from Erebus volcano. Low temperature (~750 K) emissivity spectra are marked by four sharp bands at ~535, 595, 1000, and 1110 cm^{-1} of which the exact position, widths and intensity depend on crystal orientation (perpendicular or parallel) (Figure 1-14). With the temperature increase, these bands broaden and accordingly merge as melting occurs. When the authors compared the anorthoclase mineral and Erebus magmatic glass (which have equivalent compositions in term of SiO_2, Al_2O_3, Na_2O, CaO and K_2O), they noticed different thermal emission behavior at <1200 K that can be explained by the difference in their structural arrangement between a well-ordered mineral and partially/locally organized glass-melt. Note that in the highest measured temperatures the emittance spectra of melted rock and melted minerals are very similar.

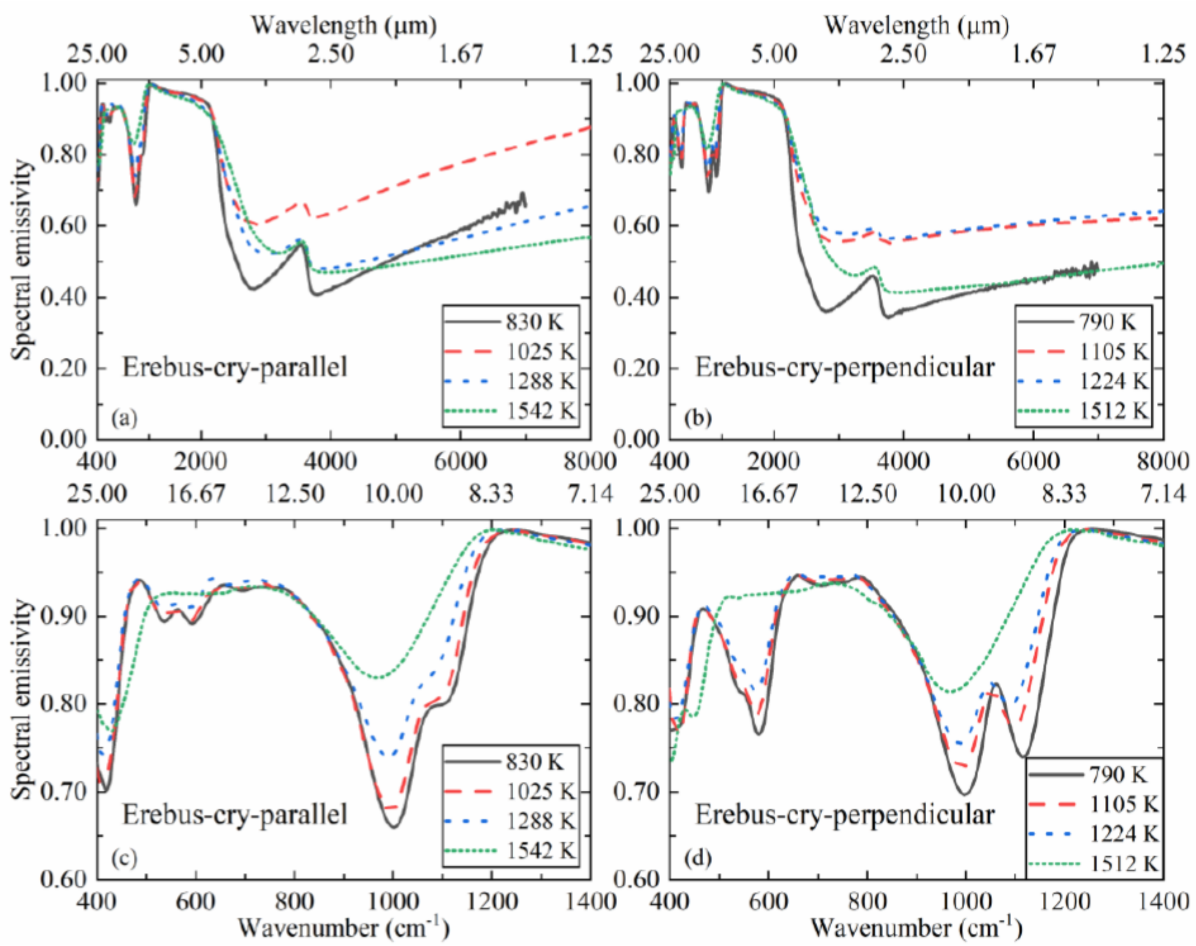

Figure 1-14: Spectral emissivity evolution with temperature for Erebus anorthoclase crystal sections parallel (a, c) and perpendicular (b,d) to main c axis (from Li et al., 2021).

In summary, the above pages demonstrate that like magmatic rocks, the radiative properties of associated minerals are highly complex and considerably vary as a function of spectral range, composition, temperature, and orientation. The results show that heating (or thermal history) of a mineral generally induce deep evolutions in its structure causing significant variation in its radiative properties. However, all these works suffer from the same caveats as for magmatic rocks, including different sensibilities or measuring conditions (i.e., limited spectral and temperature ranges, sample preparation, setups, etc.), resulting in the production of variable datasets of spectral emissivity that are difficult to compare. In contrast with magmatic rock, datasets are scarce, and several magmatic minerals have not been analyzed yet in relevant temperature range. Authors often draw conclusion on the emissivity and temperature relationship of minerals based on few data (e.g., a single spectrum taken at high temperature or even low temperature ($T < 350$ K) emissivity data), thus wrongly assuming the real behavior of the mineral. Furthermore, no study has yet explored the combined effect of multiple minerals with (dis)similar mineralogy on glass or melt. Nevertheless, these works agree on the following statement: more constrain study/measurements of the emissivity–temperature (ε–T) dependence for each mineral at high temperature and over a wide spectral range is necessary. Because lavas are generally crystal bearing, the (combined) impact of crystals on lava emissivity must be also carefully considered.

Overall, these observations call for a rigorous method for measuring glass/melt and minerals emissivity at real magmatic temperatures in wide spectral range (SWIR–MIR–TIR) to reduce emissivity uncertainty to an acceptable level, and to improve the estimations of temperature by RS techniques.

1.2. Geological settings: Eruption of Holuhraun, Bárðarbunga volcano

Iceland is one of the most active volcanic regions on the Earth. Volcanic eruptions occur every four to five years and produce more than five cubic kilometers magma per century (Thordarson and Höskuldsson 2008). The Bárðarbunga–Veiðivötn (190 km long and up to 25 km wide) is one of Iceland's largest volcanic systems (Figure 1-15; Reynolds et al. 2017). Bárðarbunga–Veiðivötn lies on the rift zone part of Eastern Volcanic Zone, and consists of a central volcano (2009 m above sea level) and a fissure swarm partly covered by the Vatnajökull ice cap. The central volcano is located within the northwestern part of the Vatnajökull ice cap and features an 8×13 km wide and 500–700 m-deep caldera (Gudmundsson et al. 2016). The eruption history of the Bárðarbunga–Veiðivötn volcanic system in the Holocene is not fully known, however the eruption frequency is suggested to be ~5 eruptions per century (Óladóttir et al. 2011). The most recent pre–2014 lava flow fields are the Holuhraun lavas of 1797 (Holuhraun I) and 1867 (Holuhraun II). The characteristic activity is explosive basaltic eruptions occurring on central volcano flanks or the fissure swarm. These basaltic lavas have chemical composition identical to that of 2014–15 lavas and chemical signatures that indicate affinity with the Bárðabunga–Veiðivötn volcanic system (Hartley and Thordarson 2013).

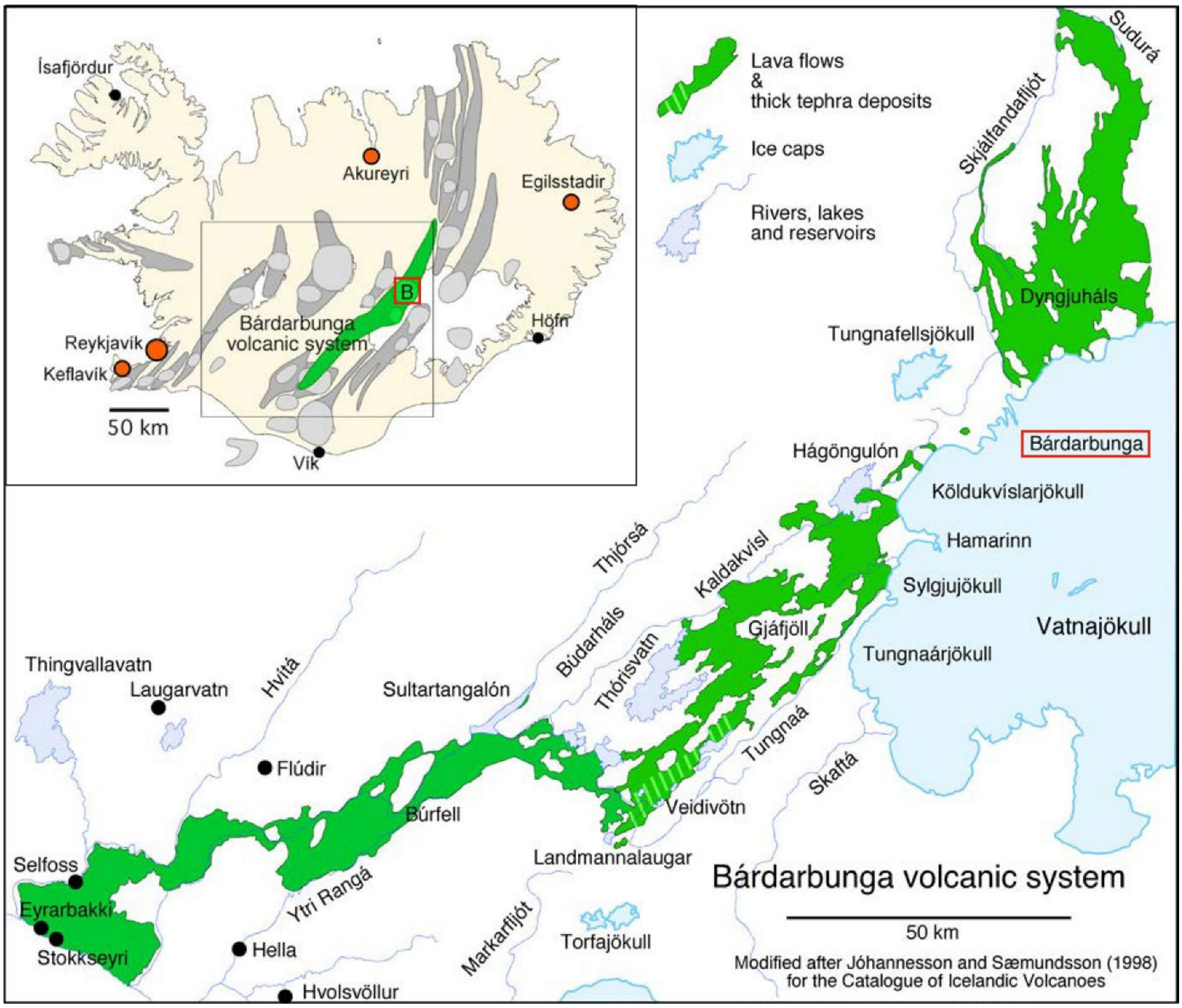

Figure 1-15: The partly ice-covered Bárðarbunga volcanic system (inset, green), central volcano is indicated by capital B. Holocene lava flows from the ice-free parts of the volcanic system are shown in green. Also shown are major rivers, lakes, and reservoirs but no discrimination is made between lava flows of different age. Modified after Johannesson and Saemundsson, (1998).

After the start of an intense seismic swarm beneath the ice-covered Bárðarbunga volcano on August 16, 2014 the eruption at Holuhraun began on 31 August on a 1.8 km long fissure that opened up at the old cone row from the Holuhraun I event, feeding incandescent sheets of slabby pāhoehoe (Pedersen et al. 2017). The fissure was continuously active until the February 27, 2015. The 6-month long eruption at Holuhraun is divided into three phases based on the lava field evolution (Pedersen et al. 2017):

- Phase I: from 31 August to mid-October. The first phase of the eruption was dominated by transport of lava through open channels and characterized by high average flux of ~90 m^3/s, and a maximum discharge rate estimated to have been $\geq$350 m^3/s (Bonny et al. 2018).

- Phase II: from mid-October to end-November and. The second phase was dominated by lava ponding and characterized by decreasing discharge rate to 50–100 m^3/s. A lava pond <1 km^2 was active at 0.8 km east of the vents and became the main point of lava distribution, controlling the emplacement of the lava flows. Towards the end of this phase, the previously active open channel in the first phase was inflated due to new lava injections.

- Phase III: from early December to 27 February 2015. The third and last phase was dominated by transport of tube-fed lavas and characterized by a discharge rate that continued to decrease from mid- January (<50 m^3/s) until the end. In this phase, the lava transport was confined to internal lava tubes pathways within flow field.

In total, the bulk volume of erupted lava has been estimated to be 1.44 km^3 based on pre and post-eruption topography derived from stereo-photogrammetry and satellite (Bonny et al. 2018). The lava flow field covered ~84 km^2 and extended up to 17 km through the emplacement of eight distinct lava flows (Figure 1-16a). The lava morphology is indicated as paired lava flow, where both spiny pāhoehoe and ‘a’a lava morphologies had similar length (Figure 1-16b-e). The erupted lava had an olivine tholeiite composition (Table 3-1) with a minor abundance of phenocrysts and a groundmass containing silicate glass with plagioclase, clinopyroxene, and olivine microlites (Geiger et al. 2016; Halldórsson et al. 2018). The 2014–15 Holuhraun eruption was the largest effusive eruption in Iceland since the 1783–1784 Laki deadly eruption (Gíslason et al. 2015; Aufaristama et al. 2019b) and emphasize the hazards that these eruptions pose.

Finally, the Holuhraun eruption represents an ideal target for the study of radiative properties behavior because of its long activity duration, extended active area, uniform lava composition, and emplacement on a low-slope floodplain (morphology was also well known thanks to the investigation of Bonnefoy et al., 2019, Figure 1-16f). These environmental effects usually play a major role in the thermal emission of a lava flow but are here minimized as they do no fluctuate much, allowing us to conveniently decipher the effect of radiative properties on the lava thermal emission during emplacement. Furthermore, Holuhraun eruption was one the first eruption that was fully monitored by multiple RS techniques (e.g., IR, photogrammetry, etc.) from its onset and until its demise. As such, it was the focus of detailed studies of thermal remote sensing and temperature monitoring. Kolzenburg et al., (2017) estimated an average temperature of 1368 K (results range from 1355 to 1401 K) at the lava flow front during emplacement using thermocouple measurements. Simultaneously, they measured temperatures of freshly exposed lava using a FLIR T650 thermal camera (7.5–14 µm; 1353–1398 K) which are in good agreement with the direct thermocouple measurements, though no information was provided on spectral emissivity values used to determine temperature. Kolzenburg et al., (2017) also estimated the range of eruption temperature at the primary vent from 1420 to 1473 K, which concurs with Nádudvari et al. (2020) who calculated high temperature values for the magmas (1323–1333 K) using satellite images (Landsat 8 OLI in SWIR and ETM+ in NIR, SWIR) and multiple emissivity values (1.00, 0.93, and 0.80). Finally, Kolzenburg et al., (2017) estimated the pre-eruptive temperatures of the lava between 1454–1464 K using MELTS software (Gualda and Ghiorso 2015), close to the liquidus temperature of approximately 1443 K estimated by Halldórsson et al., (2018). In the same manner, Geiger et al., (2016) calculated an average pre-eruptive temperature of 1466 K (model results range from 1425 to 1511 K) based on CPX-melt equilibrium thermobarometry. Finally, Aufaristama et al. (2018) compared the results derived from satellite images (Landsat 8) using constant spectral emissivity (0.97) with field measurements using FLIR thermal camera. They show that satellite- and field-based temperature estimates agree for the molten component of the lava flow: satellite images yield temperature of 1369 K, whereas retrieved field measurement is 1320 K. The volume of lava erupted and the Time-Averaged-Discharge-Rate were studied by (Bonny et al. 2018; Coppola et al. 2019), giving important insight into the lava rheology (Kolzenburg et al. 2018). Textural analyses were given by Geiger et al., (2016); and Kolzenburg et al., (2017). In all, these substantial contributions give strong background for comparison between field and laboratory works.

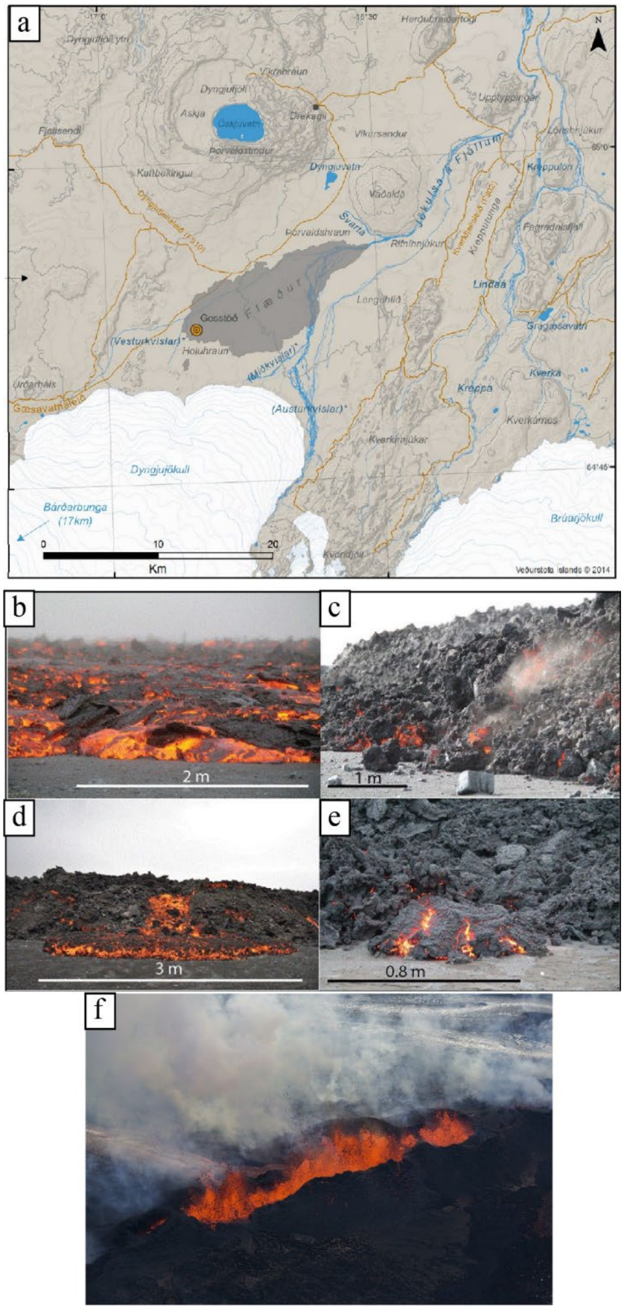

Figure 1-16: a) Holuhraun lava flow extent in grey. Eruption main vent is located with the orange dot. b-e) Four examples of morphologies observed during the 2014–2015 Holuhraun eruption: b) Slabby pāhoehoe, c) ‘A’ā, d) Rubbly pāhoehoe, and e) Spiny pāhoehoe. f) Eruptive fissure at the start of Holuhraun eruption (modified from IMO, and Pedersen et al. 2017)

Chapter 2: Experimental Methods

This chapter describes the whole array of analytical instruments and methods used in this study with a focus on InfraRed (IR) emission. Prior to IR emission measurements, the samples preparation is first described. Chemical, textural, thermal, and structural analyses carried out before and after each IR experiment are then presented.

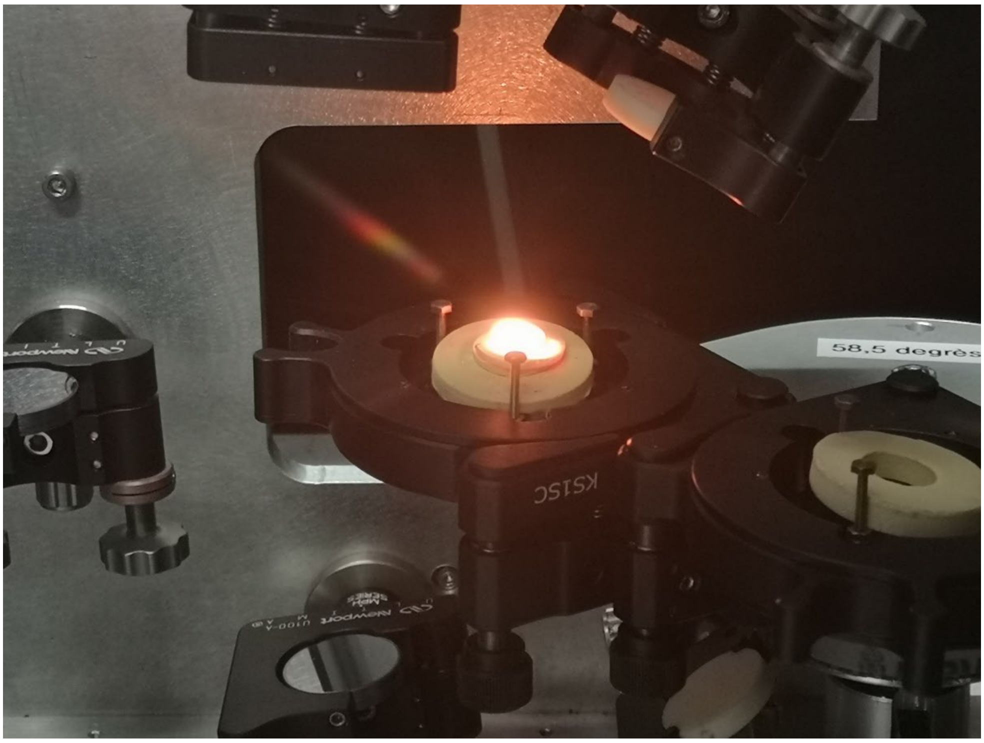

Glowing basalt sample during IR emission experiment.

2.1. Sample preparation for IR experiment

Twelve magmatic samples were studied in total. These include four with basaltic composition *lato sensu* that are the focus of this study (two of which have the same composition but differ in mineralogy), three natural basaltic minerals, and three tholeiitic samples as to cover the widest range of magmatic compositions and textures. Basalts *lato sensu* and tholeiitic samples are either scoriae or lava rocks coming from various locations and were chosen as basalts are the most abundant lava type on Earth. Basaltic minerals are monomineralic, natural (i.e., pyroxene, plagioclase, Fe-oxide), and coming from the mineral library of Institut des Sciences de la Terre d'Orléans (ISTO, France) and are representative of the primitive mantle composition. Basaltic samples were chosen because they. The full list of the samples of this study is given in Table 2-1 while the full set of run experiments is listed in Appendix A.1.

Table 2-1: Samples studied in this work (with their acronym used throughout the manuscript) and their origin.

Type	**Name**	**Origin**	**Reference**
Basalts *lato sensu*	Basalt (B-glass)	2014-2015 Holuhraun eruption of Bardarbunga (Iceland)	Kolzenburg et al. 2017
	Basalt (B-Nat)	2014-2015 Holuhraun eruption of Bardarbunga (Iceland)	Kolzenburg et al. 2017
	Basalt (B-Cryst)	2014-2015 Holuhraun eruption of Bardarbunga (Iceland)	Kolzenburg et al. 2017
	Basanite (F)	1704-1705 Fasnia eruption of Teide (Canary Islands)	Albert et al. 2015
	MORB (M)	Juan de Fuca Mid-Oceanic Ridge	Prouteau et al. 2001
	Oceanite (O-Nat)	2007 eruption of Piton de la Fournaise (Indian Ocean, France)	Pichavant et al. 2016
Basaltic minerals	Plagioclase (Pl)	Mineral library of ISTO	-
	Pyroxene (Px)	Mineral library of ISTO	-
	Oxide (Ox)	Mineral library of ISTO	-
Tholeiitic samples	Andesite (A)	80 ka Upper Scoriae 1 eruption of Santorini (Greece)	Andújar et al. 2016
	Dacite (D)	1991 eruption of Pinatubo (Philippines)	Scaillet and Evans 1999
	Rhyolite (R)	unknown Icelandic eruption (Iceland)	Jambon 1982

Crystal-free glasses of magmatic products (Table 2-1) were prepared as follow (Figure 2-1): between 30 and 50 g of material were grounded with agate mortar and pestle, then sieved as to recover the powder fraction <250 µm (Figure 2-1b), and afterwards fused in a Pt crucible at 1720 K for 2h30 in open atmospheric conditions (Figure 2-1c). The whole set was quenched in water, crushed, grounded, and fused again at the same temperature for 1h30. The resulting melt was finally quenched in air. Fragments of the starting glass were embedded in epoxy resin, polished, and initially characterized with a Scanning Electron Microscope (SEM-EDS) using visual inspection and semi-quantitative analysis to assess its homogeneity. Then, the glasses were analyzed with electron microprobe (EPMA) for determining their composition and to ensure that no alkalis or iron migration from the sample to the Pt crucible occurred. Meanwhile, the glasses were drilled to recover cores that were cut into 1.5±0.1 mm thick slices with parallel surfaces (using a diamond wire saw ESCIL WD2030 with 30 g as counterweight; Figure 2-1d,e). The surface of each wafer was optically polished (Figure 2-1f) using polishing disc from 120 to 9 µm and diamond discs from 9 to 1 µm (optical polish) as to optimize the sample response during IR experiments at T<1500 K (De Sousa Meneses et al. 2015). For measurements performed at higher temperatures (>1500 K), wafers with 3.0±0.1 mm thickness were instead prepared as to avoid the melting sample to fall in the IR measurement apparatus.

To explore the radiative properties of natural rocks (e.g., Bárðarbunga natural lava B-Nat, Oceanite O-Nat) and magmatic minerals, additional 1.5- and 3.0-mm wafers were prepared. However, the preparation of these samples requires the preservation of their structure and crystals. Therefore, they were directly drilled, cut, and polished, without being grounded, melted, and quenched beforehand (Figure 2-1). The remaining preparation follows that of crystal-free glasses. Note that the samples are sufficiently large as to consider its porphyritic to glomeroporphyritic texture representative (crystal size is <1 mm) to that of Bárðarbunga lava flow.

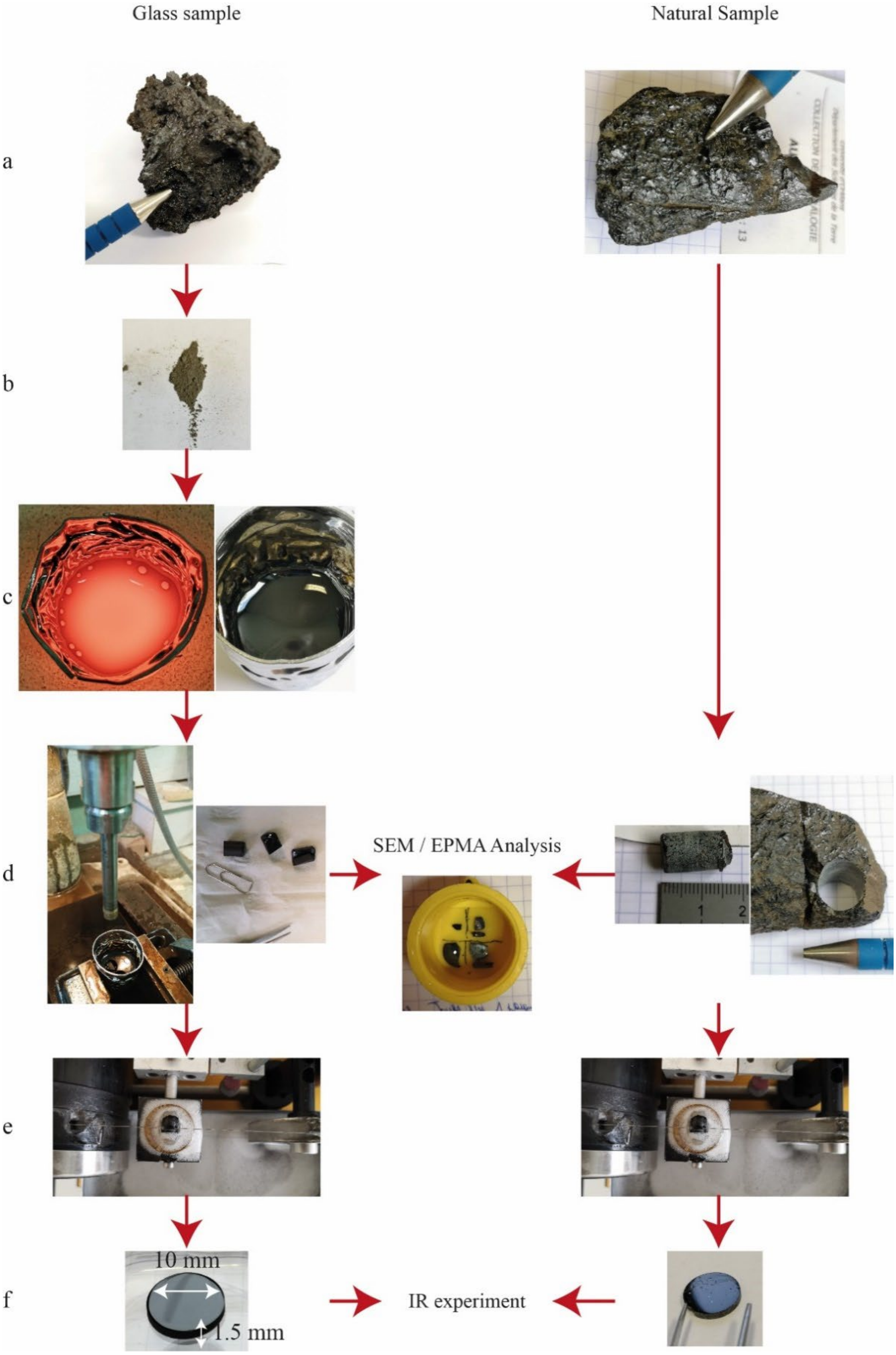

Figure 2-1: (a) Methodology of glass and natural sample preparation ; (b) crushing and sieving, (c) melting and cooling, (d) drilling, (e) cutting as to obtain dimension of 10×1.5 or 3.0 mm, and (f) polishing. Once prepared, the sample was used for SEM/EPMA analyses and IR experiment.

Finally, to explore the effect of crystals content on the radiative properties of Bárðarbunga lava, two crystal-rich samples (cf. section 4.2.3) were prepared following a two-step procedure. In the first step, the rock powder was directly heated up to 1720 K and left for approximatively two hours as to achieve the full melting of the sample. In the second step, a controlled cooling was applied to the sample to produce glasses with different crystal contents. A cooling ramp of 12° / h was applied with a dwell time of >24 hours until achieving a final T of 1323 K for the first sample and 1373 K for the second. After this time, the crucibles were removed from the furnace and quenched in air. This procedure allowed obtaining two crystal-rich samples (named hereafter "B-cryst") with crystal contents between 6 and 40% and having the mineral assemblage Fe-rich oxides + cpx + glass. The total crystal content of each sample was determined using Image-J® program based on SEM pictures representing the IR measuring spot (Figure 2-2). For each sample (B-Nat and B-cryst at 1323 and 1373 K), three images were taken at a magnification ×35 (for a total of 9 images). Images were then processed using the ImageJ® program to obtain the crystal area content and corrected for porosity. Here we considered the crystals in terms of their quantity, distribution and size, as these mineralogical parameters will affect the lava rheology (Pinkerton and Stevenson 1992; Mader et al. 2013).

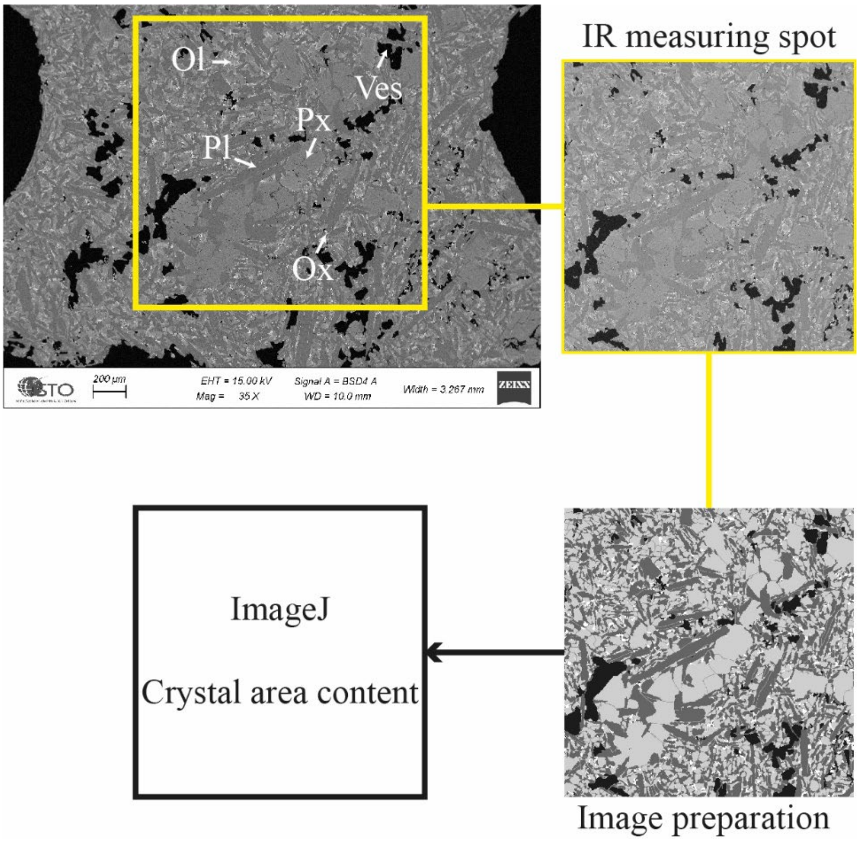

Figure 2-2: SEM image processing using ImageJ® as to obtain the crystal content of crystal-rich glasses.

2.2. Experimental measurements

As mentioned in the Introduction, spectral emissivity ε can be measured using two different methods: the direct and the indirect. Both methods were autonomously applied by Jonas Biren in this work (cf. Figure I-4).

2.2.1. Indirect method

Indirect method was used at ambient temperature (293 K) in order to retrieve spectral reflectance and transmittance using a FTIR 80v spectrometer (vacuum purged, with KBr beam splitter) equipped with a Hyperion 3000 microscope with nitrogen − cooled MCT detector (Bruker). For each sample, multiple measurements were carried out at different locations into the sample surface to assure the homogeneity of the retrieved indirect emissivity spectra. Note that the background equivalent single beam spectrum was systematically recorded in the same conditions. Moreover, additional transmittance and reflectance measurements were also carried out in macro-configuration: inside the sample chamber of the 80v spectrometer (DTGS detector), or with a gold coated integrating sphere, respectively. The spectra recorded in micro and macro configurations were generally in good agreement. Regardless of the apparatus setup, the measuring parameters were identical: 64 measuring scans, a spectral resolution of 4 cm^{-1} and a 1 mm opening diaphragm (except for the integration sphere, which requires a 4 mm diaphragm).

Although the indirect method is very useful and allows clearly distinguishing between transmittance and reflectance contributions, it is hardly applied for high temperature measurements above 1000 K. Since the principal interest of this study is to measure the spectral emissivity of magmatic rocks up to molten conditions (T>1000 K), we mostly used the direct method.

2.2.2. Direct method

Evolution of ε with temperature (from 500 K until 1800 K) was measured *in situ* by using a non–contact spectral emittance apparatus developed at CEMHTI laboratory (Orléans, France, Figure 2-3; De Sousa Meneses et al. 2015).

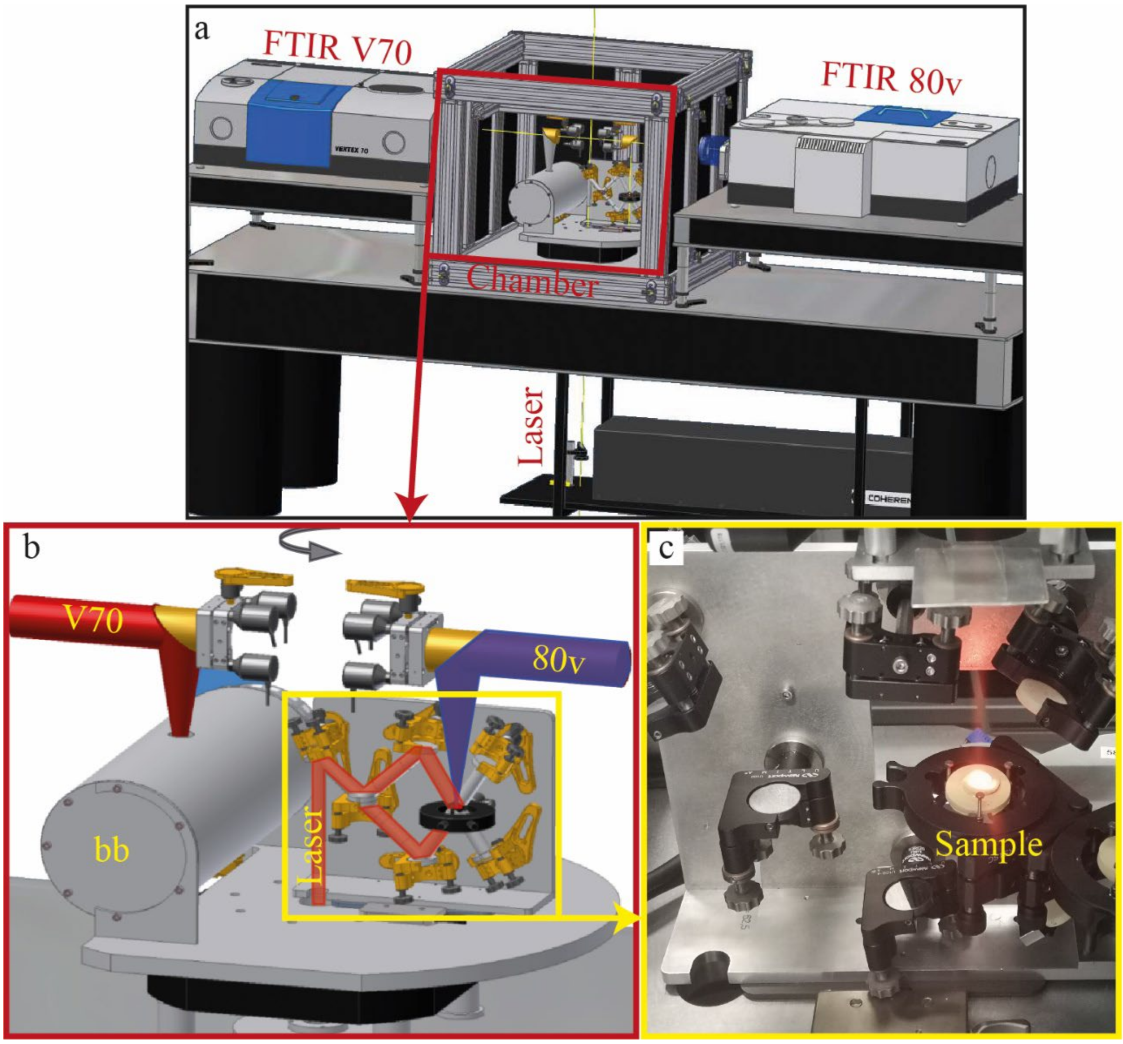

Figure 2-3: a) General schematic view of the IR emission apparatus (De Sousa Meneses et al. 2015). a) Zoom into the chamber interior: bb as the blackbody reference; optical paths in red and blue from the sample to the respective FTIR V70 and 80v spectrometers; the sample holder on a 180° rotary turntable; the CO_2 laser as the heating source (schematics courtesy of Philippe Melin). c) Picture of glowing sample on the sample holder during heating.

As shown in Figure 2-3a–b, the setup consists of a measuring chamber maintained at 295 K, purged continuously with dry air, and linked to two FTIR spectrometers set face-to-face. The chamber hosts a 180° rotating computer-controlled turntable, onto which the sample is placed in front of the blackbody reference. The latter is a Pyrox PY8 $LaCrO_3$ furnace with an aperture of 8 mm maintained at 1273 K for better stability (its maximum temperature is 1773 K). During measurements <1500 K, the sample is continuously heated with a 500 W CO_2 laser (Diamond K500, Coherent Inc.®) which is divided into two equivalent beams as to heat the entire sample (1.5 or 3.0 × 10 mm) from above and below. This configuration allowed creating a thermally homogeneous spot on the center of the sample of 4 mm in diameter (Figure 2-4a, b). In order to measure ε at >1500 K, the 3.0×10 mm wafers were heated exclusively from above, since this configuration allows creating a small "fusion pond" at the surface of the sample, which works as a "self-crucible". The use of the CO_2 laser as a heating source allows avoiding thermal interferences that may arise when the sample is heated with a classical furnace. The only contribution is the characteristic CO_2 laser emission detected at ~940 cm^{-1} (10.6 µm) and few harmonics (Figure 2-5b), which can be easily identified and eliminated from the signal, ensuring that only the emittance of the sample is recorded.

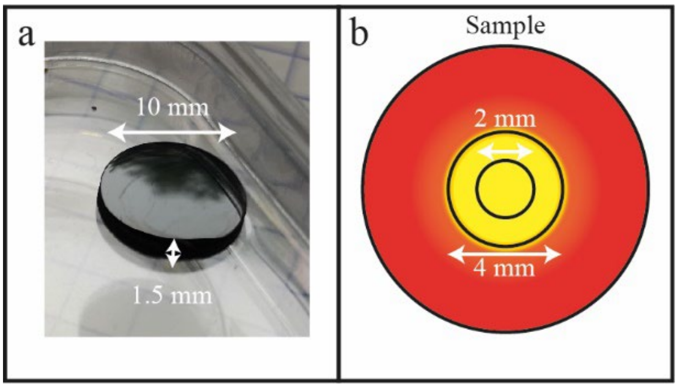

Figure 2-4: a) Pictures of the polished glass samples before IR experiment. b) Aerial schematic view of the 10 mm diameter sample with the 2 mm measuring area within the 4 mm homogeneous heating area.

The two face-to-face FTIR spectrometers are respectively a Vertex 70 (Bruker) purged with dry air and a Vertex 80v (Bruker) working under vacuum, set with multiple detectors and beam splitters (Table 2-2; De Sousa Meneses et al. 2015) that allow to record the emittance in a wide spectral range from far IR to visible (380–18000 cm^{-1}). Due to the large volume of the chamber, the fugacity of oxygen is not controlled, allowing potential oxydo-reduction phenomena (cf. 3.2.1). Such FTIR configuration allows simultaneous measurement of the sample and blackbody emittance (and inversely in the next rotation of the turntable) under the same environment and experimental conditions (Figure 2-3b). Note that in order to eliminate contributions from the apparatus environment itself, the thermal flux of the ambient background is also recorded.

Table 2-2: Detectors and beam splitters used for this study.

Spectrometer	Spectral range (cm^{-1})	Beam splitter	Detector
Vertex 80v	380-5000	Ge/KBr	DLaTGS/KBr
Vertex 70	3800-10000	Vis/CaF2	InGaAs
Vertex 70	9000-18000	Vis/CaF2	DiodeSi

When operating, the spectrometer diaphragms are set to 1 mm, which ensure a circular measuring spot of 2 mm in diameter within the 4 mm homogeneous thermal spot (Figure 2-4b). Outside the 4 mm thermally homogeneous area, radial temperature gradients can occur (Rozenbaum et al. 1999; De Sousa Meneses et al. 2015). This experimental setup ensures that the retrieved signal is representative of the 2 mm hot spot and has no contribution of the eventual textural or chemical variations occurring outside this area. The experimental configuration assures optimal measurement conditions in terms of environmental stability and single optical paths for the acquisition of thermal fluxes from ambient to extreme temperatures (De Sousa Meneses et al.

2006, 2015; Rozenbaum et al. 1999). The resulting thermal emission signals include the sample and the blackbody signatures as well as instrumentation and environment contributions that must be corrected. To eliminate these contributions, the three interferograms method developed by De Sousa Meneses et al. (2015) and derived from Planck law is applied. In this experimental procedure, we recorded three interferograms at each temperature increment, and then applied a Fourier transformation (FT) such as:

$$\varepsilon_\lambda = \frac{TF(I_s - I_a)}{TF(I_{bb} - I_a)} \frac{L_{bb}^0 - L_a^0}{L_s^0 - L_a^0} \tag{2-1}$$

Where I_a, I_{bb}, I_s are the interferograms of the parasitic ambient contribution, the blackbody emission, and the sample emission, respectively. Consequently, L_a^0, L_{bb}^0, L_s^0 are the Planck functions of the ambient, the black body and the sample.

Figure 2-5 shows how the final emissivity spectrum is retrieved from the measurements of thermal fluxes (Figure 2-5a) representative of the sample at a given temperature, blackbody reference and background thermal fluxes, for each detector (DTGS, InGaAs, and DiodeSi), and using Equation 2-1. Opus® and Origin® softwares are systematically used for processing each spectrum, which results in the raw emissivity spectrum of Figure 2-5b. Spectra are further corrected by removing Laser contribution (at 940 cm^{-1}) and eventual harmonics (e.g., at 1260–1275 cm^{-1}), as well as H_2O (e.g., at 1880–1905 cm^{-1}) and CO_2 (e.g., at 2310–2385 cm^{-1}) contributions. The resulting emissivity spectrum shown in Figure 2-5c is then built by merging the spectra from each individual detector; we superimpose spectra (the most linearly possible) on a ~100 cm^{-1} wavenumber range (i.e., DTGS with InGaAs around 4000 cm^{-1} and InGaAs with DiodeSi around 9000 cm^{-1}) and merge them as to obtain one continuous emissivity spectrum.

For each IR experiment, the spectra were collected by 50–100 K steps from 500 K to ~1800 K and the sample was quenched afterwards by shutting the laser down. In order to explore the effect of thermal history on the radiative properties of the sample, in a few measurements other heating/cooling routines (e.g., use of different temperature steps, measurement during cooling steps, etc.) were used. Note that for better readability only the most representative spectra are shown in the main text figures (e.g., cf. Figure 3-4), but Appendix B.7 shows an example of figure that includes all recorded spectra in a single experiment and illustrates the complete evolution of emissivity with temperature of the sample.

We want to stress that the measuring setup described above does not allow determining the temperature of the sample in a straightforward manner. Temperature is however precisely calculated *in situ* using the CF (Rozenbaum et al. 1999; De Sousa Meneses et al. 2015; Li et al. 2021) and with >99% accuracy (Brun 2003; Eckes et al. 2013). A comparison with emittance values acquired by direct and indirect methods led us to estimate the standard uncertainty of ε measurements to be of 1–2% at the vicinity of the CF and 5% above 2000 cm^{-1} (del Campo et al. 2011).

Finally, despite that the above measuring procedure seems relatively straightforward and easy to perform, the acquisition of ε–T data and the treatment of retrieved data by each spectrometer as to produce a complete set of spectra for a given measuring session, is a high time-consuming process. Considering that 12 samples were studied and ~50 successful experiments were performed (Appendix A.1), the ε–T dataset that is presented in this work represents a total of ~13 months of data acquisition and processing.

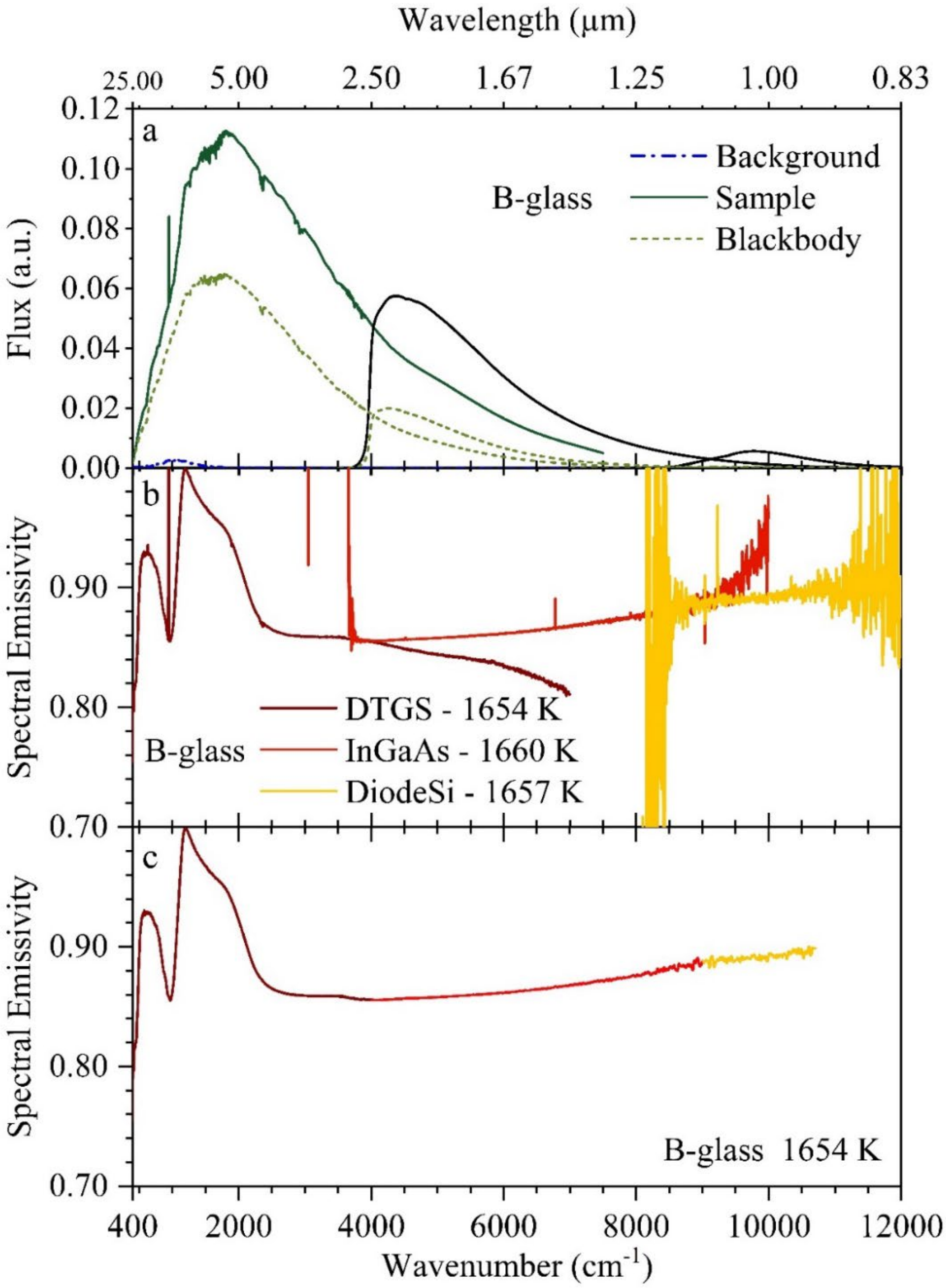

Figure 2-5: Example of the direct emissivity spectrum computation of a 3.0 mm B-glass sample. a) Raw fluxes of sample, blackbody and ambient background measured at 1654 K using three distinct detectors: DTGS, InGaAs and DiodeSi. Compute emissivity spectrum before correction (b) and merged after final correction (c).

2.3. Analytical methods for sample characterization

To understand the temperature evolution of radiative properties of investigated materials, textural, chemical, structural, and thermal analyses were performed before and after *in situ* high temperature emissivity measurements, using the experimental techniques described below.

2.3.1. Textural and chemical analysis: Scanning Electron Microscope and Electron Probe Micro Analyzer

Textural and chemical analyses were systematically used for sample characterization before and after each IR experiment as to observe any change in the sample surface. Prior to analyses, sample chips were embedded in Epoxy resin, polished, and carbon coated (15–20 nm) under vacuum. Textural analysis of the sample surface was carried out with a Merlin Compact ZEISS Scanning Electron Microscope (FEG SEM) equipped with a GEMINI I column (15 kV, 10 mm working distance) and Energy Dispersive X-Ray Spectroscopy (EDS). Single and panoramic pictures of sample cross and planar sections were taken (with the Smart Stitch software for panoramic pictures) at several consistent magnifications including ×50, ×150, ×500, and ×1000. Preliminary semi-quantitative chemical analyses (EDS) were also carried out as a first approach into surface identification. Secondly, mineral and glass chemistry analyses were performed with an Electron Probe Micro Analyzer SXFive (EPMA) at 15 kV and 8 nA current using focused beam for minerals and 5, 10, 20 µm defocused beam for glass. Major elements calibration has been performed using standards of silicate minerals: albite (Na, Si), orthoclase (K), andradite (Ca); and oxides: chromite (Cr), corundum (Al), magnesium oxide (Mg), nickel oxide (Ni), hematite (Fe) and pyrophanite (Mn, Ti). For the oxides, the relative analytical errors are 1% (SiO_2, Al_2O_3, CaO), 3% (FeO, MgO, TiO_2) and 5% (MnO, Na_2O, K_2O, P_2O_5) (Di Carlo 2006). Chemical maps and cross-section analyses of polished chips were also produced. Mineral endmembers were calculated as in Deer et al. (2004) for olivine and plagioclase and as in Morimoto (1988) for pyroxene.

2.3.2. Textural and chemical analysis: Transmission Electron Microscope

Transmission Electron Microscopy (TEM) analysis is complementary to SEM and EPMA analysis as it allows observing the sample internal structure at the highest possible resolution. TEM analysis was specifically carried out for the experimental B-glass sample as to help constraining the inner microstructure and composition after IR measurements. Two pieces were precisely extracted from the IR measuring area (Figure 2-4). Their cross sections were glued with their surfaces facing each other and then cut again to form a rectangle of ~2.5×2 mm (the so-called "sandwich" preparation; Ayache et al. 2007). The rectangular sample was mechanically polished with a tripod and inlaid diamond discs until a 50-µm thickness was reached. The resulting foil was finally obtained by PIPS argon ion milling system. Imaging, Selected Area Electron Diffraction (SAED) and TEM spectroscopy analyses were performed on a JEOL-ARM 200 Cold FEG transmission electron microscope operating at 80 kV, equipped with double spherical aberration correctors (TEM/STEM) and fitted with a JEOL SDD CENTURIO EDS system and a Gatan

Imaging Filter (GIF) Quantum ER. The microstructures of the sample surface and core were imaged by TEM bright field and Scanning Transmission Electron Microscopy –High Angle Annular Dark Field (STEM-HAADF) modes. Sample compositions (core and surface) were obtained with STEM-EDS (Energy Dispersive X-ray Spectroscopy) and STEM-EELS (Electron Energy Loss Spectroscopy). EELS can probe the local bonding environment and the electronic structure of materials (Egerton 2011). Changes in bonding, coordination or valence state are associated to the shape distribution of the energy-loss near-edge fine structure (ELNES) of core-loss edge like the $L_{2,3}$ transition metal and O–K near-edge. The ELNES data of our samples was then compared to those of sample with known structure (Colliex et al. 1991; Golla-Schindler et al. 2003, 2006). A 0.1 nm probe size was used for EDS/EELS analyses and STEM-HAADF imaging.

2.3.3. Chemical and Structural analysis: Raman spectroscopy

Based on the detection of inelastic scattering of monochromatic light, Raman spectroscopy is complementary to IR spectroscopy. In this study, Raman spectroscopy gives insights into the local structural and chemical evolution of the sample (silicate glass, magmatic mineral, etc.) that can occur with temperature during IR experiment. That is why Raman spectra were systematically recorded at room temperature on (non-) polished cross and planar sections of the sample before and after each IR experiment. The instrument used is a homemade micro-Raman apparatus equipped with a monochromatic 532 nm Coherent Genesis MX SLM laser as exciting source, a Nikon ECLIPSE Ni-U microscope, an Andor Shamrock 500i spectrometer equipped with an Edge filter cancelling intense Rayleigh elastic scattering and Peltier cooled back illuminated CCD Andor Newton detector. The use of long working distance Nikon objective (100×, N.A. 0.8) allows micro-scale analysis with lateral resolution down to 1–2 μm^2. The 600 lines/mm grating was systematically used, providing spectral window spanning from 100 to 2500 cm^{-1} as to encompass the main region of vibrations of silicate and oxide network and to exclude the eventual presence of secondary phases/pollution. For each analysis, acquisition time was set to 30–60 seconds and the laser power output varied between 100 and 300 mW. Daily calibration of the Raman micro-spectrometer was performed based on the 520.8 cm^{-1} peak of silicon.

2.3.4. Structural analysis: X-Ray Diffraction

X-Rays Diffraction (XRD) gives insights into the local structure and the geometric arrangement of atoms and was conducted as to identify B-glass crystalline phases present after IR experiment. *Ex situ* X-ray powder diffraction (XRPD) diffractograms were collected using a Bragg Brentano D8 Advance Bruker laboratory diffractometer ($CuK_{\alpha1,2}$ radiation) equipped with a lynx Eye XE detector. Data were collected from 10 to 80° (2θ) at room temperature with a 0.015° step size and an acquisition time of 2 s per step and are display in Appendix B.4. *In situ* XRD measurements were performed to follow B-glass sample evolutions with temperature increase and to identify the nature of the crystalline/glassy phases present. *In situ* high-temperature diffraction data were collected every 100 K from 873 K up to 1473 K using an Anton Paar oven chamber (HTK1200N model) in the 2θ range from 15 to 80° with a 0.021° step size and an acquisition time of 2 s per step. To avoid any textural effect (preferential orientation) after HT-XRD experiments, the sample was crushed and re-analyzed with the same parameters. Bragg peak identification for all phases was carried out in comparison with an extensive online database (PDF-4 edition 2021 from ICDD, https://www.icdd.com/, last accessed 02/02/22).

2.3.5. Thermal analysis: DSC

Differential Scanning Calorimetry (DSC) analyses were carried out with a SETARAM Multi HTC 1600 in order to measure the glass transition temperature (T_g), and eventual crystallization events of synthesized glasses and B-Nat sample. Samples were crushed and sieved as to recover the fraction between 125 and 500 µm and cleaned with ethanol. They are then dried in an oven at 393 K for one hour and kept in a hermetic box afterwards. Prior to the DSC analysis, the apparatus was calibrated against melting temperature of already known standards (gold, silver, aluminum), at different heating rates with a precision of 1%. 500 mg of starting material were separately put in platinum crucible on the first thermocouple beam, whereas the platinum crucible on the second beam remained empty to work as a reference (Figure 2-6a). The apparatus was purged with Ar at a flow rate of 20 mL min^{-1}, then, the predefined heating program started (modified from Applegarth et al. 2013): Isotherm and equilibration at 423 K for 15 min so that no oxygen is left in the oven and the signal is constant. A heating stage follows at constant rate of 10° min^{-1} until the oven temperature reaches 1723 K. Then, the cooling stage starts with a constant rate 10° min^{-1} until the temperature is cooled to 423 K. Then, an isotherm at 423 K occurred for 60 min so that the signal is equilibrated once again. Finally, the heating cycle start again with the same properties as described above. The resulting differential heat flow curve showed the endothermic events as troughs, representative of glass transition (T_g) and melting (T_m), and the exothermic events as peaks related to crystallization (T_c; Figure 2-6b). Note that melting under Ar gas has been usually identified in two events and crystallization in two to three events (Burkhard 2001). The area of a peak or trough is directly proportional to the enthalpy of formation of each phase (Denton et al. 2009; Applegarth et al. 2013).

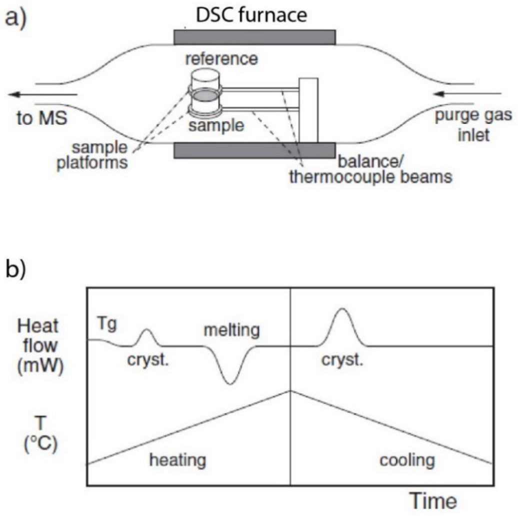

Figure 2-6: a) Sketch of a dual beam DSC instrument, showing the sample and reference beams in the furnace. b) Example output of a DSC experiment, showing typical sample heat flow curves with time. The heat flow signal shows the glass transition (T_g), which apears as a downward step, exothermic crystallization and endothermic melting during heating. A crystallization event is also shown during cooling. (modified from Applegarth et al. 2013).

Chapter 3: Radiative properties of Basalts

The apparent lack of spectral emissivity data at relevant magmatic temperatures (Chapter 1) must be fulfilled as to enhance our capacity in volcano monitoring. To this end, this chapter is focused on the *in situ* laboratory measurement of radiative properties of basaltic composition *sensu lato*. Results show principally the ε–T relationships measured for a Bárðarbunga basaltic glass and fully crystallized natural lava rock. To determine the compositional effect on emissivity, the results are then compared to those retrieved from MORB and basanitic samples. After comparison of our data with the previous literature results, the discussion focuses on the origin of the opacification phenomena observed in basalts and on the impact of crystals on radiative properties.

Pahoehoe slab, Kilauea, Hawaii (credit: unknown).

3.1. Emissivity–Temperature relation for basalts

3.1.1. Petrography of studied samples

The starting products (natural rocks and melt glasses) were characterized petrographically and chemically prior and after IR measurements, as to unravel the textural and chemical evolution experienced by the basaltic samples during the experiments. The compositions considered in this study are summarized in Figure 3-1 and Table 3-1.

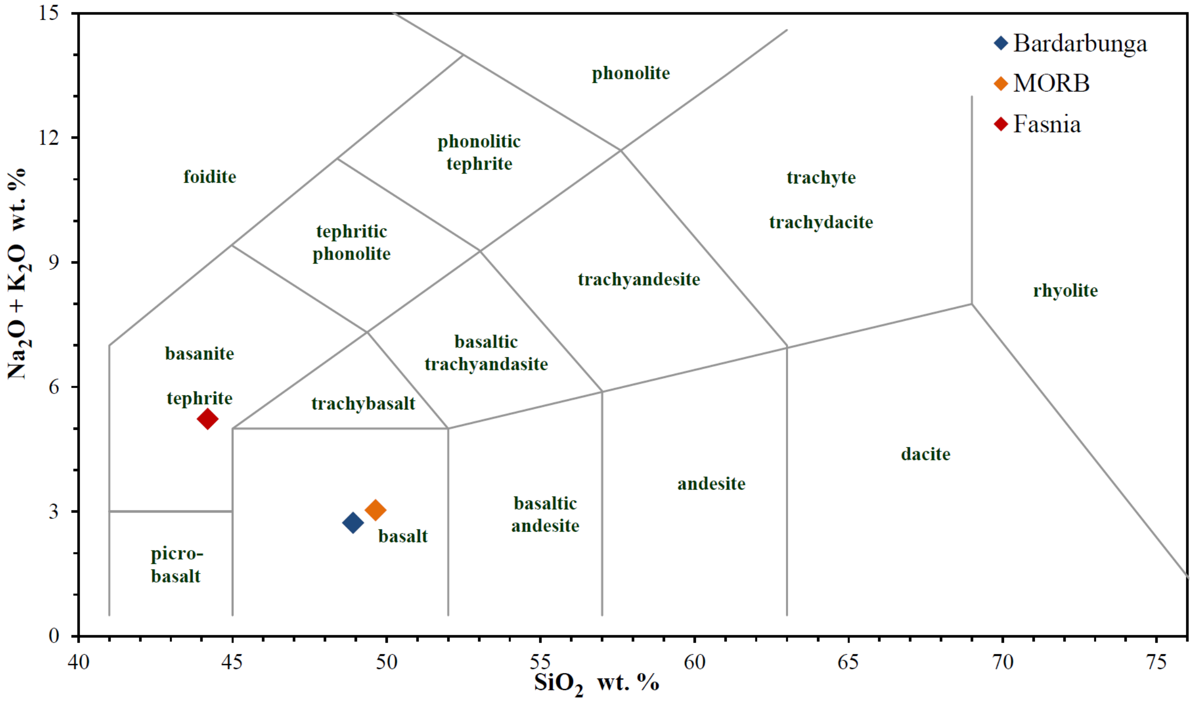

Figure 3-1: TAS diagram with basaltic compositions *sensu lato* studied in this work (from Bas et al. 1986).

3.1.1.1. Bárðarbunga natural lava product (B-Nat) and molten glass (B-glass)

As shown in Table 3-1, EPMA analysis of the starting glass obtained after melting scoriae from Bárðarbunga show that the sample is basaltic with 48.91 wt.% SiO_2 and 2.73 wt.% total alkalis (Mg# = 0.80). B-Nat sample is vesicular and crystal-poor (crystals >1 mm and up to few cm) with a mineral assemblage dominated by plagioclase (0.1–1 mm, An_{67-87}) and lesser amounts of clinopyroxene (Wo_{38-40} En_{48} Fs_{14-16}, Mg# = 0.70–0.85 defined here as cations $\frac{Mg}{Mg+Fe^{2+}}$), olivine (Fo_{69-76}), and titanomagnetite (Fe_2TiO_3). The sample contains numerous microglomerocrysts of anhedral clinopyroxene, plagioclase, minor subhedral olivine, skeletal Fe-Ti oxides, and small vesicles (0.2–0.5 mm diameter), the whole set in a groundmass consisting of the same previous mineral assemblage and glass. The chemical, textural and mineralogical features identified correspond to those of typical Icelandic tholeiites associated to the Bárðarbunga volcanic system as described in Geiger et al. (2016), Kolzenburg et al. (2017), and Halldórsson et al. (2018).

3.1.1.2. Juan de Fuca Mid-Ocean ridge basalt and molten glass

The composition of the basalt from Juan de Fuca mid-oceanic ridge (MORB; 49.65 wt.% SiO_2 and 3.03 wt.% alkalis; Table 3-1) is similar to that described in Prouteau et al. (2001) and Mottl et al. (1994; Mg# = 0.59–0.73). According to these authors, the MORB sample is microcrystalline, with crystal size <150 µm. Olivine microphenocrysts morphology varies from partially rounded to euhedral with a composition of $Fo_{77–86}$. Plagioclase microphenocrysts (~0.1 mm) are euhedral columnar crystals and have compositions ranging from An_{88} to An_{68}. Clinopyroxene phenocrysts are sub-euhedral, rounded, and are included in radiating aggregates with plagioclase. Fe-Ti oxides are skeletal individual and small (~0.01 mm), and are associated with plagioclase and ferromagnesian grains (Mottl et al. 1994).

3.1.1.3. Fasnia Alkali-basalt natural product and molten glass

The composition of Fasnia eruption products can be classified as basanitic (Figure 3-1; Table 3-1) with 44.19 wt.% SiO_2 and 5.23 wt.% alkalis, and is similar to those studied in Albert et al. (2015) and Jiménez-Mejías et al. (2021). Fasnia sample contains euhedral phenocrysts (13 wt.%) and microphenocrysts of olivine (Fo_{87-79}), clinopyroxene (Wo_{48-50} En_{35-41} Fs_{12-14}, Mg# = 72–78), Fe-Ti oxides of variable composition and plagioclase (An_{69-51}), the latter appearing only as microphenocrysts. The whole assemblage is set in a microlithic groundmass consisting of the same previous mineral assemblage and glass (Albert et al. 2015).

The results of the IR measurements for each sample are presented below.

Table 3-1: Chemical EPMA composition for basaltic samples: Bárðarbunga (B-glass, B-Nat), MORB, and Fasnia. Note that measurements were performed in glassy state after fusion or after IR measurement of ε at high temperatures. S.D.: standard deviation.

Oxide wt. %	B-glass BeforeIR		B-glass AfterIR		B-Nat-AfterIR		MORB-BeforeIR		MORB-AfterIR		FASNIA-BeforeIR		FASNIA-AfterIR	
	Glass	S.D.	Glass	S.D.	Glass	S.D.	Glass	S.D.	Glass	S.D.	Glass	S.D.	Glass	S.D.
# analysis	34	-	79	-	19	-	25	-	35	-	15	-	15	-
SiO_2	48.91	0.58	50.19	2.01	51.65	1.87	49.65	0.69	50.83	1.15	44.19	0.32	47.40	0.53
TiO_2	2.01	0.19	1.87	0.13	1.98	0.24	2.45	0.14	2.26	0.23	3.71	0.14	3.92	0.15
Al_2O_3	13.58	0.38	13.71	0.33	13.10	0.39	13.71	0.28	13.95	0.68	15.10	0.22	15.44	0.66
FeO tot	13.69	0.87	12.64	1.07	11.32	1.30	13.01	0.31	11.66	1.63	12.44	0.34	8.72	0.47
MnO	0.24	0.09	0.20	0.07	0.25	0.10	0.20	0.06	0.22	0.08	0.19	0.07	0.14	0.08
MgO	6.95	0.36	6.95	0.34	7.01	0.45	6.57	0.07	6.29	0.41	7.85	0.09	6.71	0.33
CaO	11.85	0.29	11.62	0.45	11.82	0.79	10.97	0.10	11.24	0.75	10.42	0.07	11.56	0.36
Na_2O	2.50	0.09	2.42	0.21	2.43	0.32	2.78	0.09	2.82	0.23	3.62	0.10	3.69	0.15
K_2O	0.23	0.04	0.21	0.04	0.23	0.07	0.26	0.06	0.26	0.06	1.61	0.10	1.46	0.11
Cr_2O_3	0.01	0.01	0.01	0.02	0.01	0.02	0.01	0.02	0.09	0.14	0.04	0.03	0.01	0.02
P_2O_5	-	-	-	-	0.22	0.09	0.40	0.23	0.36	0.32	0.84	0.12	0.91	0.18
NiO	0.02	0.04	0.09	0.09	-	-	-	-	-	-	-	-	0.04	0.08
Total %	100.00	-	100.00	-	100.00	-	100.00	-	100.00	-	100.00	-	100.00	-

3.1.2. Emissivity–Temperature relationship for Bárðarbunga glass (B-glass)

Prior to *in situ* high temperature ε measurements, the spectral emissivity determined at room temperature using indirect method (i.e., 1-R-T, cf. section 2.2.1) is always recorded first and is considered as a reference spectrum at room temperature; i.e., it shares similarities with amorphous spectra of quartz (Figure 1-8; De Sousa Meneses et al. 2014). As it can be seen in Figure 3-2a, spectral emissivity of B-glass determined indirectly is in good agreement with that measured with the direct method at 462 K. Note that, when the direct method is applied at such relatively low temperature (i.e. 462 K), ε can only be measured in a limited spectral range because of the insufficient thermal radiation achieving the detector. The emittance spectra (Figure 3-2) is characterized by a well visible wide Reststrahlen absorption band (at ~1000 cm^{-1}) and the presence of CF, both features are typical of dielectric glass materials. The value of spectral emissivity in the Reststrahlen band measured using the direct method is slightly higher (~0.80) than that determined from the indirect method (~0.77) because of its higher temperature. No indirect measurement was realized at high temperature even if these properties, as emittance, are known to be temperature dependent (De Sousa Meneses pers. comm.). However, the setup and the sample thickness prevent the reflectance and transmittance to significantly change with temperature to influence the opacity of the samples. As shown in Figure 3-2b-d, the emissivity spectra of B-Nat, Fasnia, and MORB basalts recorded directly and indirectly also show very good concordance.

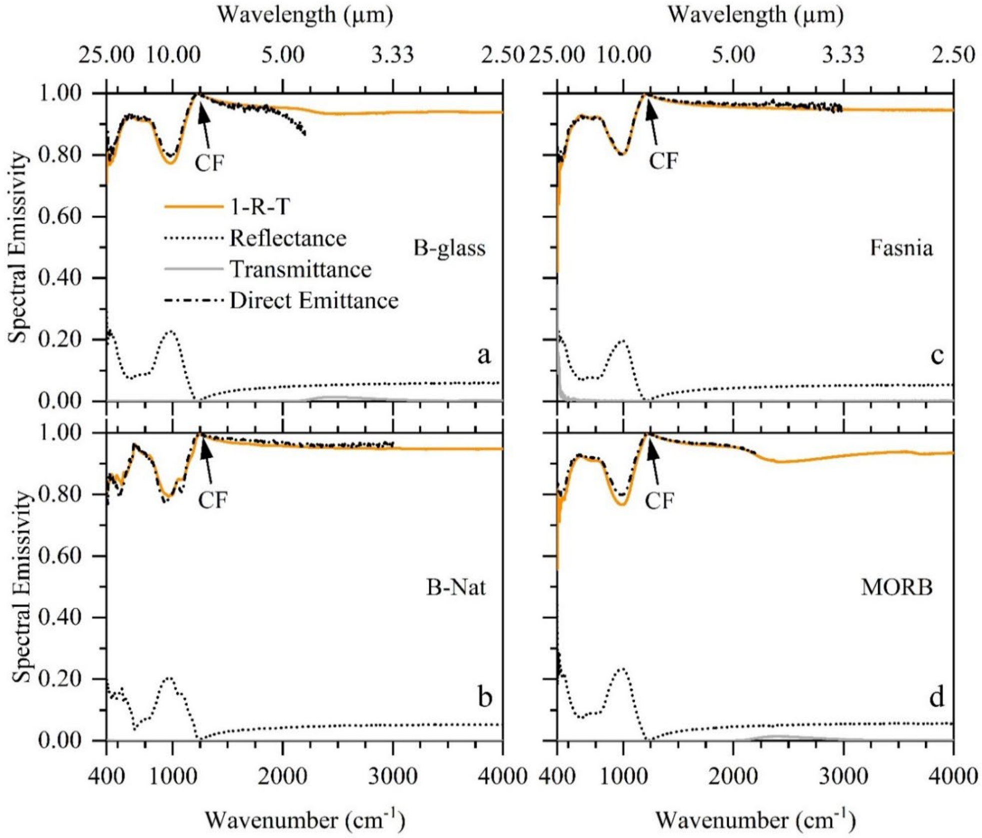

Figure 3-2: Comparison of emissivity spectra measured using indirect method (1-R-T) at room temperature and direct measurements at 462 K for B-glass (a), 655 K for B-Nat (b), 636 K for MORB (c) and 555 K for Fasnia (d). Note the 1-R-T emittance spectrum results from the combination of previously measured individual Reflectance and Transmittance spectra, also shown for each basalt (a, b, c, d).

Figure 3-3a,b shows the spectral emissivity evolution with temperature for B-glass. Panel a) shows the full spectral range investigated (TIR–MIR–SWIR, 400–8000 cm^{-1}), while panel b) focuses mostly on TIR (400–2000 cm^{-1}). Note that for better readability not all measured spectra are shown (cf. Appendix B.7 for an example of all measured spectra). Each selected spectrum is representative of the main modification of spectral emissivity behavior in each temperature range. As such, five characteristic temperature ranges were defined and are described below. The temperature is retrieved using the pyrometry at the Christiansen point.

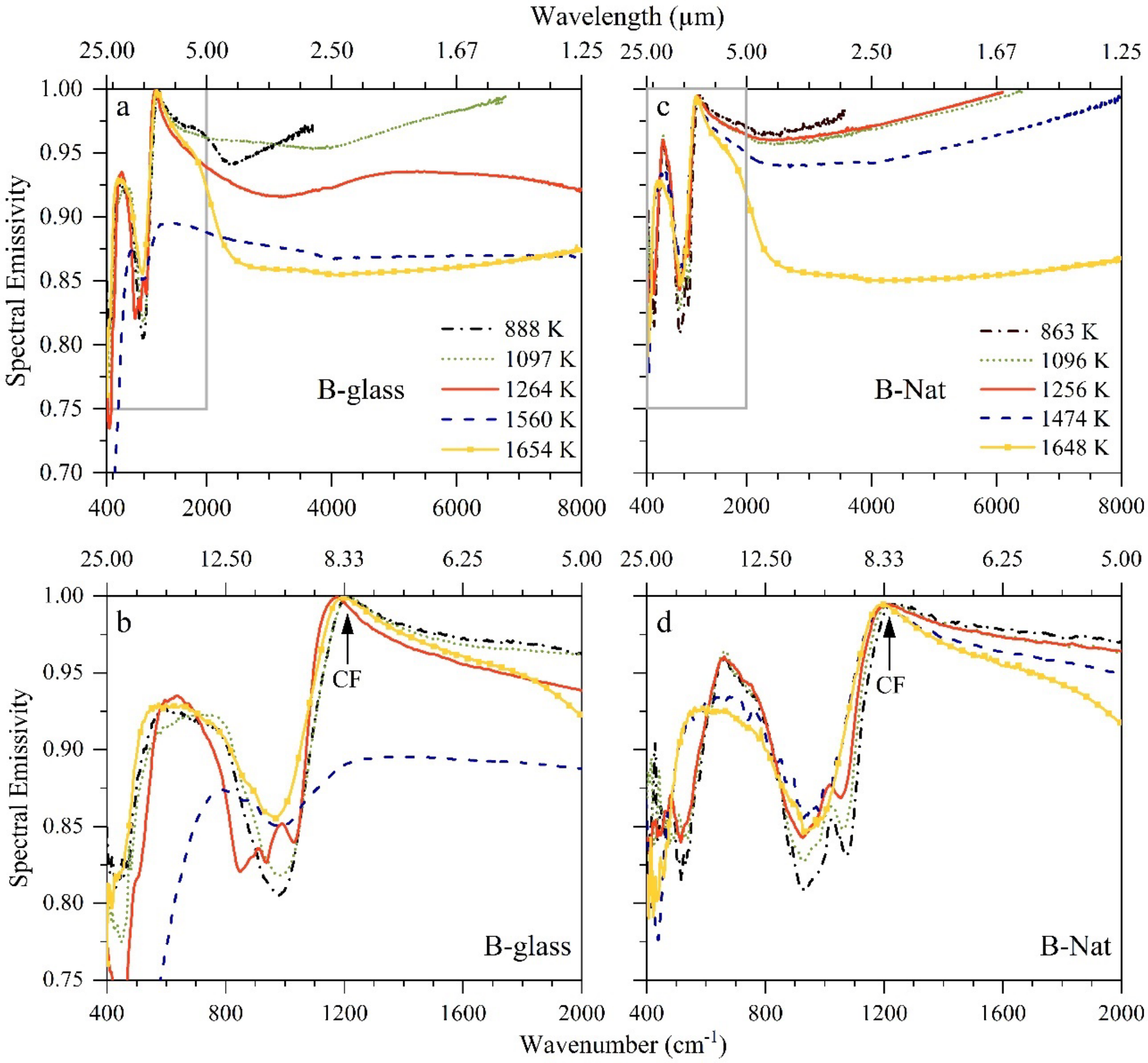

Figure 3-3: Spectral emissivity evolution with temperature and wavenumber for B-glass (a,b) and B-Nat (c,d) (thickness: 1.5 mm, and 3.0 mm at ~1650 K). Panels a) and c) full measured spectral range covering TIR, MIR and SWIR. Panels b) and d) zoom on TIR spectral range (8–12 µm). CF: Christiansen Feature.

In the first characteristic temperature region: Room Temperature (RT)–1020 K (i.e., the spectrum at 888 K is representative of the sample emissivity behavior over this T range; Figure 3-3a,b), ε slightly varies with increasing temperature. In the opaque region (<1500 cm^{-1}), the Reststrahlen bands reveal the vibrations of Si and Al-based tetrahedra of the disordered glass structure (Crisp et al. 1990; King et al. 2004). The CF is located at 1230 cm^{-1} at ambient temperature while decreases to 1210 cm^{-1} at 1020 K. With the temperature increase, ε minimum located at 980 cm^{-1} slightly increases from 0.79 to 0.82, which is the expected evolution with temperature. This behavior, comparable to that observed in pure silica (Figure 1-8; De Sousa Meneses et al. 2014, Rozenbaum et al. 1999), is related to the increasing dampening of the glass structure vibrations owing to the rise in anharmonicity and local structure reorganization. In the multiphonon region (between 1500–3500 cm^{-1}), the sample shows a transmissivity front (Figure 3-3a) indicating that B-glass behaves as a semitransparent material above CF. Therefore, the measured emittance corresponds to the addition of both contributions from the sample surface and inner volume. The degree of implication of the volume strongly depends on the optical indices of the sample (De Sousa Meneses et al. 2004). In consequence, the spectral emissivity is no longer governed by surface scattering only, and the most commonly used method to estimate spectral emissivity based exclusively on reflectance measurements, i.e. "1-R" (Harris 2013), has to be used with great care for similar compositions as B-glass.

In the second characteristic temperature range, between 1020 and 1097 K (for representativeness see the spectrum at 1097 K in Figure 3-3a,b), the ε markedly increases in the multiphonon and electronic regions (from 0.94 close to unity at 2400 cm^{-1}), making the transmissivity front indistinguishable. This rapid ε jump corresponds to an opacification phenomenon (Li et al., 2021 and references therein). In consequence, the material changes its optical properties from semitransparent (ε is driven by volume scattering) to opaque (ε is driven by surface scattering only).

Between 1097 K and 1350 K (for representativeness see the spectrum at 1264 K in Figure 3-3a,b), the temperature increase induces important changes in the ε behavior of the sample. In the TIR region, the wide Reststrahlen band splits into two distinct absorption bands centered at ~850 cm^{-1} and ~1030 cm^{-1}. These bands can be related to the presence of clinopyroxene crystals that has similar absorption bands at ~920 and 1070 cm^{-1} (exact band position is affected by composition and slight difference in contribution of glass matrix, cf. section 3.1.1). The CF shifts towards smaller wavenumbers (i.e., from 1210 cm^{-1} at 1097 K to 1080 cm^{-1} at 1350 K) until it becomes undistinguishable above 1350 K. In the multiphonon and electronic regions (>1500 cm^{-1}), ε steadily decreases first and then oscillates between 0.90–0.94 in the temperature range 1200–1350 K. These oscillations are related to the presence of constructive and destructive interferences that appear first at high wavenumbers and move towards lower wavenumbers as temperature increases. Such behavior, already observed in other materials (del Campo et al. 2008), reveals the presence of a layer of Fe-Mg-rich oxides demixing with the melting glass and clinopyroxene (cf. section 3.2.1).

Between 1350 K and 1560 K (for representativeness see the spectrum at 1560 K in Figure 3-3a,b), the progressive heating causes the collapse of the entire ε spectrum from ~0.93 to an almost invariable ε value of ~0.87. Such significant modification of the emissivity points out to the complete segregation of the Fe-Mg-rich oxides to the sample surface. These Fe-Mg-rich oxides, having different optical properties than that of the glass (i.e., a non-negligible electrical conductivity), dominate the radiative response of B-glass. Based on the complex ε−T relationship observed at 1350–1560 K, it should be stressed that the determination of the sample temperature by pyrometry using the CF wavenumber is no longer possible (as the emissivity value as this point is unknown and cannot be fixed to 1 anymore). Consequently, another method was developed. To retrieve the sample temperature, we assumed a flat spectrum having an emissivity level equivalent to that of reflectance spectrum measured after IR experiment on a sample, which was quenched before reaching melting temperature (cf. Appendix B.1). Note that this method is not as much precise as with the CF and can give temperature errors of ±30 K, but the emissivity spectra retrieved remains precise at 5%.

Above 1560 K, (see the spectrum at 1654 K in Figure 3-3a,b), ε is representative of B-glass molten state. The spectral signature is characterized by the presence of a broad Reststrahlen band in the opaque region (Rozenbaum et al. 1999) with a minimum at 980 cm^{-1}, and the recovering of CF at 1210 cm^{-1}. It also shows a well-marked transmissivity front suggesting the complete melting of previous oxides since ε is stable at 0.85 in the electronic region (Figure 3-3a,b). These observations are indicative of the progressive melting of the sample, causing the silicate network breakdown as well as the increase of the vibrational movements of the system. The main observation and interpretation of B-glass radiative properties regarding thermal and textural analyses are described further in section 3.2.1).

3.1.3. Emissivity–Temperature relationship for Bárðarbunga Natural (B-Nat)

Figure 3-3c,d show the spectral emissivity evolution with temperature for B-Nat. For better visualization and similarly to B-glass, only few representative spectra are selected.

In the opaque region (for representativeness see the spectrum at 863 K in Figure 3-3c,d), one minor and two major absorption bands are located at ~530 cm^{-1}, and ~920 and ~1080 cm^{-1} respectively. These bands can be related to the presence of clinopyroxene and plagioclase since these phases have characteristic absorptions at ~515, 920 and 1070 cm^{-1}. With temperature increase, the absorption bands slightly shift to 910 and 1050 cm^{-1} (at 1256 K) before forming a single broad band above 1256 K, while their respective ε minimum increases from 0.80 to 0.86 and from 0.82 to 0.87, respectively. That is the expected variation with temperature. Moreover, the CF initially located at 1246 cm^{-1}, shifts to 1191 cm^{-1} at 1648 K. Compared to B-glass, the CF is always well observed and is maintained at **ε** = 1 during experiment. This suggests that B-Nat is less influenced by the Fe-Mg-rich oxide segregation than B-glass. Note that vesicles strengthen the surface scattering and induce an ε increase in the opaque region (Rozenbaum et al. 2009).

In the multiphonon and electronic regions (MIR and SWIR), ε shows high values already at low temperatures (e.g., ~0.97 at 2400 cm^{-1} and 863 K) and no transmissivity front is observed. These spectral features differ from that of B-glass, revealing that B-Nat is already opacified at low temperatures. This is related to the initial organization of the silicate structure and to the presence of Fe-Mg-rich crystals (= Fe-Mg-rich oxides + clinopyroxene) at ambient temperature. With further temperature increase (>1474 K), the sample becomes semitransparent and the spectral emissivity plummets from ~0.98 (at 863 K) to ~0.85 (at 1648 K). As for B-glass, such progressive ε evolution can be associated with the disorganization of B-Nat silicate network through melting of the crystals and glass. Both samples, once melted, behave identically, namely they show typical spectrum of disordered glass. A similar ε–T relationship in these regions (MIR and SWIR) is observed by Bouvry et al., (2017) and Thompson et al., (2021). Moreover, most of published works systematically ignore MIR and SWIR spectral ranges (even with the recent development of RS-satellite focused on SWIR), missing the ranges at which the radiative properties vary the most according to our observations for basalts. Without constrained data at high temperature and wide spectral range, spectral emissivity have drastic impact on lava retrieved temperatures (c.f. Chapter 5) and ultimately have important consequences on the final modeled distance-to-run of the flow (Rogic et al. 2019b).

3.1.4. Emissivity–Temperature relationship for Fasnia and MORB

To unravel the effect of composition on radiative properties of basalts, the ε–T relationship of Bárðarbunga glass was compared to those gained on a MORB from Juan de Fuca ridge and a basanite from Fasnia eruption (Tenerife, Canary Island) and gathered in Figure 3-4. MORB ε behaves similarly to B-glass in the temperature range explored due to its close compositions (in agreement with its distinct composition (Table 3-1; Figure 3-1): Fasnia is more alkaline (44 wt.% SiO_2, 5.23 wt.% alkalis) and has a lower FeO content (12.44 wt.%). The chemical differences are also confirmed by the CF values: 1228 and 1230 cm^{-1} for MORB and Bárðarbunga respectively vs. 1215 cm^{-1} in the case of Fasnia. This is in good agreement with the general statement that the more evolved the composition, the more polymerized the structure, and the higher the wavenumber at which the CF is observed (Pisello et al. 2019).

The temperature range, in which the opacification phenomenon appears, is the major difference between basalts and basanite glasses. In the case of MORB, ε jumps from 0.89 to 0.96 in the multiphonon region between 861 K and 1046 K whereas Fasnia basanite is already opacified (with ε >0.95 in the multiphonon region) <889 K. This difference was already observed in Bouvry et al. (2017) for other basaltic compositions. Note that MORB opacification occurs at lower temperature than in the case of B-glass (1020–1097 K).

With the temperature increase, MORB and Fasnia glasses show very similar ε–T evolution to B-glass (Figure 3-4): first, they undergo the crystallization of Fe-Mg-rich oxides and then their segregation from the silicate melt. The molten state is progressively reached at >1500 K. Absolute ε values do not notably vary from one sample to another at a given temperature (Figure 3-4). The evolution of emissivity with temperature in opaque region (TIR) is however argued in the literature. Abtahi et al. (2002) and Rogic et al. (2019a, 2019b) determined high ε values (>0.8) for their basalts, but contrary to our results, they showed that spectral emissivity decreases with increasing temperature (Figure 1-6). This difference can be explained by either variations in sample composition, texture and/or the instrument setup used, as already discussed in Chapter 1. This most striking negative ε–T relationship allowed the authors to state that the emissivity of lava is lower than that of their fully crystallized rock equivalent. Moreover, this assumption was later used by Ramsey et al., (2019) to study the effect of spectral emissivity on Tolbachik lava flows using PyFlowGo model (Chevrel et al. 2018). These authors did not attain full melting and were forced to extrapolate to high temperatures the emissivity values obtained at low temperatures, putting into question their assumption, and hence its applicability to real volcanic systems.

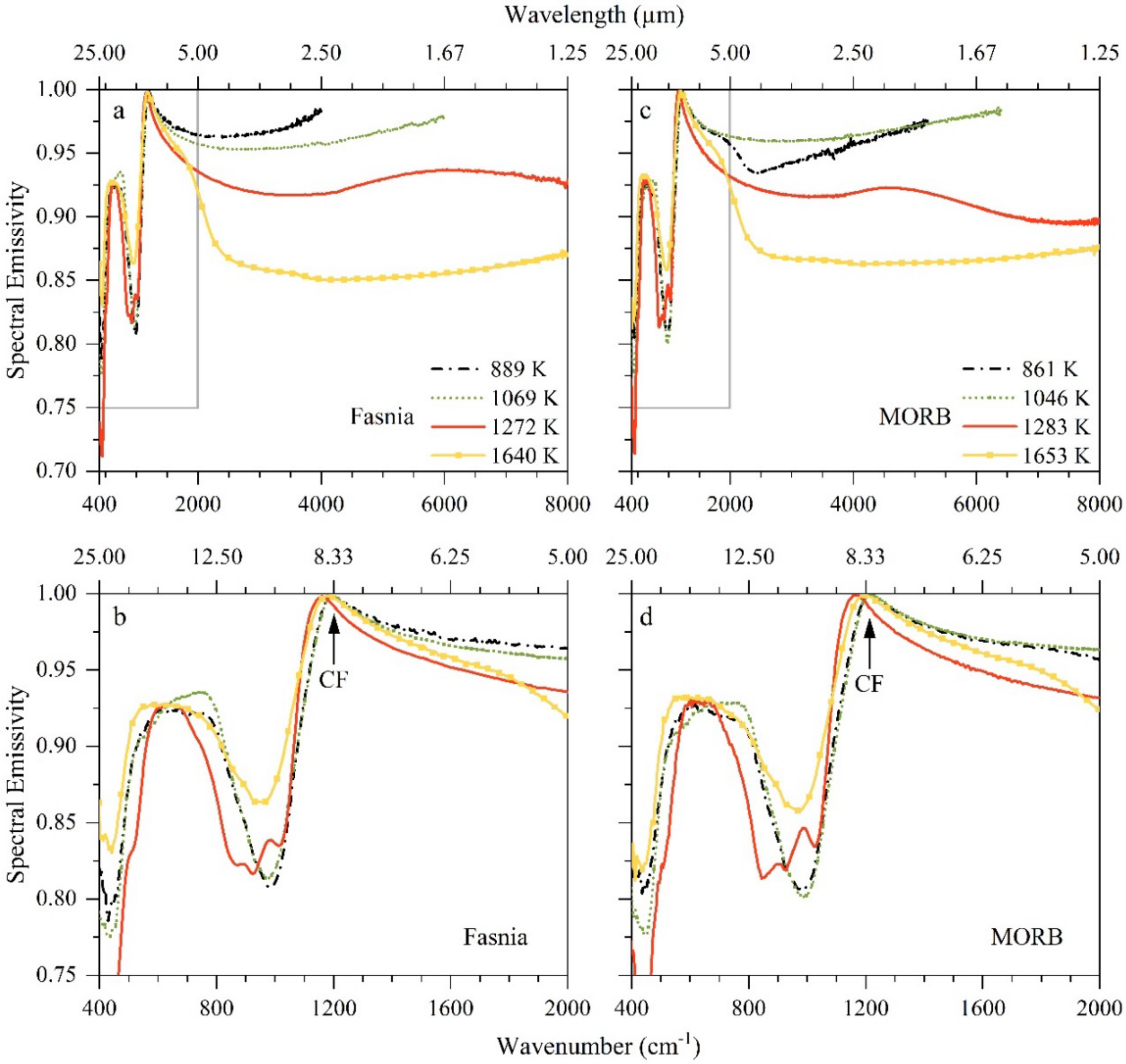

Figure 3-4: Spectral emissivity evolution with temperature and wavenumber for Fasnia (a,b) and MORB (c,d) (thickness: 1.5 mm, and 3.0 mm at ~1650 K). Panels a) and c) full measured spectral range covering TIR, MIR and SWIR. Panels b) and d) zoom on TIR spectral range (8–12 μm). CF: Christiansen Feature.

3.2. Discussion

3.2.1. High temperature radiative properties of basalts and origin of the opacification phenomenon

The three basaltic glasses (B-glass, MORB, and Fasnia) studied in this work seem to display similar emissivity evolution with temperature increase (Figure 3-3 and Figure 3-4). Their optically polished and non-porous surfaces are similar and reduce the scattering effect of rough surface, while increasing the specular scattering of the light, allowing better distinction of their spectral features especially in the opaque region. The main difference between their radiative behaviors is related to the temperature interval at which the opacification phenomenon is activated and thus when the optical properties change from semitransparent to opaque. This thermally activated process has already been observed in our previous study on Fe-rich phonolites (Li et al. 2021) and attributed to the presence of Fe-ion clusters. Based on the results presented here for basalts, we further explored by complementary analyses (FTIR, SEM, EPMA, TEM, DSC, *ex situ* Raman spectroscopy and *in situ* XRD) the structural modifications that are responsible for the opacification phenomenon. In the following paragraphs, we will focus first on the analysis of Bárðarbunga basalt before including Fasnia and MORB analyses in section 3.2.2.

SEM inspection of B-glass prior emissivity measurements reveals that the starting B-glasses are crystal-free and compositionally homogeneous (Figure 3-5). However, after the *in situ* ε measurements performed up to T ≤1550 K the presence of crystals is confirmed by SEM and TEM (Figure 3-5 and Figure 3-6). The sample core is characterized by the presence of ubiquitous small (≤ 2 µm) cubic Fe-rich oxides (bright phase in Figure 3-5, Appendix B.2, and dark phase in Figure 3-6a) along with early forms of clinopyroxene (augite) and plagioclase (light and dark grey, respectively, in Figure 3-5, Figure 3-6b), set within a dark glassy matrix. In addition, the B-glass surface (for ε experiments <1550 K) is characterized by the exsolution of a newly formed Fe-Mg-rich crystalline layer of ~2 µm thick. The sample texture is sketched in Figure 3-7. Different Selected Area Electron Diffraction patterns in zone axis (SAED, insert in Figure 3-6a) were indexed for several crystals at the sample surface and core in order to determine their structure in agreement with the chemical compositions. Given the vast array of iron oxide compositions, it is necessary to identify the structure and composition of the oxides we observed as they can have different radiative properties affecting the basalt thermal response. Those at the surface can be classified as magnesioferrite [$Mg\,(Al_x, Fe_{1-x})_2\,O_4$], with a cfc (Fd-3m) structure and a cell parameter *a* of ~8.354 Å (01-076-2852). Core crystals can be classified as iron oxides with a cfc (Fd-3m) structure (confirmed with XRD diffractograms) and a cell parameter *a* of ~8.351 Å (00-039-1346). According to the ELNES fingerprints of the Fe-$L_{2,3}$ edge (cf. Appendix B.3), the core crystals exclusively contain Fe^{3+} in their structure whereas the surface crystals contain Fe^{3+} and Mg. Moreover, the ELNES fingerprint of the O–K edge of the core crystals corresponds to that of γ-Fe_2O_3 (maghemite), confirming the presence of this phase in the core of the sample. Thus, surface and core crystals show close crystallographic structures but differ in the composition by the presence of Mg in the surface crystals (i.e., Mg diffusion).

Figure 3-5: Figure 3-6: SEM pictures of basalts texture Before and after IR (at the surface and in the core sample: a) B-glass, b) B-Nat, c) MORB, d) Fasnia. Inset in B-glass is the chemical map of Fe, highlighting the iron-rich layer at the sample surface (cf. Appendix B.2 for chemical maps of Ti, K, Al, Na, Si elements).

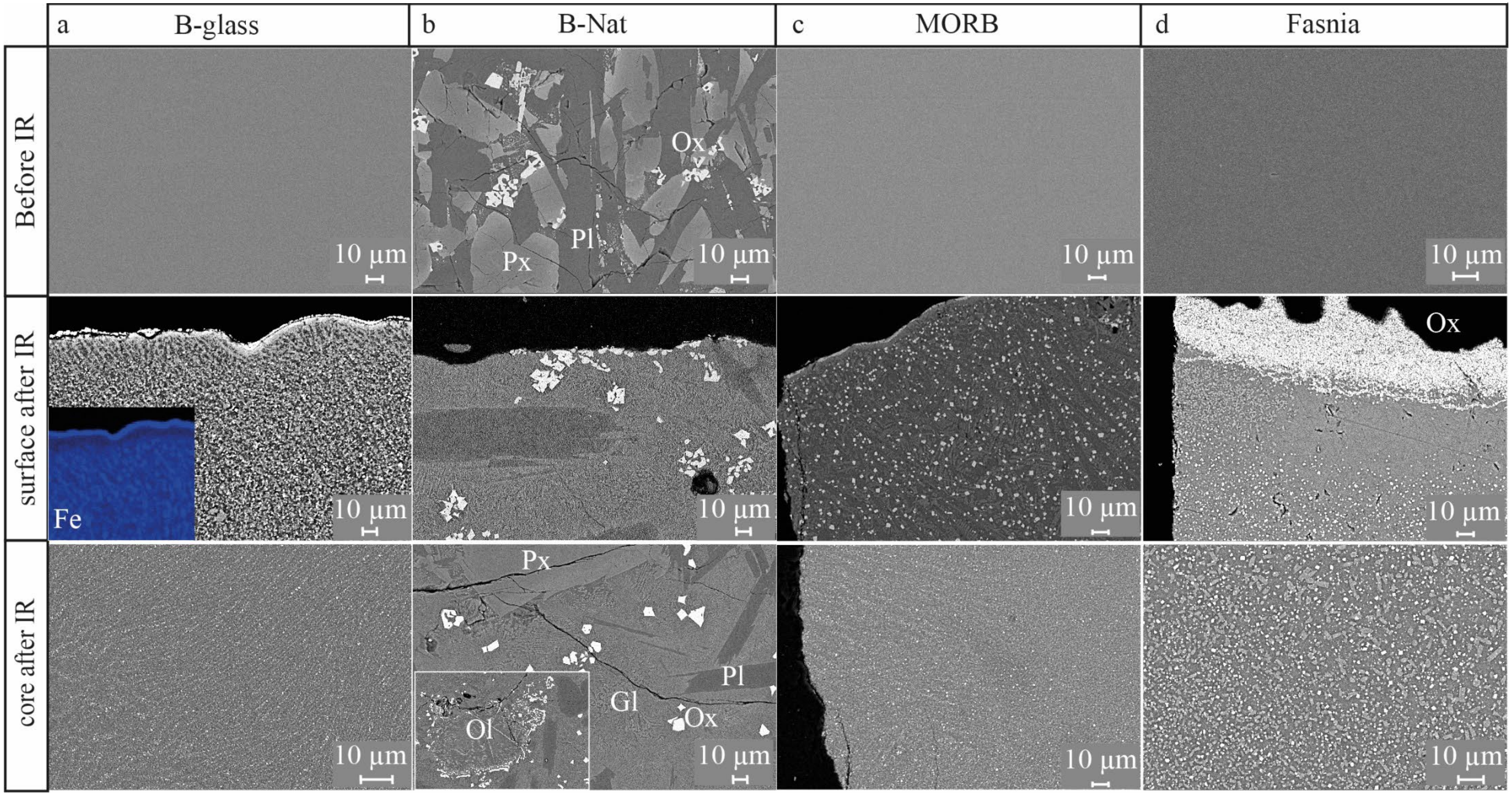

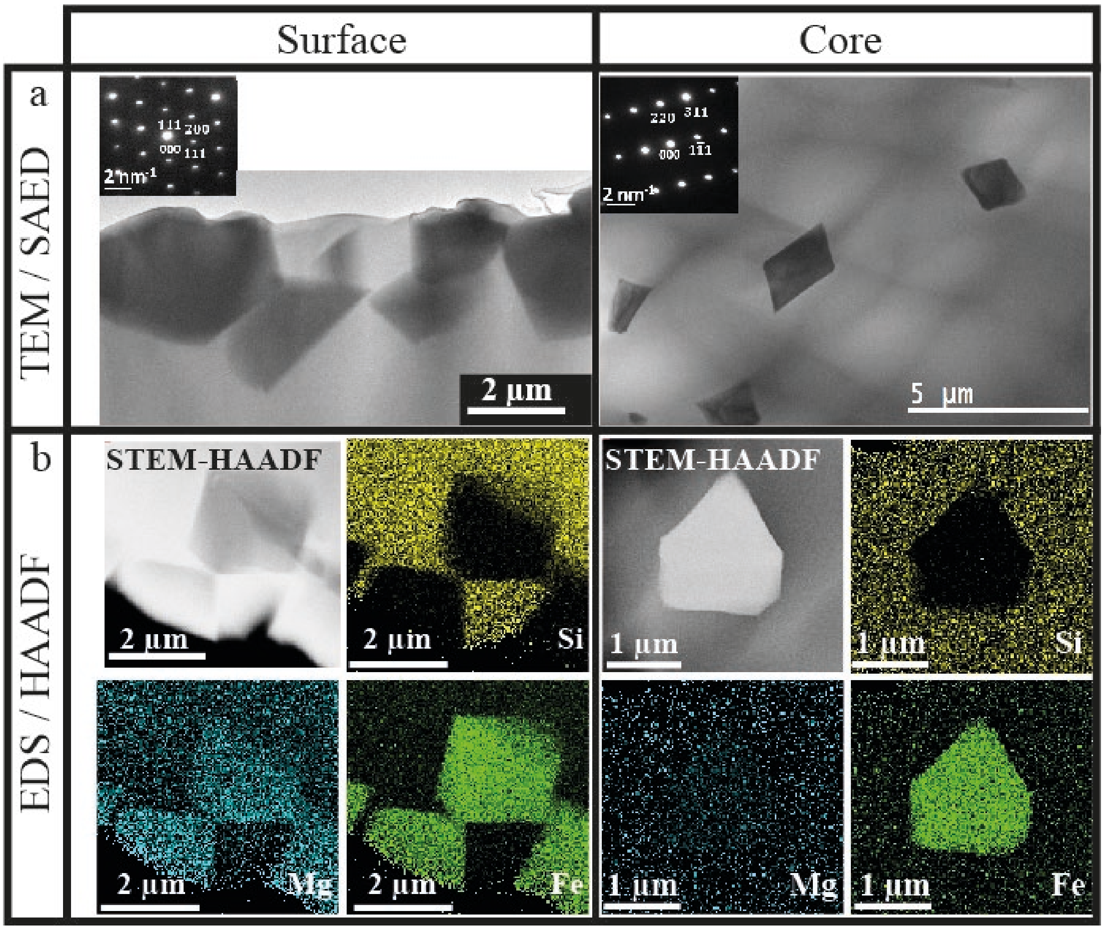

Figure 3-7: a) Bright-field TEM micrographs illustrating the microstructure after IR of B-glass surface (left) and core (right). Inserts show example of SAED patterns in zone axis [011] and [112] for crystals situated at the surface and in the core, respectively. b) STEM-HAADF images associated with STEM-EDS elemental maps of Si (yellow), Mg (blue) and Fe (green). Note the contrast inversion in STEM-HAADF image for B-glass core due to the sample thickness.

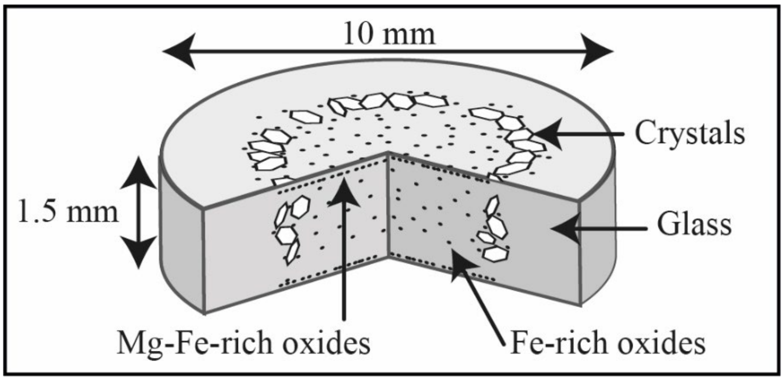

Figure 3-8: Sketch of the texture retrieved in B-glass after IR experiment <1550 K.

To assess the temperature at which each mineral phase appears during IR heating experiments, DSC analysis was performed. The DSC heating–cooling cycles (Figure 3-8a) reveal that above the temperature of glass transition, ($T_g = 939$ K), two crystallization events can be identified with temperature increase, these being in good agreement with *ex situ* Raman (Figure 3-9) and *in situ* XRD (Figure 3-10) results. A first exothermic peak (T_c) at 1132 K can be related to the crystallization of clinopyroxene and Fe-rich oxides, as suggested for Hawaiian basalts by Burkhard (2001). The second and less intense event (T_c) detected at 1370 K, points to further structure reorganization through crystallization of plagioclase. Note that Fasnia and MORB glasses display similar thermal features (Figure 3-8b). Second heating–cooling cycle in Appendix B.5 attests glass homogeneity and confirmed events observed in the first cycle.

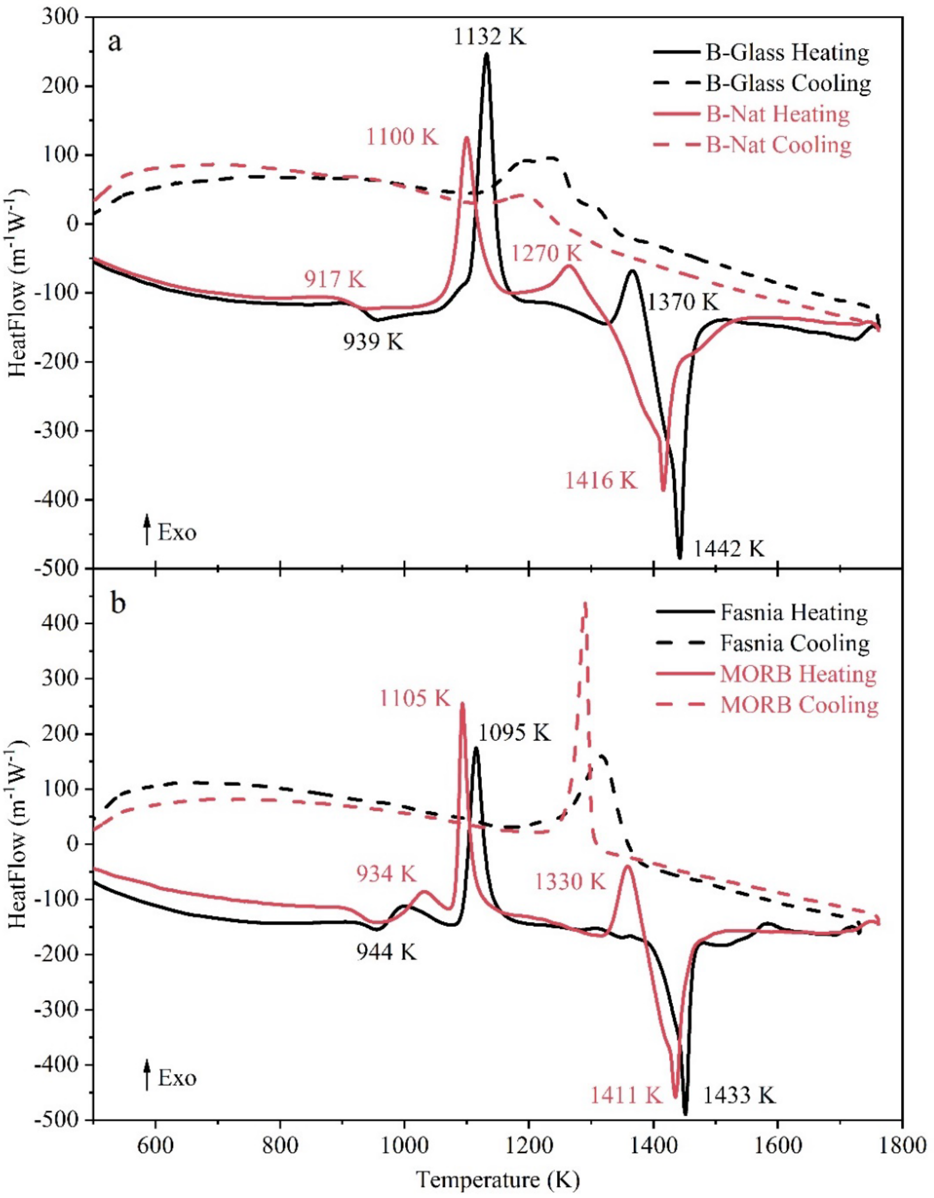

Figure 3-9: DSC heating (straight lines) and cooling (dotted lines) curves of B-glass / B-Nat (a) and Fasnia / MORB (b). Glass transition (917–944 K) and two crystallization events (1100–1132 K and 1270–1370 K) occur before melting (1411–1442 K).

Ex situ Raman spectra (Figure 3-9a) were recorded on the samples previously quenched during IR experiments at multiple temperature steps. The spectra distinctly show the transformation of B-glass from homogeneous (glass only) to heterogeneous (glass + crystals) state. Namely, the room temperature spectrum of B-glass, representing initial state before IR emission analysis, reveals the presence of characteristic bending and stretching vibrations of amorphous glassy silicate network (Colomban and Prinsloo 2009; Neuville et al. 2014; Di Genova et al. 2015). After the IR measurements performed above 1000 K, new Raman peaks are observed at 210, 287, 330 and 380 cm^{-1}, as well as more intense at 670 cm^{-1} and 700 cm^{-1}. These new Raman features in B-glass and MORB (cf. Appendix B.6) confirm the crystallization of clinopyroxene and Fe-Mg-rich oxides (Huang et al. 2000; Lalla et al. 2016; Di Genova et al. 2016, 2018; Cáceres et al. 2021). Note that contrary to B-glass where pyroxene crystals can be detected at temperatures above 1090 K, Fasnia reveals the crystal presence already at ambient temperature. The band at 700 cm^{-1}, assigned to the vibration of Fe^{3+}–O, is attributed to the formation of either Fe-Mg-rich oxides (Di Genova et al. 2020), ferrite spinel (Zinin et al. 2011; D'Ippolito et al. 2015) or maghemite (γ-hematite, metastable; Bellot-Gurlet et al. 2009; Lalla et al. 2016).

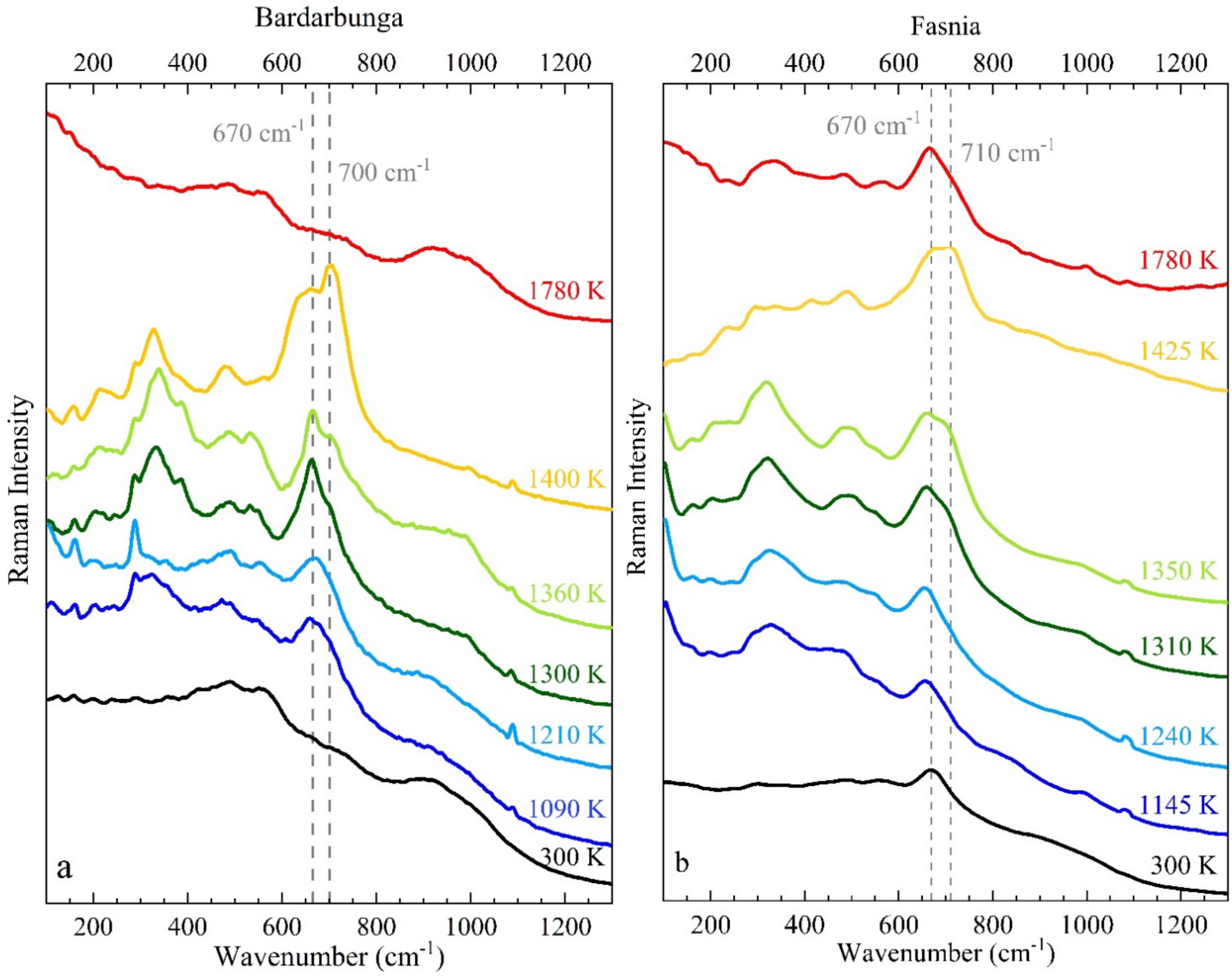

Figure 3-10: *Ex situ* Raman spectra of B-glass (a) and Fasnia (b) before (300 K) and after IR experiments (samples were quenched at multiple temperatures). Note that the two major bands at 665–670 and 700–710 cm^{-1} are related to the vibration of Fe–O and the crystallization of clinopyroxene and Fe-Mg-rich oxides in the glass structure.

In situ XRD analysis (Figure 3-10) shows amorphous glassy state without any crystallization ≤973 K. Note that the diffractograms recorded at low temperature (<973 K) present a decreasing trend at low angles between 10–40° typical of disordered glass structure. The Bragg peak of Pt (at 40°) is an artefact from the sample holder. On the other hand, the presence of Bragg peaks >973 K reveal crystallization processes with increasing temperature. *In situ* XRD analysis allowed clarifying the presence of clinopyroxene (augite) and Fe-Mg-rich oxides ($Mg[Fe^{3+}]_2O_4$, magnesioferrite) between 973 K and 1073 K; clinopyroxene being the dominant phase with higher absolute intensity. The increasing intensity of Bragg peaks (notably at ~35°, Figure 3-10) with temperature suggest that the Fe-Mg-rich oxide content progressively increases (Cullity, 1978). It also concurs with the temperature at which the Fe^{3+}–O Raman band (700 cm^{-1}) becomes the dominant spectral feature (T>1360 K). The XRD diffractogram at 1473 K (Figure 3-10) is largely modified due to textural effects (e.g., preferential orientation of crystals) created by the coexistence of B-glass molten state and crystals. Raman spectroscopy and XRD analysis confirm the micro-scale crystallization of Fe-Mg-rich oxides and clinopyroxene, and their evolution (growing + fusion) with temperature increase.

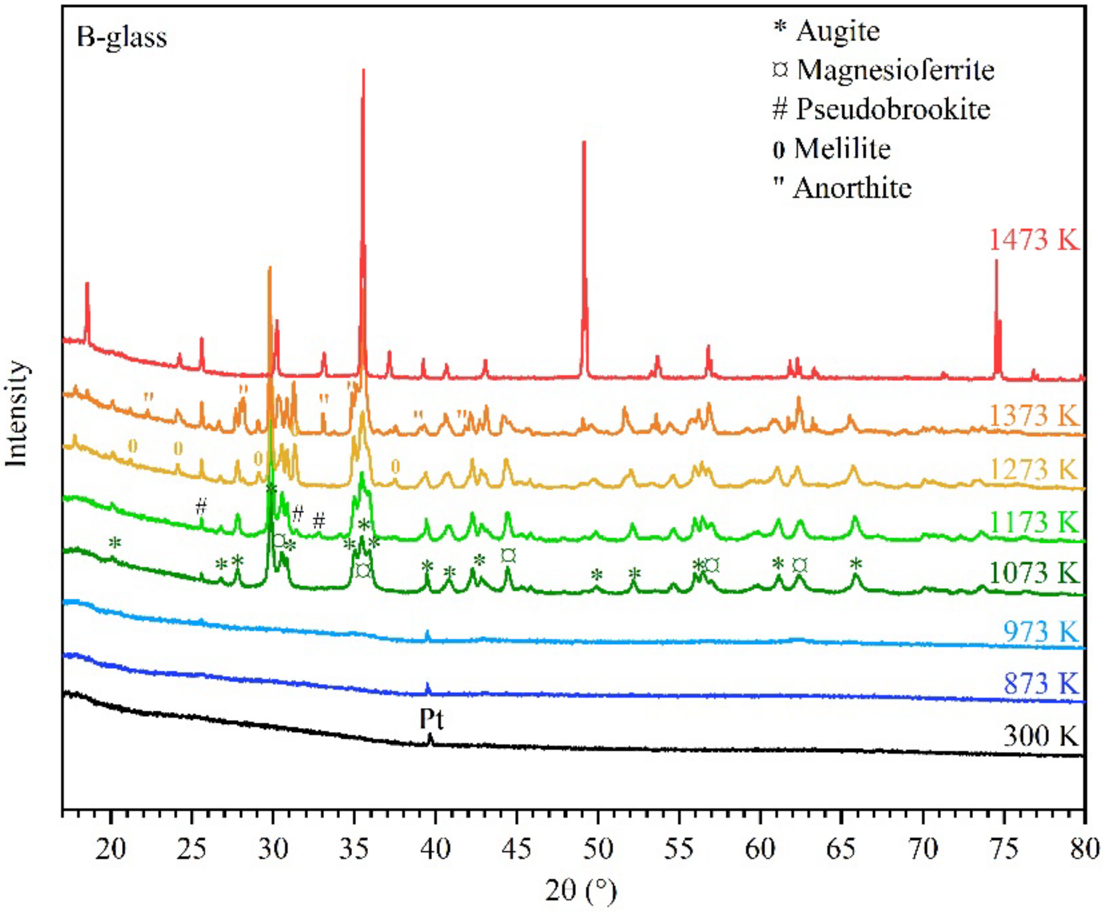

Figure 3-11: *In situ* XRD diffractograms of B-glass microstructural evolution with temperature. The principal phases: augite and magnesioferrite crystallize between 973 K and 1073 K. Note at low 2θ angles the characteristic feature of glass structure. Pt: Platinum sample holder.

Based on the above results, we can confirm the sequence of events that accounts for the opacification phenomenon in B-glass and follow the main structural observations summarized in Table 3-2. It should be first stressed that any temperature differences for crystallization and fusion events between the various techniques (IR, DSC, Raman, XRD) are related, on one side, to the starting material texture (powder vs. glass) and, on the other side to the heating history specific to each analytical device (furnace vs. laser, constant rate vs. quench). Nevertheless, the characteristic temperatures determined for each event agree within a reasonable interval (50–100 K). Thus, the progressing heating of the sample above T_g induces the silicate glass anharmonicity increase and structure relaxation, which promotes the mobility of ions. This leads first to the microstructure re-organization into clusters, then to the crystallization and growth of Fe-Mg-rich crystals and consequently ensues the sample opacification.

Table 3-2: Interpretation of the spectral emissivity behavior of B-glass with temperature increase, in agreement with DSC, XRD, and Raman analyses. CF: Christiansen Feature, TF: Transmission Front.

Temperature (K)	**Main IR Spectral Features**	**Physical Process**
<1020	Wide Reststrahlen band and CF in TIR, $\varepsilon \geq 0.9$ in MIR but presence of TF	Radiative response of semi-transparent homogeneous glass
1020-1150	jump-like increase of $\varepsilon \geq 0.95$ in MIR/SWIR	Opacification due to the formation of Fe-Mg-rich clusters
1150-1350	New thin absorption bands in TIR, Wide bands in MIR, SWIR	Crystallization of Fe-Mg-rich oxides in the melting glass
1350-1550	Overall ε decrease, loss of CF	Phase segregation: melt + Fe-rich oxides layer in surface Radiative response of Fe-rich oxides layer exclusively
>1550	Wide Reststrahlen bands in TIR, Decrease of $\varepsilon = 0.85$ in MIR/SWIR	Radiative response of homogeneous melt

Above 1150 K, the nucleation and crystallization of clinopyroxene occur along with the growth and the segregation of Fe-Mg-rich oxides from the melting glass towards the sample surface to form a Fe-Mg-rich micrometric layer (~2 µm; Figure 3-5). The formation of similar thin surface layer was already observed in del Campo et al. (2008) in the case of synthetic Fe-rich oxides. They assigned the oscillating bands observed in emissivity spectra (also seen here) to the growth of an oxide layer in the sample surface. Moreover, they observed that the maxima of oscillations shifted towards lower wavenumbers as the layer thickness increases. Thus, following their method, the oxide layer thickness in B-glass was mathematically estimated to be 0.3–1 µm depending on temperature, which is in accordance with SEM and TEM observations. Such crystal–melt segregation is also in good agreement with the works of Manylov et al. (2013), Berger et al. (2019) and Giuliani et al. (2020). These authors claim that heating basalt glass in air leads to complete iron oxidation and growth of magnesioferrite, which act as nucleation sites for pyroxene. Mujin et al. (2021) also show the formation of Fe nanometric oxides and silicates at 1220–1320 K for rhyolitic melts. Cook et al. (1990) further demonstrate that oxidation occurs by the divalent cations (Fe^{2+}) diffusion from the interior of the glass to the free surface where they subsequently react with environmental oxygen to form a micrometric ($Mg[Fe^{3+}]_2O_4$) crystalline layer which covers the (divalent cation-depleted) glass. Based on the results, the radiative properties of B-glass between 1150 and 1550 K are a mixed response from two distinct components: the near-molten glass and the Fe-Mg-rich oxides. With the further temperature increase up to 1550 K, the Fe-Mg-rich layer progressively controls the emissive behavior of B-glass sample. This should be stressed that once the oxide film with irregular shape and thickness is formed, it is responsible of the radical modification of IR spectra.

As previously shown (Figure 3-3) in the temperature range 1350–1550 K an overall fall of ε values with CF lost is observed. Since Fe-Mg-rich oxides have a high refractive index (~2) and behave as electric conductors, they have distinct radiative properties compared to those of silicate melt and crystals (both dielectric). Their emissivity spectra are not characterized by the presence of CF because the conduction electrons intensely absorb incoming energy, therefore screening the radiative response due to phonons (De Sousa Meneses, pers. com.). Furthermore, their size is comparable to the incident wavelength and therefore the optical rules are no longer defined by the geometry but by Mie diffusion. Thus, the combination of highly absorbing properties and diffusive behavior of these crystals hinders the contribution of glass emission. In consequence, Bárðarbunga thermal emission is exclusively governed by the Fe-Mg-rich oxides and is driven by surface scattering between 1350 and 1550 K. Finally, at temperature >1550 K, the spectral signature of the Fe-Mg-rich oxides decreases significantly because of their complete resorption, allowing the redetection of spectrum of molten silicate with characteristic CF. DSC and Raman observations (Figure 3-8 and Figure 3-9) attest the melting of the Fe-Mg-rich oxides >1550 K.

3.2.2. The effect of composition on the opacification phenomenon

As it was already detailed in Chapter I, prior to this work, only a handful studies investigated high temperature radiative properties of basalts (Abtahi et al. 2002; Bouvry et al. 2017; Rogic et al. 2019a, b; Pisello et al. 2019; Lombardo et al. 2020; Thompson et al. 2021). However, most of previous works did not consider melting temperatures (≤1300 K) and focused only on TIR spectral range. In order to determine the effect of composition on the radiative properties of basaltic rocks and the opacification phenomenon observed in our work, the B-glass results were carefully compared with those of MORB and Fasnia glasses (Figure 3-3 to Figure 3-9). As already showed, the ε–T relationship of MORB is very similar to that of B-glass whereas Fasnia shows distinct radiative behavior instead. As clearly depicted in Figure 3-4, Fasnia glass is already opacified in the lowest measured temperatures (<863 K) whereas the opacification of MORB, similarly to the B-glass, is observed above T_g. Note that T_g temperatures are similar: 934 and 939 K for MORB and Bárðarbunga, respectively vs. 944 K for Fasnia. This is very well supported by Raman results, which show clearly that Fasnia glass exhibits the Raman peak at ~670 cm^{-1}which can be assigned to the Fe-O bond, already at room temperature conditions. In the case of B-glass, similar Raman peak is detected above 1000 K. Bearing in mind the local probe of Raman scattering, this reveals clearly that the Fe-based clusters exist already at room temperature in Fasnia whereas in the case of B-glass (and MORB) they are formed only above T_g (Figure 3-8b). Raman spectra of Fasnia (Figure 3-9b) also show the same evolution with temperature as B-glass, the main difference between these samples corresponds to a small shift for the bands at 670 and 710 cm^{-1}. Raman spectra of MORB (Annexe B.6) display the same features as B-glass, both before and after IR experiments.

It should be stressed that since Fasnia FeO content is lower than that in the other two basalts (12.44 wt.% vs. >13 wt.%, Table 3-1), the Fe content cannot be fully responsible of the clustering and then early opacification. However, Fasnia silicate network contains more alkali ions and is more depolymerized in comparison with the more evolved, polymerized Bárðarbunga and MORB samples. In consequence, Fasnia initial silicate structure allows faster ion diffusion, which enhances the Fe-rich oxides formation. To achieve similar microstructural state in the case of MORB and B-glass, high temperature activation is necessary. These results show visibly that the opacification phenomenon affecting an optical behavior (from semitransparent to opaque) occurs in the magmatic rocks with high FeO content but must be supported by the silicate microstructure and presence of the network modifiers. In other words, the FeO content and the degree of polymerization strongly controls the spectral emissivity response. This clearly indicates the high complexity of sample radiative properties and the necessity of careful laboratory-based measurements for even individual magmatic rock, not only basalts. It is worth noting that further exploration of the composition effect on spectral emissivity was considered in this study. Indeed, additional magmatic rocks were considered in this study: andesite, dacite and rhyolite (i.e., magmas from the tholeiitic series; Figure 3-1). Their high temperature *in situ* emissivity spectra is presented and briefly discussed in Appendix C. As it is slightly out-of-scope for this study, the comparison of radiative properties between basalts and those of other compositions will be considered in a future perspective.

3.2.3. The effect of crystals on spectral emissivity: B-glass vs. B-Nat

We demonstrated that the spectral emissivity of B-glass is dominated by the presence of Fe-rich crystals, as well as the radiative properties of crystallized natural basalt slightly differ from its glassy counterpart. Since the natural sample (B-Nat) is a heterogeneous mixture of glass/melt, crystals, and vesicles, we must consider that each component exhibits specific radiative properties that will affect the sample overall emissive response. The comparison of B-glass and B-Nat results is thus a first step to understand the effect of crystals on the lava radiative properties.

At low temperature (<900 K; Figure 3-3), the main difference between the emissive behavior of the glassy (B-glass) and crystalline Bárðarbunga (B-Nat) samples is related to the presence of a transmissivity front. Glass sample reveals the semitransparent optical behavior whereas the crystalline counterpart shows opaque optical behavior (i.e., ε>0.95) since the opacification phenomenon is already activated at this temperature. As previously described, the presence of Fe-Mg-rich crystals (both oxides and clinopyroxene, with size >5 µm; Figure 3-5) in the initial texture of B-Nat, already at ambient temperature, result in the opacification phenomenon and is responsible of such high emissivity value. In contrast, the glassy counterpart reaches similar emissivity values at much higher temperatures, i.e., $T>T_g$, the conditions at which the Fe-Mg-rich crystals are formed. Note, as shown in Figure 3-5, in comparison with B-Nat, these newly formed crystals in glassy matrix have smaller size (~2 µm) but are present in higher proportions. Moreover, at high melt fractions and low crystal proportions, the sample radiative properties would be dominated by the liquid (spectra at ~1650 K in Figure 3-3) even if small amount of crystals were still present in the system (Figure 3-5). Another difference between Bárðarbunga B-glass and B-Nat samples is the absence of segregation phenomenon in the crystalline sample. This is evidenced by the fact that B-Nat sample never lose its CF, compared to B-glass at equivalent temperature range. This can be explained by their different kinetics occurring with the temperature increase. Homogenous B-glass reveals the crystallization processes through migration and segregation phenomena giving rise to the formation of an oxide film at the sample surface as well as the nucleation and crystal growth. The temperature evolution of heterogeneous B-Nat instead allows following the continuous melting process. For this reason, B-glass and B-Nat samples show relatively similar but not identical ε–T relationships.

Hence, in both cases, the measured emissivity of the samples is the results of the addition of the response from glass/melt and oxides, these having different proportions as temperature evolves. However, as each crystal have different emissivity behavior; their contribution to the bulk (melt + crystals) emissivity will strongly depend on their proportion and the spectral range we are looking at. As each crystal have different contribution to the sample radiative properties, we highlight that the composition, content, and microstructure of crystals are crucial to unravel the spectral emissivity behavior of lava flow rich in crystals. To that end, the effects of magmatic crystals on lava spectral emissivity are further explored in the next chapter. Note that the above chapter is articulated stand on an accepted publication in the Journal of Geothermal and Volcanological Research.

To summarize, the spectral emissivity of three different basaltic magmas was successfully recorded up to melting conditions and over a wide spectral range, which is one of the most important achievements of our study. The structural modifications that are responsible for the opacification phenomenon are succinctly explored and discussed via a large array of analytical techniques. The composition control on spectral emissivity was highlighted by the high FeO content in combination with the degree of polymerization of the silicate structure. Finally, the effect of crystal was introduced.

Chapter 4: Radiative properties of magmatic minerals

As indicated in Chapter 1, magmas and hence lavas are a mixture of melt-glass containing different mineral phases with variable abundances. In the previous chapter, the ε–T relationship of basaltic glasses was studied, and their radiative properties explored. Therefore, the study of mineral radiative properties is the next logical step and is at the heart of this chapter. The latter described in a first part the emissivity-temperature relationship for three magmatic minerals. As for basaltic glasses, chemical, textural, and structural analyses were also carried out for minerals. In a second part, we model the spectral emissivity of Holuhraun natural basalt with different textures. Finally, further analysis was carried out as to explore the effect of olivine on a crystal-rich oceanite. The results emphasize the importance of crystals in lava flow radiative properties.

Fagradalsfjall 2021 eruption, Iceland (credit: Icelandic Meteorological Office).

4.1. Emissivity–Temperature relationship for magmatic minerals

4.1.1. Characterization of studied magmatic minerals

As for basalts in Chapter 3, the chemical, textural, and structural evolution of magmatic minerals were studied prior and after each IR experiment. Three minerals were chosen as to best represent those currently found in basaltic magmas: one pyroxene, one plagioclase, and one iron-rich oxide. Note that the dominant phases in Holuhraun lava flows are by decreasing order of abundance: plagioclase–Pl, pyroxene–Px, olivine–Ol, and oxide–Ox. Despite that olivine is a common phase in basaltic magmas, the radiative properties of this mineral was not explored in this study as this is a minor phase in Bárðarbunga magmas (Gíslason et al. 2015; Lavallee et al. 2015; Halldórsson et al. 2018), and the ε−T relationships were already studied by Eckes et al., (2013). All considered minerals are unoriented, natural, and polycrystalline, and present smooth surface with little to no fracture and no porosity. Compositions are summarized in Table 4-1 and ternary diagrams (i.e., graphical representation of a mineral composition in function of the mineral solid solution endmembers represented at the poles of that graph) are given in Figure 4-1. The solid solution of Na-K feldspar–plagioclase includes the pure endmembers An-Anorthite (Ca, Al_2, Si_2O_8), Ab-Albite (Na, Al, Si_3O_8), and Or-Orthoclase (K, Al, Si_3O_8). The composition of a feldspar crystal can be then expressed as function of these three poles as follows: An=Ca/(Ca+Na+K); Ab= Na/(Ca+Na+K); Or= K/(Ca+Na+K).

The composition of a pyroxene can be similarly expressed based on the endmembers Wo-Wollastonite (Ca, SiO_3), En-Enstatite (Mg, SiO_3), and Fs-Ferrosilite (Fe, SiO_3) as Wo=Ca/(Ca+Fe+Mg); Fs= Fe/(Ca+Fe+Mg); En= Mg/(Ca+Fe+Mg). The composition of a mineral (Table 4-1) is given by the proportion of these endmembers such as $En_{37}Wo_{51}Fs_{12}$ in the case of an augite from the pyroxene series (Figure 4-1). The structure of minerals was confirmed with Raman spectroscopy while their texture was characterized by SEM image analysis.

According to EPMA analysis, all crystals show similar composition with little to no variation before and after IR experiment. As for composition, textural homogeneity was confirmed for all three minerals and no variation in surface or in cross-section were observed (Figure 4-2). Characterization of mineral structure with Raman spectroscopy support previous textural and chemical observation and shows that the mineral structure is preserved after IR experiment (Figure 4-3). The minor differences (e.g., the 332 and 395 cm^{-1} peak intensities of Augite vary after IR experiment) could be related to the relaxation of the mineral structure as results of rapid decrease in temperature experienced by the sample after IR experiments.

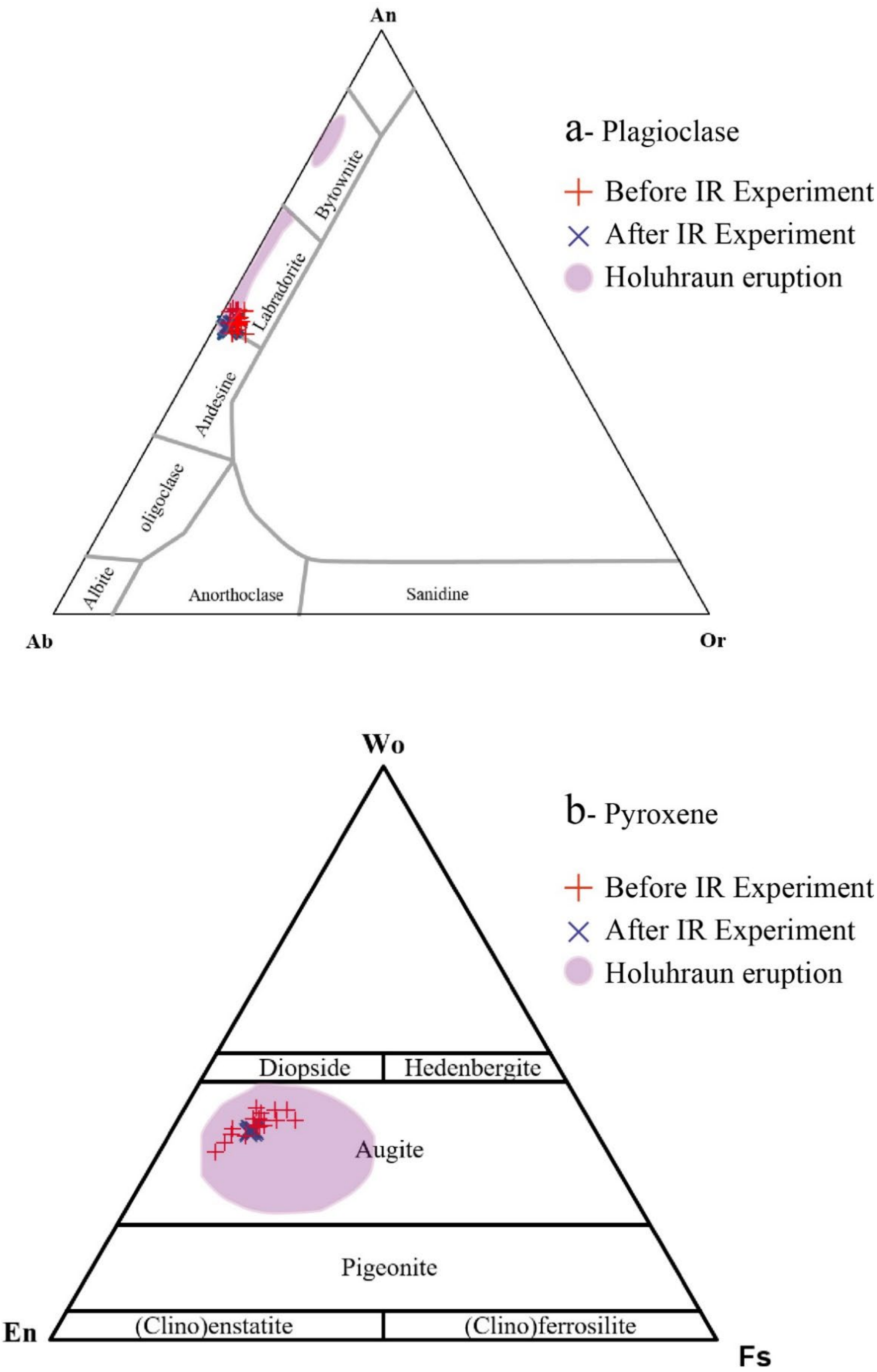

Figure 4-1: a) Ternary diagram for Feldspar-plagioclase; endmembers are An-Anorthite (Ca, Al_2, Si_2O_8), Ab-Albite (Na, Al, Si_3O_8), Or-Orthoclase (K, Al, Si_3O_8). b) Ternary diagram for Pyroxene; endmembers are Wo-Wollastonite (Ca SiO_3), En-Enstatite (Mg SiO_3), Fs-Ferrosilite (Fe SiO_3). At the pole, the amount of a given endmember is 100% whereas 0% at its opposite base. In blue and in red are respectively the labradorite before and after IR experiment. In pink are the range of composition found in Holuhraun product following Geiger et al., (2016) (diagram from Marshall, 1996).

Table 4-1: Chemical compositions by EPMA analysis for Labradorite, Augite and Hematite, respectively before and after IR experiment. N.D.: Not Detected, under detection limit.

Oxide wt. %	Labradorite beforeIR		Labradorite AfterIR		Augite beforeIR		Augite afterIR		Hematite beforeIR		Hematite afterIR	
		S.D.		S.D.		S.D.		S.D.		S.D.		S.D.
# analysis	10	-	21	-	10	-	18	-	15	-	21	-
SiO_2	55.90	0.29	56.23	0.92	50.90	0.53	50.55	0.81	0.07	0.06	0.04	0.03
TiO_2	N.D.	N.D.	N.D.	N.D.	0.67	0.07	0.60	0.17	N.D.	N.D.	N.D.	N.D.
Al_2O_3	27.52	0.26	27.38	0.65	6.70	0.11	5.84	1.61	0.19	0.05	0.17	0.05
FeO tot	N.D.	N.D.	0.19	0.09	6.85	0.31	7.20	1.03	99.57	1.19	99.67	0.62
MnO	-	-	-	-	0.17	0.04	0.13	0.07	N.D.	N.D.	N.D.	N.D.
MgO	N.D.	N.D.	0.07	0.03	16.85	0.10	17.19	2.45	N.D.	N.D.	N.D.	N.D.
CaO	10.35	0.14	9.99	1.08	16.58	0.21	17.77	1.00	N.D.	N.D.	N.D.	N.D.
Na_2O	5.60	0.09	5.35	0.51	1.14	0.04	0.61	0.35	N.D.	N.D.	N.D.	N.D.
K_2O	0.44	0.07	0.63	0.38	-	-	-	-	N.D.	N.D.	N.D.	N.D.
Cr_2O_3	-	-	-	-	0.09	0.03	0.06	0.03	N.D.	N.D.	N.D.	N.D.
P_2O_5	N.D.	N.D.	N.D.	N.D.	-	-	-	-	N.D.	N.D.	N.D.	N.D.
Total %	100	-	100	-	100	-	100	-	100	-	100	-
End-members	An_{49}-Ab_{48}-Or_3		An_{49}-Ab_{47}-Or_4		$Wo_{36}En_{52}Fs_{12}$		$Wo_{37}En_{50}Fs_{12}$		-	-	-	-

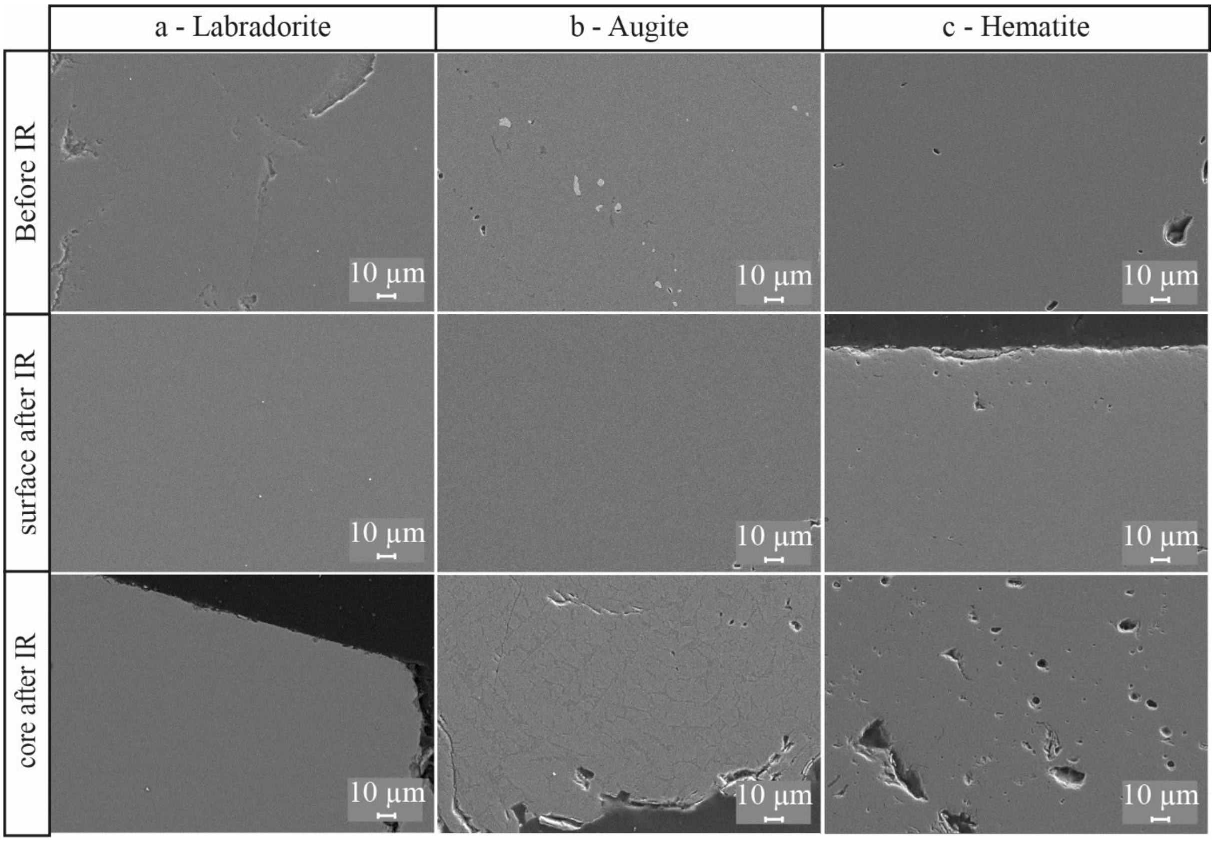

Figure 4-2: SEM pictures of Labradorite, Augite and Hematite before and after IR experiment (in core and at the sample surface).

In details, the plagioclase is a labradorite with composition of An_{49}-Ab_{48}-Or_3, this encompassing the lower end composition of the Holuhraun plagioclases (An_{54-75} and An_{65-75} respectively) identified by Geiger et al., (2016) and Halldórsson et al., (2018) in the products of this eruption. The labradorite surface has a semi-transparent aspect presenting few rare inclusions of micrometric minor phases such as iron-rich oxides. The impact of these minor phases to the retrieved radiative properties of the labradorite are considered negligible. The Raman spectra of the feldspars are readily recognized by the presence of two major Raman peaks lying between 450 and 515 cm^{-1} (Freeman et al. 2008). According to Lalla et al., (2016), the feldspars of intermediate composition such as Labradorite have major peaks at 510 cm^{-1} and 478–481 cm^{-1}. Here, we detect in Raman spectra prior and after IR experiments four major peaks at 178–187, 281–286, 479–482, and 507–508 cm^{-1} and two minor peaks at 406 and 559–565 cm^{-1} , that are in good agreement with literature identification of Labradorite (Freeman et al. 2008; Bottger et al. 2009; Angel et al. 2012; Buzgar et al. 2013; Lalla et al. 2016; Berlanga et al. 2019). Attribution of bands is detailed in Table 4-2.

Table 4-2: Assignment of Raman bands for Labradorite, Augite, and Hematite magmatic minerals. Raman band intensity are in parenthesis; s-strong, m-medium, w-weak.

Sample	Wavenumber (cm^{-1})	Raman assignements	References
Labradorite	178 (m)	M-O (metal - oxygen bending and stretching vibrations)	Buzgar et al. 2013; Angel et al. 2012; Freeman et al. 2008; Berlanga et al.2019
	286 (m)	M-O (metal - oxygen bending and stretching vibrations)	Buzgar et al. 2013; Angel et al. 2012; Freeman et al. 2008; Berlanga et al.2019; Huang et al. 2000
	406 (w)	M-O (metal - oxygen bending and stretching vibrations)	Buzgar et al. 2013; Angel et al. 2012; Freeman et al. 2008; Berlanga et al.2019
	479 (s)	deformation of (T-O-T)	Buzgar et al. 2013; Angel et al. 2012; Freeman et al. 2008; Lalla et al. 2016; Berlanga et al.2019
	508 (s)	deformation of (T-O-T)	Buzgar et al. 2013; Angel et al. 2012; Freeman et al. 2008; Lalla et al. 2016; Berlanga et al.2019
	565 (w)	deformation of (O-T-O)	Buzgar et al. 2013; Freeman et al. 2008; Lalla et al. 2016; Berlanga et al.2019
Augite	232 (w)	M-O (metal - oxygen bending and stretching vibrations)	Buzgar et al. 2013;; Huang et al. 2000; Berlanga et al. 2019
	332 (s)	M-O (metal - oxygen bending and stretching vibrations)	Buzgar et al. 2013; Huang et al. 2000; Wang et al. 2001; Berlanga et al. 2019
	395 (s)	M-O (metal - oxygen bending and stretching vibrations)	Buzgar et al. 2013; Huang et al. 2000; Berlanga et al. 2019
	541 (w)	deformation of (O-Si-O)	Buzgar et al. 2013; Huang et al. 2000; Berlanga et al. 2019
	668 (s)	Symmetric Stretching of Si-O bridging oxygen / Fe-O vibration	Angel et al. 2012; Zinin et al. 2011; Huang et al. 2000; Wang et al. 2001; Berlanga et al. 2019
	709 (w)	Symmetric Stretching of Si-O non bridging oxygen	Buzgar et al. 2013
	769 (w)	Symmetric Stretching of Si-O non bridging oxygen	Buzgar et al. 2013; Huang et al. 2000
	1009 (s)	Symmetric Stretching of Si-O non bridging oxygen	Angel et al. 2012; Buzgar et al. 2013; Huang et al. 2000; Wang et al. 2001; Berlanga et al. 2019
Hematite	225 (s)	α-Fe_2O_3 vibrations	Buzgar et al. 2013; de Faria and Lopes 2007
	248 (w)	α-Fe_2O_3 vibrations	de Faria and Lopes 2007
	296 (s)	α-Fe_2O_3 vibrations	Buzgar et al. 2013; de Faria and Lopes 2007
	413 (s)	α-Fe_2O_3 vibrations	Buzgar et al. 2013; de Faria and Lopes 2007
	503 (w)	α-Fe_2O_3 vibrations	Buzgar et al. 2013; de Faria and Lopes 2007
	615 (m)	α-Fe_2O_3 vibrations	Buzgar et al. 2013; de Faria and Lopes 2007
	668 (s)	α-Fe_2O_3 vibrations	Buzgar et al. 2013; Lalla et al. 2016; Caceres et al. 2021
	825 (w)	α-Fe_2O_3 vibrations	Buzgar et al. 2013; Lalla et al. 2016
	1323 (s)	α-Fe_2O_3 vibrations	Buzgar et al. 2013; de Faria and Lopes 2007

The pyroxene can be classified as augite (a monoclinic Ca-Na pyroxene) with composition Wo_{36}-En_{52}-Fs_{12} (Mg# = 0.86 defined here as cations $\frac{Mg}{Mg+Fe^{2+}}$). This mineral fall into the composition range of Holuhraun clinopyroxenes according to Geiger et al., (2016; Mg# 43–85) and Halldórsson et al., (2018; Mg# 76–87). Raman spectra of Augite are characterized by major peaks located at 332, 395, 668, and 1009 cm^{-1} and minor peaks located at 232, 541, 769, and 882 cm^{-1}. Peaks at ~325, ~670, and ~1000 cm^{-1} are commonly used for pyroxene distinction as they correlate well with the proportion of Fe^{2+}, Mg^{2+} and Ca^{2+}, respectively (Huang et al. 2000; Wang et al. 2001; Angel et al. 2012; Buzgar et al. 2013; Lalla et al. 2016; Berlanga et al. 2019). Augite after IR experiment shows different peaks in the region 200–500 cm^{-1} that can be attributed to variation in crystal lattice modes Mg–O (375–490 cm^{-1}) and Fe–O (225–325 cm^{-1}) and Ca–O stretching (320–360 cm^{-1}; Huang et al., 2000). The origin of the variation in crystal lattice modes is possibly related to the increase mobility of one of the major cations in the silicate structure induced by its relaxation during melting. Moreover, Raman mode at 769 cm^{-1}, related to Si–O–Si bending (Huang et al. 2000), is not visible after IR experiment, which can be explained by the small modifications of Si-network local structure.

The oxide is a hematite Fe_2O_3 as determined with Raman spectroscopy, which is a product of alteration retrieved in Holuhraun lava. The textural analysis reveals the presence of vesicles after IR experiment resulting from the exsolution of volatile during the experiment. The Raman spectra for Hematite are characterized by major Raman features at 225, 296, 413, 503, 616, and 1323 cm^{-1} and minor features at 248, 668, and 825 cm^{-1}. These features are in good agreement with literature (de Faria and Lopes 2007; Buzgar et al. 2013; Lalla et al. 2016; Di Genova et al. 2017a). The weak Raman band at 668 cm^{-1} is linked to the partial transformation into magnetite under the laser (Buzgar et al. 2013).

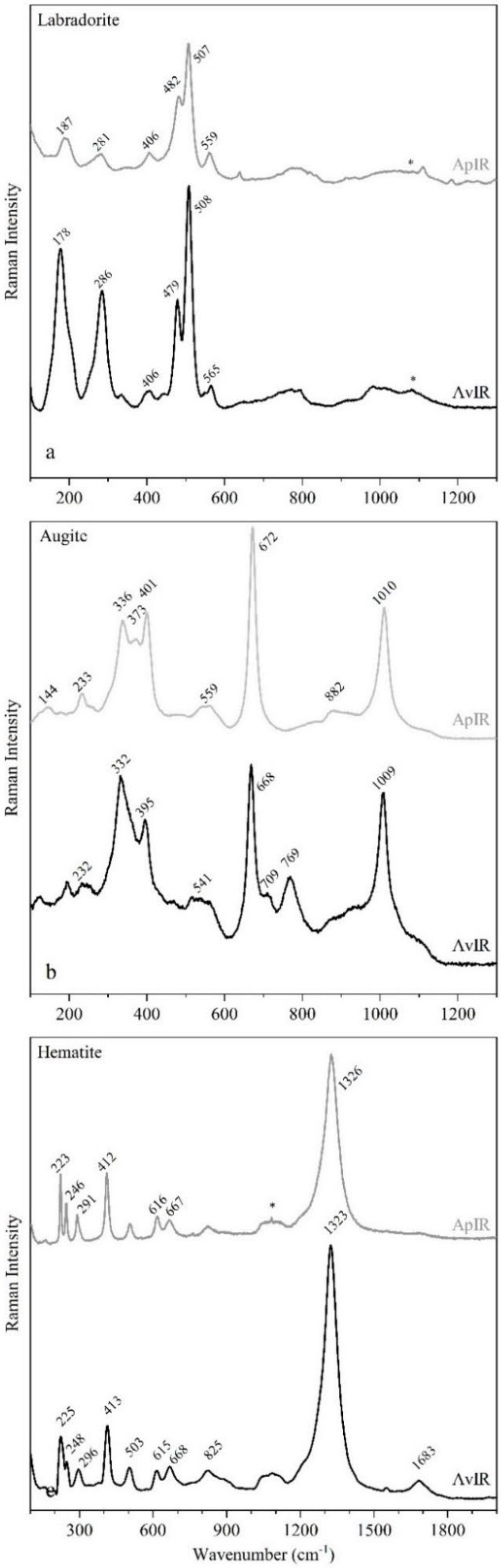

Figure 4-3: Raman spectra of Labradorite, Augite and Hematite before and after IR experiment. * are artefacts.

4.1.2. Spectral Emissivity of magmatic minerals at ambient temperature

The comparison of emissivity spectra determined using indirect method at ambient temperature and direct method for the three minerals of interest is shown in Figure 4-4. Note that the direct emissivity spectra were recorded at 647 K for Labradorite, at 755 K for Augite and at 618 K for Hematite. As it can be clearly seen in Figure 4-4, there is very good agreement between the directly and indirectly recorded emissivity spectra. In comparison with B-glass (cf. Chapter 3) the emissivity spectra of three minerals show well organized crystals structure with numerous, well developed absorption bands, in good agreement with Raman spectra (Figure 4-3). Labradorite and Augite are typical silicate-based minerals showing the prominent Reststrahlen bands, Christiansen feature as well as pronounced transmission front evidencing their optical semi-transparent behavior (Figure 4-4). The emissivity spectrum of hematite, Fe-oxide, is different in agreement with its distinct structural and chemical properties. As already stated in Chapter 3, the Fe-rich oxides exhibit different optical and electric properties in comparison with dielectric silicates. This should be stressed that the studied minerals were unoriented, preventing the study of orientation effect on the crystal radiative properties with temperature, although literature data clearly show the dependence of emissivity spectra on crystal orientation (Eckes et al. 2013; Ye et al. 2019; Li et al. 2021).

Christiansen feature (CF) of Labradorite is located at 1260 cm^{-1} at ambient temperature (Figure 4-4a). Note that the CF position varies systematically with Na–Ca concentration, where Na-rich endmember (albite) has a CF position at the highest wavenumber (1300 cm^{-1}) whereas Ca-rich endmember (anorthite) exhibits CF at the lowest wavenumber (1220 cm^{-1}; Donaldson Hanna et al., 2014, 2012; Sprague et al., 2009). Since the investigated plagioclase has a composition of An# = 49, its CF is accordingly located in between these endmembers. Numerous, intense absorption bands with low values of full widths at half maximum can be clearly detected in Figure 4-4a in good agreement with long range ordered triclinic symmetry. Three major absorptions regions can be distinguished: i) the first centered at 581 cm^{-1} that encompasses three absorption bands of lower amplitude at 542, 602, and 633 cm^{-1}, ii) the second centered at 1009 cm^{-1} and including another band at 953 cm^{-1} and iii) the third centered at 1139 cm^{-1} that comprises another band at 1186 cm^{-1}. The remaining absorption bands (at 463, and 740 cm^{-1}) are minors. In the opaque region, between 400 and 2000 cm^{-1}, the spectral emissivity of Labradorite is high (>0.80), whereas above >2000 cm^{-1} the spectral emissivity plummets to ~0.40. This clearly shows that in the multiphonon and electronic regions, Labradorite exhibits a markedly semi-transparent behavior. In higher wavenumbers, the absorption bands of fundamental O–H stretching are present between 3400–3800 cm^{-1}. Moreover, traces of CO_2 doublet can also be visible.

The room temperature emissivity spectrum of Augite (Figure 4-4b) shows clearly the presence of CF located at 1175 cm^{-1} in good agreement with Arnold et al., (2014) and Lyon, (1965). Augite is characterized by the presence of three major absorption bands located at 518, 920 and 1084 cm^{-1}, and two minors ones at 558 and 1028 cm^{-1}. Note that the exact position of the major bands have been previously recognized by Ferrari et al., (2014) and Hamilton, (2000) to be strongly dependent on the Fe content. The position of the band minima is generally shifted to lower wavenumbers (higher wavelengths) with increasing Fe content (Hamilton 2000; Ferrari et al. 2014). As it can be clearly seen in Figure 4-4b, Augite reveals very high emissivity values, i.e.,

>0.80, in the investigated spectral range. Such high emissivity values in electronic regions are directly related to the electronic absorption of Fe ions. The presence of TF and lower intensity emittance spectrum above ~2200 cm^{-1} reveals however that this pyroxene mineral shows semi-transparent optical properties. Finally, three additional absorption bands are observed at ~3650, 3520, and 3460 cm^{-1} and can be assigned to the stretching vibration of O-H in molecular H_2O (Hamilton, 2000; Yang et al., 2010 and references therein).

The emissivity spectrum of Hematite oxide shown in Figure 4-4c, is significantly different than those of plagioclase and pyroxene. Hematite belongs to the metal oxides family and exhibits different structural, electric, and optical properties when compared to the dielectric silicate-based minerals. One particularity of such oxides is that they do not show a CF *sensu stricto*. Since at room temperature Hematite sample can emit electromagnetic radiation as a blackbody at very critical wavenumber (i.e., ~700 cm^{-1}; Sako et al., 2020), this feature will be called hereafter "false CF". Note that we have set the highest emissivity value as a false CF for a more comprehensive description of the process occurring during heating, although some difference in "CF" intensity between direct (~0.95) and indirect (~0.99) methods cannot be avoided during the spectra treatment. Hematite is an example of opaque mineral, where the light is purely reflected and with transmission equals 0 (τ~0) in the spectral range explored. Thus, spectral emissivity relies entirely on simplified Kirchoff law "1-R" implying that no volume effect affects the radiative properties of Hematite at ambient temperature. In the main network vibration region, Hematite is characterized by the presence of two bands located at 460 and 567 cm^{-1} concurring with the works of Glotch et al., (2004) and Lane et al., (2002) exploring the hematite oxide of Mars. Note that the presence of solely two absorption bands reflects its high symmetry (i.e., cubic). In the multiphonon and electronic regions, spectral emissivity is perfectly constant with a very high value of 0.85.

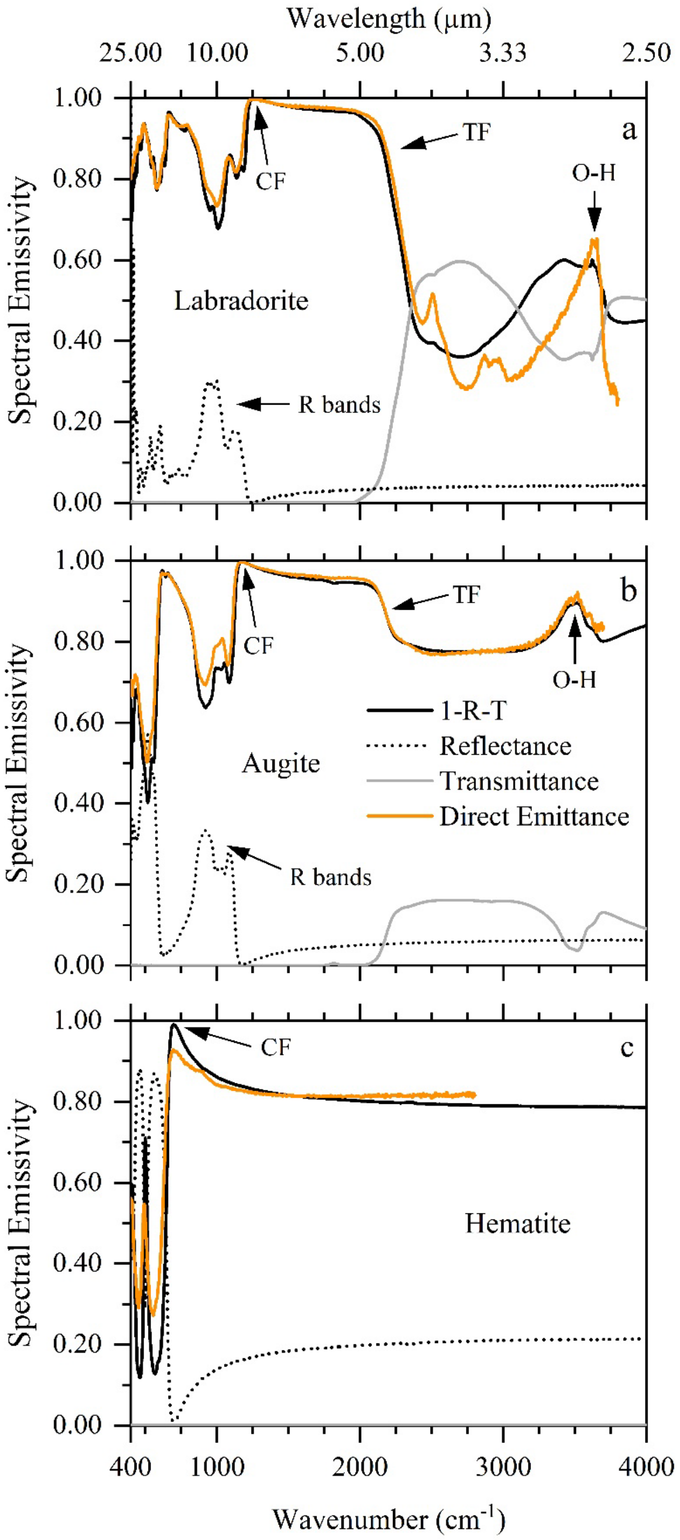

Figure 4-4: Indirect measurement (1-R-T) of spectral emissivity at room temperature for each mineral (1.5 mm thickness); the indirect emittance spectrum results from the combination of individual Reflectance and Transmittance spectra. The former is compared to direct measurement of spectral emissivity, at 647 K for labradorite (a), 755 K for Augite (b), and 618 K for Hematite (c).

4.1.3. Emissivity–Temperature relationship for Labradorite

Figure 4-5a,b shows the spectral emissivity evolution with temperature for Labradorite. Panel a) shows the full spectral range investigated (TIR–MIR–SWIR, 400–8000 cm^{-1}) while panel b) focus mostly on TIR (400–2000 cm^{-1}). Note that for better readability, not all measured spectra are shown, and instead the most representative spectrum is selected for each characteristic temperature range.

As shown in Figure 4-5, with increasing temperature from ~800 K to ~1400 K, significant and progressive modifications of emittance spectral features occur. Compared to ambient temperature data (Figure 4-4a), the CF shifts to 1220 cm^{-1} and absorption bands significantly broaden with increasing temperature, proof of the enhancement of anharmonicity in good agreement with the observations of Helbert and Maturilli, (2009). In details, the absorption band initially detected at 581 cm^{-1} shifts to lower wavenumbers (560 cm^{-1}) and is accompanied by an ε increase from 0.74 to 0.88. The major bands at 1009 and 1139 cm^{-1} merge to form a single broad band at 977 cm^{-1} where ε increases from 0.70 to 0.82. The Transmission Front (TF) shifts towards higher wavenumbers due to the strengthening of multiphonon processes. In the multiphonon region, the intensity of symmetric stretching band assigned to hydroxyl groups (O–H), and well visible near 800 K (Klopprogge and Frost 2004; Preston et al. 2011; Alemanno et al. 2021) progressively decrease during heating, either because of its evaporation from the silicate structure or because of significant increase of emissivity (from 0.28 to 0.57) in this spectral range that masking the O–H vibration. In the electronic region, ε follows an identical trend as in the multiphonon region, namely ε increases from 0.30 to 0.67 with temperature increase.

Above 1450 K, Labradorite shows the typical behavior of molten state (for representativeness, see the spectrum at 1990 K in Figure 4-5a,b). Labradorite molten state is characterized by constant spectral emissivity behavior (up to 2000 K). The CF further shift towards lower wavenumber to reach 1200 cm^{-1}. In the opaque region, the absorption bands (at 560 cm^{-1}) related to the bending of silicate tetrahedra disappears whereas ε of the absorption feature at 977 cm^{-1} further increases to reach ~0.86. In the multiphonon and electronic regions, ε decreases with temperature from 0.37 to 0.10. Such important emissivity decrease is related to the reduction of the sample thickness observed in that temperature range (cf. section 4.1.6). With such low spectral emissivity (~0.10), the Labradorite radiative behavior can be considered transparent in that spectral and temperature range.

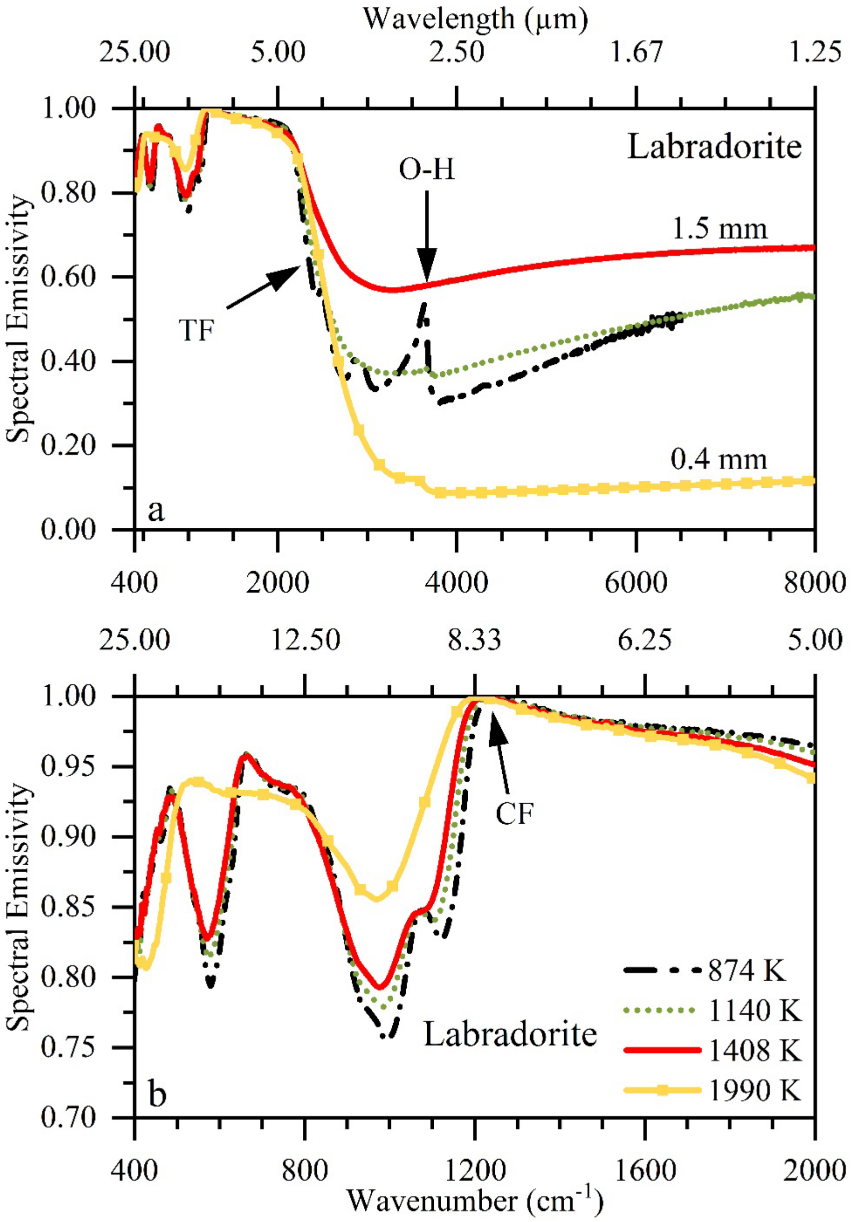

Figure 4-5: Spectral emissivity evolution with temperature and wavenumber for Labradorite (thickness: 1.5 mm <1400 K, 0.4 at 1990 K) in wide spectral range including TIR–MIR–SWIR, and b) Zoom on TIR spectral range (8–12 µm). CF: Christiansen Feature. TF: Transmissivity Front.

4.1.4. Emissivity–Temperature relationship for Augite

Figure 4-6 shows the evolution of spectral emissivity with temperature for Augite. Emittance spectra recorded at 873, 1152, and 1368 K are comparable, and ε varies slightly below 1368 K. The CF (1175 cm^{-1}) and principal absorption bands (518, 920, and 1084 cm^{-1}) shift to lower wavenumbers. CF is then observed at 1150 cm^{-1}, whereas the bands are detected at 505, 886, and 1050 cm^{-1}. Their emissivity values increase from 0.43, 0.67, and 0.72 to 0.63, 0.75, and 0.84, respectively. The same behavior was observed by Ferrari et al., (2014) and related to the changes in volume thermal expansion coefficient. In the multiphonon region the TF is less contrasted with increasing temperature, i.e., TF flattens progressively and ε increases from 0.77 to 0.85 because of the growing population of phonons (strengthening of multiphonon processes, Rozenbaum et al., 1999). The characteristic O–H band (~3500 cm^{-1}) can be also detected in this spectral region and its intensity decreases significantly from 1040 K to be almost invisible at 1368 K. In the electronic region (>3500 cm^{-1}), ε is high and progressively increases up to ~0.90 (i.e., progressive opacification) compared to more variable and lower values at ambient temperature (~0.80). Spectra also show a slightly curved shape in agreement with the Fe absorption bands present at ~8000 cm^{-1} (Li PhD, 2018).

Above 1400 K (for representativeness, see the emittance spectrum recorded at 1690 K in Figure 4-6a,b), Augite is progressively melting. In the opaque region, molten state of Augite silicate structure is evidenced by the merging of the two major absorption bands at 886 and 1050 cm^{-1} into one single broad Reststrahlen band centered at ~930 cm^{-1} with ε ~0.87. The CF is slightly shifted to 1160 cm^{-1}. In the multiphonon and electronic regions, emissivity shows more variation. Near TF, ε plummets and reaches the lowest value: ~0.79 at ~2500 cm^{-1}. At higher wavenumbers ε increases progressively. It should be stressed that similarly to Labradorite mineral, the melting process induces a gradual decreasing of the sample thickness, i.e., ~0.85 mm (cf. section 4.1.6). However, in contrast to Labradorite, Augite mineral does not change its optical properties, i.e., it keeps the opaque optical behavior in electronic region. This reveals that the impact of electronic absorptions of Fe ions on optical properties is higher than that related to the sample thickness.

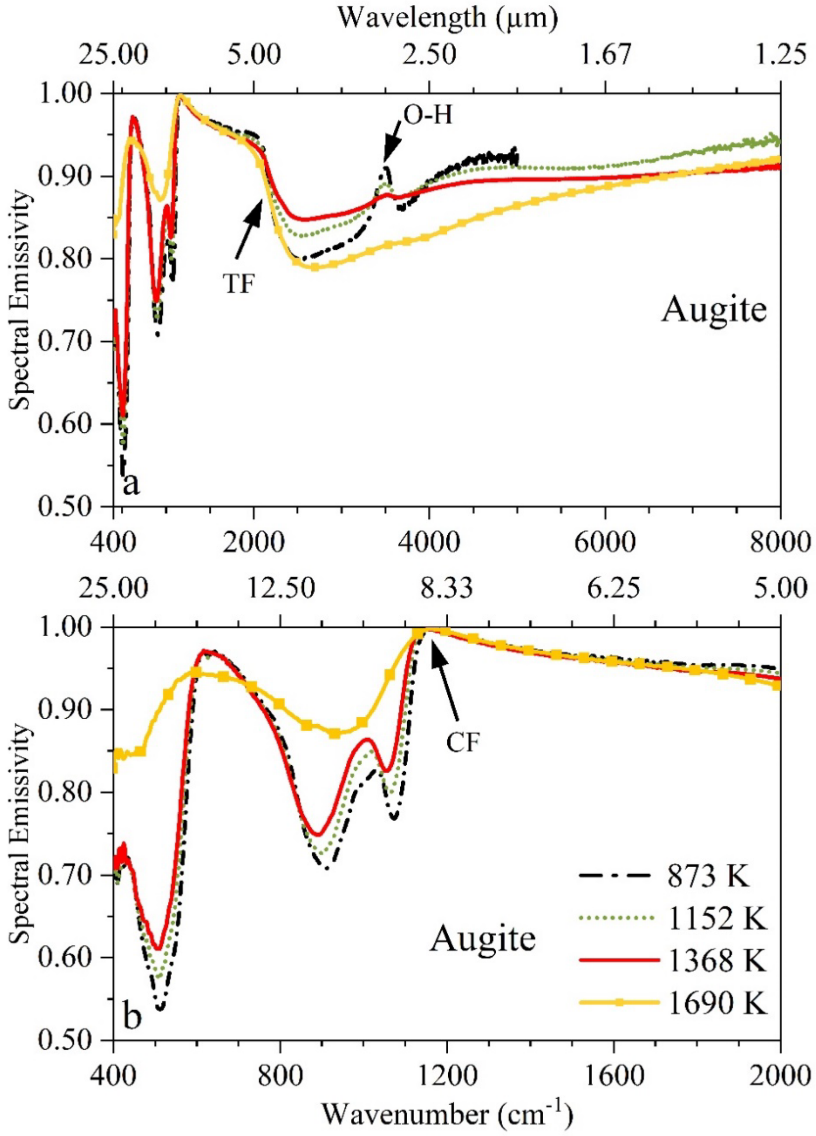

Figure 4-6: Spectral emissivity evolution with temperature and wavenumber for Augite (thickness: 1.5 mm below 1400 K, 0.85 mm at 1690 K) in wide spectral range including TIR–MIR–SWIR, and b) Zoom on TIR spectral range (8–12 μm). CF: Christiansen Feature. TF: Transmissivity Front.

4.1.5. Emissivity–Temperature relationship for Hematite

As observed in Figure 4-7, spectral emissivity of Hematite seems not to be affected by changes in temperature and remains constant with the mean value of ~0.80 (above 700 cm^{-1}). With the temperature increase, two absorption bands at 460 and 567 cm^{-1} shift progressively towards lower wavenumbers. Above 1300 K, they merge, and form one single broad band centered at 440 cm^{-1} with ε ~0.50 (Figure 4-7b). The "false CF" exhibits no temperature dependence. In the multiphonon and electronic regions, Hematite has a constant ε ~0.80 without any noticeable spectral feature. Above 1629 K (see Figure 4-7 and the spectrum recorded at the highest temperature), the fusion of Hematite takes place. Consequently, thermal response of the sample was lost at T >1650 K.

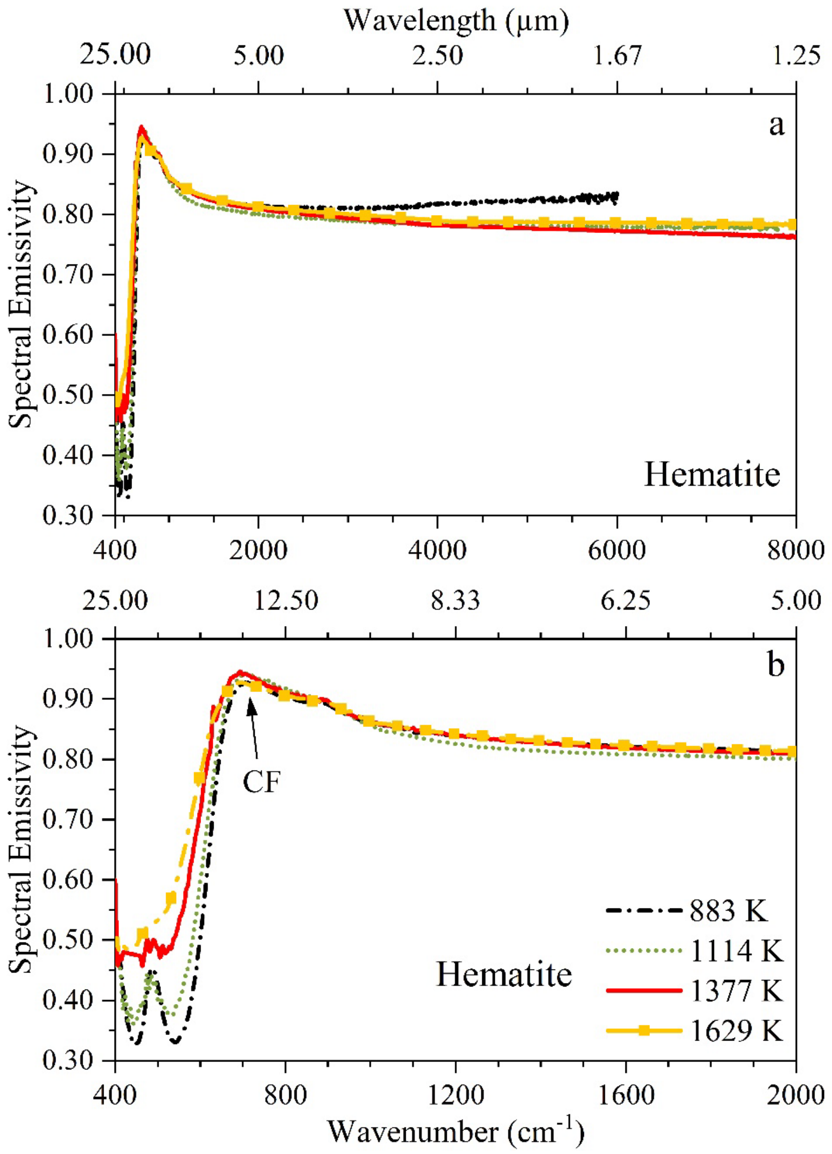

Figure 4-7: Spectral emissivity evolution with temperature and wavenumber for Hematite (thickness: 1.5 mm) in wide spectral range including TIR–MIR–SWIR, and b) Zoom on TIR spectral range (8–12 µm). CF: Christiansen Feature, note that it is not a physically true CF.

4.2. Discussion

4.2.1. High temperature radiative properties of minerals

The comparison of emissivity-temperature relationships of three investigated minerals shows clearly, that similarly to magmatic glasses, the spectral emissivity of minerals is highly dependent on temperature, wavenumber, and composition. This confirms well that the knowledge of high temperature emissivity behavior of every magmatic crystal is crucial since spectral emissivity at room temperature cannot be extrapolated to high temperature or assumed constant. Our results show that the radiative properties of Labradorite and Augite, silicate-based minerals, evolve significantly with the temperature increase. In contrast, the radiative properties of Hematite, Fe-oxide, are distinctively different and show very little temperature dependences.

As for basaltic glasses, the structural, textural, and chemical analyses, performed before and after IR experiments, were compared to unravel the factors controlling the ε−T evolution. Pre and post IR chemical analyses (Table 1-1) in combination with Raman data (Figure 4-3) reveal that the composition and structure of minerals were well preserved during the heating-cooling cycle. Note that slight differences observed in Raman spectra are related to dynamics/kinetic of crystal growth process. After achieving molten state, the laser is turned off and temperature decreases very quickly. Consequently, the thermodynamic conditions of re-crystallization process are different from those governing slow initial crystallization, and then can give rise to some Raman peak broadening, shifts or relative intensity modifications. As a result, all analyses of minerals reveal that no transformation other than melting occurs in the minerals during IR experiment.

For all three crystals, the spectral emissivity differences observed in TIR region are result of the melting process and reorganization of their inner molecular structure with the temperature increase. The absorption bands first broaden due to the anharmonicity and thermal expansion volume coefficient increase, then merge and reveal typical spectrum of molten state in the fusion temperature (Adams 1974; Bowey et al. 2001; Yang et al. 2010a; Ferrari et al. 2014).

The most important differences in ε intensity between investigated minerals are detected in MIR and SWIR spectral regions since each mineral exhibits distinct optical behavior: opaque (case of Hematite), semi-transparent (case of Augite) or transparent (case of Labradorite). As we already showed in previous section the size of Labradorite, and Augite samples decreases significantly once molten state was reached (>1400 K; Figure 4-8a). After visual inspection and measurements using SEM pictures, Labradorite sample thickness decreases from ~1.5 mm to ~0.4 mm whereas Augite's thickness changes from ~1.5 mm to ~0.85 mm. Such dimension modification can be easily explained by the lowering of the mineral viscosity when melting, allowing it to flow into the sample holder and form (by capillarity) a thick rim and a thin sample center (Figure 4-8b). Since spectral emissivity depends strongly on optical thickness (De Sousa Meneses et al. 2004; Li et al. 2021), this transformation can be responsible for the drastic decrease of ε in the multiphonon and electronics regions in the same temperature range (1400–2000 K) as melting. We also observed that the thickness modification has greater effect on the optical properties of Labradorite, which becomes transparent with very low emissivity value ~0.1, than on Augite, which maintains its very high level of spectral emissivity. These results emphasize that although measured radiative properties depend on sample thickness, the spectral emissivity should be considered as complex function of sample composition, structure, and ion abundance.

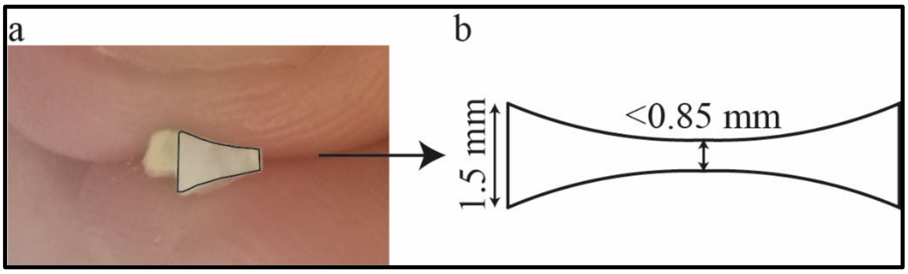

Figure 4-8: a) picture and b) sketch of thickness variation for Augite and Labradorite during IR experiment.

Finally, we cannot omit the forsterite ε−T behavior as Olivine is a major component in basaltic lavas (cf. Chapter 1; Bowey et al., 2001; Eckes et al., 2013; Hamilton, 2010; Helbert et al., 2013; Koike et al., 2006; Thompson et al., 2021). Note that Forsterite exhibits similar structure and composition to the pyroxene, however the element's abundance is different, especially in term of Fe content: 15% in the case of natural magmatic Forsterite vs. 8% for Pyroxene. Since the emissivity spectra of forsterite were not measured directly in this study, the data will be discussed based on Eckes et al., (2013) data (Figures 4-9, 1-10), as their measurements were performed using the same experimental procedure as the one applied in this work. Results show that Forsterite emissivity strongly increases with heating (from ~0.10 to 0.50 at 2200 cm^{-1}) in MIR while being transparent in electronic region. As showed in Figure 1-11, Thomson et al., (2021) observed the emissivity of natural Forsterite decreases with temperature increase (from 0.70 to 0.50 in MIR). The emissivity values determined above 1200 K are in good agreements with those of Eckes et al., (2013), ~0.40 near 2500 cm^{-1}.

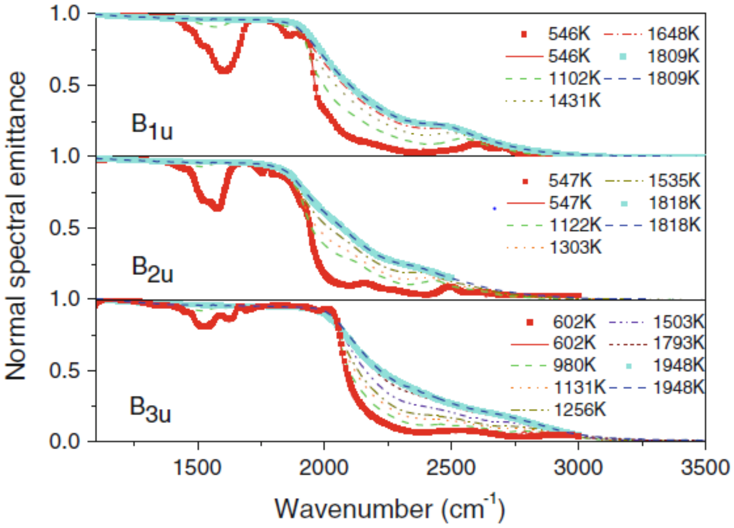

Figure 4-9: High temperature spectral emittance of forsterite (from Eckes et al. 2013).

4.2.2. Effect of crystals and modelling of basalt radiative properties

Now that the ε−T relationships of the different phases present in a basaltic magma (minerals and glass/melt) have been determined, this section addresses for the first time, the modeling of the resulting spectra at different temperatures by considering the radiative contribution of each phase present in the basaltic magma. This exercise attempts to elucidate the impact of elements like crystals, mineral assemblage, or crystal composition on the thermal emission of a magma.

To achieve this goal, the spectra retrieved from B-Nat sample at 864 and 1610 K (Figure 3-3) were selected since these runs contain contrasted crystal contents (100% crystals and 17% respectively. Initially, the crystal proportions (areal percentage) of each B-Nat run were estimated using backscatter SEM images. Three to four images were taken at a magnification ×35 (for a total of 7 images) along with one or two extra images of 1800×1800 µm from each ×35 image (for a total of 16 images), these trying to be representative of the IR measuring area (Figure 2-4), without including textural features outside this area). The images were then processed using ImageJ® software as to obtain the area fraction of vesicles, plagioclase, Fe-oxides, combined proportions of pyroxene and olivine as well as glass (Figure 2-2). Note, pyroxene and olivine contents were combined as this last mineral was difficult to be identified in the 864 K sample because of its low abundance (Halldórsson et al., 2018; Kolzenburg et al., 2017). For processing, the minimum particle area was set to 10 µm^2 (Heilbronner and Barrett 2014). The resulting area fractions are shown in Table 4-3. Note that these area fractions were corrected for porosity (i.e., porosity of B-Nat at 1610 K is 9% whereas at 864 K is 24%).

Table 4-3: Areal fraction of vesicles, crystals (pl-plagioclase, px-pyroxene, ol-olivine, ox-oxides) and glass, corrected for porosity (vesicles) and representative of high temperature (molten state at vent) and low temperature (cooled state at front) lava flow texture.

	Low Temperature (%)	High Temeperature (%)
Vesicles	9	24
Plagioclase	43	8
Pyroxene + Olivine	41	6
Oxide	4	3
Glass	12	83

B-Nat emissivity spectra was linearly modeled considering the emissivity spectra at a given wavelength (λ) and temperature (T) of each mineral species and glass along with their respective proportions. The retrieved expression is:

$$\varepsilon_{(\lambda,T)}^{B-Nat} = p_1\,\varepsilon_{(\lambda,T)}^{Pl} + p_2\,\varepsilon_{(\lambda,T)}^{Px,Ol} + p_3\,\varepsilon_{(\lambda,T)}^{Ox} + p_4\,\varepsilon_{(\lambda,T)}^{gl} \qquad 4\text{-}1$$

Where p_{1-4} are the area fraction (Table 4-4) occupied by feldspar plagioclase (Pl), pyroxene (Px) and olivine (Ol), oxides (Ox) and glass (gl) respectively.

It should be stressed that the linear regression considered in this calculation is an oversimplification of the real process since the radiative properties are not directly linked to the abundance of each phase. However, this assumption can provide a first sight about the contribution of each single element to the total emitted flux.

Figure 4-10c,d shows the modeling results at low (864 K) and high (1614 K) temperatures, respectively. At high temperature, the overall shape of the measured spectra and the position of absorption bands are closely reproduced by the model both in the TIR and MIR-SWIR ranges (within errors). B-Nat emittance spectrum characteristic of high temperature (1614 K) is dominated by the glass thermal emission because of the high proportion of melt-glass present in the sample (83%) and shows high emissivity values (ε = 0.85–87; Figure 3-3). It should be stressed that despite of the presence of 17% crystals, they seem to have no effect on the overall radiative response of the sample.

Compared to the high temperature counterpart, the spectra of B-Nat at low temperature was modeled with more or less success depending on the spectral region (Figure 4-10a,b). This was closely accomplished since the modeled spectra in TIR almost mimics the location of the different absorption bands of the natural sample at 540, 960, and 1000–1010 cm^{-1}, which are associated to the presence of high amount of plagioclase (43%) along with lesser amounts of olivine, which are instead located at ca. 410, 504, 611 and 960 cm^{-1} (Eckes et al. 2013). Similarly, the modeled spectra also account for the bands associated to the presence of oxide minerals, these being located at 460 and 540 cm^{-1}. However, their contribution to the total emissive response in TIR is relatively low, in agreement with their low abundance phase (4%, Table 4-4) compared to Pl and Px + Ol.

Despite of the overall broad agreement, the modelled spectra usually show higher emissivity in all absorption bands (with intensity difference up to 0.06) compared to the measured emissivity spectra. Such relatively small difference could be explained by the fact that the composition of Pl and Px considered in the calculations does not strictly match such found in the natural rock (Figure 4-1a,b).

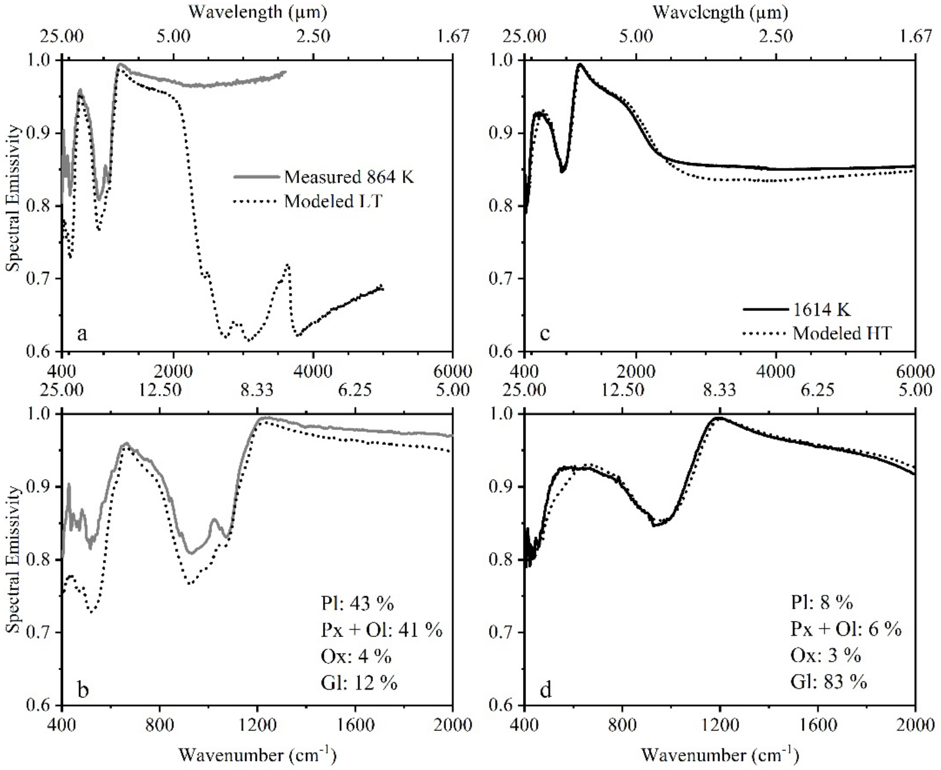

Figure 4-10: Modeled vs. Measured spectral emissivity of B-Nat at low (864 K, a, b) and high (1614 K, c, d) temperatures. Panels a and c show wide spectral range (TIR–MIR–SWIR) whereas panels b and d focus on TIR.

In contrast to TIR, MIR and SWIR regions show an important discrepancy between the modeled and the measured spectra at low temperature. When considering the mineral and glass proportions determined in the rock along with their respective emissivity spectra, the applied method leads to the appearance of a transmission front and important emissivity decrease from 0.95 to 0.65 at > 2500 cm^{-1} (Figure 4-10a) in modeled spectrum. Considering that Px, Oxides and glass have the highest emissivity in this spectral region, the relative proportions of these phases were then progressively modified (by tuning p in Equation 1.1) as to reproduce the emissivity spectra in MIR–SWIR measured at 864 K. By considering only the contributions related to the presence of glass, the closest fitting agreement was obtained when the proportions of this phase achieved ≥85% and the Px–Ox proportions were instead reduced to ≤2% (Figure 4-11c,d). However, at 864 K the presence of such high proportion of glass is unlikely (Figure 3-5). On the other hand, the proportions of oxide and minerals were progressively increased (while proportion of glass was kept constant) until the modeled spectra achieved emissivities of 0.97–0.98 in the SWIR–MIR regions. Only when the proportions of oxides and Px exceeded 110%, the modeled spectrum broadly resemble to the measured one at low temperature. Figure 4-11a,b show an example of model with high Px–Ox content. Such high crystal contents are obviously unrealistic.

Figure 4-11: Comparison of between measured emissivity spectra and modeled with adapted crystal proportions for B-Nat at low temperature (864 K, a,b) with a focus on crystal content, low temperature (864 K, c,d) with a focus on glass content, and high temperature (1610 K, e,f). The crystal contents are adapted as to best fit the spectra of B-Nat.

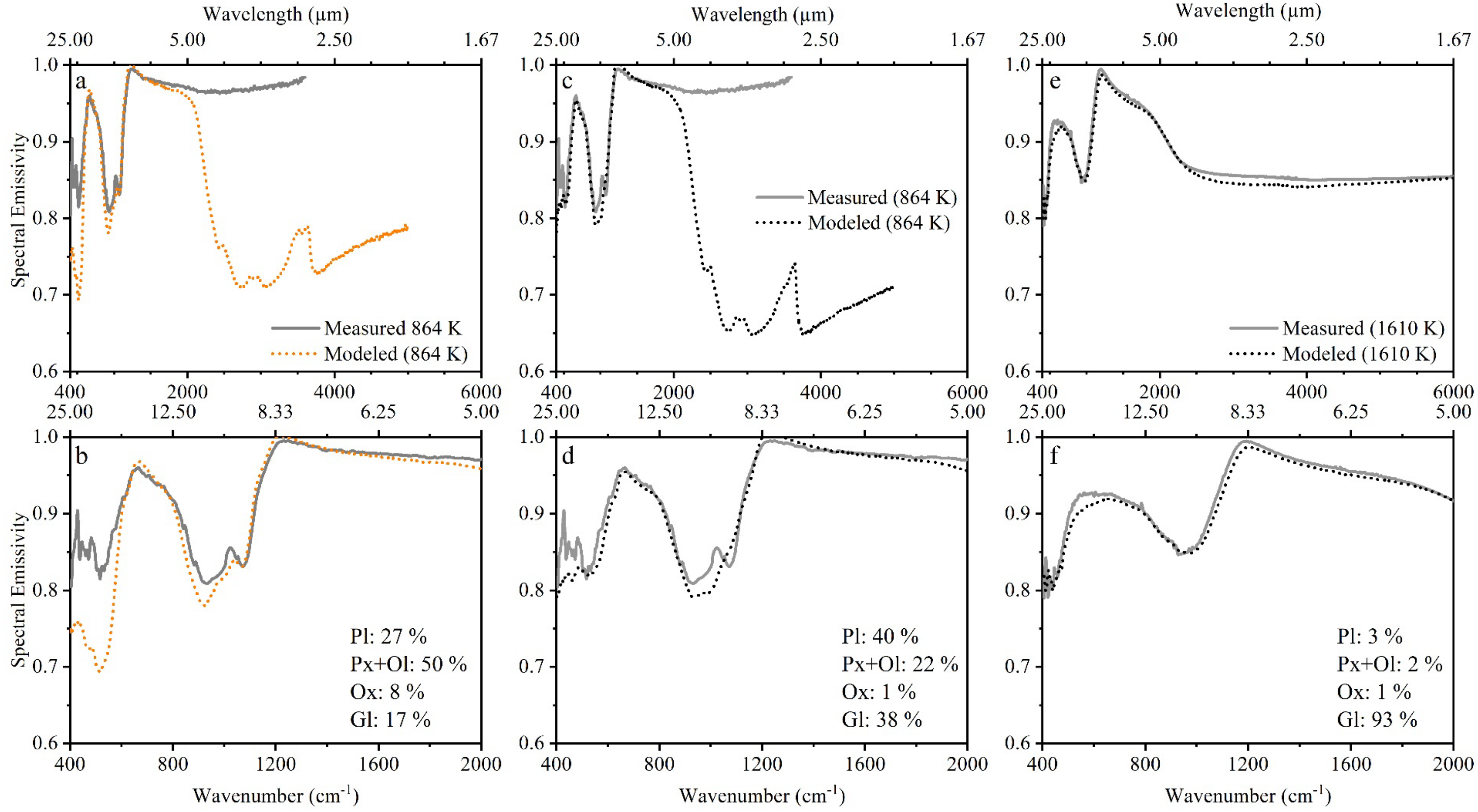

In summary, the linear deconvolution successfully reproduced the high temperature measured spectrum in the TIR–SWIR–MIR ranges; this was not fully accomplished for low temperature-high crystal conditions. This raises the limitation of using of a linear approach for reproducing the emissive response of a highly crystallized magma. It was previously stated that linear deconvolution only considers the properties retrieved at the surface of the sample and thus is an oversimplification of the emissive phenomena. In practice, the measured ε in this highly crystalized sample does not only correspond to that retrieved from surface alone, but also to contributions from absorption and scattering phenomena operating inside the whole magma volume (i.e., plagioclase which is dominant phase on the natural samples is relatively transparent on the MIR–SWIR). Hence, to better model the emissive response of the material at such high crystal conditions, it would be necessary: i) to have detailed 3D textural information about the distribution of crystal, melt, and porosity, and ii) to evaluate and quantify the contribution of these heterogeneities into global effective ε by performing sophisticated numerical modeling (e.g., Ray tracing or Symbolic Monte Carlo methods; Galtier et al., 2017; Rozenbaum et al., 2019). This method would account for appropriated optical properties of the melt and crystals (i.e., adapted absorption and scattering coefficients, phase function parameters; Galtier et al., 2017; Maanane et al., 2020).

4.2.3. Effect of crystal content on B-Nat radiative properties

In the previous section, modelling B-Nat radiative response at various temperatures and using adapted crystal contents was carefully considered. The attempts to model radiative properties allowed us to distinguish two opposite behaviors: i) high temperature (1610 K) − low crystal content (17%) and ii) low temperature (~860 K) – high crystals content (100%). Without surprise, in the first case, the radiative properties of B-Nat are governed exclusively by melt whereas in the second one, the emissivity is mainly controlled by the Fe-bearing crystals. In between these two extremes would certainly lie a crystal threshold at which the radiative properties of basalts change from a melt-dominated to crystal-dominated. Knowing this threshold would help better understand the crystal effect on ε–T relationships. To approach that critical value, the spectral emissivity of two additional samples containing intermediate crystal contents was measured.

For this purpose, samples were synthesized following the method described in section 2.1, and their texture were analyzed with SEM (Figure 4-12). Since these two samples were synthesized at T = 1050 ºC (1325 K) and 1100 ºC (1375 K), their crystal content falling in between those determined for B-Nat before and after IR experiments. However, these slightly differ in their mineralogy since plagioclase was present in the natural products and this phase is absent in the synthetic ones. B-cryst1050 contains 30% of pyroxene, 10% of Fe-Ti-Mg-rich oxides (for a total of ~40% of crystals) and 60% of glass (Table 4-5). On the other hand, glass-dominated (94%) B-cryst1100 possesses 2% of pyroxene and 4% of Fe-Ti-Mg-rich oxides (for a total of ~6% of crystals; Table 4-5). Their usefulness is thus two-fold: they first inform on the effect of initial mineralogy on the lava radiative properties. To this end, their ε–T relationships are explored. Secondly, their initial texture informs on the crystal threshold responsible for the lava radiative control from glass or crystals. Consequently, their crystal contents were used to re-examine the lava (B-Nat) emissivity at which the radiative properties of a basaltic magma can be modeled using a linear approach.

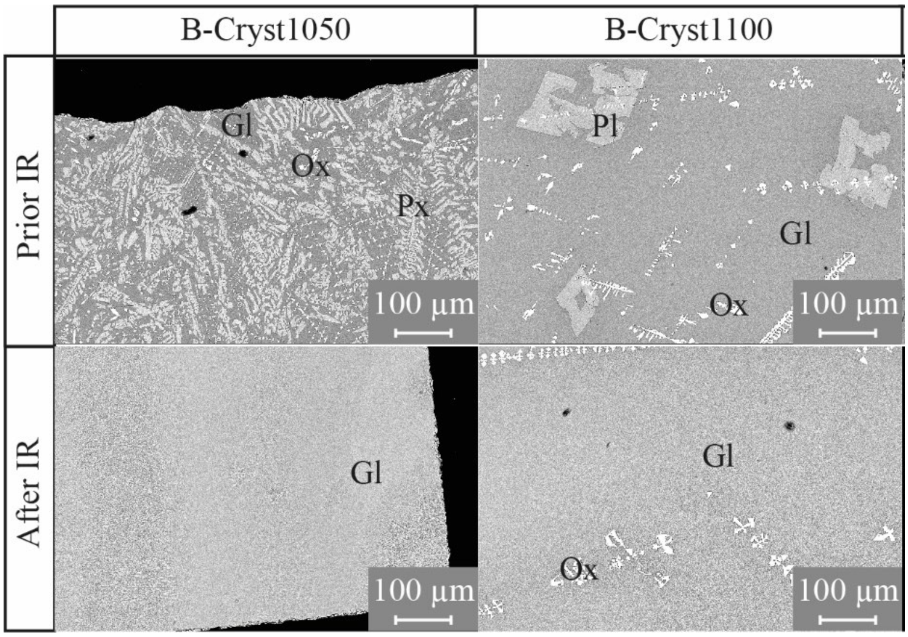

Figure 4-12: SEM pictures of B-cryst1050 and B-Cryst1100 samples before and after IR experiment.

Table 4-4: Mineral content before IR experiment for B-Cryst1050 and B-cryst1100

	B-Cryst1050 (%)	B-Cryst1100 (%)
Vesicles	2	1
Pyroxene	30	2
Oxides	10	4
Glass	60	94

The temperature evolutions of spectral emissivity of both B-cryst samples are shown in Figure 4-13 and their respective texture in Figure 4-12. The comparison of emittance spectra reveals clearly different radiative behavior below 1400 K. B-cryst1050 shows comparable spectral emissivity evolution with the temperature increase to fully crystalized B-Nat (Figure 3-3). Such high similarity of ε–T behavior despite of different mineralogical content suggests that the contribution of plagioclase and olivine on radiative properties in SWIR and MIR is negligible. Fe-rich crystals are at the origin of the very high emissivity values (close to 1, meaning opaque optical properties in MIR and SWIR ranges) shown by the sample during the measurements. Comparatively, the ε–T behavior characteristic of B-cryst1100 clearly resembles such of B-glass (Figure 3-3). Thus, the threshold at which radiative properties are crystal-dominated can be placed between 17% (B-Nat) and 40% (B-cryst1050). Above 1400 K the radiative properties of both samples are very similar in agreement with the progressive melting of crystals which are progressively being dominated by the spectral signature of the forming melt.

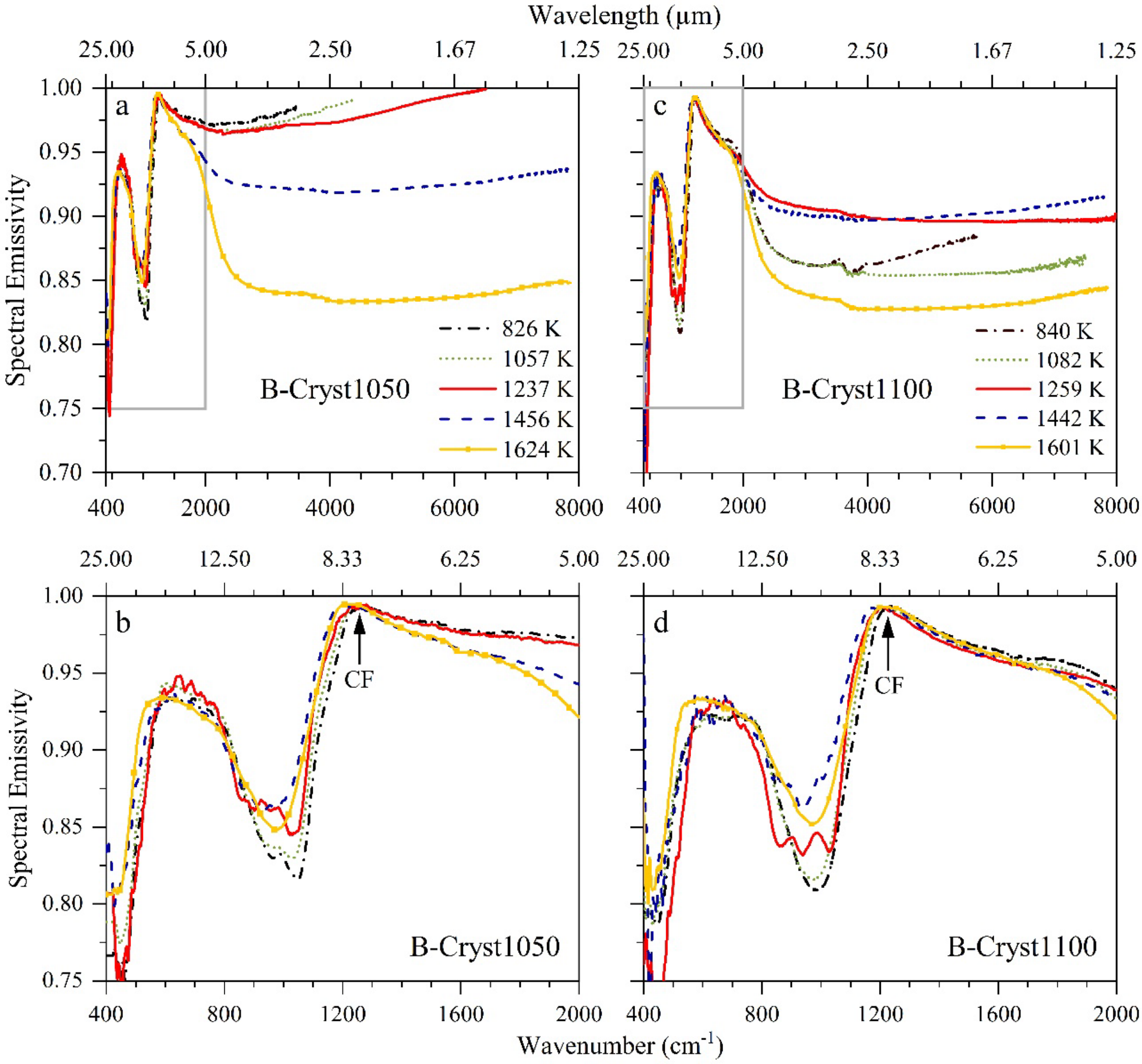

Figure 4-13: Spectral emissivity evolution with temperature of Bárðarbunga "synthesized" samples containing different crystal contents: B-cryst1050 with 40% crystals and B-cryst1100 with 6%. a) and c) whole measured spectral range covering TIR, MIR and SWIR. b) and d) zoom on TIR spectral region

The characteristic emittance spectra of B-Nat-cryst samples (Figure 4-13) with 40% and 6% of crystals can be further used as references spectra of dry Bárðarbunga magma with particular mineralogy and texture (Figure 4-14) specific of lava at 1325 K (B-cryst1050) or lava at 1375 K (B-cryst1100). In other words, we assume that both B-cryst samples before IR experiments have the same texture as B-Nat sample at 1325–1375 K.

Figure 4-14 shows the modeling attempts to reproduce the emittance spectra of B-Nat acquired at 1325 K and 1375 K as achieved in section 4.1.7. The comparison of measured and modeled results for 1325 K shows quite good agreement in TIR spectral range whereas this exhibits a reasonable discrepancy in MIR and SWIR. As it can be clearly seen, the emissivity of measured sample, above 2000 cm^{-1}, is higher (0.95) than that of the modeled spectrum with ε equals to 0.90. The difference can be explained by the method of texture determination based on the 2D-SEM images. Such approach does not allow to determine the crystal content in precise and representative way since volume effects are not considered. As stated above, for improving this type of procedure, this should account for the 3D-distribution of crystals in the sample.

Hence, we can conclude that the emissive properties can be satisfactory modeled by applying linear deconvolution for crystal contents up to 40%. Above this threshold value, the spectral simulations must consider the 3D distribution of crystals in the sample, along with adapted absorption and scattering coefficients, phase function parameters for each phase present in the target. Moreover, this threshold corresponds to the crystal content at which a lava flow ceases flowing, implying that the crystal content range (0–40%) encompasses all possible lava flow radiative properties.

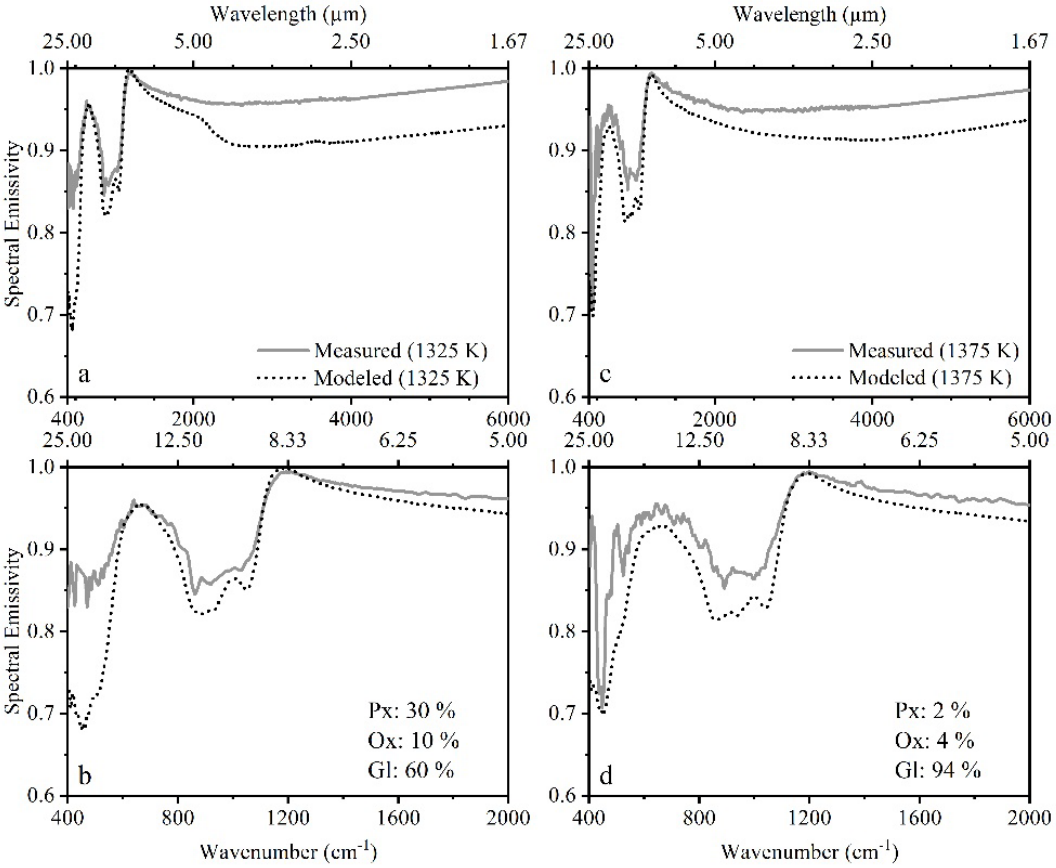

Figure 4-14: Measured and modeled emittance spectra of B-Nat recorded at 1325 and 1375 K using the B-cryst1050 and B-cryst1100 crystal content, respectively. a,c) whole measured spectral range covering TIR, MIR and SWIR, b,d) zoom on TIR spectral range.

4.2.4. Case study: lava flow from the 2007 Piton de la Fournaise eruption

The lavas from the 2007 eruption of Piton de la Fournaise are classified as Oceanite, a type of basaltic magma which is characterized by the presence of high amounts of olivine (≥30%) having sizes ≥500 µm to up to few mm, the whole set in a microlithic matrix that includes plagioclase, pyroxene, iron-oxide and glass (Figure 4-15, Clocchiatti et al., 1979). The mineralogy of this magma differs from the one commonly found in arc or alkaline basaltic compositions, where olivine rarely exceeds 15% of abundance, being instead clinopyroxene the most abundant mineral as basalts cool down and crystallize (as for example occurs in the natural products of Holuhraun, MORB and Fasnia studied in this work (Andújar et al., 2015; Pichavant et al. 2009). Hence, the study of the radiative properties of such oceanitic composition containing high proportions of olivine, when compared to such gained on the basaltic magma from Iceland, allows exploring the impact of a given mineralogy in the radiative properties of basalts. To achieve this goal, the ε–T relationship of a natural Oceanite sample (O-Nat) from the 2007 eruption of Piton de la Fournaise (La Réunion) was determined, following the same methodology applied to the previous basaltic samples. The composition of O-Nat before and after IR measurements is given in Table 4-6 and agrees with results obtained in previous studies (Clocchiatti et al. 1979; Pichavant et al. 2016; Thivet 2016). Olivine macrocristals are Fo_{82}, with total MgO= 43.60 wt.% and FeO= 16.63 wt.% (Table 4-6).

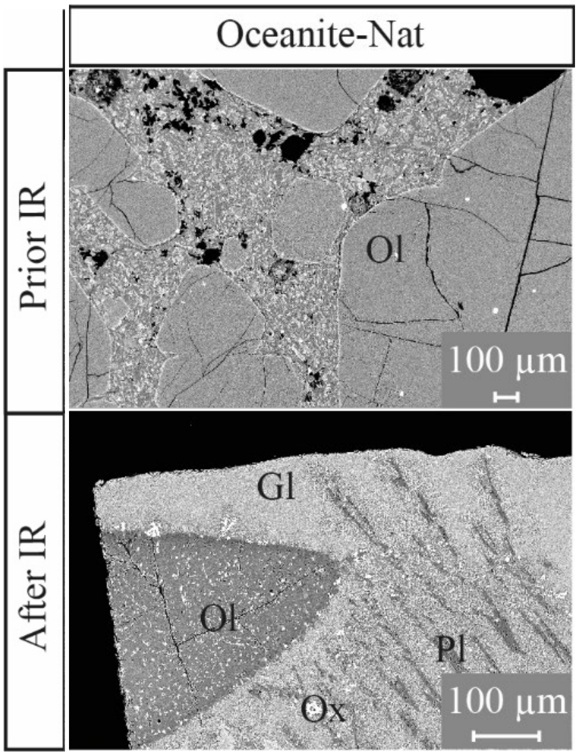

Figure 4-15: SEM images prior and after IR experiment for O-Nat. Gl: glass, Ol: olivine, Pl: plagioclase, Ox: oxide.

Table 4-5: EMPA composition for O-Nat before and after IR and the composition of their individual olivine (Forsterite). Results are in good agreement with Clocchiatti et al., (1979).

Oxide wt. %	O-Natural-gl-ApIR	S.D.	Forsterite	S.D.
# analysis	12	-	12	-
SiO_2	48.78	1.21	39.04	1.00
TiO_2	2.38	0.11	0.01	0.01
Al_2O_3	13.11	0.49	0.06	0.01
FeO tot	10.86	1.25	16.63	1.43
MnO	0.13	0.09	0.24	0.09
MgO	9.59	1.31	43.60	0.84
CaO	11.64	0.99	0.29	0.01
Na_2O	2.59	0.28	0.02	0.02
K_2O	0.58	0.09	0.01	0.01
Cr_2O_3	0.02	0.02	0.05	0.02
P_2O_5	0.32	0.05	0.06	0.10
Total %	100	-	100	-

The mineral proportions found in O-Nat before and after IR measurements were calculated and results are shown in Table 4-6. Note the crystal content is corrected from porosity as to study only the impact of crystals.

Table 4-6: Porosity and Mineral content for O-Nat sample equivalent at low and high temperature.

	Low Temperature (%)	High Temperature (%)
Vesicles	6	17
Plagioclase	17	7
Pyroxene	15	3
Olivine	52	48
Oxides	1	1
Glass	15	40

Results in Figure 4-16 show that at low temperatures (<1200 K), the spectral emissivity is dominated by the forsterite according to the presence of the characteristic absorption bands of this mineral in the opaque region (TIR) at ~500, ~600, and ~920 cm^{-1}, the minimum of emissivity of these bands varying between 0.57 and 0.70. This contrasts with the results obtained for the B-Nat sample at similar T, which systematically showed higher emissivities (>0.80) compared to O-Nat. The higher ε of the former sample can be explained as a result of the contributions of pl and px + ox mineral phases that are strong emitters in this spectral region when compared to olivine Figure 1-11, (Figures 4-5, 4-6; Eckes et al., 2013).

The temperature increase results in a progressively rise of O-Nat emissivity until 1501 K, temperature at which the CF disappears. Despite of not having direct evidence of this process (i.e., SEM pictures at that given stage), the loss of the CF feature at this temperature suggests that the sample experienced the crystallization and/or segregation of iron-oxide crystals/layer, in a similar way to B-glass. The observed spectral response comes from the iron oxide exclusively. The further increase in T produces the progressively melting of the sample as indicated by the characteristic spectral shape of molten silicate state, this resembling to those already observed in the previous studied basaltic compositions (cf. Chapter 3). However, when compared to B-Nat sample, the Oceanite is relatively opacified in the MIR–SWIR region, as evidenced by the lack of a TF and the very high emissivity of the sample (~0.90) at this temperature. It should be noted that at 1688 K, the O-Nat sample is not fully molten and still contains a high proportion of crystals (48% of olivine, 3% of pyroxene, 7% of plagioclase, 1% of oxide) compared to its Icelandic counterpart, which only contains <5% of Px, Pl, oxide and olivine, the radiative response being dominated by the high amounts of melt (95%).

In this case, the difference in the crystal content and mineralogy could account as an explanation of the relatively high emissivity of the Oceanite (0.90) compared to the Icelandic sample (0.85) at 1640–1688 K. However, it should be noted that, according to the works of Eckes et al., (2013) and Thompson et al., (2021), olivine is relatively transparent in the MIR–SWIR region. Hence, the presence of such a high concentration of olivine in the sample cannot really explain the high emissivity of the Oceanite, nor the presence of 40% of melt.

The detailed inspection of the olivine crystals after the IR experiment (Figure 4-15) revealed that the inner parts of the olivine are characterized by the presence of small but relatively abundant and newly formed iron-rich oxide crystals (probably as a results of a destabilization reaction of Olivine with the surrounding melt at such temperature). Considering that the abundance of olivine at these conditions is still high (48%; Table 4-6), the oxide inclusions can reach a concentration which is high enough to increase the emissivity of the sample up to 0.90 and opacify the system (see dashed spectrum in Figure 4-16). This contrasts with the information obtained for B-Nat at similar temperature. At 1648 K the Icelandic sample also contains iron oxides but their proportion (17%) is not high enough to increase the emissivity to values equivalent to those of O-Nat, nor to produce the opacification of the sample at this temperature.

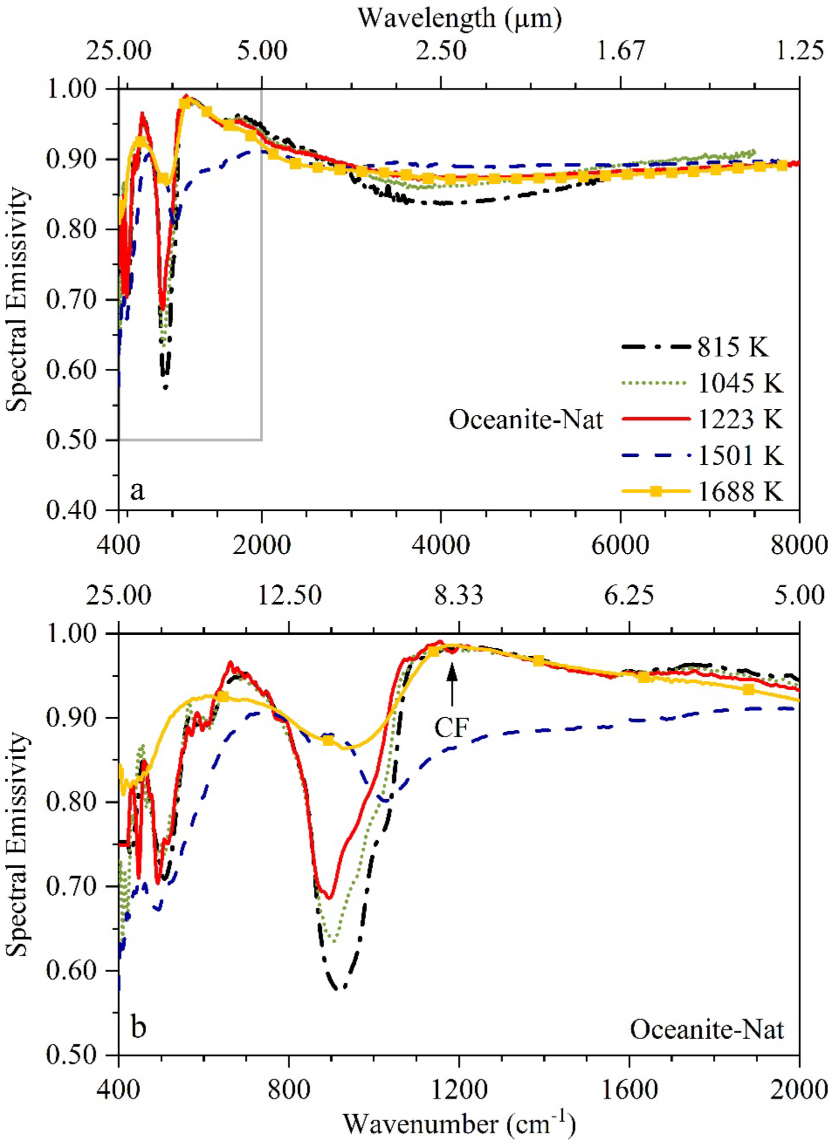

Figure 4-16: Spectral emissivity evolution with temperature for O-Nat from Piton de la Fournaise.

As a conclusion of this chapter, we measured the spectral emissivity at high temperature of representative minerals (labradorite, augite, and hematite) that are commonly found in basaltic magmas. Spectral emissivity of minerals is highly dependent on temperature, wavenumber, structure, and composition, all of which greatly evolve upon an active lava flow emplacement (King et al. 2004; De Sousa Meneses et al. 2006; Mysen and Toplis 2007; Lee et al. 2013). Specific absorption bands and their locations are directly related to the mineral inner structure and composition (e.g., emissivity of pyroxene is controlled by Ca, Fe and Mg content). These absorption bands merge when minerals attain molten state and display the typical Reststrahlen band (except for hematite). The wavenumber dependence is characterized by large variation of emissivity between TIR and MIR, SWIR (e.g., plagioclase spectral emissivity varies from 0.8 in TIR to 0.1 in SWIR). Based on this dataset, we attempt to model the radiative properties of Bárðarbunga Natural sample using a linear regression at 864 and 1640 K. Whereas this simplistic approach satisfactorily models the full emissivity spectra at high temperature with the crystal content up to 40%, whereas for low temperature and highly crystallized samples, it shows reasonable agreement in TIR spectral and fails in MIR and SWIR. One hypothesis to explain these discrepancies might be linked to the sample crystal content, which we tested afterwards. Results reveal that crystal content itself does not play a significant role in MIR and SWIR since after adjustment, fitting is still incorrect. We further postulate that the nature of the mineral can be a critical parameter. To test this hypothesis, we measured the spectral emissivity of a natural forsterite-rich basalt ("Oceanite" from PdF). We observed that although forsterite emissivity controls the Oceanite radiative properties in TIR, it is however not the case of MIR–SWIR because neither the forsterite high proportion, nor the forsterite high Fe content explain the high emissivity value found. We suggest therefore that the lava radiative behavior is controlled by (from the most to the least important): the local structure, the composition, and the mineral abundance. The radiative properties of lava are highly sensible to minerals; mineral content can be low in the case of high-ε minerals to play a significant role on the sample radiative properties; or very high for low-ε minerals to play no significant role on the sample radiative properties.

To conclude, the ε–T relationship for three basaltic minerals (i.e., plagioclase, clinopyroxene, oxide) were described and were used to model B-Nat radiative properties. With the help of a case study from Piton de la Fournaise and further IR experiments with samples having variable crystal contents, we were able to demonstrate that the presence of mineral affects differently the lava radiative properties, depending on the spectral range of interest, and the mineral microstructure, composition, and content. Combining our observations on the radiative properties of basalt melt and minerals allow us to explore in the next chapter the impact of variable radiative properties on lava flow temperature retrieval.

Chapter 5: Application

Previous chapters were dedicated to the *in situ* laboratory-measurements of spectral emissivity at relevant magmatic temperatures of basalts. In this chapter, these data will be used to refine the temperature model of Holuhraun eruption determined previously by remote sensing techniques. To do so, radiative equations expressing the emissivity–temperature relationship are implemented in the newly developed model of Aufaristama et al. (2018) for temperature estimation. This application case confronts field and laboratory approaches and reveals how important the knowledge of spectral emissivity in remote sensing volcano monitoring is.

Ropy Pahoehoe lava at Kilauea volcano (credit: USGS).

5.1. The latest development for RS application using constrained emissivity values

As discussed in Chapter 1, the use of different apparatus having different setups, sensibilities, loaded with synthetic compositions and different textures (e.g., rock powders, glassy materials), results in the production of uncertain spectral emissivity values and contrasting ε–T relationships. This implies that prior heat budget calculations and lava flow propagation models may have wrongly estimated the heat flux. In consequence, variable datasets of spectral emissivity values have inherent impacts on lava flow modeling and temperature determination.

Today, more attention to the spectral emissivity implications in RS applications has led several authors to use more accurate emissivity datasets to better quantify the variability of active lava surface and to model its emplacement. The work of Thompson and Ramsey, (2020a) studied the uncertainty of emissivity and temperature estimation using satellite-based remote sensing techniques. Their approach allows reducing for satellite sensors the uncertainty on emissivity (from 20% to 8% uncertainty) and temperature (from 200 to 12%) retrieval, proving that more constrained emissivity values are needed. In turn, it will ultimately improve the accuracy in estimated heat fluxes and in future lava flow models that rely upon these properties.

Rogic et al., (2019a) address the later statement by assessing the sensitivity of lava effusion rates and distance-to-run (i.e., maximum extent of lava flow) estimated with MAGFLOW (Ganci 2012) physical model using varying emissivities (from literature and their laboratory-based data described in Chapter 1). Their modeling results, iterated with different but single "static" (i.e., not variable with temperature) emissivity value, lead to 15% difference in radiant fluxes. On the other hand, their calculations based on a two-component emissivity approach, suggest that a 35% emissivity variation (from 0.95 to 0.60) can produce up to 46% overestimation in simulated lava flow lengths compared to observed data. In the same manner, Ramsey et al., (2019) modifies PyFlowGo physical model (Chevrel et al. 2018) to incorporate a two-component emissivity model to study the emplacement of Tolbachik lava flows. The adaptation of the model produced better fits to the final flow length, thus showing that spectral emissivity is an important factor for model accuracy. Later, Rogic et al., (2022) modeled the Etna lava flow with GPUSPH physical model (Bilotta et al. 2016) that includes a "dynamic" (i.e., variable in function of temperature) emissivity component they created based on laboratory emissivity measurements. Their modeling results show that that for a given mass flux rate, the "dynamic" emissivity component can lead to lava flow emplacement differences with respect to simulations with a "static" emissivity. Secondly, the "dynamic" emissivity component affects the mass flux rate estimation itself. In combination, both effects can lead to differences of 10–20% in the distance-to-run of the flow. Other than emissivity, critical parameters such as viscosity, effusion rate are equally important in these models. But these recent studies highlight the importance to accurately model the lava surface evolution for predicting its potential run-out distance.

These most recent works are the premises of incoming improvements in RS applications for the detection of volcanic effusive activity. While their methodology is sound, these studies potentially suffer from inappropriate emissivity values, those used to be not necessarily specific to the studied magmas. For instance, Rogic et al., (2022) assumed a mean spectral emissivity in the 2.17–21.00 µm spectral range for a given temperature to derive their multicomponent emissivity relation, notwithstanding that emissivity is wavelength dependent. Nevertheless, they shed insights on the importance of the relation between emissivity and temperature and its impact on RS application. Together with Ramsey et al., (2019) and Rogic et al., (2019a), they insist that a reliable and exploitable predictive emissivity trend including wavelength and temperature dependence is needed. They also highlight the need of more sophisticated physical models that include this predictive ε–T relationship to improve both RS and lava flow modeling applications. In turn, this will lead to more complex and realistic volcano monitoring systems for hazard assessment. In the following, we describe our own improvements in RS application.

5.2. Lava flow temperature retrieval by RS and laboratory emissivity measurements

In this section, we aim at reducing the uncertainty in lava flow temperature measurements by RS techniques. We compare temperature estimations of Holuhraun lava flow modeled with commonly used constant emissivity or with our laboratory-based emissivity data. This allows us to explore the impact of emissivity measured in the laboratory on the RS retrieval of field temperature. The activity of the 2014–2015 Holuhraun eruption was thoroughly monitored from its start to end thanks to the broad range of RS apparatus available at the time (cf. section 1.3). This gave the opportunity to obtain large amount of thermal emission data (ground- and satellite-based temperature measurements range between 1320 and 1466 K) and provide the ideal conditions for the comparison of field-based and laboratory-based temperature retrieval. Our objective is twofold: first, the development of radiative equations that express the ε–T relationship and second, the implementation of these equations into RS model as to improve the temperature retrieval for each pixel. To do so, we use our laboratory ε–T data, the thermal data from Aufaristama et al. (2018) and, we refine the model they developed.

5.2.1. Model of Aufaristama et al. (2018)

In Aufaristama et al. (2018) model, called hereafter Aufaristama model, thermal fluxes from band 6 (1.56–1.66 µm; SWIR) and band 10 (10.60–11.19 µm; TIR) of Landsat-8 infrared datasets (acquisition date: 06 September 2014) are first acquired, and then convert to sensor radiance for both SWIR and TIR bands. Despite that Landsat-8 has low temporal resolution (revisit of the object every 16 days), its spatial resolution makes it a good tool to derive thermal properties of a lava flow: 30 m for band 6 and 100 m for band 10. The selection of these bands is considered to minimize oversaturation effects on the detector over active lava flows (Aufaristama et al. 2018). The Aufaristama model also uses thermal camera measurements (Forward Looking InfraRed; FLIR) that overlap with the satellite data for better result comparison.

Secondly, the model applies a correction for atmospheric effect and spectral emissivity for both SWIR and TIR bands since these effects are wavelength dependent. The following equations that allow the correction of atmospheric and emissivity effects are respectively based on MODTRAN model atmosphere (i.e., the MODerate resolution atmospheric TRANsmission is a software embedded in many sensors that predicts and analyses the contribution of atmosphere as to remove its effects; Lombardo and Buongiorno, 2006; Oppenheimer, 1993):

$$R_{SWIR} = \frac{[L(\lambda_{SWIR}) - L_R(\lambda_{SWIR})]}{\tau\ \varepsilon_{SWIR}} \tag{5-1}$$

$$R_{TIR} = \frac{[L(\lambda_{TIR}) - L_U(\lambda_{TIR})]}{\tau\ \varepsilon_{TIR}} \tag{5-2}$$

Where R_{SWIR} and R_{TIR} are the corrected spectral radiances at wavelength λ_{SWIR} and λ_{TIR}, respectively, $L(\lambda_{SWIR})$ and $L(\lambda_{TIR})$ are the spectral radiances at the sensor, $L_U(\lambda_{TIR})$ is the atmospheric upwelling radiance, $L_R(\lambda_{SWIR})$ is the atmospheric reflected radiance, τ is the atmospheric transmissivity, and ε is the surface spectral emissivity, which in this case was considered constant and fixed to 0.97.

Finally, the Aufaristama model simulates the temperature distribution for Bárðarbunga lava flow using the corrected radiance datasets and the dual-band method of Dozier, (1981). This last gives a solution for the following equation system for simultaneous TIR and SWIR:

$$L(\lambda_{TIR-SWIR}, T_{int}) = p\ L(\lambda_{TIR-SWIR}, T_h) + (1-p)\ L(\lambda_{TIR-SWIR}, T_c) \tag{5-3}$$

Where T_h and T_c are the temperatures of the hot and cold components, respectively, p is the proportion of the pixel occupied by the surface at T_h, L is the spectral radiance, T_{int} is the pixel-integrated temperature for the pixel in $\lambda_{TIR-SWIR}$. The solution allows the calculation of the 'sub-pixel' coverage and temperature of cool (T_c) and hot components (T_h) by assuming one of three unknowns, T_h, T_c, and p. In Aufaristama model, the authors assumed a two thermal component scenario and defined T_h as temperature of lava surface and T_c as temperature surrounding the lava (even if lava can have multiple thermal domains in each pixel). In consequence, T_c is equal to the lowest brightness temperature detected in TIR for each thermal domain considered, namely $T_c = 293\,K$ in the cold surrounding, $T_c = 323\,K$ in the surrounding hot crust, and $T_c = 358\,K$ in the active lava. The dual-band technique solves p by iterating T_h, until $p(R_{SWIR}) = p(R_{TIR})$, giving rise to following equations:

$$p(R_{SWIR}) = \frac{R_{SWIR} - R(\lambda_{SWIR}, T_c)}{R(\lambda_{SWIR}, T_h) - R(\lambda_{SWIR}, T_c)} \tag{5-4}$$

and

$$p(R_{TIR}) = \frac{R_{TIR} - R(\lambda_{TIR}, T_c)}{R(\lambda_{TIR}, T_h) - R(\lambda_{TIR}, T_c)} \tag{5-5}$$

5.2.2. Model improvement

To improve Aufaristama model that considered a constant emissivity value in the radiance calculations, we first must develop radiative equations that take into account the temperature and textural dependence of spectral emissivity for the Bárðarbunga composition. To do so, the emissivity data retrieved from Bárðarbunga natural sample (B-Nat, Figure 3-3) was chosen as this closely simulate the crystal content vs. emissivity evolution expected for the cooling Bárðarbunga magma at temperatures between 1500 K and ambient. Note, that emissivity data for B-glass was instead disregarded since this sample was severely affected by the Fe-oxides segregation (Figure 3-3). Despite that this process strongly impacts the emissive behavior of the sample, we consider that it is unlikely to occur in nature.

In a first step, the B-Nat emissivity vs. temperature database for the two specific bands considered in Aufaristama model (i.e., 10.9 µm for TIR, and 1.6 µm for SWIR; Figure I-4a) were mathematically regressed (Figure 5-1) in order to determine the equations which relate these two parameters :

For a given pixel at 1.6 µm (SWIR):

$$\varepsilon_{SWIR} = 0.586 + 7.123\ 10^{-4}\ \times T - 3.084\ 10^{-7} \qquad 5\text{-}6$$

For a given pixel at 10.9 µm (TIR):

$$\varepsilon_{TIR} = 0.826 - 8.235\ 10^{-5}\ \times T + 7.818\ 10^{-8} \qquad 5\text{-}7$$

With Adjacent $R^2 = 0.904$ and 0.968 for 1.6 and 10.9 µm, respectively. These regressions back-calculate emissivity ±0.002 at 1.6 and ±0.003 at 10.9 µm. T refers to the temperature of the pixel.

The derived mathematical expressions for both TIR and SWIR bands (eq. 5-6 and 5-7) will be applied to replace the constant ε in Equation 5-1 and 5-2 from Aufaristama model. With this procedure, the correction of radiance data therefore considers the temperature, crystal content, spectral and compositional dependence of emissivity.

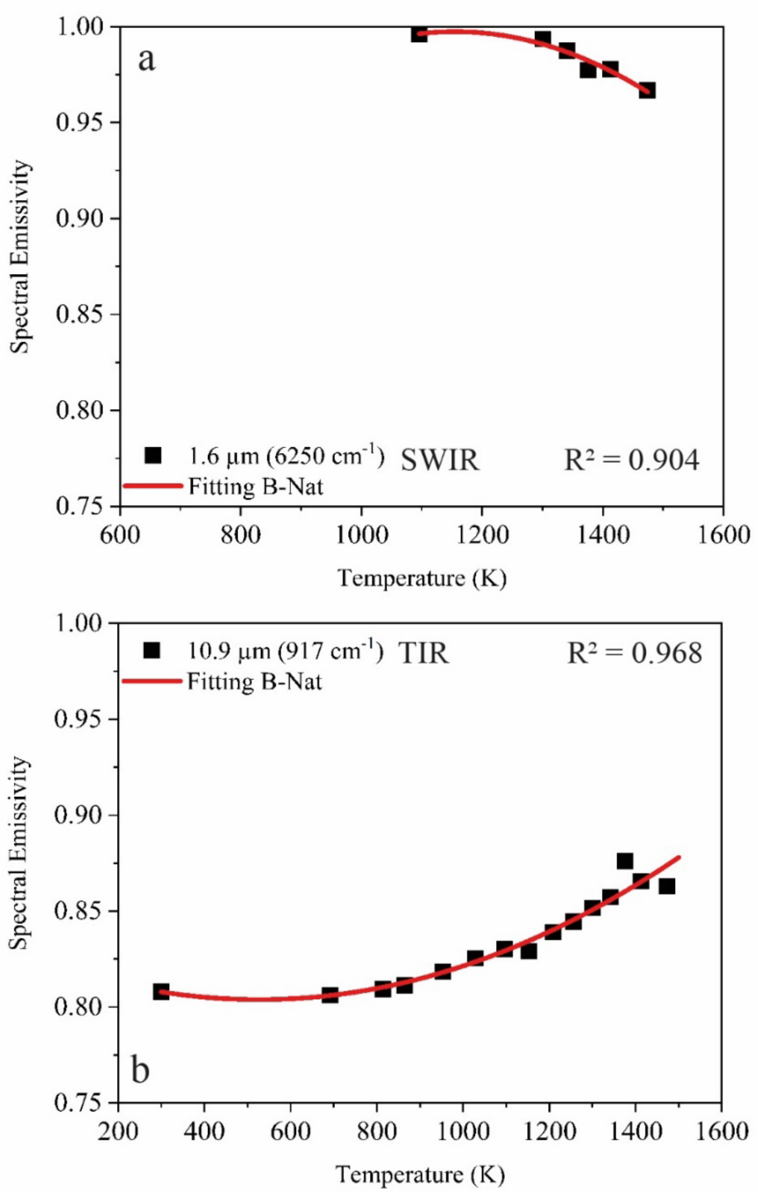

Figure 5-1: Temperature evolution of spectral Emissivity values for B-Nat in SWIR band 1.6 µm (a) and TIR band 10.9µm (b) that allows deriving equations for ε−T relationship. Note that the sample must first reach high temperature before emitting in SWIR, thus explaining the limited number of data compared to TIR.

These new corrected spectral radiance equations were then used to re-calculate the temperature distribution across Holuhraun lava flow field, and then compared with the results of Aufaristama model based on constant emissivity. Nevertheless, due to the non-deterministic nature of the mixed pixel problem (i.e., there are more variables to solve than equations), the model cannot give straightforward results. To solve it, additional constrain (either on temperature or spectral emissivity) must be included in the system (Alvez Rolim et al. 2016). Since at least one of the input parameters must be known or assumed, the refined model was run as follows:

1- A first iteration of the model was made using raw thermal fluxes from RS methods along with constant ε of 0.97 to determine an approximate temperature for each pixel. Note that this procedure is similar to such applied in Aufaristama model. Hence, since no modification was provided, the thermal map distribution encompasses the temperatures previously determined by Aufaristama et al., (2018; Figure 5-2a).

2- Once the individual pixel temperature was approximated, the radiance correction model was iterated considering Equation 5–6 and 5–7 as to determine the ε for each pixel at its respective approximate temperature. These calculations yield new emissivity maps for the 1.6 and 10.9 µm spectral bands Figure 5-2b,c).

3- Last, the temperature of each pixel was finally calculated considering the emissivity values obtained in step 2 and by applying the dual band method. New thermal map with refined temperatures was finally produced (Figure 5-2d). Note that such method is also used for TES algorithm (Gillespie et al. 1998) and was already applied to lava flows (Harris et al. 1997; Lombardo and Buongiorno 2006).

5.2.3. Model Application

The application of the step 1 methodology generated a single thermal map considering a constant ε (Figure 5-2a). In this map, temperatures are distributed between 650–1450 K (mean: 961 ± 225 K; Figure 5-4a), showing two near-equivalent modes around 825 and 1375 K, which represent the cooled crusted lava surrounding the molten lava channel and the channel itself, respectively. Aufaristama et al., (2018) reports temperatures between 617 and 1481 K (mean of 1042 K) and p range between 0.10 and 13% (mean of 1.5%), values that agrees with those produced in this step. The highest temperatures and lowest p mostly relate to active lava locations such as channels, lava ponds and breakouts. Meanwhile, the lowest temperature and highest p correspond to crust zone in the edge of active lava and flow fronts that indicates lava cooling and formed thick crust. As lava cools, the crust component increases from the vent towards the distal end. These results are broadly consistent with observed emplacement processes of a'a flows.

As a result of step 2, the spectral emissivity distribution across Holuhraun lava flow is presented for SWIR and TIR bands in Figure 5-2b,c. These maps show respectively that spectral emissivity values are highly variable across the lava flow field. Spectral emissivity varies between 0.91–0.99 in SWIR (weighted average: 0.97±0.02) and 0.81–0.89 in TIR (weighted average: 0.82±0.02; Figure 5-4b,c). In both bands, spectral emissivity is higher at the lava channel and levees than at the borders and remains constant with distance from vent to front. Therefore, as SWIR band is more sensible to higher temperatures than TIR, the hot component (molten lava) is well visible in these figures at vents and at lava breakouts at the progressing front (e.g., note red color regions in Figure 5-4b).

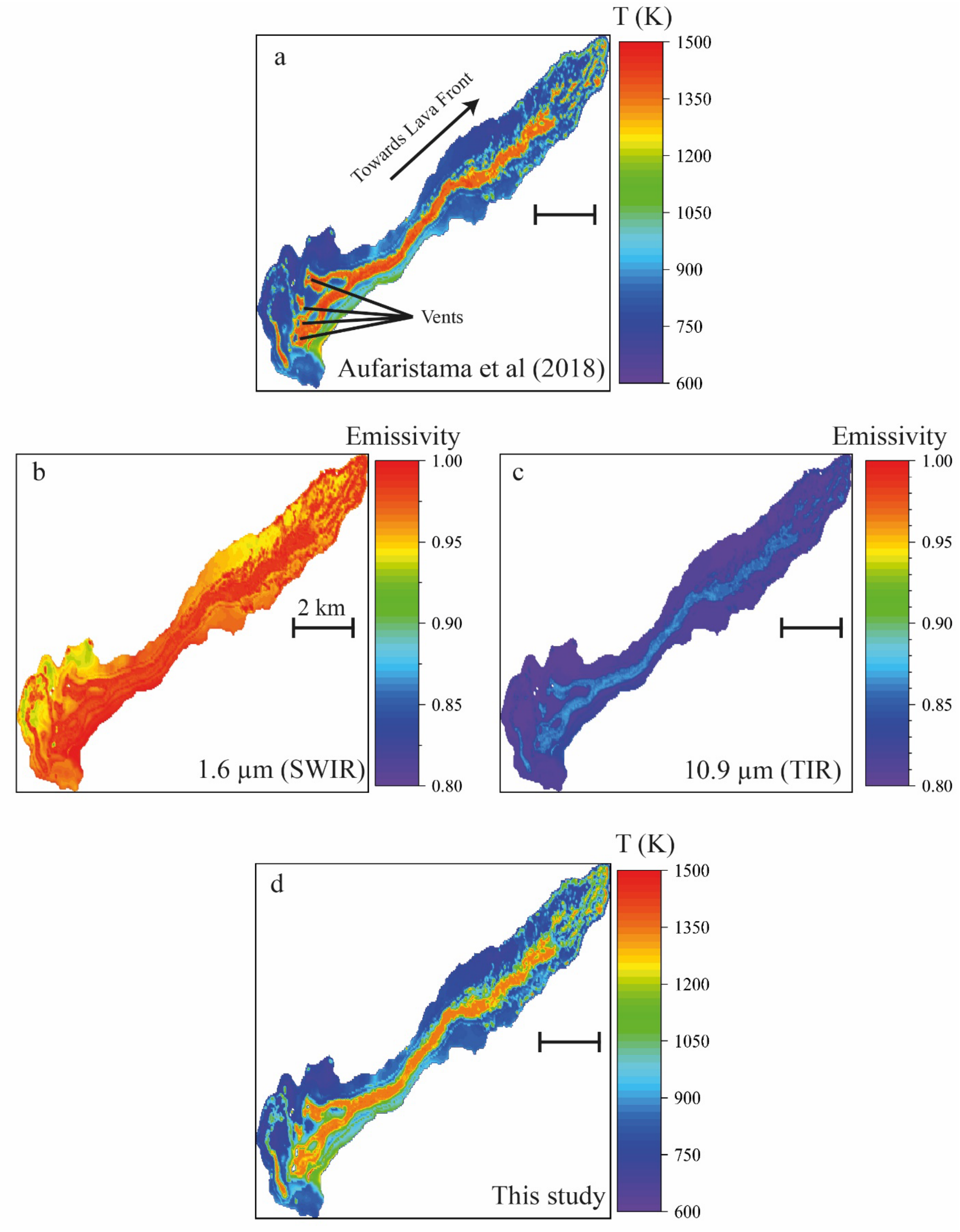

Figure 5-2: Results from Aufaristama and the refined models for thermal distribution of Holuhraun lava flow. a) Thermal maps obtained with Aufaristama model (constant ε). b,c) Emissivity maps obtained in the refine model –based on laboratory data for 1.6 µm SWIR and 10.9 µm TIR bands, respectively. d) Thermal maps obtained with the refined model from this study.

In the refined thermal map produced in step 3 (Figure 5-2d), high values of temperature (orange and red color in Figure 5-2d T>1300 K) are precisely located at active lava locations such as lava flow vents, channels, and breakouts. Moderate temperatures (green) are related to the levees, and low temperatures (blue) to the cold surroundings of the lava flow. At the lava front however, the temperature distribution is sparce due to multiple lava breakouts and cooling. In this new map, temperature is distributed between 650–1400 K and shows bimodal distribution with two major temperature modes at 775 K and 1325 K (mean temperature: 932±254 K; Figure 5-4d). The temperature distribution shows slightly lower temperatures than that of Aufaristama and field observation (Kolzenburg et al. 2017). The two modes retrieved at low and high temperature are interpreted to respectively represent the cooled lava surrounding and the channel itself.

When both models are compared, the refined thermal map shows lower temperatures in the channel (orange color instead of red) but higher temperatures in the levees (at the lava front and near the vents; green over blue). The temperatures of the cooled surroundings remain constant between thermal maps. In details, Figure 5-3a shows the absolute temperature difference between Aufaristama and refined models. The sign of temperature (+ or −) has no physical meaning at that step of the mathematical development, hence why the absolute temperatures are shown. Difference varies from 0 to 300 degrees at most and has a mean absolute temperature difference of 44 degrees. According to the temperature distribution in Figure 5-3b, the temperature difference shows three modes corresponding to the three major thermal components: i) ~80 degrees difference for the lava channel, ii) ~125 degrees difference for the levees, and iii) ~15 degrees difference for the cooled surroundings. This map emphasizes the sensibility of our model to moderate temperatures near the channel, as the temperature difference is greater in levees. Note that the dimensions of the lava flow are deliberately kept constant to focus on temperature variation but would undoubtedly change when modeling its distance-to-run due to the implication of temperature in lava flow rheology. Note also that no temperature is retrieved at the exact location of vents due to oversaturation effect during satellite measurement (radiance for saturated data is considered null).

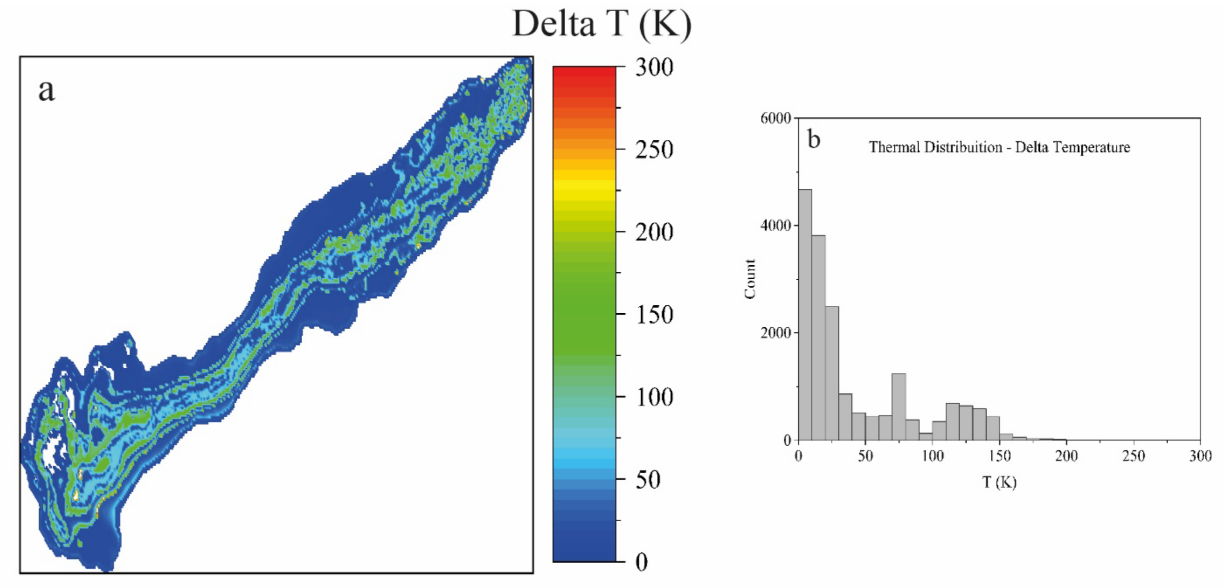

Figure 5-3: a) Temperature difference between Aufaristama and the refined model of this study. b) Temperature difference distribution between these two models.

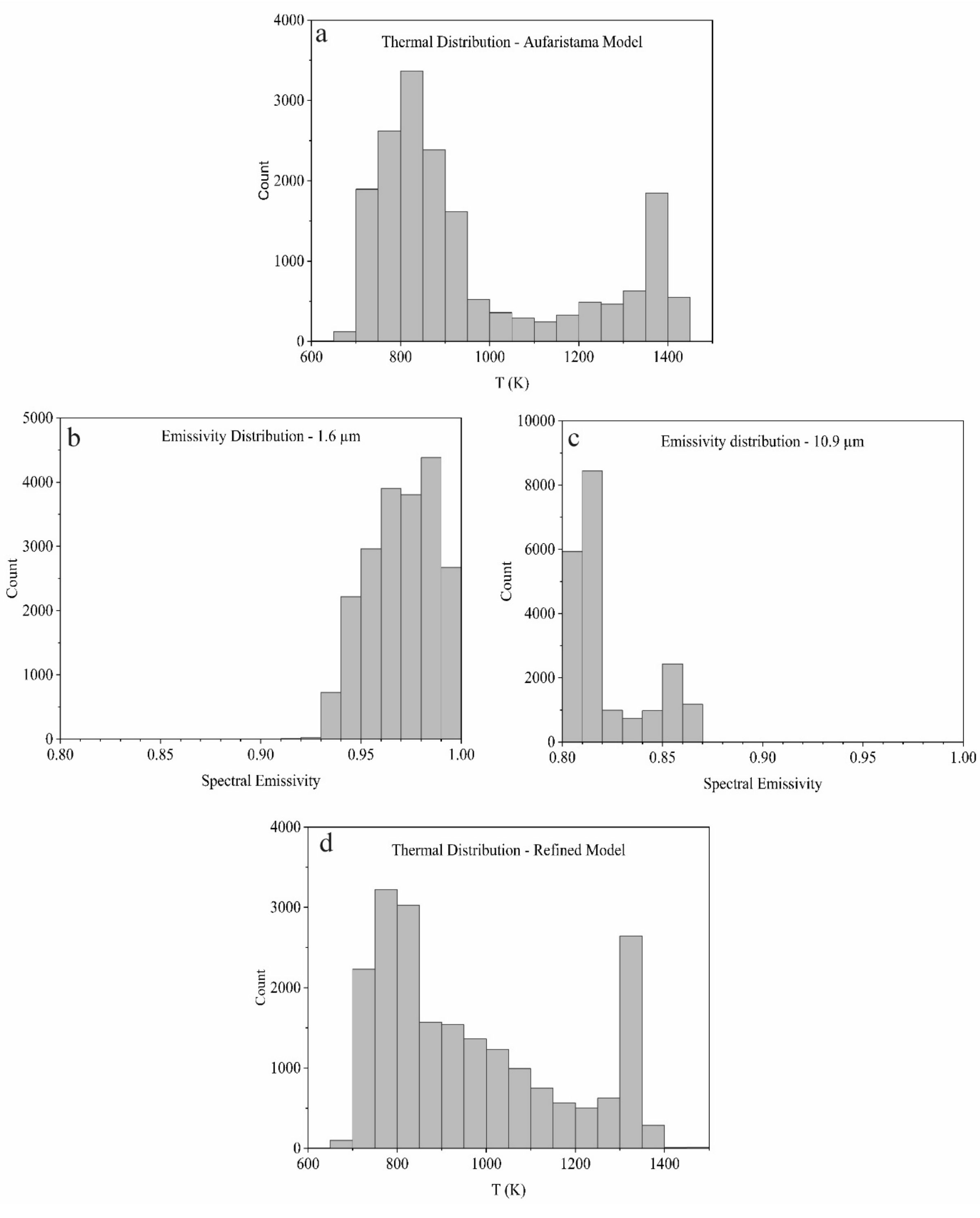

Figure 5-4: Results from Aufaristama and the refined models. a) Temperature distribution of Aufaristama model. b,c) Emissivity distribution for 1.6 µm SWIR and 10.9 µm TIR bands, respectively. d) Temperature distribution of the refined model from this study.

5.2.4. Implication for remote sensing application

As it was already shown in the previous section, the new calculated values of emissivity for the Holuhraun lava flow field are highly variable (0.80–1.00) for products having different rheological properties (i.e., from crystal poor magma, rapid cooled crust, highly crystallized levees). Therefore, the assumed constant value of 0.97 appears clearly as important oversimplification of the real spectral emissivity of a magma or evolving lava flow, especially in TIR where ε is lower than in SWIR according to the laboratory results of B-Nat. If the spectral and temperature dependence of the emissivity are not considered, then the derived surface temperature measured by remote sensing techniques can be over- or underestimated.

When compared, the absolute temperature difference between Aufaristama model and ours, the refined one, is ~44 degrees, with generally lower temperatures retrieved when using *in situ* laboratory emissivity compared to those determined using a constant value. Such temperature variation may seem small but can infer great consequences on lava rheology (e.g., the lava state can shift from liquidus to sub-solidus) as suggested in Andújar and Scaillet (2012; Figure I-1). For this reason, laboratories studies such as reported in this manuscript are of valuable interest while carrying out data post-processing, as they offer the opportunity to correct properly the retrieved temperature and derived rheological parameters. Accordingly, lab-based IR results when confronted to the field IR data help increasing accuracy in temperature retrieval by RS techniques.

Moreover, the high emissivity values retrieved for the partially molten magma and the crystallized lava zones suggests that, even if the ε of these products is <1, these are less likely to lose heat radiatively. Consequently, lava flow takes longer time to dissipate its heat, allowing longer distances to be reached. The latter modification increases ultimately the associated hazard, which is of utmost importance in the case of lava flow inundating inhabited area (e.g., the recent eruption at La Palma, Spain). Consecutively, our new insights will help in reducing the error related to thermo-rheological models of lava flows and support hazard assessment during effusive volcanic crisis.

This chapter summarizes our knowledge of lava radiative properties to apply them to refine remote sensing data. Building on Aufaristama et al. (2018), a new model for temperature retrieval was developed. As initially developed for a single value of emissivity, the later takes now into account the thermo-rheological evolution (ε–T) of the lava flow as to obtained more precise temperature data. The studied case was a lava flow from the 2014–2015 eruption of Holuhraun and demonstrates that temperature was improved by ~44 degrees in average, potentially allowing the lava flow to reach longer distance and put into risk possible inhabited area.

Chapter 6: Conclusion and Perspectives

This final chapter presents a summary of the main findings and highlights of this study before giving the perspective of further works.

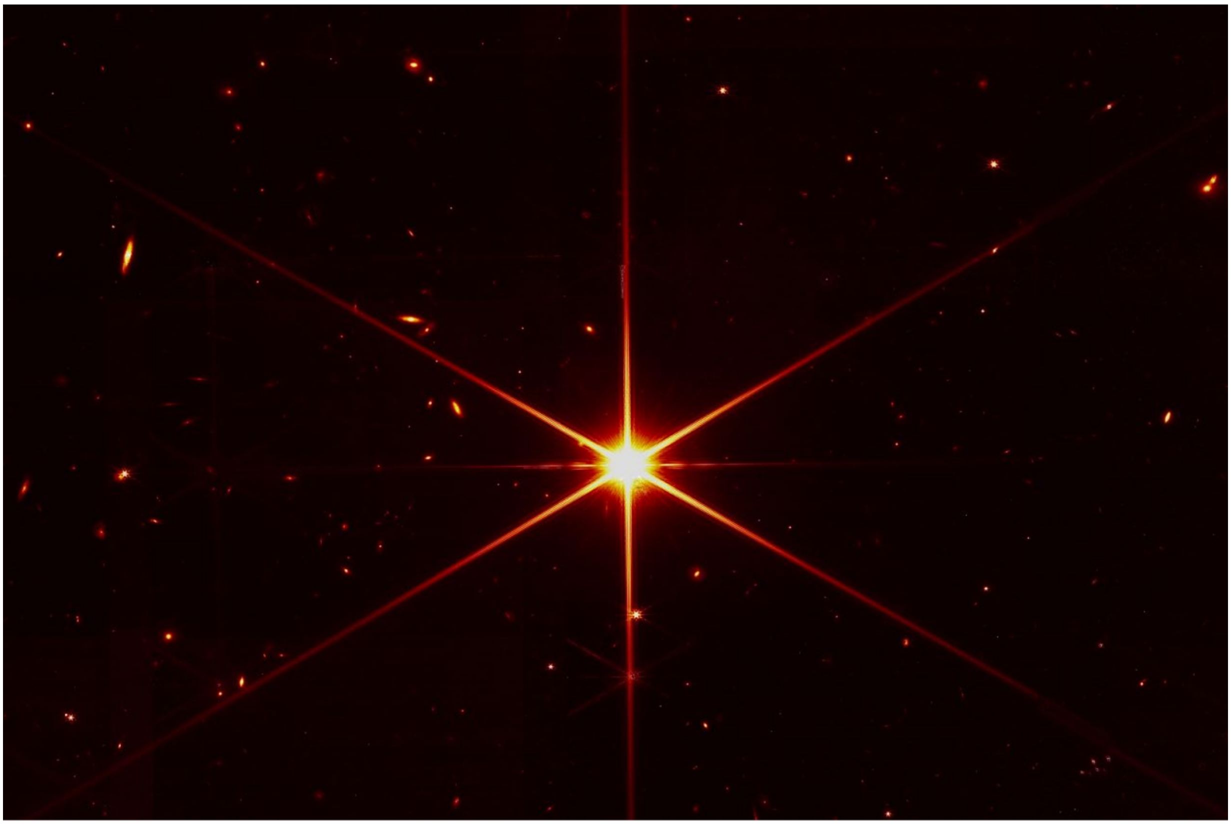

First high-resolution image of a star from James Webb Space Telescope (credit: NASA).

6.1. General conclusion

Temperature is a crucial parameter that controls lava rheology and distance-to-run. The unpredictable lava flow hazard prevents however direct measurements of lava temperature (T). Satellite or ground-based remote sensing techniques are key tools to monitor thermal anomalies associated with active lava flows and to evaluate their risks on the environment (e.g., destruction of properties such as houses and crops, human and wildlife loss, etc). Nevertheless, they rely on a not well-known parameter that controls temperature retrieval, namely spectral emissivity (ε). Nowadays spectral emissivity of magmatic rocks and minerals has been studied mostly at ambient temperature and with identification purposes. The few works devoted to the exploration of the ε–T relationship of different geological materials were mainly carried out far from relevant lava flow temperatures and in limited spectral range.

6.1.1. Highlights of this study

Therefore, the main goal of this study was to provide a comprehensive understanding of the radiative properties of dry and crystal-rich basaltic natural compositions through *in situ* high temperature (293–1800 K), wide spectral range (350–8000 cm^{-1}; TIR–MIR–SWIR) emissivity measurements. In order to determine ε–T relationship, a cross-disciplinary methodology based on petrological, structural, chemical, textural and thermal analyses was applied before and after IR experiments. Four basalts *lato sensu* were investigated in this project (Bárðarbunga basalt, Fasnia Basanite, MORB from Juan de Fuca and Oceanite from Piton de la Fournaise) with the emphasis on Holuhraun eruption (Bárðarbunga, Iceland). In parallel, three different minerals (pyroxene, plagioclase, and iron oxide) commonly occurring in basaltic magmas were also studied under the same experimental conditions to determine the impact of crystal on basalt radiative properties.

The obtained results are of high importance for the remote sensing community. First, to the best of our knowledge, it was the first systematic study of the spectral emissivity measured up to molten state and in wide spectral range of homogeneous basaltic glasses, heterogeneous crystal-bearing natural basaltic magmas and basaltic mineral endmembers. Moreover, this work showed that spectral emissivity is highly sensible to any change in temperature, wavelength, and primarily depends on sample composition, microstructure, and texture. Results revealed that the ε–T relationship for basaltic glass is complex. With the temperature increase, silicate glass anharmonicity increase and promotes the ion mobility. This leads to the microstructure re-organization, clustering, and progressive growth of Fe-Mg-rich crystals, and consequently ensues the sample opacification affecting its optical behavior. The opacification phenomenon naturally occurs in the magmatic rocks with high FeO content, but it is greatly supported by the silicate microstructure, i.e., degree of polymerization, and presence of the network modifiers. The temperatures of crystallization processes, phase segregation and the appearance of opacification phenomenon are well distinct for every basaltic composition.

This study also showed that spectral emissivity of crystallized natural basalts slightly differs from its glassy counterpart. Since the natural sample is a heterogeneous mixture of glass/melt, crystals, and vesicles, each component exhibits specific radiative properties that would affect the sample's overall emissive response. Thus, the basalt radiative properties will differ depending on the crystal composition, size, content, and distribution.

The results clearly indicate the high complexity of radiative properties of basalts; each composition has specific ε−T relationship. In all investigated compositions, spectral emissivity increases in TIR and decreases in MIR and SWIR spectral regions with increasing temperature, contrasting with the commonly found literature data. Finally, the ultimate goal of this research was to understand the radiative properties of volcanic molten rocks and hence, better refine temperature determination from remote sensing radiance data. Consequently, our newly acquired laboratory-based emissivity data were used to refine Holuhraun lava field temperatures estimated by remote sensing techniques by ~44 degrees on average through improved version of Aufaristama et al., (2018) model. Such temperature variation can infer great consequences on lava flow modeling with appropriate rheological information, thus improving hazard assessment in volcanic systems. Despite that measuring spectral emissivity for fully melted magmatic rocks is difficult and time-consuming, it is crucial for volcanology and geothermal research.

6.2. Perspectives

The interesting results obtained in this study for basaltic magmatic rocks open the doors to new future considerations. Below are briefly described a few perspectives that should be conducted:

1) Important differences in radiative properties of basalts with similar compositions show clearly that ε–T relationship of compositions like Andesite, Dacite, and Rhyolite must be carried out as to evaluate the effect of composition on the radiative properties of various Earth lavas. Our preliminary results (see high temperature emissivity spectra of Dacite as example Figure 6-1, and others in Appendix C.1–5) reveal distinct optical properties of Dacite when compared to basalts, especially in MIR ad SWIR spectral ranges. This result demonstrates clearly that each lava composition must be meticulously studied to determine their exact spectral emissivity.

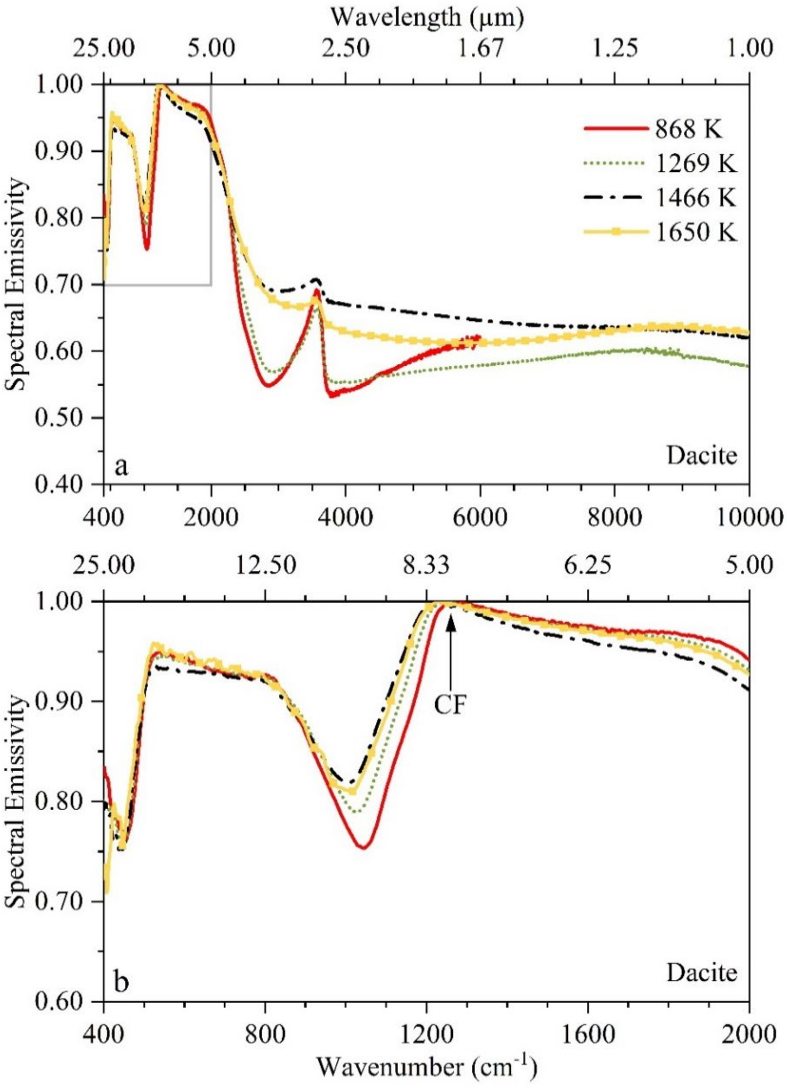

Figure 6-1: Spectral emissivity evolution with temperature for Dacite.

2) The presence of high amounts of oxide minerals in the experimental glassy samples, as well as the formation of relatively thin layers of Fe-rich composition in these, has an important impact on controlling the radiative properties of the studied glasses at temperatures, which are of paramount importance for understanding the volcanic-magmatic system. Hence, for retrieving the ε–T relationships on glassy basaltic samples without the interference of these iron-oxide phases, it would be necessary to perform the same type of IR measurements but under a more reduced environment. These conditions will considerably reduce or even prevent the formation of these oxides as to retrieve the response of the true glassy liquid without having any Fe-rich phase parasite signals.

3) This study was exclusively devoted to the radiative properties of volatile-free lavas. However, to evaluate the thermal budget of a magmatic chamber, the impact of volatiles on radiative properties of magmas must be carefully determined. Note that the thermal emission of the chamber would depend on the volatile content (magma can be hydrated as much of 10 wt.% H_2O; Pichavant 2011), composition and state (dissolved or exsolved). Such study requires commonly used of high temperature (HT) and high pressure (HP) experimental conditions. On-going experiments using the newly high-temperature/high-pressure apparatus developed by ISTO-CEMHTI research group in the framework of Equipex Planex project (Experimental Planet-HP-HT *in situ* analyses) is giving promising results.

4) This study considered the spectral emissivity of magmatic rocks mostly from geological point of view. In consequence, physical aspects of spectral emissivity were faintly brushed but must be explored more thoroughly as they have non-negligible impact on understanding the optical and radiative properties of highly heterogeneous materials. Note that magma–glassy matrix containing crystals and vesicles, is a perfect example of a highly heterogeneous physical object.

   Based on spectral emissivity data, it is possible to obtain the optical functions which are the fundamental parameters controlling an object radiative thermal behavior. To do so, time must be allocated to the modelling of emissivity spectra using for example the CEMHTI homemade FOCUS software (De Sousa Meneses et al. 2004). Our preliminary results show good agreement between modeled and measured spectra and should allow us to retrieve the distribution of bridging and non-bridging oxygen of the silicate network in the future. This modelling can be combined with more advanced textural and structural analysis such as TEM, 3D micro tomography, and FOAMS (Shea et al. 2010). This could give substantial insights into the spectral emissivity behavior in MIR and SWIR spectral ranges, especially in the case of transparent materials, in which temperature gradients can be observed in matrix volume. In similar way, the up scaling from laboratory samples to natural materials should be carried out via numerical simulations of radiative transfer inside semitransparent materials. This can be done with different numerical methods, for example symbolic Monte Carlo or ray tracing.

5) The next logical step of this study is to explore the impact of spectral emissivity on the-distance-to-run of emplacing lava flows using thermo-rheological models. As mentioned in Introduction, Rogic et al., (2022) made a first but arguable step in that direction by modeling lava flow distance-to-run using lab-based spectral emissivity data. They demonstrated that spectral emissivity is an important factor for model lava flows with accuracy. Note that lava flow modeling can drastically impacts the risk associated with lava flow and mislead or the people in charge of the volcanic crisis (e.g., civil protection) because of the inaccurate data provided. Therefore, we suggest pursuing the development of radiative equations that would take into consideration the spectral, composition, structural and temperature dependence of emissivity, and that would be easily implement into any RS temperature retrieval algorithm and thermorheological models of lava flows. Note that application of our refined model to lava flow modelling using PyFlowGo is currently being carried out. Note that this implementation allows to dispose of the dual-band method that rely on the important assumption of two thermal components for a lava (when for better modeling results, at least seven thermal components should be considered; Islam et al., 2017; Li et al., 2013). This is especially well sound when it has been demonstrated that the dual-band method breaks down when the sample emissivity changes considerably with temperature (such as for basalt), even when two close temperatures are chosen (Xiao et al., 2020). By implementing a temperature-dependent equation of emissivity, we can get rid of the emissivity dependence, i.e., the surface temperature will be the only unknown in the non-deterministic nature of the mixed pixel problem. Combined with continuous monitoring of the lava flow propagation, this will ultimately help propagation models to predict lava flow distance-to-run with higher accuracy and minimize its impact on surrounding locations during emplacement. It will also allow better quantification of other eruptive parameter such as erupted volume of lava, time-average discharge rates (Bonny et al. 2018; Coppola et al. 2019).

6) Finally, as remote sensing is expanding to planetary observations as to explore the composition of planets (e.g., on Mars, Farrand et al. 2016; Edwards et Christensen 2013; Johnson et al. 2006; Nair et Mathew 2017); on Venus, Gilmore et al., 2017; Helbert et al., 2015; Toner et al., 2019; on Mercury, Sprague et al. 2009) or exoplanets (with IR based telescope) new and numerous emissivity spectra from unknown surfaces will become available. To better identify and interpret these spectra, laboratory emissivity data measured in the same environmental conditions (e.g., oxidizing conditions, sulfur-rich atmosphere, high temperatures and pressures) and with the same physical properties (roughness, particle size, volatile-rich conditions) of an extraterrestrial surface analog are highly needed. As a consequence, new laboratory facilities are emerging as to further study the emissivity of rock under these particular atmospheric (e.g., under vacuum, in oxidizing conditions) and physical conditions (e.g., particle size, high temperature, volatile-rich composition) (Helbert et al. 2017; Davies et al. 2017; Thompson et al. 2021; Alemanno et al. 2021). Furthermore, several authors are publishing not only on other planet surface but on the volcanic activity on these planets (e.g., on Jupiter, Davies, Keszthelyi, et McEwen 2016); on Mars, Kraft, Michalski, et Sharp 2003; Minitti 2002; Minitti et Hamilton 2010) which further highlights the need of spectral emissivity data at high temperatures.

Chapter 7: Appendix

Complementary information and materials on the study presented here above. The bibliography closes this chapter and this study.

Entry sign of a Voodoo shop in New Orleans, USA.

7.1. Contents

Appendix A: Supplementary Methods

A.1. Table of Experiments

Table 7-1: List of experiments (~50) carried out in this study for basaltic glass, natural rocks, and minerals. Note that FTIR spectra acquisition and processing are time-consuming. Data treatment of the experiments in this table took approximatively 13 months. Single step: measurements made at a single temperature vs. Multiple steps: measurements made at different temperatures. The asterisk denotes the laser configuration: either the sample was heated only from above (in the case of 3 mm samples) or was heated from above and below simultaneously. The type of analysis performed for each investigated sample before and after IR are also denoted.

		Preparation			Prior IR			IR Experiment	After IR					
	Name	Fusion	Diameter (mm)	Thickness (mm)	Raman	SEM	EMPA	Conditions	Raman	SEM	EMPA	DSC	DRX	TEM
MORB	M1	✓	6	3				Heating/Cooling - multiple steps	✓	✓	✓			
	M2	✓	6	3				Heating - multiple steps	✓	✓	✓			
	M3	✓	10	1.511		✓	✓	Heating/Cooling - multiple steps	✓	✓	✓			
	M4	✓	10	3.077	✓			Heating/Cooling* - multiple steps						
	M_Glass	✓			✓						✓	✓		
FASNIA	F1	✓	6	3.307		✓		Heating - multiple steps	✓	✓	✓			
	F2	✓	10	1.572	✓			Heating/Cooling - multiple steps	✓					
	F3	✓	10	1.49				Heating - multiple steps	✓	✓				
	F4	✓	10	1.509				Heating - multiple steps	✓	✓				
	F5	✓	10	1.552				Heating - single step (1350 K)	✓	✓				
	F6	✓	10	1.422	✓			Heating - multiple steps	✓					
	F7	✓	10	1.573				Heating - single step (1250 K)	✓					
	F8	✓	10	1.501				Heating - single step (1300 K)	✓					
	F9	✓	10	1.516				Heating - single step (1350 K)	✓					
	F10	✓	10	1.482				Heating - single step (1400 K)	✓					
	F11	✓	10	1.424	✓			Cooling - multiple steps	✓					
	F12	✓	10	1.542	✓			Heating - single step (1450 K)	✓	✓	✓			
	F13	✓	10	1.494	✓			Heating/Cooling* - multiple steps						
	F_Glass	✓								✓	✓	✓		
BARDARBUNGA	B1	✓	10	1.520	✓	✓	✓	Heating - multiple steps	✓	✓	✓			
	B2	✓	10	1.411	✓			Heating - multiple steps	✓					
	B3	✓	10	1.545	✓			Heating - single step (1100 K)	✓	✓	✓			
	B4	✓	10	1.440	✓			Heating - single step (1200 K)	✓					
	B5	✓	10	1.564	✓			Heating - single step (1300 K)	✓					
	B6	✓	10	1.549	✓			Heating - single step (1350 K)	✓					
	B7	✓	10	1.518	✓			Heating/Cooling - multiple steps	✓	✓	✓			
	B8	✓	10	1.518				Heating - evolution through time + Cooling - multiple steps	✓					
	B9	✓	10	1.512	✓			Heating - multiple steps	✓					
	B10	✓	10	3.025				Heating - multiple steps	✓	✓	✓			
	B11	✓	10	3.029				Heating - multiple steps - Roughness						
	B12	✓	10	3.018				Heating/Cooling* - multiple steps	✓	✓				
	B_Crist1100	✓	10	3.001	✓	✓	✓	Heating/Cooling - multiple steps		✓	✓			
	B_Crist1050	✓	10	3.009	✓	✓	✓	Heating/Cooling* - multiple steps		✓	✓			
	B_Nat1		10	1.491	✓	✓		Heating/Cooling - multiple steps	✓	✓	✓			
	B_Nat2		10	3.000	✓			Heating/Cooling* - multiple steps	✓	✓				
	B_Glass	✓			✓				✓	✓	✓	✓	✓	✓
MINERALS	Augite		10	1.424	✓	✓	✓	Heating/Cooling - multiple steps	✓	✓	✓			
	Hematite		10	1.48	✓	✓	✓	Heating/Cooling - multiple steps	✓	✓	✓			
	Labradorite		10	1.464	✓	✓	✓	Heating/Cooling - multiple steps	✓	✓	✓			
OTHERS	D1	✓	10	3.084	✓	✓	✓	Heating/Cooling* - multiple steps	✓	✓	✓			
	A1	✓	10	2.859	✓	✓	✓	Heating* - multiple steps	✓	✓	✓			
	R1	✓	10	1.42	✓			Heating/Cooling* - multiple steps	✓	✓	✓			
	E1	✓	10	1.49	✓	✓	✓	Heating - multiple steps	✓					
	O-Nat1		10	2.99	✓	✓	✓	Heating/Cooling* - multiple steps		✓	✓			

Figure 7-1

Appendix B: Supplementary results for Basalts

B.1. Indirect Emissivity measurement

Indirect emissivity measurement (1-R-T) can be carried out using two different techniques: by FTIR microscopy and by using integrating sphere (cf. Methods). Figure 7-2 shows emissivity spectra retrieved at room temperature, before IR experiment using microscope (black spectrum) and the integrating sphere (blue). Both techniques concur but the signal to noise ratio is much better when the microscope is used. The red spectrum was recorded after IR experiment when the sample was quenched at ~1300 K. The spectrum served as a reference for fitting direct emissivity spectra and helped retrieve a temperature value when the CF was no longer reliable (Chapters 2, 3).

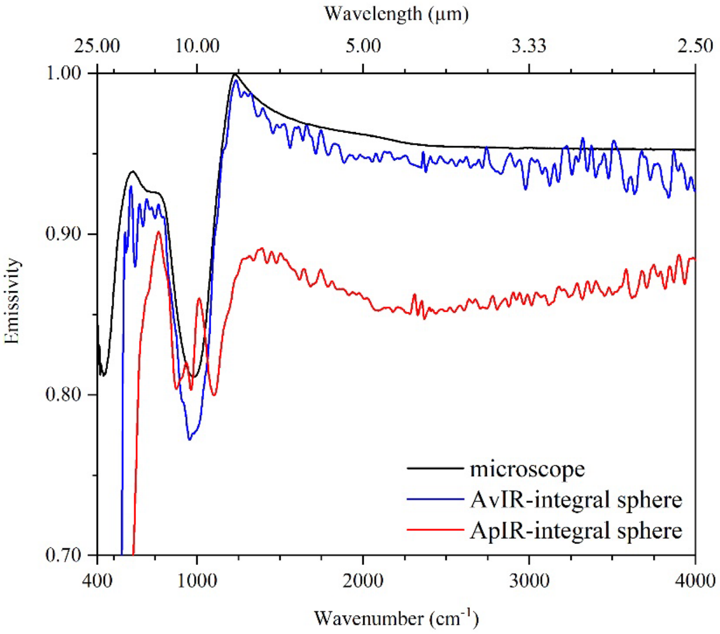

Figure 7-2

B.2. EPMA analyses

Figure 7-3 shows the complete chemical mapping analysis carried out with EPMA for B-glass cross section after IR experiment. Only Fe chemical map is shown in Chapter 3 as it shows an iron-rich layer at the surface of the sample. The other elements (Ti, K, Al, Na, and Si) show no particular feature.

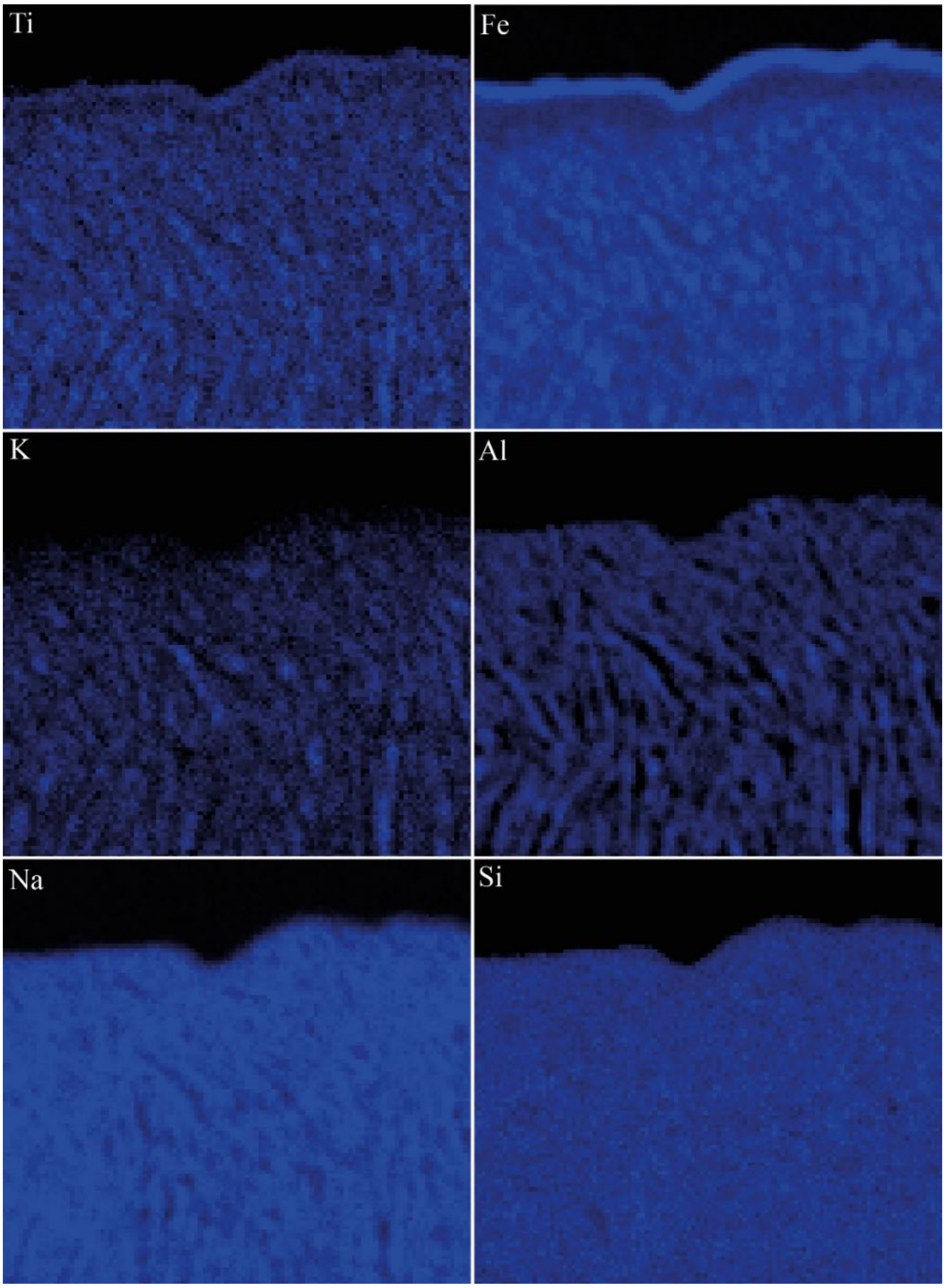

Figure 7-3

B.3. TEM analyses

Elemental composition using TEM of B-glass glass and crystals grown *in situ* during IR experiments were carried out by EDS analysis using single point, line, and mapping techniques. Results show that glass composition matches with that retrieved by EPMA. At the surface, crystals cationic composition is around 66 at.% Fe, 26 at.% Mg and 8 at.% Al whereas surrounding glass where the cationic composition is 49 at.% Si, 16 at.% Al, 13 at.% Ca, 9 at.% Mg, 7 at.% Fe, 5 at.% Na and 1 at.% Ti. In the core of the sample, crystals have a cationic composition of 88 at.% Fe, 6 at.% Mg, 3 at.% Al and <2 at.% for the other elements (Na, Si, Ca and Ti) whereas surrounding glass has a cationic composition of 41 at.% Si, 19 at.% Ca, 14 at.% Fe, 13 at.% Al, 7 at.% Mg, 4 at.% Na and 2 at.% Ti. Elemental mapping of the core and surface crystals are detailed in Figure 7-4a and c, respectively (see main text for results). As discussed in chapter 3, the surface and core compositions of crystal differ. Composition determined across a crystal shown in Figure 7-4b and d reveal respectively an enrichment of Fe and Mg for surface crystals and Fe only for core crystal.

Combined EELS spectra, XRD diffractograms and literature (i.e., EELS spectra of iron oxide species in Figure 7-5c are from Colliex, Manoubi, and Ortiz 1991) allowed to precisely identifying the nature of the iron species in B-glass core structure. First, the morphology of EELS spectrum of Fe is characterized by a single band centered at 711 eV (Figure 7-5a) and compared to that of oxygen (Figure 7-5b). In the literature, the Fe^{3+} threshold is located at 710±1 eV whereas Fe^{2+} threshold is located at 708 eV. As no Fe^{2+} threshold is observed in Figure 7-5a, Fe-rich oxides at the surface contain only Fe^{3+}. Based on these observations, several Fe-rich species are eliminated: FeOOH because the sample is not hydrated, $Mg(Al_x,Fe_{1-x})_2O_4$ because no Mg is found in the sample core (Figure 7-4c), and Fe_2O_3 and Fe_3O_4 were eliminated because they respectively have non-matching diffractogram in XRD, and contain Fe^{2+} and Fe^{3+} species. To find corresponding species, the morphology of the EELS oxygen spectrum was studied (Figure 7-5b) and reveals that the intensity of the c peak (at ~550 eV; Figure 7-5c) corresponds to that of γ-Fe_2O_3 when compared to literature. The latter is also in good agreement with XRD diffractograms. Thus, B-glass core crystals are identified as Maghemite (γ-Fe_2O_3).

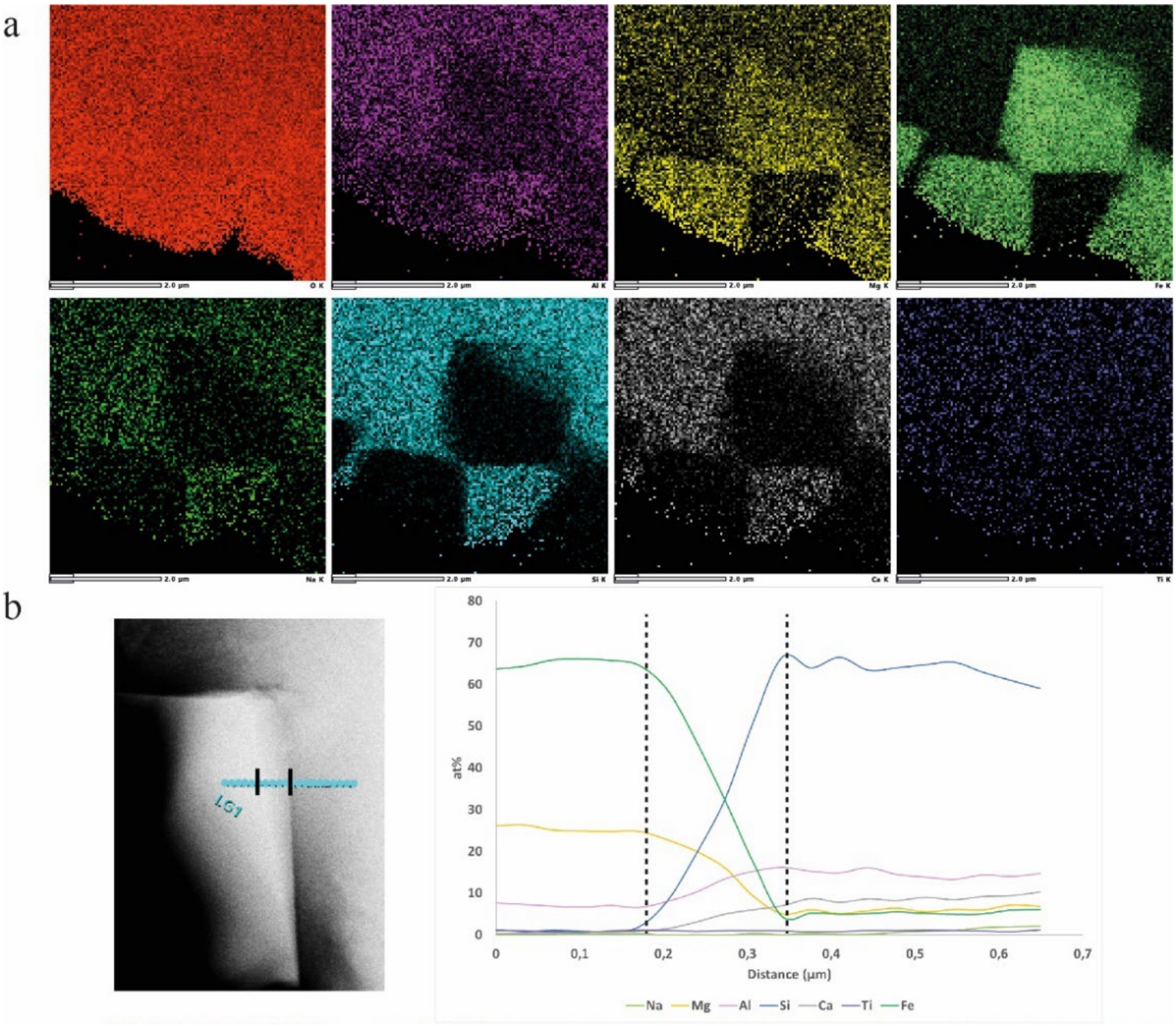
a
2.0 µm
O K
Al K
Mg K
Fe K
Na K
Si K
Ca K
Ti K
b
LG1
80
70
60
50
40
30
20
10
0
at%
0
0,1
0,2
0,3
0,4
0,5
0,6
0,7
Distance (µm)
Na
Mg
Al
Si
Ca
Ti
Fe

Figure 7-4

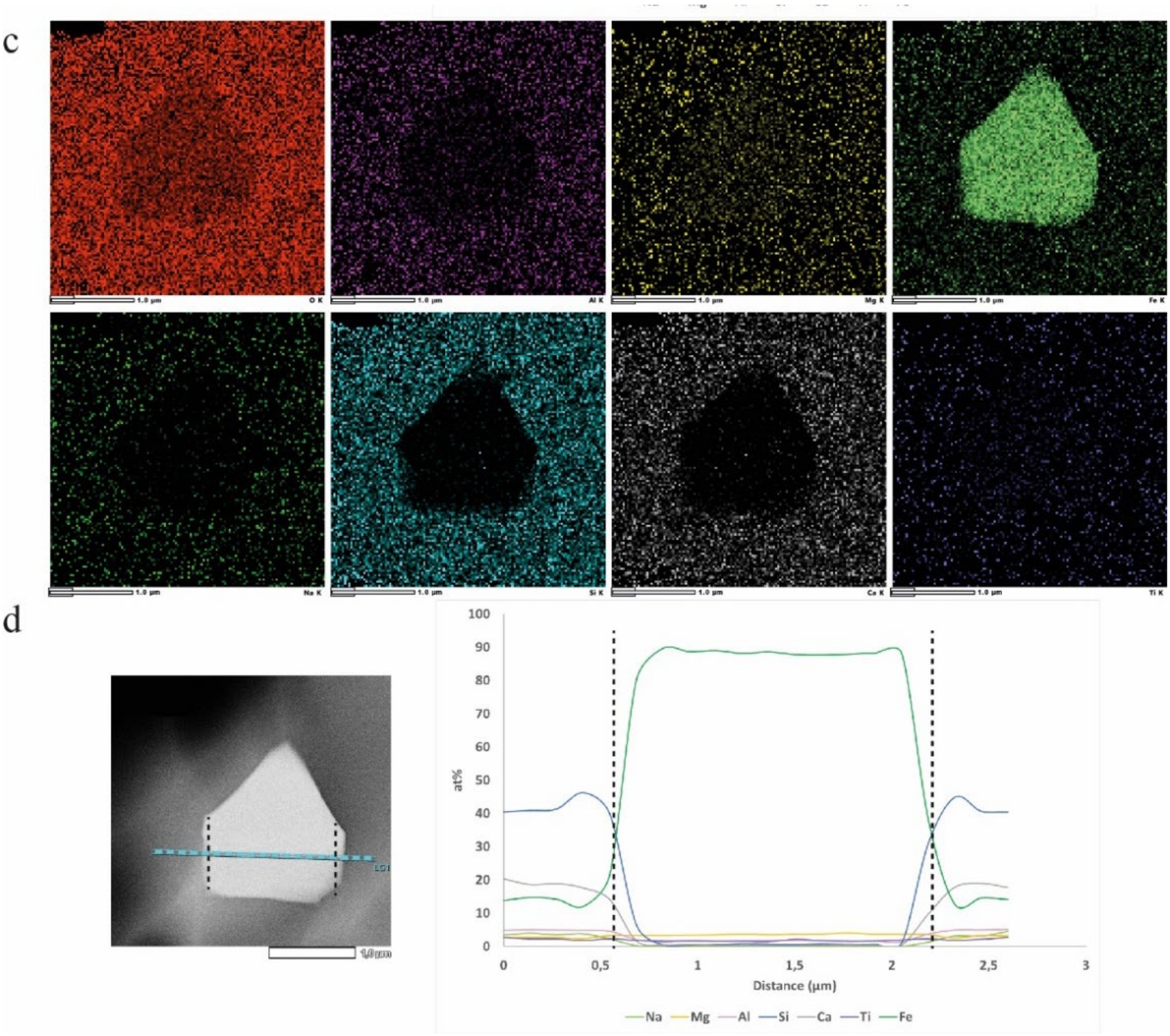

Figure 7-4 continue

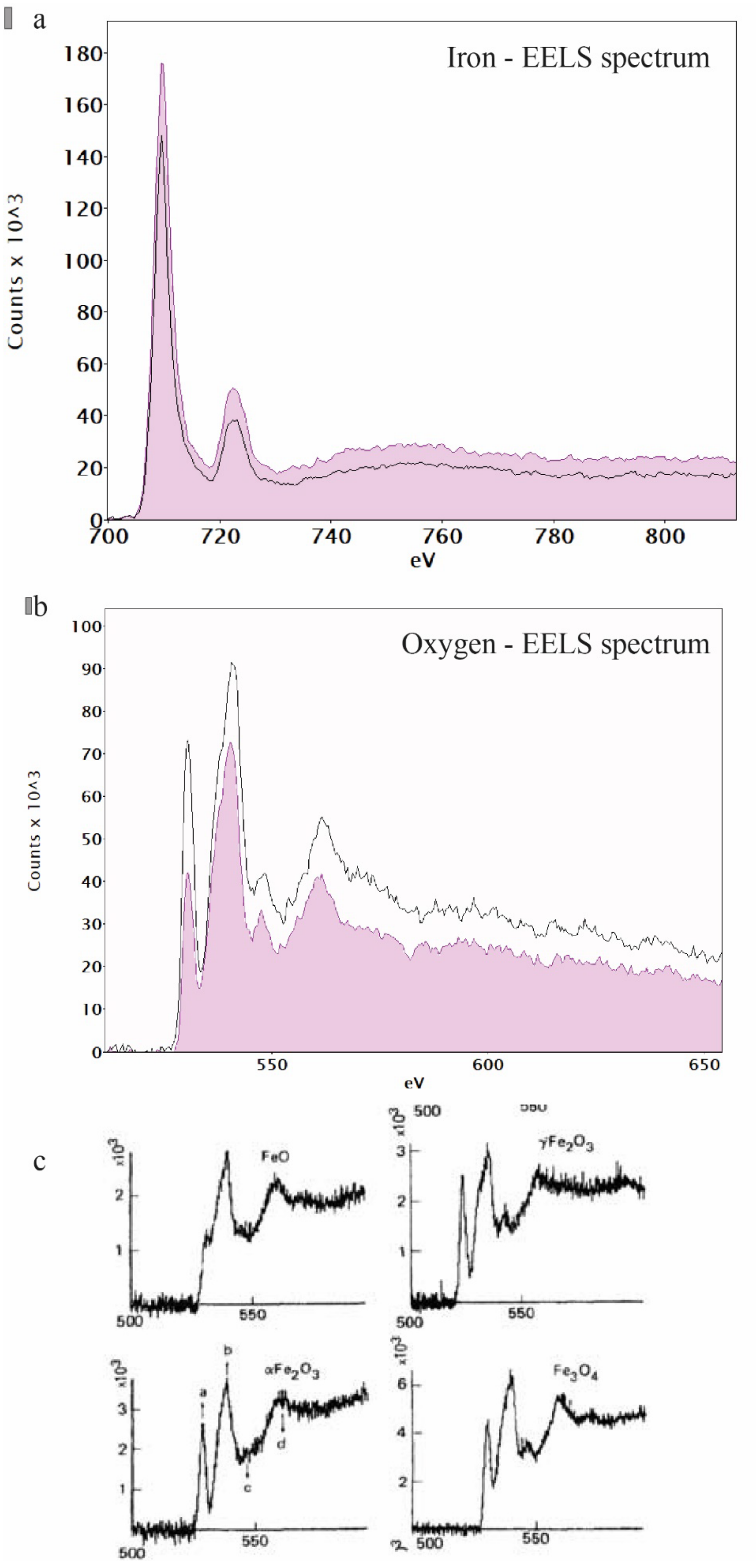
a
Iron - EELS spectrum
Counts x 10^3
180
160
140
120
100
80
60
40
20
0
700
720
740
760
780
800
eV
b
Oxygen - EELS spectrum
Counts x 10^3
100
90
80
70
60
50
40
30
20
10
0
550
600
650
eV
c
FeO
γFe2O3
αFe2O3
Fe3O4
x10^3
a
b
c
d
500
550

Figure 7-5

B.4. XRD ex situ analyses

To identify the nature of the crystalline phases present in B-glass sample after IR experiments, XRD *ex situ* experiment was carried out. Figure 7-6 shows the resulting diffractogram for B-glass after IR experiment where Augite, Hematite and Magnesioferrite were identified. XRD identification, combined with TEM and Raman analyses allowed confirming the nature of oxides present in B-glass sample.

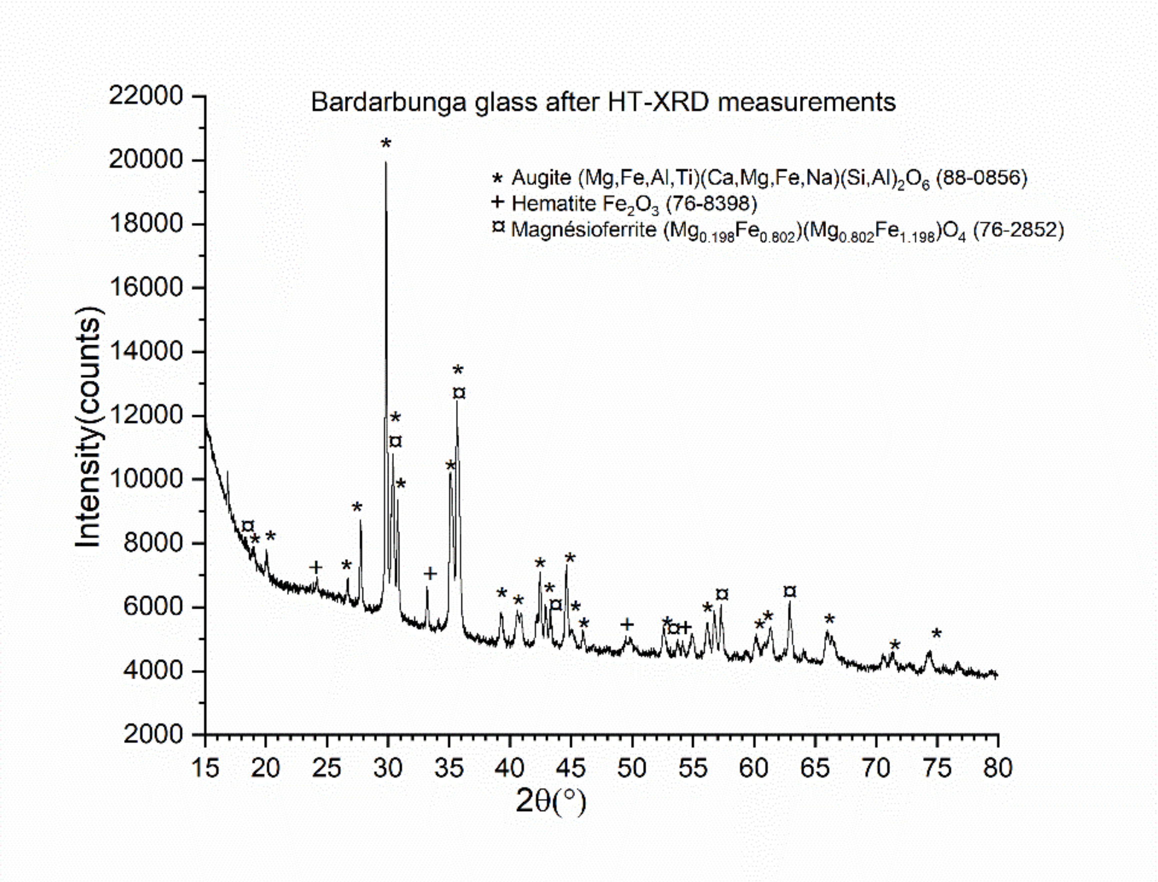

Figure 7-6

B.5. DSC Second heating/cooling cycle

The first Heating/Cooling acquired during DSC measurements is presented in main text (Figure 3-8). The second Heating/Cooling cycles of B-glass and B-Nat in Figure 7-8a, and for Fasnia and MORB in Figure 7-8b, account for the homogeneity of the sample. Since the melting and crystallization events (and their amplitudes) are similar but not identical to those recorded during the first cycle, the sensibility of sample of thermal history can be supposed.

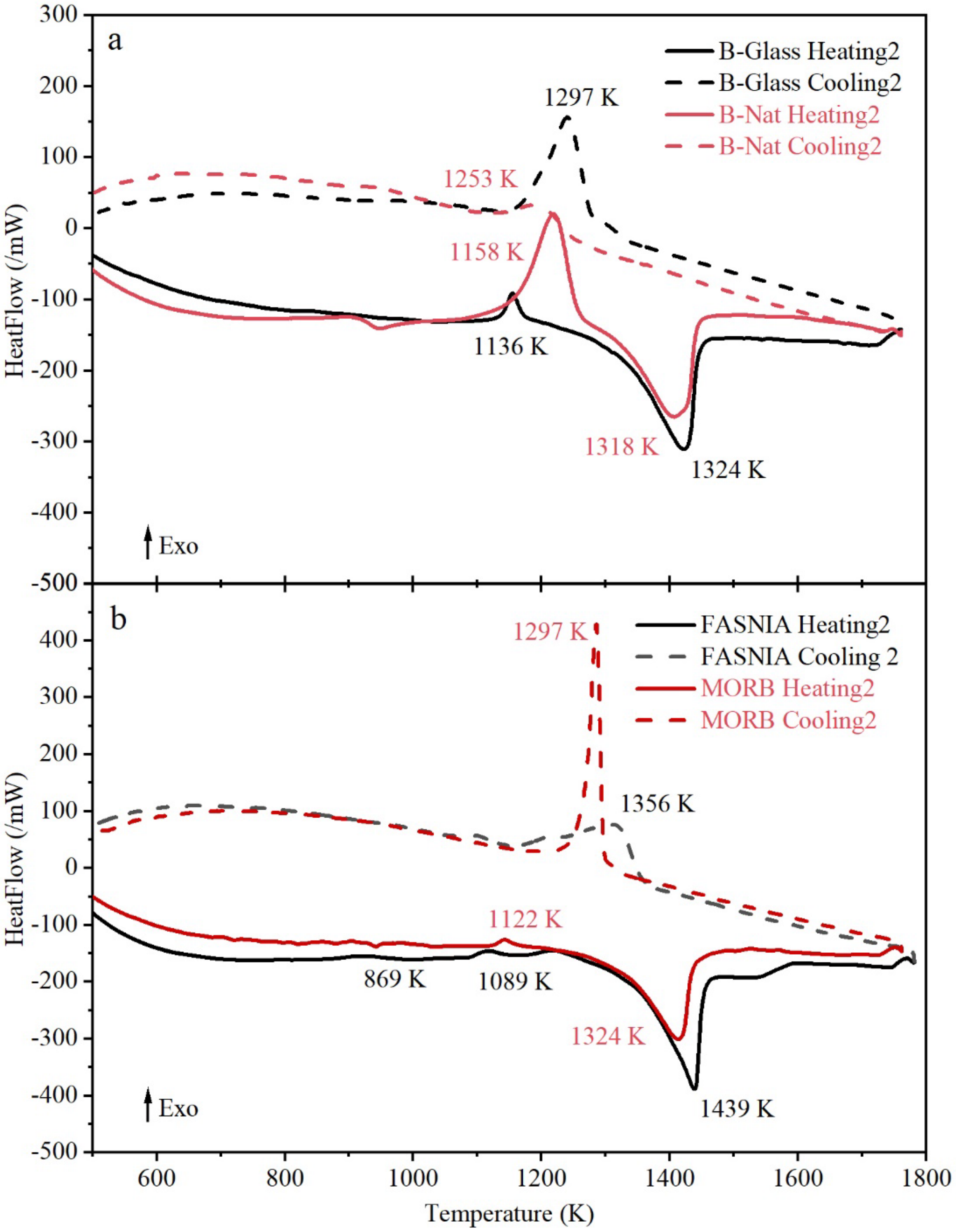

Figure 7-7

B.6. Raman spectra for MORB

Figure 7-8 compares the Raman spectra of MORB glass recorded before and after IR experiment. The spectrum recorded before IR is representative of homogeneous basaltic glass, as demonstrated by stretching and bending vibration bands of silicate network. Raman spectrum after IR was recorded at room temperature after quench at 1450 K. The differences reveal the modification of local silicate structure as well as the presence of Fe-rich crystal since characteristic Fe-O vibration is visible at ca. 666 cm^{-1}. Thus, MORB-glass structural modifications appearing with the temperature increase are very close to those observed in B-glass.

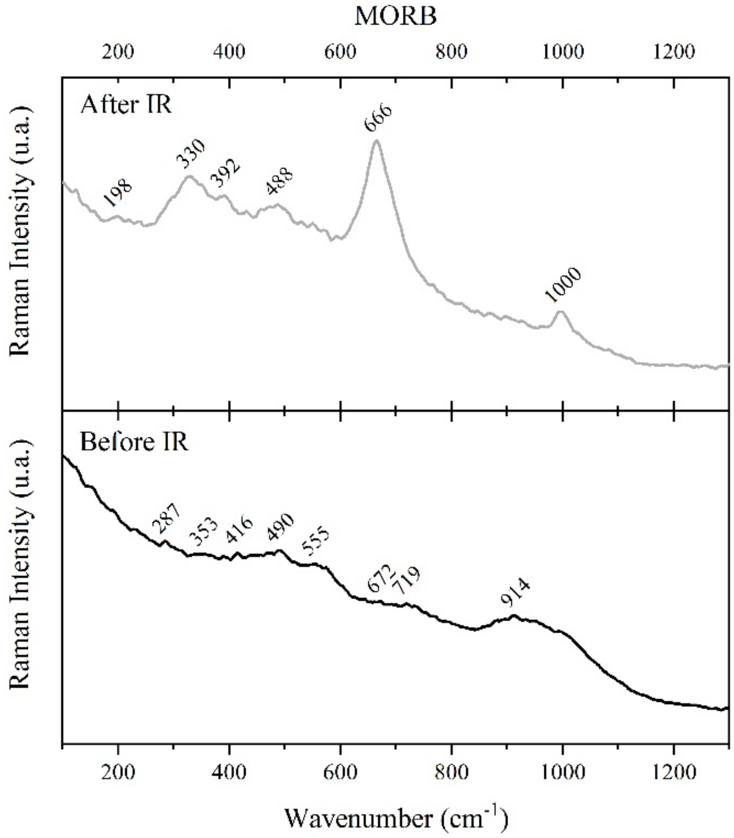

Figure 7-8

B.7. All emissivity spectra for a single experiment: B-glass

During *in situ* IR emission experiments, the emittance spectra of every sample were recorded as a function of increasing temperature in numerous steps y (usually ~20). The full set of emittance spectra recorded during 1 measurement for B-glass sample is shown in Figure 7-9. As it can be clearly seen, a few different temperature regions can be distinguished; in every region, the spectra are very similar and reveal the same information/behavior. Consequently, for better and easier readability the Figures presented in Chapters 3, 4, and 7 show only the most representative spectra.

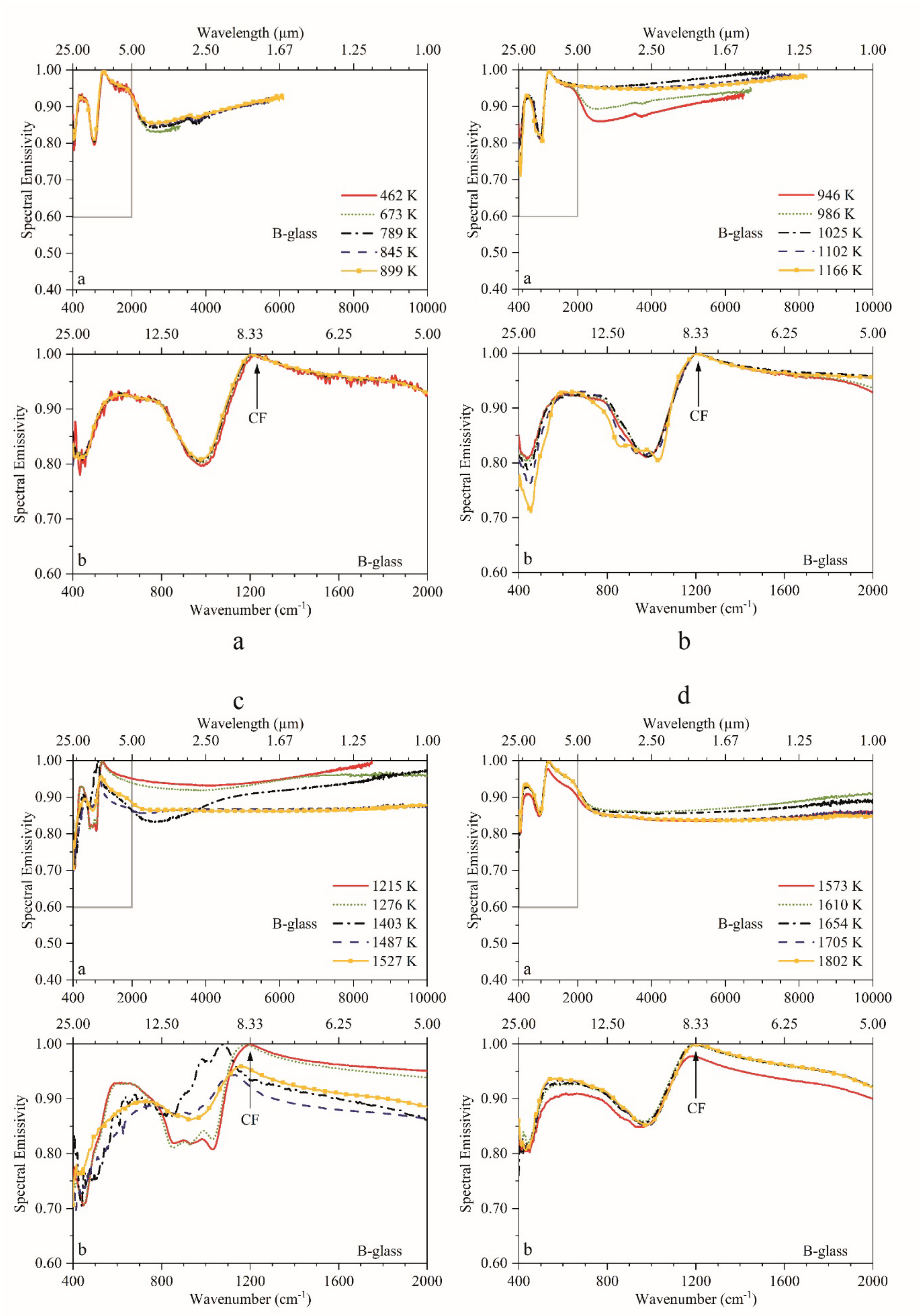
a
b
c
d
Wavelength (µm)
25.00
5.00
2.50
1.67
1.25
1.00
Spectral Emissivity
Wavenumber (cm⁻¹)
400
800
1200
1600
2000
4000
6000
8000
10000
12.50
8.33
6.25
B-glass
CF
462 K
673 K
789 K
845 K
899 K
946 K
986 K
1025 K
1102 K
1166 K
1215 K
1276 K
1403 K
1487 K
1527 K
1573 K
1610 K
1654 K
1705 K
1802 K

Figure 7-9

Appendix C: Supplementary results for Andesite, Dacite and Rhyolite.

The results acquired in this work show clearly high complexity of radiative properties in the case of basaltic magmas. Although basaltic magmatism is the most abundant in Earth, other magmatic compositions and their radiative properties deserve also particular attention as they were observed and studied by the RS community. Thus, to enhance our study of high temperature radiative properties of dry magmatic rocks, the other Earth magmas were also considered: Andesite, Dacite and Rhyolite. This study is the object of scientific article, in preparation. Some results with brief description are presented below.

C.1. Indirect Emissivity measurements

Figure 7-10 shows the good concordance between spectral emissivity spectrum obtained indirectly at room temperature and that recorded directly at lowest measured temperature, ~850 K, for Andesite, Dacite, and Rhyolite. Reflectance and Transmittance spectra used to calculate 1-R-T spectrum are also displayed. Note important spectral feature differences between the samples revealed already at room temperature. The most important differences are observed in the MIR and SWIR spectral regions.

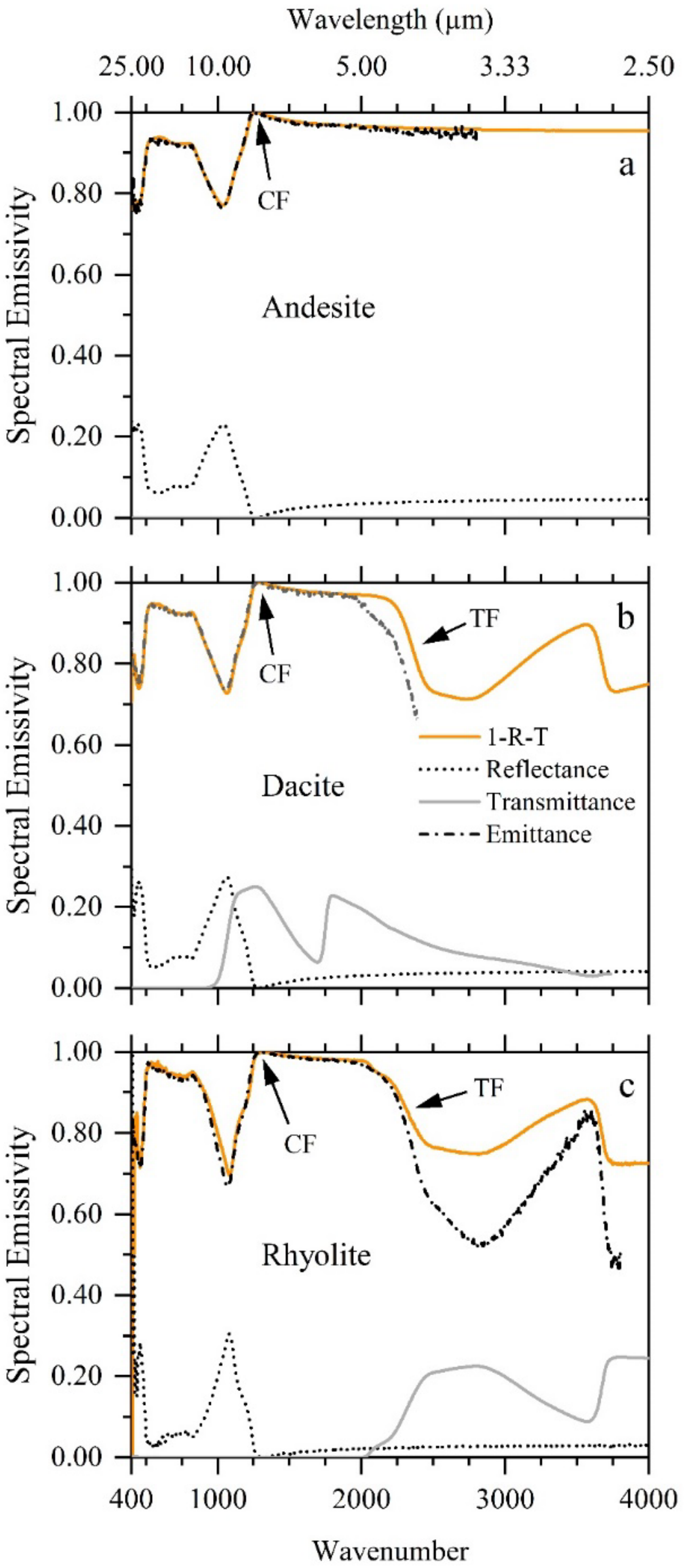
Wavelength (μm)
25.00
10.00
5.00
3.33
2.50
Spectral Emissivity
1.00
0.80
0.60
0.40
0.20
0.00
a
CF
Andesite
b
TF
CF
Dacite
1-R-T
Reflectance
Transmittance
Emittance
c
TF
CF
Rhyolite
400
1000
2000
3000
4000
Wavenumber

Figure 7-10

C.2. SEM and EPMA analyses

Figure 7-11 shows SEM pictures before and after IR experiments for Andesite, Dacite and Rhyolite demonstrating that the sample texture, both in cross or planar section, remains homogeneous and no variation occur after IR experiment.

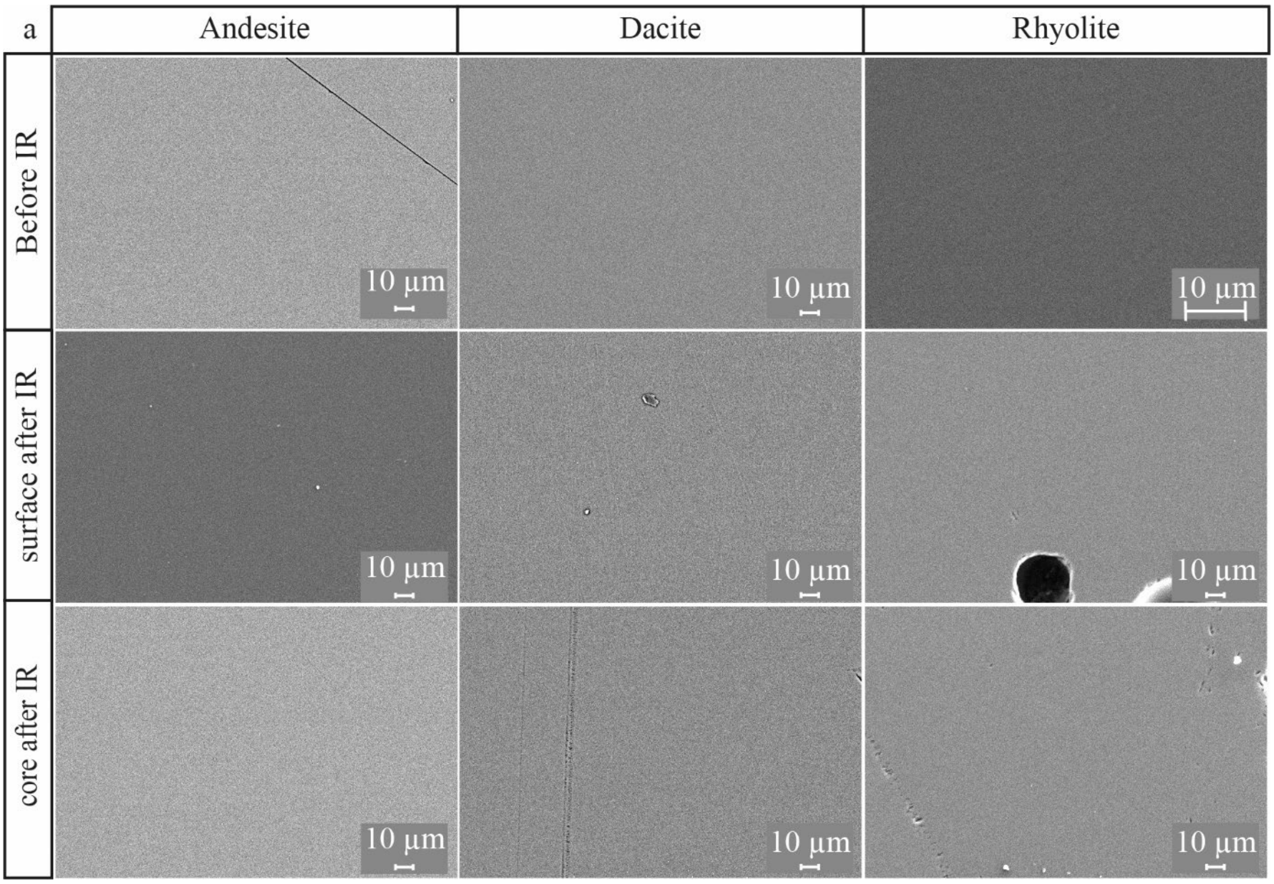

Figure 7-11

The TAS diagram in Figure 7-12 reports the main composition studied; the basalts *lato sensu* as well as the phonolite (Li et al. 2021) previously investigated in our group are also marked. The figure is accompanied by the Table 7-2 that gathers chemical data retrieved by EPMA analyses. Results confirm SEM observations: no variation occurs during IR experiment. S.D.: standard deviation.

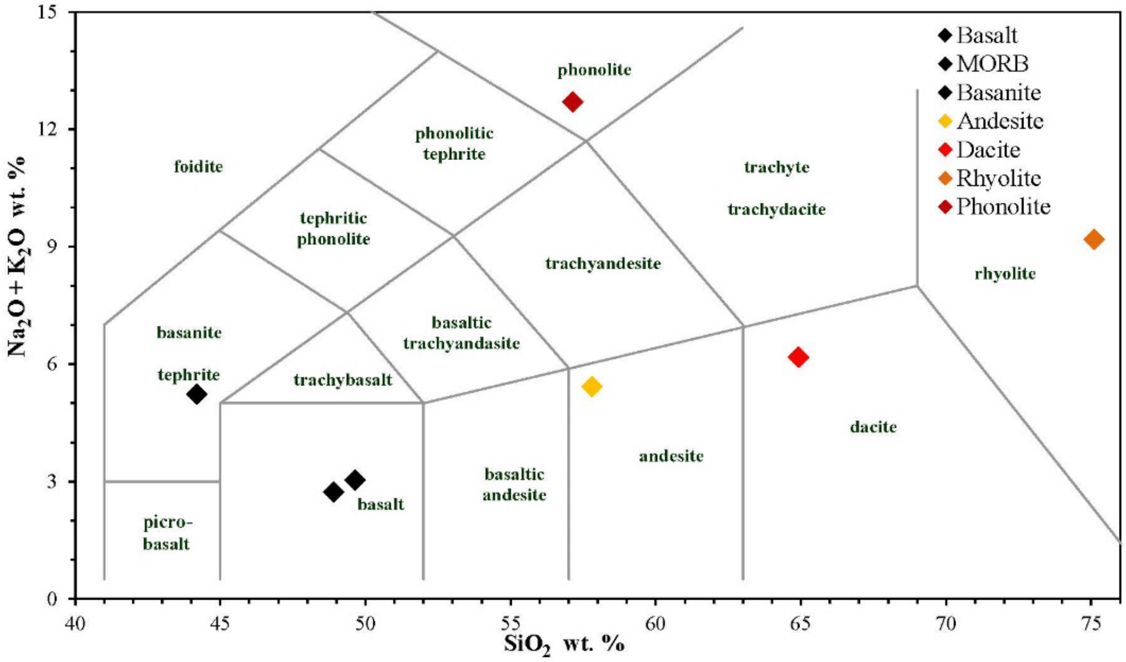

Figure 7-12

Table 7-2

Oxide wt. %	Andesite BeforeIR		Andesite AfterIR		Dacite BeforeIR		Dacite AfterIR		Rhyolite BeforeIR		Rhyolite AfterIR	
	Glass	S.D.	Glass	S.D.	Glass	S.D.	Glass	S.D.	Glass	S.D.	Glass	S.D.
# analysis	10	-	22	-	23	-	31	-	10	-	17	-
SiO_2	57,80	0,21	57,96	0,50	64,92	0,53	65,65	0,63	75,10	0,30	74,75	0,58
TiO_2	1,28	0,07	1,25	0,10	0,60	0,15	0,44	0,07	0,07	0,05	0,06	0,05
Al_2O_3	16,40	0,19	16,44	0,17	16,32	0,28	16,61	0,22	13,12	0,13	13,41	0,25
FeO tot	9,36	0,31	9,14	0,42	4,24	0,24	4,02	0,20	1,66	0,11	1,75	0,10
MnO	0,16	0,05	0,20	0,08	0,12	0,07	0,10	0,08	0,10	0,05	0,04	0,04
MgO	2,84	0,06	2,81	0,06	2,35	0,07	2,23	0,09	0,04	0,02	0,06	0,02
CaO	6,49	0,09	6,56	0,16	5,07	0,11	4,90	0,13	0,70	0,05	0,76	0,04
Na_2O	4,13	0,07	4,11	0,10	4,75	0,12	4,50	0,09	3,98	0,09	4,25	0,10
K_2O	1,28	0,05	1,28	0,07	1,42	0,08	1,36	0,08	5,20	0,16	4,91	0,16
Cr_2O_3	-	-	-	-	-	-	-	-	-	-	-	-
P_2O_5	0,24	0,05	0,24	0,04	0,21	0,05	0,18	0,05	0,03	0,02	0,01	0,01
NiO	-	-	-	-	-	-	-	-	-	-	-	-
Total %	100,00	-	100,00	-	100,00	-	100,00	-	100,00	-	100,00	-

C.3. DSC analyses

Figure 7-13 shows the heat flow curves (heating in solid lines, and cooling in dash lines) for Andesite, Dacite and Rhyolite samples as to explore their thermal history. Note the important differences in T_g: 916 K in the case of Andesite whereas 991 K for Rhyolite. Melting temperature are also very different. The results show some small events during heating and very homogenous behavior during cooling. Compared to the basaltic samples, no complex crystallization occurs. All these structural modifications are probably related to the thermal expansion exclusively but need further consideration.

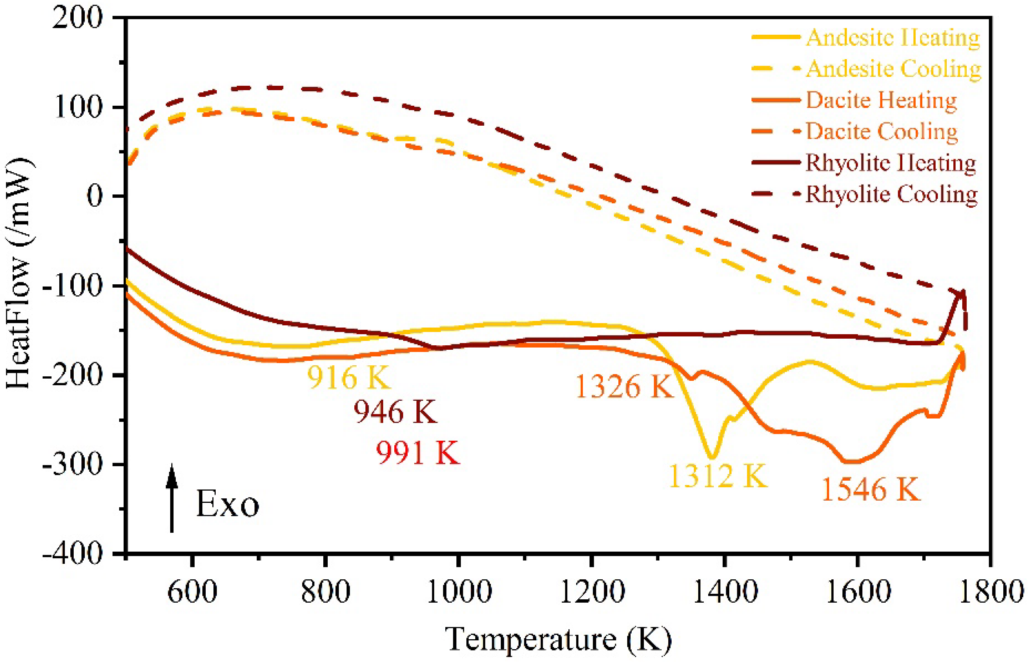

Figure 7-13

C.4. Raman analyses

Figure 7-14 shows Raman spectra for Andesite, Dacite, and Rhyolite before and After IR as to analyze their structure and chemical compositions. Raman spectrum of Andesite shows the coexistence of glass matrix and Fe-rich crystals. The higher intensity of the peak detected at ~670 cm^{-1} after IR experiment suggests that the crystal content increases during the thermal treatment. Note that Andesite has low viscosity allowing favoring the formation of iron-rich phases in its structure, as we observed for Bárðarbunga basalt. Dacite and Rhyolite show similar spectra with well-developed, intense bending Si-vibrations. Some differences can be seen however in the stretching massive suggesting different local structure and different degree of Si-network polymerization. No spectral variation is observed after IR experiment; sample structure remains constant during heating. Note that Fluorescence is systematically detected in Rhyolitic composition after IR experiments.

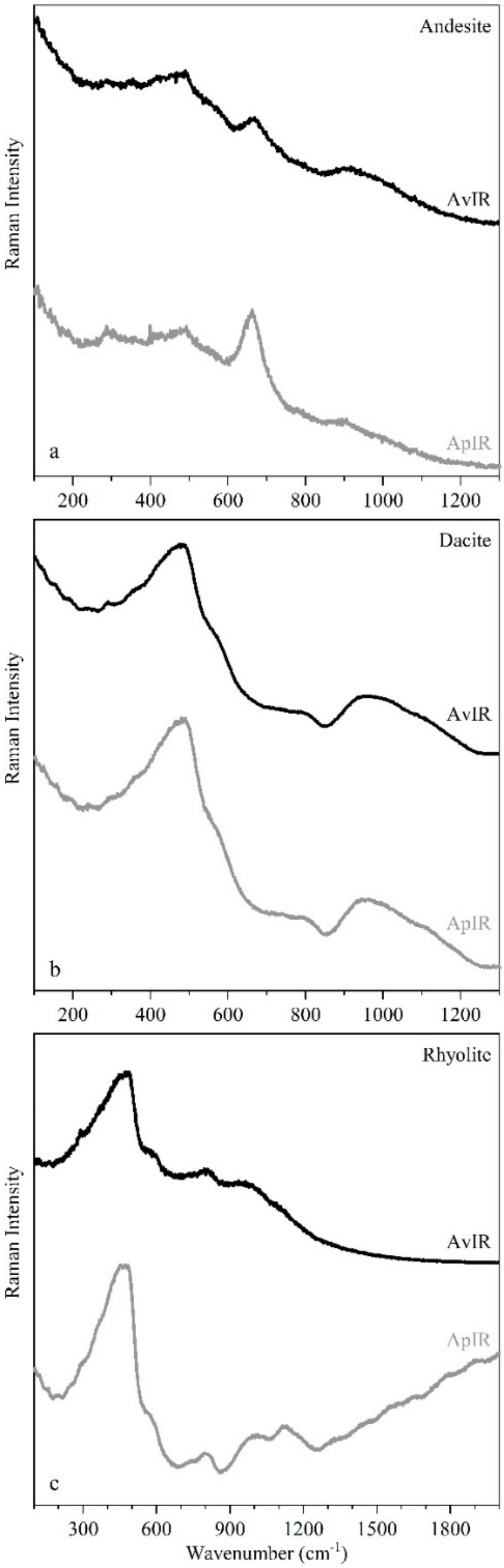
Andesite
AvIR
ApIR
a
Raman Intensity
200
400
600
800
1000
1200
Dacite
AvIR
ApIR
b
Raman Intensity
200
400
600
800
1000
1200
Rhyolite
AvIR
ApIR
c
Raman Intensity
300
600
900
1200
1500
1800
Wavenumber (cm^{-1})

Figure 7-14

C.5. Spectral emissivity evolution with temperature for Andesite, Dacite et Rhyolite

Figure 7-15: Spectral emissivity evolution with temperature and wavenumber for Andesite (a,b) (thickness: 3.0 mm). Panels a) and c) full measured spectral range covering TIR, MIR and SWIR. Panels b) and d) zoom on TIR spectral range (8–12 µm). CF: Christiansen Feature.
Figure 7-16: *Idem* for Dacite.
Figure 7-17: *Idem* for Rhyolite.

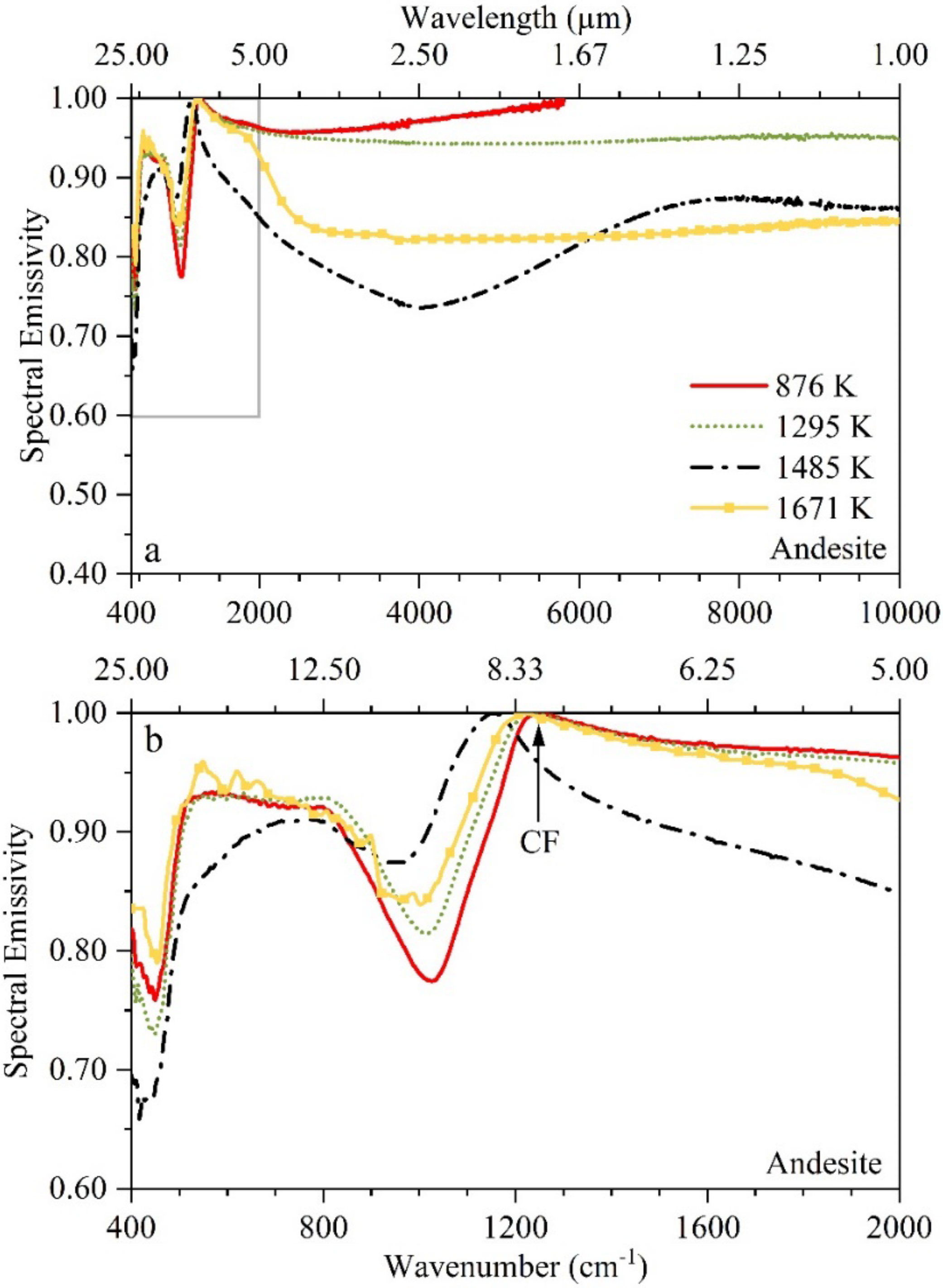
Wavelength (µm)
25.00
5.00
2.50
1.67
1.25
1.00
1.00
0.90
0.80
0.70
0.60
0.50
0.40
Spectral Emissivity
876 K
1295 K
1485 K
1671 K
a
Andesite
400
2000
4000
6000
8000
10000
25.00
12.50
8.33
6.25
5.00
1.00
0.90
0.80
0.70
0.60
b
CF
Spectral Emissivity
Andesite
400
800
1200
1600
2000
Wavenumber (cm-1)

Figure 7-15

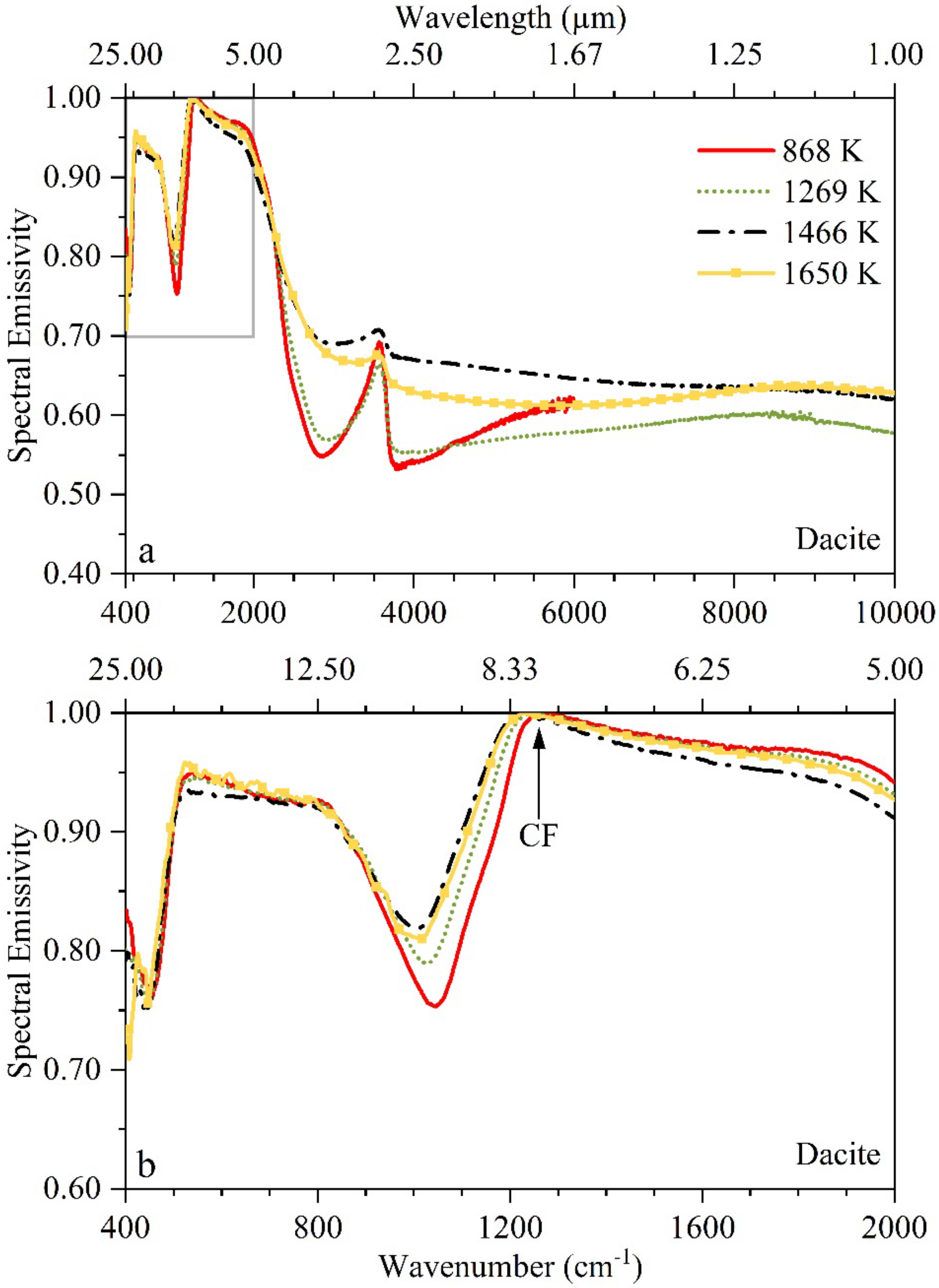
Wavelength (µm)
25.00
5.00
2.50
1.67
1.25
1.00
1.00
0.90
0.80
0.70
0.60
0.50
0.40
Spectral Emissivity
868 K
1269 K
1466 K
1650 K
Dacite
a
400
2000
4000
6000
8000
10000
25.00
12.50
8.33
6.25
5.00
1.00
0.90
0.80
0.70
0.60
Spectral Emissivity
CF
Dacite
b
400
800
1200
1600
2000
Wavenumber (cm-1)

Figure 7-16

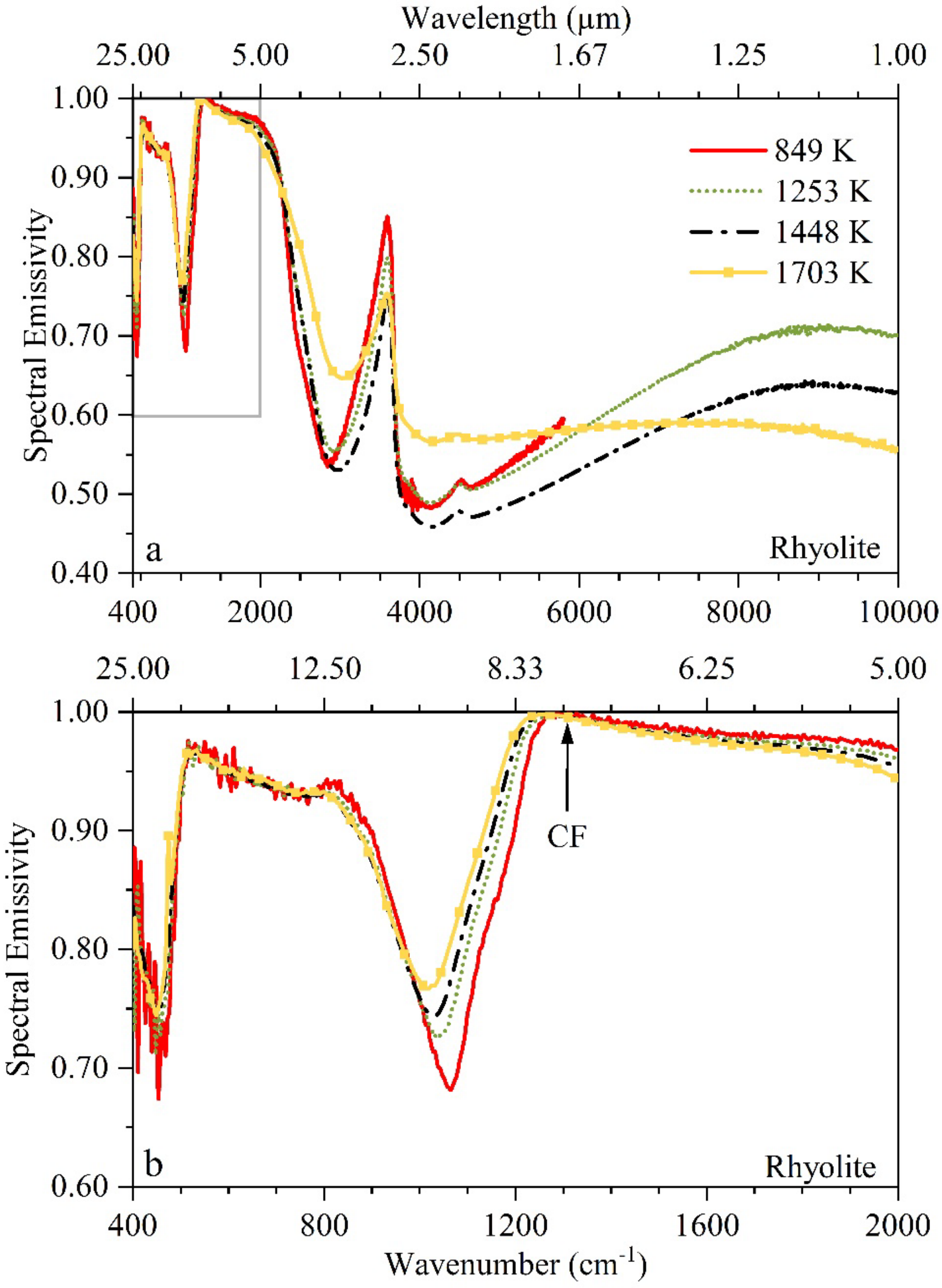
Wavelength (μm)
25.00
5.00
2.50
1.67
1.25
1.00
Spectral Emissivity
1.00
0.90
0.80
0.70
0.60
0.50
0.40
849 K
1253 K
1448 K
1703 K
a
Rhyolite
400
2000
4000
6000
8000
10000
25.00
12.50
8.33
6.25
5.00
Spectral Emissivity
1.00
0.90
0.80
0.70
0.60
CF
b
Rhyolite
400
800
1200
1600
2000
Wavenumber (cm^{-1})

Figure 7-17

All three samples share a single absorption band (~950 cm^{-1}) in TIR spectral range, representative of the sample glass homogeneity. They however greatly differ in the specific MIR–SWIR spectral range. Andesite, like basalts, shows very high emissivity values and characteristic opacification phenomenon below 1300 K in good agreement with the presence of Fe-rich crystals detected by Raman spectroscopy. With temperature increase some small Fe-segregation is observed first and then above 1600 K the sample becomes semi-transparent with very stable emissivity value, 0.8 in MIR and SWIR. The other two samples are semi-transparent in MIR and SWIR and shows the moderate emissivity values that increase slightly with T increase: from ~ 0.55 to 0.65 in the case of Dacite and from 0.45 to 0.55 for Rhyolite. Note that Rhyolite clearly shows the presence of electronic absorptions bands in SWIR regions. They can explain the fluorescence presence in Raman spectra after IR experiments. Both magmatic rocks also show presence of O-H stretching bands at ca. 3600 cm^{-1}. Thus, these samples emphasize the complexity of spectral emissivity in magmatic conditions.

7.2. Résumé étendu

7.2.1. Introduction

Les coulées de laves sont un des aléas liés aux éruptions effusives basaltiques (i.e., Bardarbunga en Islande, Piton de la Fournaise sur l'île de la Réunion, etc.) qui peuvent être responsables de considérables dégâts. Pour minimiser ces derniers, il est nécessaire de comprendre et modéliser leurs processus de mise en place et requière des données précises sur leurs propriétés radiatives. La température en fait partie et est un paramètre clé contrôlant la rhéologie d'une coulée de lave. Une légère variation de température (25–30 K) peut induire une augmentation de la teneur en cristaux du magma de 50% permettant à la viscosité de passer d'un régime peu visqueux à très visqueux (Figure 7-18).

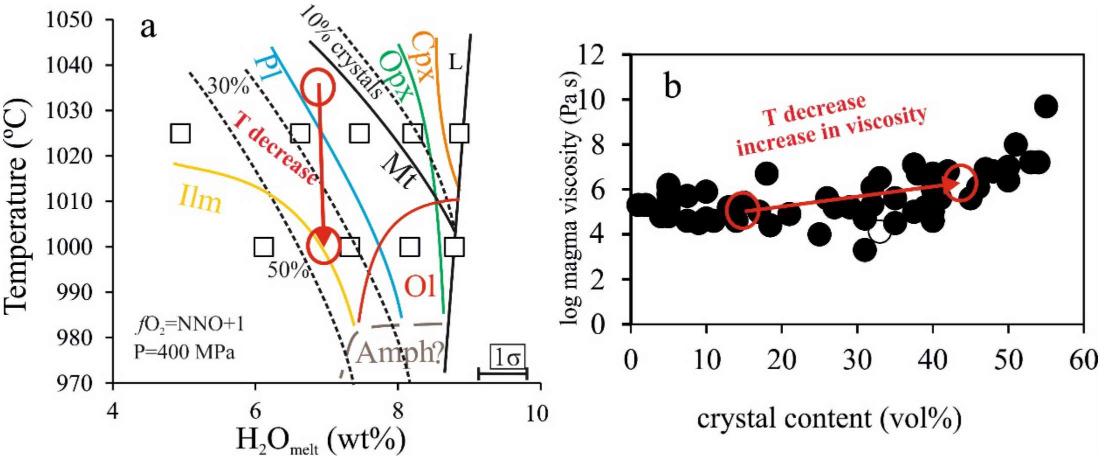

Figure 7-18: Diagramme de phase d'une andésite à 4 kbr. L'augmentation de la teneur en cristaux lorsque la température diminue de 35 °C (modifié d'après Andújar et al. 2017). b) Evolution de la viscosité en fonction de la teneur en cristaux dans les magmas (modifié d'après Andújar and Scaillet 2012).

Cependant, le comportement imprévisible des éruptions empêche les mesures directes de températures. Par conséquent, ces mesures sont régulièrement effectuées par des techniques de télédétection (avec des détecteurs sur le terrain ou depuis l'espace) développées pour mesurer la radiation Infra-Rouge (IR). Ces techniques mesurent le flux d'émission (radiance) de la lave à différentes gammes spectrales (Infra-Rouge lointain, TIR, 8–14 µm ; Infra-Rouge moyen MIR, 3–5 µm ; et Infra-Rouge proche, SWIR, 1–2.5 µm) qui est ensuite converti en température en utilisant la loi de Planck. Ces techniques bien établies sont malgré tout sujettes à d'importantes erreurs et limitations qui peuvent se propager à la détermination de la température (i.e., absorption atmosphérique, rapide changement de la température de la lave). Celles-ci sont reliées au manque de connaissance de l'un des paramètres les plus important, dénommé l'émissivité spectrale. Par exemple, un changement d'émissivité de 10% induit une différence de température de 83 K (Mouginis-Mark et al. 1991 ; Ball and Pinkerton 2006) et jusqu'à 300 m de différence sur la longueur de la coulée de lave (Rogic et al., 2019a, 2019b).

L'émissivité (ε) est la capacité physique d'un matériau (ex : coulée de lave) d'émettre de la chaleur par radiation. La structure micro- et macroscopique du corps (i.e., le degré de polymérisation, la composition, la présence d'hétérogénéité –cristaux ou vésicules–, la rugosité) exerce un contrôle important sur la propagation des phonons et sur son comportement émissif. Comme la composition et la teneur en cristaux d'un magma dépendent de la température, l'évolution progressive de la cristallisation lors du refroidissement d'une coulée de lave résulte nécessairement en l'évolution continue de ses propriétés radiatives. Un spectre d'émissivité caractéristique (cas d'un matériel diélectrique) se distingue en trois régions : 1– la région <1500 cm^{-1} (couvrant le TIR) révèle les principales vibrations du réseau silicaté. Nos échantillons apparaissent optiquement opaques dans cette région et sont caractérisés par le nombre de Christiansen (utilisé pour déterminer la température) et les bandes d'absorption Reststrahlen. 2– la région entre 1500 cm^{-1} et 3500 cm^{-1} (couvrant le MIR), attribuée aux phénomènes de multiphonon, est caractérisée par la présence d'un front de transmission où le comportement optique de l'échantillon devient semi-transparent. 3– la région >3500 cm^{-1} (couvrant le SWIR) est associée avec les processus électroniques et est caractérisée par un comportement optique transparent pour les échantillons pauvres en Fe.

L'objectif de cette étude, articulée en sept chapitres, est de combler ce manque en explorant : 1– la relation émissivité–température de basaltes *lato sensu* (basalte de Bardarbunga, basanite de Fasnia, MORB basalte de Juan de Fuca, et océanite du Piton de la Fournaise). 2– l'impact des cristaux magmatiques (pyroxène, plagioclase, et oxyde de fer), leur composition et teneur sur les propriétés radiatives de basaltes. 3– l'amélioration de la mesure de température, dérivée par les techniques de télédétection, de la coulée de lave Holuhraun.

Revue de la littérature

La littérature démontre que les propriétés radiatives des roches et minéraux magmatiques sont très complexes et varient considérablement en fonction de la longueur d'onde, la composition, la température et l'orientation. A température ambiante (<350 K), les travaux sont abondants mais couvrent rarement la gamme spectrale utilisée par les techniques de télédétection et ne prennent pas en compte la dépendance de la température des objets magmatiques. A haute température, les bases de données sont éparses et l'application de ces rares données à des systèmes naturels est limitée par le fait que la plupart des travaux ont été réalisés sur des poudres, cristaux ou verres synthétiques, sur une gamme de température limitée (jusqu'aux alentours de T_g) et une gamme spectrale limitée (typiquement limitée à la région TIR). De plus, les configurations expérimentales actuelles souffrent de restrictions qui affectent la mesure précise de l'émissivité spectrale. L'emploi de verres/roches naturelles/poudres ayant des tailles de particule, des compositions, et des porosités différentes peuvent ajouter des biais supplémentaires sur la mesure d'émissivité. En effet, l'utilisation de poudres de roches ou verres peuvent conduire à d'importants changements de texture et d'effets de volume induisant des réflexions indésirables dans l'échantillon, ce qui peut artificiellement augmenter l'émissivité effective de l'échantillon chauffé. Des valeurs anormales d'émissivité (dépassant celle d'un corps-noir idéal) ont été ainsi mesurées. A cela s'ajoutent le fréquent manque de précision dans la méthodologie appliquée (i.e., manque d'informations cruciales) et la pauvre description des spectres obtenus, rendant très compliquée la comparaison entre les travaux ayant déjà des données avec des valeurs d'émissivité variables. Toutes ces différences amènent la production de bases de données d'émissivité variables (et pauvres dans le cas des cristaux) et des relations contrastées entre émissivité et température. De plus, aucune étude n'a encore étudié les effets combinés des verres et des cristaux avec des minéralogies différentes (qui sont par définition, les composants naturels d'une lave) sur l'émissivité. Tout cela porte à confusion les scientifiques qui incluent l'émissivité dans leurs modèles de mise en place de coulées de lave.

Dans l'ensemble, ces travaux démontrent le besoin d'avoir une méthode rigoureuse pour mesurer l'émissivité des verres (fondus) et minéraux aux températures réelles des laves dans une large gamme spectrale (SWIR–MIR–TIR) afin de réduire les incertitudes liées à ce paramètre et améliorer les estimations de la température par les techniques de télédétection.

L'étude se concentre principalement sur l'éruption d'Holuhraun en 2014–2015 (Bardarbunga, Islande) car elle représente une cible idéale : longue activité, large zone couverte sans de forte variation de topographie, composition uniforme de la coulée, et nombreuses études qui ont travaillé avec plusieurs instruments de télédétection pour étudier la température de la coulée. Ces contributions substantielles permettent d'avoir un bagage important afin de comparer mesures de laboratoire et de terrain.

7.2.2. Méthodes

L'émissivité spectrale de 10 échantillons magmatiques, incluant quatre basaltes *lato sensu* (au cœur de cette étude), trois minéraux basaltiques, et trois compositions tholéiitiques, a été mesurée. Pour ce faire, les échantillons ont été préparés pour faire 1.5–3.0 mm × 10 mm diamètre avec une face polie (1 µm) et leurs propriétés radiatives ont été mesurées en utilisant les méthodes directe et indirecte (via les lois de Kirchhoff). Avec la méthode directe, l'émissivité spectrale (ε_λ) est définie comme étant le ratio entre la radiance normale spectrale de l'échantillon (L_λ) et celle d'un corps noir (L_λ^0), dans les mêmes conditions thermique et optique (Stefan 1879 ; Boltzmann 1884) :

$$\varepsilon_\lambda(\sigma,T,\theta)=\frac{L_\lambda(\sigma,T,\theta)}{L_\lambda^0(\sigma,T,\theta)}$$

L'émissivité est obtenue de façon *in situ* à températures magmatiques (échelonné de 50–100 K jusqu'à 1800 K) sur une large gamme spectrale (350–8000 cm^{-1} ; 1.25–28.6 µm), à l'aide d'un appareil IR avec chauffage sans contact développé au laboratoire CEMTHI (De Sousa Meneses et al. 2015). La mesure de température est mesurée *in situ* en utilisant la pyrométrie au point de Christiansen. Pour éclaircir le comportement radiatif complexe de ces échantillons en fonction de la température, des analyses systématiques de la texture, de la composition, de la structure, et du comportement thermique de ceux-ci ont été effectuées avant et après chaque expérience IR à l'aide des instruments analytiques suivants : MEB, Microsonde, spectroscopie Raman, Diffraction RX, MET, et DSC.

7.2.3. Résultats

Après avoir caractérisé la pétrographie des échantillons, leur propriétés radiatives entre la méthode directe à basse température et indirecte ont été démontrées comme correspondantes. La Figure 7-19 montre l'évolution de l'émissivité spectrale avec la température pour le basalte Bardarbunga-glass et Bardarbunga-Natural. De façon générale dans la zone « opaque », l'intensité des bandes Reststrahlen augmentent et deviennent moins complexe (une seule absorption au lieu de plusieurs) avec l'augmentation de la température. Tandis que l'émissivité diminue continuellement dans la région « multiphonon » et « électronique » et l'échantillon devient semi-transparent. Néanmoins, entre 1020 et 1097 K, un phénomène d'opacification est observé (augmentation brusque de l'émissivité). A plus haute température, la formation d'oxydes riche en fer et de clinopyroxènes altèrent puis domine la réponse radiative du verre silicaté car ils ont des propriétés optiques différentes. Ces microcristaux ont été identifié à l'aide des techniques analytiques complémentaires (Spectroscopie Raman, MET, MEB, DSC, et diffraction RX). Au-delà de 1560 K, l'émissivité du verre fondu est atteinte et se caractérise par une large bande Reststrahlen dans la région opaque, un front de transmission bien visible et une valeur d'émissivité stable à 0.85 aux grands nombres d'ondes.

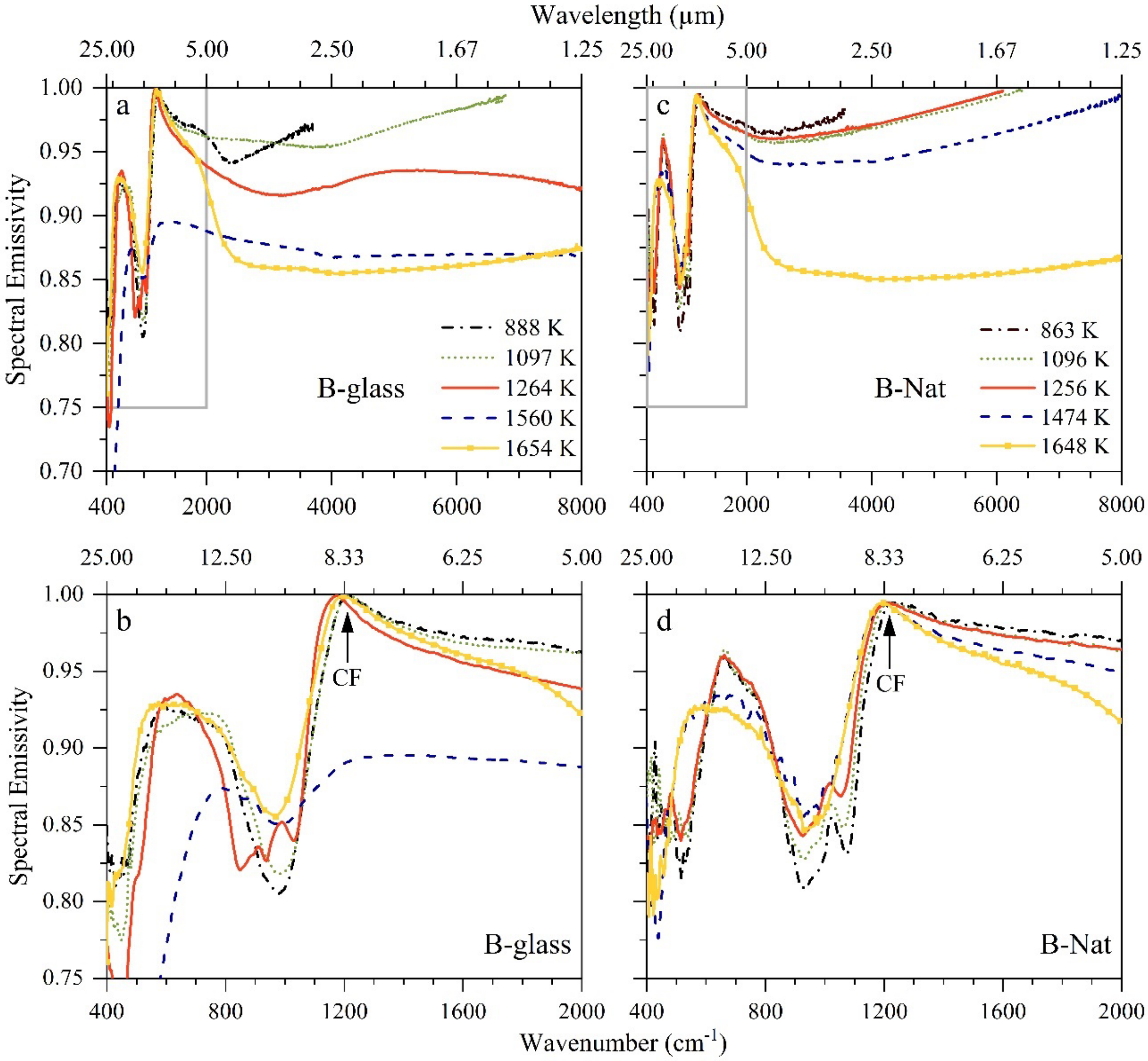

Figure 7-19: Evolution de l'émissivité spectrale en fonction de la température pour Bardarbunga-glass (a,b) et Bardarbunga-Nat (c,d) (épaisseur : 1.5 mm ; et 3.0 mm à 1650 K). a) et c) couvrent l'ensemble de la gamme spectrale étudiée (TIR, MIR, SWIR), tandis que b) et d) se concentre sur le TIR. CF : point de Christiansen.

Le comportement radiatif de l'échantillon naturel se distingue par la présence de clinopyroxène, de plagioclase et d'oxyde riche en fer dans sa structure initiale. L'échantillon naturel se comporte dès lors comme un basalte déjà opacifié à température ambiante. Le reste de son évolution est similaire à l'échantillon du verre. Les mêmes évolutions thermiques de l'émissivité ont été acquises pour les basaltes de MORB et Fasnia afin d'étudier l'effet de la composition. Le premier basalte, ayant une composition similaire, montre la même évolution avec un léger décalage de température pour le phénomène d'opacification, tandis que le deuxième basalte est déjà opacifié à température ambiante.

Etant donné qu'une lave est un mélange de verre solide et fondu avec des cristaux, ces derniers ont également leur importance sur les propriétés radiatives des laves. Ainsi, les relations ε–T pour trois différents minéraux basaltiques (labradorite, augite, and hématite) ont été étudiées. Les résultats démontrent que leurs comportements radiatifs sont très différents pour chacun d'entre eux et dépendent de la température, du nombre d'onde, de la structure et la composition. La position des bandes d'absorption dépend directement de la structure interne du minéral et de la nature de la liaison. Avec l'augmentation de la température, les minéraux atteignent la fusion et les bandes Reststrahlen se simplifient. La dépendance au nombre d'onde est très variable avec des valeurs d'émissivité qui varient entre 0.1 dans le SWIR et 0.8 dans le TIR.

7.2.4. Discussion

Le comportement de l'émissivité en fonction de la température est relié à l'augmentation de l'amortissement des vibrations de la structure du verre, ce qui induit une augmentation de l'anharmonicité et une réorganisation locale de la structure. Le phénomène d'opacification est thermiquement activé et trouve son origine dans la formation (nucléation + cristallisation), la réorganisation et la ségrégation des oxydes riche en fer (~2 mm ; type magnésioferrite) à la surface de l'échantillon. Ces oxydes, par leur nature optique différente (conducteur électrique), modifient drastiquement les propriétés radiatives de l'échantillon qui se traduisent par la combinaison des comportements d'absorption et diffusion des oxydes plutôt que de l'émission du verre. L'opacification dans les roches magmatiques est contrôlée par la teneur de FeO et le degré de polymérisation de la structure silicaté. Au-delà de ces températures, l'évolution de l'émissivité indique la progression de la fusion de l'échantillon provoquant la désintégration de la structure silicatée et des oxydes et l'augmentation des mouvements vibrationnel du système.

En utilisant les relations ε–T des minéraux, les propriétés radiatives de l'échantillon naturel ont été modélisées en utilisant une simple régression linéaire à deux températures auxquels la texture de l'échantillon correspond à l'évent (1640 K) et au front de coulée (864 K). Bien que cette méthode simplifiée donne des résultats satisfaisants à haute température et des teneurs de cristaux jusqu'à 40%, elle ne fonctionne pas à basse température et des teneurs de cristaux élevées (>40%). Cet effet est limité aux régions MIR et SWIR (TIR est peu affecté), différence que nous avons prouvée (avec une étude de cas au Piton de la Fournaise) ne pas être lié à la teneur en cristaux. Nous avançons dès lors que la nature (opaque vs transparent) des minéraux est à l'origine de cette différence.

En combinant l'ensemble de nos observations sur les propriétés radiatives à l'amélioration de l'acquisition des données de télédétection, un nouveau modèle pour déterminer la température a été développé. Le modèle préexistant d'Aufaristama et al. (2018) prend en compte à présent l'évolution thermo-rhéologique de l'émissivité (ε–T) plutôt qu'une valeur unique d'émissivité (0.97). En étudiant la coulée de lave de 2014–2015 Holuhraun avec ce modèle, nous avons obtenus des données de température plus précise (amélioration de ~44 degrés en moyenne ; Figure 7-20). La valeur d'émissivité 0.97 paraît comme une exagération des réelles valeurs d'émissivité, et donc comme une exagération des valeurs de température. Si la température réelle de la coulée de lave est en moyenne plus froide, cela a pour conséquence une coulée qui prend plus de temps pour dissiper sa chaleur de manière radiative et donc des distances atteintes plus grandes. Ainsi, nous démontrons que la coulée peut comporter un risque plus grand pour les zones habitées qu'initialement prévu.

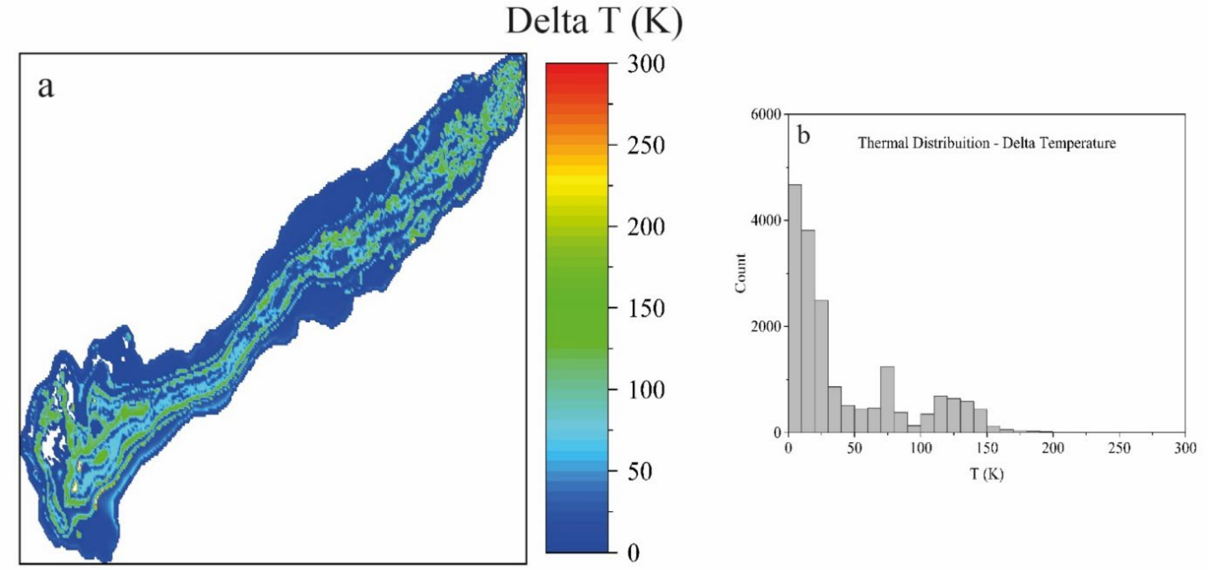

Figure 7-20: a) Différence de température entre le modèle d'Aufaristama et le nouveau modèle raffiné de cette étude. b) Distribution de la différence de température entre ces mêmes modèles.

7.2.5. Conclusion

La température est un paramètre qui contrôle la rhéologie et l'épanchement d'une lave. Les techniques de télédétection sont des outils indispensables pour mesurer les anomalies thermiques associées aux coulées de lave actives et pour évaluer leurs risques sur l'environnement (cultures, réserves naturelles, construction, perte humaine ou animale). Néanmoins, elles dépendent d'un paramètre peu connu qui contrôle la mesure de température et qui est dénommé émissivité spectrale (ε). De nos jours, l'émissivité des roches magmatiques a été principalement étudiée à température ambiante à des buts d'identification. Les rares travaux sur l'exploration de la relation entre l'émissivité et la température sur différents matériaux géologiques ont été poursuivis sur des gammes spectrale et de température réduites.

Dès lors, l'objectif principal de cette étude était de fournir une compréhension complète des propriétés radiatives des basaltes naturels secs et riches en cristaux à travers la mesure de l'émissivité spectrale sur une large gamme de température (293–1800 K) et de nombre d'onde (350–8000 cm^{-1} ; TIR–MIR–SWIR). Pour déterminer les relations ε–T, une méthodologie multidisciplinaire basée sur des analyses pétrologiques, texturales, chimiques, texturales et thermiques a été appliquée avant et après chaque expérience IR.

Les résultats obtenus sont importants pour la communauté de télédétection. Premièrement, d'après nos connaissances, c'est la première étude systématique sur l'émissivité des verres naturels homogènes et contenant des cristaux ainsi que l'émissivité des cristaux de ces basaltes naturels. Deuxièmement, cette étude prouve que l'émissivité spectrale pour une composition magmatique donnée ne peut pas être considérée comme constante ; elle est sensible à tout changement en température, composition, longueur d'onde, et dépend fondamentalement de la composition, la microstructure et la texture de l'échantillon. Les résultats montrent que la relation ε–T est complexe ; avec l'augmentation de la température l'anharmonicité du verre augmente et permet la mobilité des ions. Cela conduit à une réorganisation micro structurelle suivie d'une formation et d'une croissance de cristaux riches en Fe et Mg, qui se conclue par une opacification du comportement optique de l'échantillon. Ce phénomène est naturel dans les roches magmatiques avec un taux de FeO élevé en association avec le degré de polymérisation de la structure silicaté. La température de cristallisation, de ségrégation et l'apparition de ce phénomène sont très distinctes pour chaque composition basaltique étudiée.

Cette étude montre aussi que l'émissivité spectrale d'un basalte naturel (cristallisé) diffère légèrement de son équivalent vitreux. Dès lors qu'un échantillon naturel est le mélange en proportion différentes de verre fondus ou non avec des cristaux et des vésicules, chaque composant exhibe des propriétés radiatives uniques qui vont différer en fonction de la composition, la taille, la teneur et la distribution de la phase en question. Dans chaque composition explorée, l'émissivité spectrale augmente dans la région TIR et diminue dans les régions MIR et SWIR avec l'augmentation de la température, contrastant avec les conclusions générales trouvées dans la littérature. Enfin, l'objectif ultime de ce travail était d'améliorer la détermination de la température à partir de données réelles de terrain par télédétection. Par conséquent, les données de laboratoire d'émissivité ont été utilisées pour développer un modèle basé sur le travail d'Aufaristama et al. (2018) et améliorer les valeurs de température pour la coulée de lave de Holuhraun de 44 degrés en moyenne. Une telle variation de température peut impliquer de grandes conséquences sur les modèles de mise en place de coulée de lave, avec les informations rhéologiques appropriées, et ainsi améliorer l'évaluation des risques associés à un système volcanique. Malgré le fait que les mesures d'émissivité spectrale sont complexes, elles sont néanmoins nécessaires pour la recherche en volcanologie.

Perspectives futures

Les résultats probants de cette étude sur les roches basaltiques permettent d'ouvrir les portes pour de nouvelles considérations qui peuvent être conduites dans le futur et brièvement décrites ici: 1) Etudier la relation ε–T pour d'autres compositions magmatiques : andésite, dacite, rhyolite. 2) Développer les mesures d'émissivité avec un environnement contrôlé afin d'empêcher la formation des oxides de Fer discuté dans ce travail. 3) Explorer l'effet des volatiles sur les propriétés radiatives des roches magmatiques. Pour ce faire, le projet Equipex Planex porté par l'ISTO-CEMHTI sont en train de développer un instrument capable de mesurer les propriétés radiatives des roches (contenant H_2O et CO_2) à haute température et haute pression. Les résultats préliminaires permettraient d'évaluer le budget thermique d'une chambre magmatique par exemple. 4) Approfondir les connaissances en physique des matériaux hétérogènes naturels. Les magmas sont à cet égard, des objets complexes sur lesquels il mérite de se pencher afin de mieux comprendre leur comportement émissif. Pour se faire, leurs fonctions optiques peuvent être modélisées et les analyses texturales et structurale peuvent être approfondies avec l'analyse par des techniques de laboratoire (MET, micro-tomographie 3D) ou méthodes numériques (ray tracing, ou Monte Carlo symbolique). 5) Etudier l'impact de l'émissivité sur la modélisation des coulées de lave afin d'améliorer la précision sur l'étendue de leurs épanchements. Il faudrait implémenter les modèles thermo-rhéologiques des coulées de lave (exemple : PyFlowGo) avec des équations à développer qui reprennent les relations entre l'émissivité et la température, l'évolution de la texture et la composition avec le temps. 6) Explorer les propriétés radiatives des exoplanètes. Avec la mise en place du télescope James Webb, des données d'émissions infrarouges provenant d'autres mondes magmatiques vont nous parvenir prochainement et devrons être analysés et interprétés. Avec pour objectif de trouver la vie sur une autre planète et de mieux comprendre la formation de notre Terre, les spectres d'émissivités de roches synthétiques et naturelles à haute température sont primordiaux.

7.3. Bibliography

Abtahi AA, Kahle AB, Abbott EA, et al (2002) Emissivity Changes in Basalt Cooling After Eruption From PU'U O'O, Kilauea, Hawaii. In: AGU Fall Meeting Abstracts. pp V71A-1263

Adams JB (1974) Visible and near-infrared diffuse reflectance spectra of pyroxenes as applied to remote sensing of solid objects in the solar system. J Geophys Res 79:4829–4836. https://doi.org/10.1029/JB079i032p04829

Alavipanah SK, Matinfar HR, Emam AR, et al (2010) Criteria of selecting satellite data for studying land resources. 21

Albert H, Costa F, Martí J (2015) Timing of Magmatic Processes and Unrest Associated with Mafic Historical Monogenetic Eruptions in Tenerife Island. J Petrol 56:1945–1966. https://doi.org/10.1093/petrology/egv058

Alemanno G, Maturilli A, D'Amore M, Helbert J (2021) A new laboratory emissivity and reflectance spectral library for the interpretation of Mars thermal infrared spectral data. Icarus 368:114622. https://doi.org/10.1016/j.icarus.2021.114622

Allred K (1998) Lava tube remelt by radiant heat and burning gasses. Int J Speleol 27:125–134. https://doi.org/10.5038/1827-806X.27.1.13

Alvez Rolim SB, Grondona A, Hackmann CL, Rocha C (2016) Thermal Infrared, Temperature Emissivity Separation, Temperature Retrieval, Emissivity Retrieval, TIR, TES. Am J Environ Eng 10

Andújar J, Costa F, Scaillet B (2013) Storage conditions and eruptive dynamics of central versus flank eruptions in volcanic islands: The case of Tenerife (Canary Islands, Spain). J Volcanol Geotherm Res 260:62–79. https://doi.org/10.1016/j.jvolgeores.2013.05.004

Andújar J, Martel C, Pichavant M, et al (2017) Structure of the Plumbing System at Tungurahua Volcano, Ecuador: Insights from Phase Equilibrium Experiments on July–August 2006 Eruption Products. J Petrol 58:1249–1278. https://doi.org/10.1093/petrology/egx054

Andújar J, Scaillet B (2012) Relationships between pre-eruptive conditions and eruptive styles of phonolite–trachyte magmas. Lithos 152:122–131. https://doi.org/10.1016/j.lithos.2012.05.009

Andújar J, Scaillet B, Pichavant M, Druitt TH (2015) Differentiation Conditions of a Basaltic Magma from Santorini, and its Bearing on the Production of Andesite in Arc Settings. J Petrol 56:765–794. https://doi.org/10.1093/petrology/egv016

Angel SM, Gomer NR, Sharma SK, McKay C (2012) Remote Raman Spectroscopy for Planetary Exploration: A Review. Appl Spectrosc 66:137–150. https://doi.org/10.1366/11-06535

Applegarth LJ, Tuffen H, James MR, Pinkerton H (2013) Degassing-driven crystallisation in basalts. Earth-Sci Rev 116:1–16. https://doi.org/10.1016/j.earscirev.2012.10.007

Arnold JA, Glotch TD, Plonka AM (2014) Mid-infrared optical constants of clinopyroxene and orthoclase derived from oriented single-crystal reflectance spectra. Am Mineral 99:1942–1955. https://doi.org/10.2138/am-2014-4828

Aronson JR, Bellotti LH, Eckroad SW, et al (1970) Infrared spectra and radiative thermal conductivity of minerals at high temperatures. J Geophys Res 75:3443–3456. https://doi.org/10.1029/JB075i017p03443

Aufaristama M, Hoskuldsson A, Jonsdottir I, et al (2019a) Thermal model of lava in Mt. Agung during December 2017 episodes derived from Integrated SENTINEL 2A and ASTER remote sensing datasets. IOP Conf Ser Earth Environ Sci 311:012016. https://doi.org/10.1088/1755-1315/311/1/012016

Aufaristama M, Hoskuldsson A, Jonsdottir I, et al (2018) New Insights for Detecting and Deriving Thermal Properties of Lava Flow Using Infrared Satellite during 2014–2015 Effusive Eruption at Holuhraun, Iceland. Remote Sens 10:151. https://doi.org/10.3390/rs10010151

Aufaristama M, Hoskuldsson A, Ulfarsson M, et al (2019b) The 2014–2015 Lava Flow Field at Holuhraun, Iceland: Using Airborne Hyperspectral Remote Sensing for Discriminating the Lava Surface. Remote Sens 11:476. https://doi.org/10.3390/rs11050476

Ayache J, Beaunier L, Pottu-Boumendil J, et al (2007) Guide de préparation des échantillons pour la microscopie électronique en transmission. Tome II, Tome II,. Publications de l'Université de Saint-Etienne

Baldridge AM, Hook SJ, Grove CI, Rivera G (2009) The ASTER spectral library version 2.0. Remote Sens Environ 113:711–715. https://doi.org/10.1016/j.rse.2008.11.007

Ball M, Pinkerton H (2006) Factors affecting the accuracy of thermal imaging cameras in volcanology. J Geophys Res Solid Earth 111:14. https://doi.org/10.1029/2005JB003829

Bas MJL, Maitre RWL, Streckeisen A, et al (1986) A Chemical Classification of Volcanic Rocks Based on the Total Alkali-Silica Diagram. J Petrol 27:745–750. https://doi.org/10.1093/petrology/27.3.745

Bellot-Gurlet L, Neff D, Réguer S, et al (2009) Raman Studies of Corrosion Layers Formed on Archaeological Irons in Various Media. J Nano Res 8:147–156. https://doi.org/10.4028/www.scientific.net/JNanoR.8.147

Berger G, Cathala A, Fabre S, et al (2019) Experimental exploration of volcanic rocks-atmosphere interaction under Venus surface conditions. Icarus 329:8–23. https://doi.org/10.1016/j.icarus.2019.03.033

Berlanga G, Acosta-Maeda TE, Sharma SK, et al (2019) Remote Raman spectroscopy of natural rocks. Appl Opt 58:8971. https://doi.org/10.1364/AO.58.008971

Bilotta G, Hérault A, Cappello A, et al (2016) GPUSPH: a Smoothed Particle Hydrodynamics model for the thermal and rheological evolution of lava flows. Geol Soc Lond Spec Publ 426:387–408. https://doi.org/10.1144/SP426.24

Biren J, Harris A, Tuffen H, et al (2020) Chemical, Textural and Thermal Analyses of Local Interactions Between Lava Flow and a Tree – Case Study From Pāhoa, Hawai'i. Front Earth Sci 8:233. https://doi.org/10.3389/feart.2020.00233

Blackett M (2017) An Overview of Infrared Remote Sensing of Volcanic Activity. J Imaging 3:13. https://doi.org/10.3390/jimaging3020013

Boltzmann L (1884) Ableitung des Stefan'schen Gesetzes, betreffend die Abhängigkeit der Wärmestrahlung von der Temperatur aus der electromagnetischen Lichttheorie. Ann Phys 258:291–294. https://doi.org/10.1002/andp.18842580616

Bonnefoy LE, Hamilton CW, Scheidt SP, et al (2019) Landscape evolution associated with the 2014–2015 Holuhraun eruption in Iceland. J Volcanol Geotherm Res 387:106652. https://doi.org/10.1016/j.jvolgeores.2019.07.019

Bonny E, Thordarson T, Wright R, et al (2018) The Volume of Lava Erupted During the 2014 to 2015 Eruption at Holuhraun, Iceland: A Comparison Between Satellite- and Ground-Based Measurements. J Geophys Res Solid Earth 123:5412–5426.

https://doi.org/10.1029/2017JB015008

Bottger U, Helbert J, Maturilli A (2009) Raman Measurements of a Fine-Grained Labradorite Sample Heated to Typical Mercury Dayside Temperatures. 2

Bouvry B, Fernández Carrión AJ, Andújar J, et al (2017) Mediterranean basin basalts as potential materials for thermal energy storage in concentrated solar plants. Sol Energy Mater Sol Cells 171:50–59. https://doi.org/10.1016/j.solmat.2017.06.030

Bowey JE, Lee C, Tucker C, et al (2001) Temperature effects on the 15-85 m spectra of olivines and pyroxenes. Mon Not R Astron Soc 325:886–896. https://doi.org/10.1046/j.1365-8711.2001.04523.x

Brun J-F (2003) Mesure et analyse de l'émittance spectrale d'oxydes diélectriques à haute température. Une approche des phénomènes préfusionnels. Physique, Université d'Orléans

Buettner KJK, Kern CD (1965) The determination of infrared emissivities of terrestrial surfaces. J Geophys Res 70:1329–1337. https://doi.org/10.1029/JZ070i006p01329

Burgi P-Y, Caillet M, Haefeli S (2002) FIeld temperature measurements at Erta'Ale Lava Lake, Ethiopia. Bull Volcanol 64:472 485. https://doi.org/10.1007/s00445-002-0224-3

Burkhard DJM (2001) Crystallization and Oxidation of Kilauea Basalt Glass: Processes during Reheating Experiments. J Petrol 42:507–527. https://doi.org/10.1093/petrology/42.3.507

Buzgar N, Apopei AI, Diaconu V, Buzatu A (2013) The composition and source of the raw material of two stone axes of Late Bronze Age from Neamț County (Romania) - A Raman study. 59:5–22

Byrnes JM, Ramsey MS, King PL, Lee RJ (2007) Thermal infrared reflectance and emission spectroscopy of quartzofeldspathic glasses. Geophys Res Lett 34:. https://doi.org/10.1029/2006GL027893

Cáceres F, Scheu B, Hess K-U, et al (2021) From melt to crystals: The effects of cooling on Fe Ti oxide nanolites crystallisation and melt polymerisation at oxidising conditions. Chem Geol 563:120057. https://doi.org/10.1016/j.chemgeo.2021.120057

Calvari S, Giudicepietro F, Di Traglia F, et al (2021) Variable Magnitude and Intensity of Strombolian Explosions: Focus on the Eruptive Processes for a First Classification Scheme for Stromboli Volcano (Italy). Remote Sens 13:944. https://doi.org/10.3390/rs13050944

Calvari S, Pinkerton H (1999) Lava tube morphology on Etna and evidence for lava flow emplacement mechanisms. J Volcanol Geotherm Res 90:263–280. https://doi.org/10.1016/S0377-0273(99)00024-4

Calvari S, Spampinato L, Lodato L, et al (2005) Chronology and complex volcanic processes during the 2002-2003 flank eruption at Stromboli volcano (Italy) reconstructed from direct observations and surveys with a handheld thermal camera. J Geophys Res Solid Earth 110:. https://doi.org/10.1029/2004JB003129

Carracedo JC, Troll V, Day J, et al (2022) The 2021 eruption of the Cumbre Vieja Volcanic Ridge on La Palma, Canary Islands. Physical Sciences and Mathematics

Chen Y, Zou C, Mastalerz M, et al (2015) Applications of Micro-Fourier Transform Infrared Spectroscopy (FTIR) in the Geological Sciences-A Review. Int J Mol Sci 16:30223–30250. https://doi.org/10.3390/ijms161226227

Chevrel MO, Favalli M, Villeneuve N, et al (2021) Lava flow hazard map of Piton de la Fournaise volcano. Nat Hazards Earth Syst Sci 21:2355–2377. https://doi.org/10.5194/nhess-21-2355-2021

Chevrel MO, Labroquère J, Harris AJL, Rowland SK (2018) PyFLOWGO: An open-source platform for simulation of channelized lava thermo-rheological properties. Comput Geosci 111:167–180. https://doi.org/10.1016/j.cageo.2017.11.009

Chevrel MO, Pinkerton H, Harris AJL (2019) Measuring the viscosity of lava in the field: A review. Earth-Sci Rev 196:102852. https://doi.org/10.1016/j.earscirev.2019.04.024

Christensen PR, Howard D, Lane M, et al (2000) A thermal emission spectral library of rock-forming minerals. J Geophys Res 105:9735–9739. https://doi.org/10.1029/1998JE000624

Clocchiatti R, Havette Ledebt A, Nativel P (1979) Relations pétrogénétiques entre les basaltes transitionnels et les océanites du Piton de la Fournaise (île de la Réunion, océan Indien) à partir de la composition chimique des inclusions vitreuses des olivines et des spinelles. Bull Minéralogie 102:511–525. https://doi.org/10.3406/bulmi.1979.7300

Colliex C, Manoubi T, Ortiz C (1991) Electron-energy-loss-spectroscopy near-edge fine structures in the iron-oxygen system. Phys Rev B 44:11402–11411. https://doi.org/10.1103/PhysRevB.44.11402

Colomban P, Prinsloo LC (2009) Optical spectroscopy of silicates and glasses. In: Yarwood J, Douthwaite R, Duckett S (eds) Spectroscopic Properties of Inorganic and Organometallic Compounds. Royal Society of Chemistry, Cambridge, pp 128–149

Conroy CJ, Lev E (2021) A discontinuous Galerkin finite-element model for fast channelized lava flows v1.0. Geosci Model Dev 23

Cook GB, Cooper RF, Wu T (1990) Chemical diffusion and crystalline nucleation during oxidation of ferrous iron-bearing magnesium aluminosilicate glass. J Non-Cryst Solids 120:207–222. https://doi.org/10.1016/0022-3093(90)90205-Z

Cooper BL, Salisbury JW, Killen RM, Potter AE (2002) Midinfrared spectral features of rocks and their powders. J Geophys Res 107:5017. https://doi.org/10.1029/2000JE001462

Coppola D, Barsotti S, Cigolini C, et al (2019) Monitoring the time-averaged discharge rates, volumes and emplacement style of large lava flows by using MIROVA system: the case of the 2014-2015 eruption at Holuhraun (Iceland). Ann Geophys 61:10. https://doi.org/10.4401/ag-7749

Crisp J, Kahle AB, Abbott EA (1990) Thermal infrared spectral character of Hawaiian basaltic glasses. J Geophys Res 95:21657–21669. https://doi.org/10.1029/JB095iB13p21657

Cui J, Yan B, Dong X, et al (2015) Temperature and emissivity separation and mineral mapping based on airborne TASI hyperspectral thermal infrared data. Int J Appl Earth Obs Geoinformation 40:19–28. https://doi.org/10.1016/j.jag.2015.03.014

Dash P, Göttsche F-M, Olesen F-S, Fischer H (2002) Land surface temperature and emissivity estimation from passive sensor data: Theory and practice-current trends. Int J Remote Sens 23:2563–2594. https://doi.org/10.1080/01431160110115041

Davies AG, Gunapala S, Soibel A, et al (2017) A novel technology for measuring the eruption temperature of silicate lavas with remote sensing: Application to Io and other planets. J Volcanol Geotherm Res 343:1–16. https://doi.org/10.1016/j.jvolgeores.2017.04.016

Davies AG, Keszthelyi LP, McEwen AS (2016) Determination of eruption temperature of Io's lavas using lava tube skylights. Icarus 278:266–278. https://doi.org/10.1016/j.icarus.2016.06.003

de Faria DLA, Lopes FN (2007) Heated goethite and natural hematite: Can Raman spectroscopy be used to differentiate them? Vib Spectrosc 45:117–121. https://doi.org/10.1016/j.vibspec.2007.07.003

De Sousa Meneses D, Brun J-F, Echegut P, Simon P (2004) Contribution of Semi-Quantum

Dielectric Function Models to the Analysis of Infrared Spectra. Appl Spectrosc 58:969–974. https://doi.org/10.1366/0003702041655467

De Sousa Meneses D, Eckes M, del Campo L, Echegut P (2014) Phase transformations of crystalline SiO2 versus dynamic disorder between room temperature and liquid state. J Phys Condens Matter 26:255402. https://doi.org/10.1088/0953-8984/26/25/255402

De Sousa Meneses D, Malki M, Echegut P (2006) Optical and structural properties of calcium silicate glasses. J Non-Cryst Solids 352:5301–5308. https://doi.org/10.1016/j.jnoncrysol.2006.08.022

De Sousa Meneses D, Melin P, del Campo L, et al (2015) Apparatus for measuring the emittance of materials from far infrared to visible wavelengths in extreme conditions of temperature. Infrared Phys Technol 69:96–101. https://doi.org/10.1016/j.infrared.2015.01.011

Deer WA, Howie RA, Zussman J (eds) (2004) Framework silicates: silica minerals, feldspathoids and the zeolites, 2. ed. Geological Society, London

del Campo L, De Sousa Meneses D, Blin A, et al (2011) High-Temperature Radiative Properties of an Yttria-Stabilized Hafnia Ceramic: High Temperature Radiative Properties of an YSH Ceramic. J Am Ceram Soc 94:1859–1864. https://doi.org/10.1111/j.1551-2916.2010.04336.x

del Campo L, Pérez-Sáez RB, Tello MJ (2008) Iron oxidation kinetics study by using infrared spectral emissivity measurements below 570°C. Corros Sci 50:194–199. https://doi.org/10.1016/j.corsci.2007.05.029

Denton JS, Tuffen H, Gilbert JS, Odling N (2009) The hydration and alteration of perlite and rhyolite. J Geol Soc 166:895–904. https://doi.org/10.1144/0016-76492008-007

Di Carlo I (2006) Experimental Crystallization of a High-K Arc Basalt: the Golden Pumice, Stromboli Volcano (Italy). J Petrol 47:1317–1343. https://doi.org/10.1093/petrology/egl011

Di Genova D, Caracciolo A, Kolzenburg S (2018) Measuring the degree of “nanotilization” of volcanic glasses: Understanding syn-eruptive processes recorded in melt inclusions. Lithos 318–319:209–218. https://doi.org/10.1016/j.lithos.2018.08.011

Di Genova D, Kolzenburg S, Vona A, et al (2016) Raman spectra of Martian glass analogues: A tool to approximate their chemical composition: Raman Spectra of Martian Glass Analogues. J Geophys Res Planets 121:740–752. https://doi.org/10.1002/2016JE005010

Di Genova D, Morgavi D, Hess K-U, et al (2015) Approximate chemical analysis of volcanic glasses using Raman spectroscopy. J Raman Spectrosc 46:1235–1244. https://doi.org/10.1002/jrs.4751

Di Genova D, Sicola S, Romano C, et al (2017a) Effect of iron and nanolites on Raman spectra of volcanic glasses: A reassessment of existing strategies to estimate the water content. Chem Geol 475:76–86. https://doi.org/10.1016/j.chemgeo.2017.10.035

Di Genova D, Vasseur J, Hess K-U, et al (2017b) Effect of oxygen fugacity on the glass transition, viscosity and structure of silica- and iron-rich magmatic melts. J Non-Cryst Solids 470:78–85. https://doi.org/10.1016/j.jnoncrysol.2017.05.013

Di Genova D, Zandona A, Deubener J (2020) Unravelling the effect of nano-heterogeneity on the viscosity of silicate melts: Implications for glass manufacturing and volcanic eruptions. J Non-Cryst Solids 545:120248. https://doi.org/10.1016/j.jnoncrysol.2020.120248

D’Ippolito V, Andreozzi GB, Bersani D, Lottici PP (2015) Raman fingerprint of chromate, aluminate and ferrite spinels. J Raman Spectrosc 46:1255–1264.

https://doi.org/10.1002/jrs.4764

Donaldson Hanna KL, Cheek LC, Pieters CM, et al (2014) Global assessment of pure crystalline plagioclase across the Moon and implications for the evolution of the primary crust: Pure Plagioclase on the Moon. J Geophys Res Planets 119:1516–1545. https://doi.org/10.1002/2013JE004476

Donaldson Hanna KL, Thomas IR, Bowles NE, et al (2012) Laboratory emissivity measurements of the plagioclase solid solution series under varying environmental conditions. J Geophys Res Planets 117:n/a-n/a. https://doi.org/10.1029/2012JE004184

Dozier J (1981) A method for satellite identification of surface temperature fields of subpixel resolution. Remote Sens Environ 11:221–229. https://doi.org/10.1016/0034-4257(81)90021-3

Eckes M, Gibert B, De Sousa Meneses D, et al (2013) High-temperature infrared properties of forsterite. Phys Chem Miner 40:287–298. https://doi.org/10.1007/s00269-013-0570-z

Edwards CS, Christensen PR (2013) Microscopic emission and reflectance thermal infrared spectroscopy: instrumentation for quantitative in situ mineralogy of complex planetary surfaces. Appl Opt 52:2200. https://doi.org/10.1364/AO.52.002200

Egerton RF (2011) Electron Energy-Loss Spectroscopy in the Electron Microscope. Springer US, Boston, MA

Farrand WH, Wright SP, Rogers AD, Glotch TD (2016) Basaltic glass formed from hydrovolcanism and impact processes: Characterization and clues for detection of mode of origin from VNIR through MWIR reflectance and emission spectroscopy. Icarus 275:16–28. https://doi.org/10.1016/j.icarus.2016.03.027

Ferrari S, Nestola F, Massironi M, et al (2014) In-situ high-temperature emissivity spectra and thermal expansion of C2/c pyroxenes: Implications for the surface of Mercury. Am Mineral 99:786–792. https://doi.org/10.2138/am.2014.4698

Freeman JJ, Wang A, Kuebler KE, et al (2008) Characterization of Natural Feldspars by Raman Spectroscopy for Future Planetary Exploration. Can Mineral 46:1477–1500. https://doi.org/10.3749/canmin.46.6.1477

Galtier M, Roger M, André F, Delmas A (2017) A symbolic approach for the identification of radiative properties. J Quant Spectrosc Radiat Transf 196:130–141. https://doi.org/10.1016/j.jqsrt.2017.03.026

Ganci G (2012) An emergent strategy for volcano hazard assessment: From thermal satellite monitoring to lava flow modeling. Remote Sens Environ 11

Garel F, Kaminski É, Tait S, Limare A (2016) A fluid dynamics perspective on the interpretation of the surface thermal signal of lava flows. Geol Soc Lond Spec Publ 426:243–256. https://doi.org/10.1144/SP426.6

Geiger H, Mattsson T, Deegan FM, et al (2016) Magma plumbing for the 2014-2015 Holuhraun eruption, Iceland: Magma Plumbing for Holuhraun. Geochem Geophys Geosystems 17:2953–2968. https://doi.org/10.1002/2016GC006317

Gillespie A, Rokugawa S, Matsunaga T, et al (1998) A temperature and emissivity separation algorithm for Advanced Spaceborne Thermal Emission and Reflection Radiometer (ASTER) images. IEEE Trans Geosci Remote Sens 36:1113–1126. https://doi.org/10.1109/36.700995

Gilmore M, Treiman A, Helbert J, Smrekar S (2017) Venus Surface Composition Constrained by Observation and Experiment. Space Sci Rev 212:1511–1540.

https://doi.org/10.1007/s11214-017-0370-8

Giordano D, Russell JK, González-García D, et al (2020) Raman Spectroscopy from Laboratory and Proximal to Remote Sensing: A Tool for the Volcanological Sciences. Remote Sens 12:805. https://doi.org/10.3390/rs12050805

Gíslason SR, Stefánsdóttir G, Pfeffer MA, et al (2015) Environmental pressure from the 2014–15 eruption of Bárðarbunga volcano, Iceland. Geochem Perspect Lett 1:84–93. https://doi.org/10.7185/geochemlet.1509

Giuliani L, Iezzi G, Hippeli T, et al (2020) The Onset and Solidification Path of a Basaltic Melt by in situ Differential Scanning Calorimetry (DSC) and ex situ Investigations. Front Earth Sci 8:337. https://doi.org/10.3389/feart.2020.00337

Glotch TD, Morris RV, Christensen PR, Sharp TG (2004) Effect of precursor mineralogy on the thermal infrared emission spectra of hematite: Application to Martian hematite mineralization. J Geophys Res 109:E07003. https://doi.org/10.1029/2003JE002224

Golla-Schindler U, Benner G, Putnis A (2003) Laterally resolved EELS for ELNES mapping of the Fe L2,3- and O K-edge. Ultramicroscopy 96:573–582. https://doi.org/10.1016/S0304-3991(03)00118-9

Golla-Schindler U, Hinrichs R, Bomati-Miguel O, Putnis A (2006) Determination of the oxidation state for iron oxide minerals by energy-filtering TEM. Micron 37:473–477. https://doi.org/10.1016/j.micron.2005.11.002

Gualda GAR, Ghiorso MS (2015) MELTS_Excel: AMicrosoft Excel-based MELTS interface for research and teaching of magma properties and evolution. Geochem Geophys Geosystems 16:315–324. https://doi.org/10.1002/2014GC005545

Gudmundsson MT, Jónsdóttir K, Hooper A, et al (2016) Gradual caldera collapse at Bárdarbunga volcano, Iceland, regulated by lateral magma outflow. Science 353:aaf8988. https://doi.org/10.1126/science.aaf8988

Halldórsson SA, Bali E, Hartley ME, et al (2018) Petrology and geochemistry of the 2014–2015 Holuhraun eruption, central Iceland: compositional and mineralogical characteristics, temporal variability and magma storage. Contrib Mineral Petrol 173:64. https://doi.org/10.1007/s00410-018-1487-9

Hamilton VE (2000) Thermal infrared emission spectroscopy of the pyroxene mineral series. J Geophys Res Planets 105:9701–9716. https://doi.org/10.1029/1999JE001112

Hamilton VE (2010) Thermal infrared (vibrational) spectroscopy of Mg–Fe olivines: A review and applications to determining the composition of planetary surfaces. Geochemistry 70:7–33. https://doi.org/10.1016/j.chemer.2009.12.005

Hanna KLD, Cheek LC, Pieters CM, et al (2014) Global assessment of pure crystalline plagioclase across the Moon and implications for the evolution of the primary crust. J Geophys Res 30. https://doi.org/10.1002/2013JE004476

Harris A (2013) Thermal remote sensing of active volcanoes: a user's manual. Cambridge Univ. Press, Cambridge

Harris A, Bailey J, Calvari S, Dehn J (2005) Heat loss measured at a lava channel and its implications for down-channel cooling and rheology. In: Kinematics and dynamics of lava flows. Geological Society of America, pp 125–146

Harris AJL, Blake S, Rothery DA, Stevens NF (1997) A chronology of the 1991 to 1993 Mount Etna eruption using advanced very high resolution radiometer data: Implications for real-time thermal volcano monitoring. J Geophys Res Solid Earth 102:7985–8003.

https://doi.org/10.1029/96JB03388

Harris AJL, De Groeve T, Garel F, Carn SA (2016) Detecting, modelling and responding to effusive eruptions. Geological Society of London

Harris AJL, Thornber CR (1999) Complex effusive events at Kīlauea as documented by the GOES satellite and remote video cameras. Bull Volcanol 61:382–395. https://doi.org/10.1007/s004450050280

Hartley ME, Thordarson T (2013) The 1874-1876 volcano-tectonic episode at Askja, North Iceland: Lateral flow revisited: Askja 1874-1876 Volcano-Tectonic Episode. Geochem Geophys Geosystems 14:2286–2309. https://doi.org/10.1002/ggge.20151

Hecker C, der Meijde M van, van der Meer FD (2010) Thermal infrared spectroscopy on feldspars — Successes, limitations and their implications for remote sensing. Earth-Sci Rev 103:60–70. https://doi.org/10.1016/j.earscirev.2010.07.005

Heilbronner R, Barrett S (2014) Image Analysis in Earth Sciences: Microstructures and Textures of Earth Materials. Springer Berlin Heidelberg, Berlin, Heidelberg

Helbert J, Ferrari S, Maturilli A, et al (2015) Studying the surface composition of Venus in the near infrared. 2

Helbert J, Maturilli A (2009) The emissivity of a fine-grained labradorite sample at typical Mercury dayside temperatures. Earth Planet Sci Lett 285:347–354. https://doi.org/10.1016/j.epsl.2009.02.031

Helbert J, Maturilli A, Dyar MD, et al (2017) First set of laboratory Venus analog spectra for all atmospheric windows. 2

Helbert J, Nestola F, Ferrari S, et al (2013) Olivine thermal emissivity under extreme temperature ranges: Implication for Mercury surface. Earth Planet Sci Lett 371–372:252–257. https://doi.org/10.1016/j.epsl.2013.03.038

Huang E, Chen CH, Huang T, et al (2000) Raman spectroscopic characteristics of Mg-Fe-Ca pyroxenes. Am Mineral 85:473–479. https://doi.org/10.2138/am-2000-0408

Islam T, Hulley GC, Malakar NK, et al (2017) A Physics-Based Algorithm for the Simultaneous Retrieval of Land Surface Temperature and Emissivity From VIIRS Thermal Infrared Data. IEEE Trans Geosci Remote Sens 55:563–576. https://doi.org/10.1109/TGRS.2016.2611566

Izawa MRM, Cloutis EA, Rhind T, et al (2019) Spectral reflectance properties of magnetites: Implications for remote sensing. Icarus 319:525–539. https://doi.org/10.1016/j.icarus.2018.10.002

Jiménez-Mejías M, Andújar J, Scaillet B, Casillas R (2021) Experimental determination of H2O and CO2 solubilities of mafic alkaline magmas from Canary Islands. Comptes Rendus Géoscience 353:1–26. https://doi.org/10.5802/crgeos.84

Johannesson H, Saemundsson K (1998) Geological map of Iceland: 1:500 000 bedrock geology

Johnson J, Staid M, Titus T, Becker K (2006) Shocked plagioclase signatures in Thermal Emission Spectrometer data of Mars. Icarus 180:60–74. https://doi.org/10.1016/j.icarus.2005.08.010

Kaneko T, Yasuda A, Fujii T (2021) Simple empirical method for estimating lava-effusion rate using nighttime Himawari-8 1.6-µm infrared images. Earth Planets Space 73:37. https://doi.org/10.1186/s40623-021-01372-w

King PL, McMillan PF, Moore GM (2004) Chapter 4. Infrared spectroscopy of silicate glasses with application to natural systems. p 42

Klopprogge JT, Frost RL (2004) Infrared emission spectroscopy of clay minerals. In:

Theapplication of vibrational spectroscopy to clay minerals and layered double hydroxides, J. Theo Kloprogge. The Clay Mineral Society, Aurora, CO, pp 99–124

Koike C, Mutschke H, Suto H, et al (2006) Temperature effects on the mid-and far-infrared spectra of olivine particles. Astron Astrophys 449:583–596. https://doi.org/10.1051/0004-6361:20053256

Kolzenburg S, Giordano D, Giordano D, et al (2018) Equilibrium Viscosity and Disequilibrium Rheology of a high Magnesium Basalt from Piton De La Fournaise volcano, La Reunion, Indian Ocean, France. Ann Geophys 61:4. https://doi.org/10.4401/ag-7839

Kolzenburg S, Giordano D, Thordarson T, et al (2017) The rheological evolution of the 2014/2015 eruption at Holuhraun, central Iceland. Bull Volcanol 79:16. https://doi.org/10.1007/s00445-017-1128-6

Kraft MD, Michalski JR, Sharp TG (2003) Effects of pure silica coatings on thermal emission spectra of basaltic rocks: Considerations for Martian surface mineralogy. Geophys Res Lett 30:2288. https://doi.org/10.1029/2003GL018848

Lalla EA, Lopez-Reyes G, Sansano A, et al (2016) Raman-IR vibrational and XRD characterization of ancient and modern mineralogy from volcanic eruption in Tenerife Island: Implication for Mars. Geosci Front 7:673–681. https://doi.org/10.1016/j.gsf.2015.07.009

Lane MD, Morris RV, Mertzman SA, Christensen PR (2002) Evidence for platy hematite grains in Sinus Meridiani, Mars. J Geophys Res Planets 107:16. https://doi.org/10.1029/2001JE001832

Lavallee Y, Kendrick J, Wall R, et al (2015) Experimental constraints on the rheology and mechanical properties of lava erupted in the Holuhraun area during the 2014 rifting event at Bárðarbunga, Iceland. Geophys Res Abstr EGU General Assembly 2015:1

Lee RJ, King PL, Ramsey MS (2010) Spectral analysis of synthetic quartzofeldspathic glasses using laboratory thermal infrared spectroscopy. J Geophys Res 115:9. https://doi.org/10.1029/2009JB006672

Lee RJ, Ramsey MS, King PL (2013) Development of a new laboratory technique for high-temperature thermal emission spectroscopy of silicate melts. J Geophys Res Solid Earth 118:1968–1983. https://doi.org/10.1002/jgrb.50197

Li H (2018) Approche Structurale in situ des milieux fondus sous conditions extrêmes de Température et de Pression. Géologie, Université d'Orléans

Li H, Andujar J, Slodczyk A, et al (2021) Spectral Emissivity of Phonolite Lava at High Temperature. IEEE Trans Geosci Remote Sens 1–15. https://doi.org/10.1109/TGRS.2021.3104657

Li Z-L, Wu H, Wang N, et al (2013) Land surface emissivity retrieval from satellite data. Int J Remote Sens 34:3084–3127. https://doi.org/10.1080/01431161.2012.716540

Logan LM, Hunt GR, Salisbury JW, Balsamo SR (1973) Compositional implications of Christiansen frequency maximums for infrared remote sensing applications. J Geophys Res 78:4983–5003. https://doi.org/10.1029/JB078i023p04983

Lombardo V, Buongiorno MF (2006) Lava flow thermal analysis using three infrared bands of remote-sensing imagery: A study case from Mount Etna 2001 eruption. Remote Sens Environ 101:141–149. https://doi.org/10.1016/j.rse.2005.12.008

Lombardo V, Pick L, Spinetti C, et al (2020) Temperature and Emissivity Separation 'Draping' Algorithm Applied to Hyperspectral Infrared Data. Remote Sens 12:2046.

https://doi.org/10.3390/rs12122046

Lucey PG, Greenhagen BT, Song E, et al (2017) Space weathering effects in Diviner Lunar Radiometer multispectral infrared measurements of the lunar Christiansen Feature: Characteristics and mitigation. Icarus 283:343–351. https://doi.org/10.1016/j.icarus.2016.05.010

Lyon RJP (1965) Analysis of rocks by spectral infrared emission (8 to 25 microns). Econ Geol 60:715–736. https://doi.org/10.2113/gsecongeo.60.4.715

Lyon RJP (1964) Evaluation of infrared spectrophotometry for compositional analysis of lunar and planetary soils. Part II: rough and powdered sufaces. Proj No PSU-3943 290

Maanane Y, Roger M, Delmas A, et al (2020) Symbolic Monte Carlo method applied to the identification of radiative properties of a heterogeneous material. J Quant Spectrosc Radiat Transf 249:107019. https://doi.org/10.1016/j.jqsrt.2020.107019

Mader HM, Llewellin EW, Mueller SP (2013) The rheology of two-phase magmas: A review and analysis. J Volcanol Geotherm Res 257:135–158. https://doi.org/10.1016/j.jvolgeores.2013.02.014

Manylov MS, Gutnikov SI, Pokholok KV, et al (2013) Crystallization mechanism of basalt glass fibers in air. Mendeleev Commun 23:361–363. https://doi.org/10.1016/j.mencom.2013.11.021

Marshall D (1996) Ternplot: An excel spreadsheet for ternary diagrams. Comput Geosci 22:697–699. https://doi.org/10.1016/0098-3004(96)00012-X

Massimetti F, Coppola D, Laiolo M, et al (2020) Volcanic Hot-Spot Detection Using SENTINEL-2: A Comparison with MODIS–MIROVA Thermal Data Series. Remote Sens 12:33. https://doi.org/10.3390/rs12050820

McMillan P (1984) Structural studies of silicate glasses and melts—applications and limitations of Raman spectroscopy. Am Mineral 69:622–644

Minitti ME (2002) Effects of glass content and oxidation on the spectra of SNC-like basalts: Applications to Mars remote sensing. J Geophys Res 107:5030. https://doi.org/10.1029/2001JE001518

Minitti ME, Hamilton VE (2010) A search for basaltic-to-intermediate glasses on Mars: Assessing martian crustal mineralogy. Icarus 210:135–149. https://doi.org/10.1016/j.icarus.2010.06.028

Morimoto N (1988) Nomenclature of pyroxenes. Bull Minéralogie 111:535–550. https://doi.org/10.3406/bulmi.1988.8099

Mottl MJ, Davis EE, Fisher AT, Slack JF (eds) (1994) Proceedings of the Ocean Drilling Program, 139 Scientific Results. Ocean Drilling Program

Mouginis-Mark P, Rowland S, Francis P, et al (1991) Analysis of active volcanoes from the earth observing system. Remote Sens Environ 36:1–12. https://doi.org/10.1016/0034-4257(91)90027-4

Mujin M, Nakamura M, Matsumoto M (2021) In-situ FE-SEM observation of the growth behaviors of Fe particles at magmatic temperatures. J Cryst Growth 560–561:126043. https://doi.org/10.1016/j.jcrysgro.2021.126043

Mysen BO, Toplis MJ (2007) Structural behavior of Al3+ in peralkaline, metaluminous, and peraluminous silicate melts and glasses at ambient pressure. Am Mineral 92:933–946. https://doi.org/10.2138/am.2007.2334

Nair AM, Mathew G (2017) Geochemical modelling of terrestrial igneous rock compositions using laboratory thermal emission spectroscopy with an overview on its applications to Indian Mars Mission. Planet Space Sci 140:62–73. https://doi.org/10.1016/j.pss.2017.04.009

Neal CA, Brantley SR, Antolik L, et al (2019) The 2018 rift eruption and summit collapse of Kīlauea Volcano. Science 363:367–374. https://doi.org/10.1126/science.aav7046

Neuville DR, de Ligny D, Henderson GS (2014) Advances in Raman Spectroscopy Applied to Earth and Material Sciences. Rev Mineral Geochem 78:509–541. https://doi.org/10.2138/rmg.2013.78.13

Nuevo M, Sandford SA, Flynn GJ, Wirick S (2014) Mid-infrared study of stones from the Sutter's Mill meteorite. Meteorit Planet Sci 49:2017–2026. https://doi.org/10.1111/maps.12269

Óladóttir BA, Larsen G, Sigmarsson O (2011) Holocene volcanic activity at Grímsvötn, Bárdarbunga and Kverkfjöll subglacial centres beneath Vatnajökull, Iceland. Bull Volcanol 73:1187–1208. https://doi.org/10.1007/s00445-011-0461-4

Oppenheimer C (1993) Thermal distributions of hot volcanic surfaces constrained using three infrared bands of remote sensing data. Geophys Res Lett 20:431–434. https://doi.org/10.1029/93GL00500

Pedersen GBM, Höskuldsson A, Dürig T, et al (2017) Lava field evolution and emplacement dynamics of the 2014–2015 basaltic fissure eruption at Holuhraun, Iceland. J Volcanol Geotherm Res 340:155–169. https://doi.org/10.1016/j.jvolgeores.2017.02.027

Peterson DW, Tilling RI (1980) Transition of basaltic lava from pahoehoe to aa, Kilauea Volcano, Hawaii: Field observations and key factors. J Volcanol Geotherm Res 7:271–293. https://doi.org/10.1016/0377-0273(80)90033-5

Pichavant M (2011) De l'eau dans les magmas. Géosciences 13:24–29

Pichavant M, Brugier Y, Di Muro A (2016) Petrological and Experimental Constraints on the Evolution of Piton de la Fournaise Magmas. In: Bachelery P, Lenat J-F, Di Muro A, Michon L (eds) Active Volcanoes of the Southwest Indian Ocean: Piton de la Fournaise and Karthala. Springer, Berlin, Heidelberg, pp 171–184

Pinkerton H, Norton G (1995) Rheological properties of basaltic lavas at sub-liquidus temperatures: laboratory and field measurements on lavas from Mount Etna. J Volcanol Geotherm Res 68:307–323. https://doi.org/10.1016/0377-0273(95)00018-7

Pinkerton H, Stevenson RJ (1992) Methods of determining the rheological properties of magmas at sub-liquidus temperatures. J Volcanol Geotherm Res 53:47–66. https://doi.org/10.1016/0377-0273(92)90073-M

Pinkerton H, Wilson L (1994) Factors controlling the lengths of channel-fed lava flows. Bull Volcanol 56:108–120. https://doi.org/10.1007/BF00304106

Pisello A, Vetere FP, Bisolfati M, et al (2019) Retrieving magma composition from TIR spectra: implications for terrestrial planets investigations. Sci Rep 9:15200. https://doi.org/10.1038/s41598-019-51543-9

Preston LJ, Izawa MRM, Banerjee NR (2011) Infrared Spectroscopic Characterization of Organic Matter Associated with Microbial Bioalteration Textures in Basaltic Glass. Astrobiology 11:585–599. https://doi.org/10.1089/ast.2010.0604

Price JC (1983) Estimating surface temperatures from satellite thermal infrared data—A simple formulation for the atmospheric effect. Remote Sens Environ 13:353–361. https://doi.org/10.1016/0034-4257(83)90036-6

Prouteau G, Scaillet B, Pichavant M, Maury R (2001) Evidence for mantle metasomatism by hydrous silicic melts derived from subducted oceanic crust. Nature 410:197–200.

https://doi.org/10.1038/35065583

Putirka KD (2008) Thermometers and Barometers for Volcanic Systems. Rev Mineral Geochem 69:61–120. https://doi.org/10.2138/rmg.2008.69.3

Ramírez-González LM, Aufaristama M, Jónsdóttir I, et al (2019) Remote sensing of surface Hydrothermal Alteration, identification of Minerals and Thermal anomalies at Sveifluháls-Krýsuvík high-temperature Geothermal field, SW Iceland. IOP Conf Ser Earth Environ Sci 254:13. https://doi.org/10.1088/1755-1315/254/1/012005

Ramsey M, Chevrel MO, Coppola D, Harris AJL (2019) The influence of emissivity on the thermo-rheological modeling of the channelized lava flows at Tolbachik volcano. Ann Geophys 62:15. https://doi.org/10.4401/ag-8077

Ramsey MS, Christensen PR (1998) Mineral abundance determination: Quantitative deconvolution of thermal emission spectra. J Geophys Res Solid Earth 103:577–596. https://doi.org/10.1029/97JB02784

Ramsey MS, Harris AJL (2013) Volcanology 2020: How will thermal remote sensing of volcanic surface activity evolve over the next decade? J Volcanol Geotherm Res 249:217–233. https://doi.org/10.1016/j.jvolgeores.2012.05.011

Ramsey MS, Harris AJL, Crown DA (2016) What can thermal infrared remote sensing of terrestrial volcanoes tell us about processes past and present on Mars? J Volcanol Geotherm Res 311:198–216. https://doi.org/10.1016/j.jvolgeores.2016.01.012

Re G, Corsaro RA, D'Oriano C, Pompilio M (2021) Petrological monitoring of active volcanoes: A review of existing procedures to achieve best practices and operative protocols during eruptions. J Volcanol Geotherm Res 419:107365. https://doi.org/10.1016/j.jvolgeores.2021.107365

Reynolds HI, Gudmundsson MT, Högnadóttir T, et al (2017) Subglacial volcanic activity above a lateral dyke path during the 2014–2015 Bárdarbunga-Holuhraun rifting episode, Iceland. Bull Volcanol 79:38. https://doi.org/10.1007/s00445-017-1122-z

Roberts IL, Coney JER, Gibbs BM (2011) Estimation of radiation losses from sheathed thermocouples. Appl Therm Eng 31:2262–2270. https://doi.org/10.1016/j.applthermaleng.2011.03.020

Rodriguez-Gonzalez A, Aulinas M, Mossoux S, et al (2021) Comparison of real and simulated lava flows in the Holocene volcanism of Gran Canaria (Canary Islands, Spain) with Q-LavHA: contribution to volcanic hazard management. Nat Hazards 107:1785–1819. https://doi.org/10.1007/s11069-021-04660-6

Rogic N, Bilotta G, Ganci G, et al (2022a) The Impact of Dynamic Emissivity–Temperature Trends on Spaceborne Data: Applications to the 2001 Mount Etna Eruption. Remote Sens 14:1641. https://doi.org/10.3390/rs14071641

Rogic N, Bilotta G, Ganci G, et al (2022b) The Impact of Dynamic Emissivity–Temperature Trends on Spaceborne Data: Applications to the 2001 Mount Etna Eruption. Remote Sens 14:1641. https://doi.org/10.3390/rs14071641

Rogic N, Cappello A, Ferrucci F (2019a) Role of Emissivity in Lava Flow 'Distance-to-Run' Estimates from Satellite-Based Volcano Monitoring. Remote Sens 11:662. https://doi.org/10.3390/rs11060662

Rogic N, Cappello A, Ganci G, et al (2019b) Spaceborne EO and a Combination of Inverse and Forward Modelling for Monitoring Lava Flow Advance. Remote Sens 11:3032. https://doi.org/10.3390/rs11243032

Rose SR, Watson IM, Ramsey MS, Hughes CG (2014) Thermal deconvolution: Accurate retrieval of multispectral infrared emissivity from thermally-mixed volcanic surfaces. Remote Sens Environ 140:690–703. https://doi.org/10.1016/j.rse.2013.10.009

Rozenbaum O, Blanchard C, De Sousa Meneses D (2019) Determination of high-temperature radiative properties of porous silica by combined image analysis, infrared spectroscopy and numerical simulation. Int J Therm Sci 137:552–559. https://doi.org/10.1016/j.ijthermalsci.2018.12.025

Rozenbaum O, De Sousa Meneses D, Echegut P (2009) Texture and Porosity Effects on the Thermal Radiative Behavior of Alumina Ceramics. Int J Thermophys 30:580–590. https://doi.org/10.1007/s10765-008-0510-1

Rozenbaum O, Meneses DDS, Auger Y, et al (1999) A spectroscopic method to measure the spectral emissivity of semi-transparent materials up to high temperature. Rev Sci Instrum 70:4020–4025. https://doi.org/10.1063/1.1150028

Ruff SW, Christensen PR, Barbera PW, Anderson DL (1997) Quantitative thermal emission spectroscopy of minerals: A laboratory technique for measurement and calibration. J Geophys Res Solid Earth 102:14899–14913. https://doi.org/10.1029/97JB00593

Sako EY, Orsolini HD, Moreira M, et al (2020) Emissivity of spinel and titanate structures aiming at the development of industrial high-temperature ceramic coatings. J Eur Ceram Soc S0955221920309109. https://doi.org/10.1016/j.jeurceramsoc.2020.11.010

Salisbury JW, D'Aria DM (1994) Emissivity of terrestrial materials in the 3–5 µm atmospheric window. Remote Sens Environ 47:345–361. https://doi.org/10.1016/0034-4257(94)90102-3

Salisbury JW, D'Aria DM (1992) Emissivity of terrestrial materials in the 8–14 µm atmospheric window. Remote Sens Environ 42:83–106. https://doi.org/10.1016/0034-4257(92)90092-X

Scaillet B, Pichavant M, Cioni R (2008) Upward migration of Vesuvius magma chamber over the past 20,000 years. Nature 455:216–219. https://doi.org/10.1038/nature07232

Shea T, Houghton BF, Gurioli L, et al (2010) Textural studies of vesicles in volcanic rocks: An integrated methodology. J Volcanol Geotherm Res 190:271–289. https://doi.org/10.1016/j.jvolgeores.2009.12.003

Sobrino JA, Li Z-L, Stoll MP, Becker F (1994) Improvements in the split-window technique for land surface temperature determination. IEEE Trans Geosci Remote Sens 32:243–253. https://doi.org/10.1109/36.295038

Sprague AL, Donaldson Hanna KL, Kozlowski RWH, et al (2009) Spectral emissivity measurements of Mercury's surface indicate Mg- and Ca-rich mineralogy, K-spar, Na-rich plagioclase, rutile, with possible perovskite, and garnet. Planet Space Sci 57:364–383. https://doi.org/10.1016/j.pss.2009.01.006

Stefan J (1879) Über die Beziehung zwischen der Wärmestrahlung und der Temperatur. Sitzungsberichte Math-Naturwissenschaftlichen Cl Kais Akad Wiss 391–428

Takeuchi S (2011) Preeruptive magma viscosity: An important measure of magma eruptibility. J Geophys Res 116:B10201. https://doi.org/10.1029/2011JB008243

Thivet S (2016) Caractérisation magmatique du système superficiel du Piton de la Fournaise à travers l'étude texturale e. Laboratoire Magmas et Volcans, Clermont-Ferrand

Thompson JO, Ramsey MS (2020a) Spatiotemporal variability of active lava surface radiative properties using ground-based multispectral thermal infrared data. J Volcanol Geotherm Res 408:107077. https://doi.org/10.1016/j.jvolgeores.2020.107077

Thompson JO, Ramsey MS (2021) The influence of variable emissivity on lava flow propagation modeling. Bull Volcanol 83:41. https://doi.org/10.1007/s00445-021-01462-3

Thompson JO, Ramsey MS (2020b) Uncertainty Analysis of Remotely-Acquired Thermal Infrared Data to Extract the Thermal Properties of Active Lava Surfaces. Remote Sens 12:193. https://doi.org/10.3390/rs12010193

Thompson JO, Williams DB, Lee RJ, Ramsey MS (2021) Quantitative Thermal Emission Spectroscopy at High Temperatures: A Laboratory Approach for Measurement and Calibration. J Geophys Res Solid Earth 126:. https://doi.org/10.1029/2021JB022157

Thomson JL, Salisbury JW (1993) The mid-infrared reflectance of mineral mixtures (7–14 µm). Remote Sens Environ 45:1–13. https://doi.org/10.1016/0034-4257(93)90077-B

Thordarson T, Höskuldsson Á Postglacial volcanism in Iceland. 32

Toner K, Brossier J, Gilmore M (2019) Complex Radar Emissivity Variations At Some Large Venusian Volcanoes. p 3

Vaughan RG, Calvin WM, Taranik JV (2003) SEBASS hyperspectral thermal infrared data: surface emissivity measurement and mineral mapping. Remote Sens Environ 85:48–63. https://doi.org/10.1016/S0034-4257(02)00186-4

Veneranda M, Aramendia J, Bellot-Gurlet L, et al (2018) FTIR spectroscopic semi-quantification of iron phases: A new method to evaluate the protection ability index (PAI) of archaeological artefacts corrosion systems. Corros Sci 133:68–77. https://doi.org/10.1016/j.corsci.2018.01.016

Vincent RK, Rowan LC, Gillespie RE, Knapp C (1975) Thermal-infrared spectra and chemical analyses of twenty-six igneous rock samples. Remote Sens Environ 4:199–209. https://doi.org/10.1016/0034-4257(75)90016-4

Walker GPL (1993) Basaltic-volcano systems. Geol Soc Lond Spec Publ 76:3–38. https://doi.org/10.1144/GSL.SP.1993.076.01.01

Wang A, Jolliff BL, Haskin LA, et al (2001) Characterization and comparison of structural and compositional features of planetary quadrilateral pyroxenes by Raman spectroscopy. Am Mineral 86:790–806. https://doi.org/10.2138/am-2001-0703

Wooster MJ, Rothery DA (1997) Thermal monitoring of Lascar Volcano, Chile, using infrared data from the along-track scanning radiometer: a 1992-1995 time series. Bull Volcanol 58:566–579. https://doi.org/10.1007/s004450050163

Wright R, Rothery DA, Blake S, Pieri DC (2000) Improved remote sensing estimates of lava flow cooling: A case study of the 1991-1993 Mount Etna eruption. J Geophys Res Solid Earth 105:23681–23694. https://doi.org/10.1029/2000JB900225

Wyatt MB, Hamilton VE, McSween Jr HY, et al (2001) Analysis of terrestrial and Martian volcanic compositions using thermal emission spectroscopy: 1. Determination of mineralogy, chemistry, and classification strategies. J Geophys Res Planets 106:14711–14732. https://doi.org/10.1029/2000JE001356

Xiao Y, Wan C, Shahsafi A, et al (2020) Precision Measurements of Temperature-Dependent and Nonequilibrium Thermal Emitters. Laser Photonics Rev 14:1900443. https://doi.org/10.1002/lpor.201900443

Yang J, Duan S-B, Zhang X, et al (2020) Evaluation of Seven Atmospheric Profiles from Reanalysis and Satellite-Derived Products: Implication for Single-Channel Land Surface Temperature Retrieval. Remote Sens 12:791. https://doi.org/10.3390/rs12050791

Yang Y, Xia Q, Feng M, Zhang P (2010a) Temperature dependence of IR absorption of OH species in clinopyroxene. Am Mineral 95:1439–1443. https://doi.org/10.2138/am.2010.3501

Yang Y, Xia Q, Feng M, Zhang P (2010b) Temperature dependence of IR absorption of OH species in clinopyroxene. Am Mineral 95:1439–1443. https://doi.org/10.2138/am.2010.3501

Ye C, Rucks MJ, Arnold JA, Glotch TD (2019) Mid-Infrared Optical Constants of Labradorite, a Triclinic Plagioclase Mineral. Earth Space Sci 6:2410–2422. https://doi.org/10.1029/2019EA000915

Zakšek K, Shirzaei M, Hort M (2013) Constraining the uncertainties of volcano thermal anomaly monitoring using a Kalman filter technique. Geol Soc Lond Spec Publ 380:137–160. https://doi.org/10.1144/SP380.5

Zinin P, Tatsumi-Petrochilos L, Bonal L, et al (2011) Raman spectroscopy of titanomagnetites: Calibration of the intensity of Raman peaks as a sensitive indicator for their Ti content. Am Mineral 96:1537–1546. https://doi.org/10.2138/am.2011.3745

7.4. Table of captions

Institut des Sciences de la Terre d'Orléans
1A, Rue de la Férollerie, 45100 Orléans (France)

Jonas BIREN

PROPRIÉTÉS RADIATIVES des MAGMAS SECS et RICHES en CRISTAUX

Résumé : La température est un paramètre clé contrôlant la rhéologie d'une coulée de lave. Cependant, le comportement imprévisible des éruptions empêche les mesures directes de températures. Par conséquent, ces mesures sont régulièrement effectuées par des techniques de télédétection (avec des détecteurs sur le terrain ou depuis l'espace) développées pour mesurer la radiation Infra-Rouge (IR). Ces techniques bien établies sont malgré tout sujettes à d'importantes erreurs reliées au manque de connaissance de l'un des paramètres les plus important, dénommé l'émissivité spectrale. L'objectif de cette étude est de combler ce manque en explorant la relation émissivité–température de basaltes lato sensu (basalte de Bardarbunga, basanite de Fasnia, MORB basalte de Juan de Fuca, et océanite du Piton de la Fournaise), et de cristaux magmatiques (pyroxène, plagioclase, et oxyde de fer). L'émissivité spectrale a été mesurée de façon *in situ* à températures magmatiques (jusqu'à 1800 K) sur une large gamme spectrale (350–8000 cm^{-1}; 1.25–28.6 µm), à l'aide d'un appareil IR sans contact. Pour éclaircir le comportement radiatif complexe de ces échantillons en fonction de la température, des analyses systématiques de la texture, de la composition, de la structure, et du comportement thermique de ceux-ci ont été effectuées à l'aide des MEB, Microsonde, spectroscopie Raman, DRX, MET, et DSC. Les résultats démontrent que l'émissivité spectrale est dépendante de la température, du nombre d'onde, ainsi que du degré de polymérisation combiné à la teneur en FeO. L'émissivité spectrale est grandement influencée par la présence de cristaux qui ont des propriétés radiatives distinctes et plus particulièrement par l'agglomération et la cristallisation à l'échelle microscopique d'oxydes riche en Fe. Dès lors, cette étude prouve que l'émissivité spectrale pour une composition magmatique donnée ne peut pas être considérée comme constante. Pour finir, les mesures de laboratoire sur l'émissivité spectrale permettent de raffiner de 50 degrés la valeur de température de la coulée de lave d'Holuhraun (2014–2015) initialement mesurée par télédétection. Ces nouvelles connaissances pourront permettre dans le futur de réduire l'erreur associée aux estimations de température faites par télédétection IR, cette dernière étant indispensable pour l'amélioration de l'évaluation des risques lors d'une crise volcanique.

Mots clés : Emissivité / Température / Spectroscopie Vibrationnelle / Télédétection / Volcanologie / Pétrologie

RADIATIVE PROPERTIES of DRY and CRYSTAL-BEARING LAVAS

Summary: Temperature is a key parameter controlling the rheology of lava flows. However, the unpredictable hazard of eruptions prevents direct measurements of hot magmatic bodies. Thus, the temperature of lava is mostly retrieved by remote sensing techniques (ground- or satellite-based detectors) build on measuring infrared (IR) radiance. These well-established techniques are however subjected to important errors related to the poor knowledge of one of the most critical parameters, namely spectral emissivity. The aim of this study is to fill this gap by exploring the emissivity–temperature relationship of different basalts *lato sensu* (Bardarbunga basalt, Fasnia basanite, Juan de Fuca MORB basalt, and Oceanite from Piton de la Fournaise) and magmatic minerals (pyroxene, plagioclase, iron-rich oxide). *In situ* emissivity measurements were performed at magmatic temperatures (up to 1800 K) over a wide spectral range (350–8000 cm^{-1}; 1.25–28.6 µm), using a non-contact IR apparatus. To unravel the complex radiative behavior of the samples with temperature, structural, chemical, textural, and thermal analyses using SEM, EMPA Raman spectroscopy, XRD, TEM, and DSC, were systematically performed. Results show that spectral emissivity varies with temperature, wavenumber, and the sample degree of polymerization combined with FeO content. Spectral emissivity is greatly affected by the presence of crystals with distinct radiative properties and specifically by the clustering and crystallization of Fe-rich crystals at the micro-scale. Consequently, this study proves that spectral emissivity cannot be assumed constant for a given magma composition. Finally, laboratory-measured values of spectral emissivity allowed refining the remote sensing temperature of the 2014–2015 Holuhraun lava by ~50 degrees. These new insights will ultimately reduce uncertainties in temperature estimates based on IR technology, information that are crucial to improve hazard assessment in volcanic crisis.

Keywords: Emissivity / Temperature / Vibrational Spectroscopy / Remote Sensing / Volcanology / Petrology

Earth Sciences Institute of Orléans